新 制
工
887
京大附図

Numerical Modeling of Mass Transport in Rock Mass

1992

Akira Kobayashi

CONTENTS

Chapter 1 INTRODUCTION 1 - 9

1.1 Background 1

1.2 Scope of Work 3

1.3 Perspective from Conservation Law 5

Chapter 2 NUMERICAL METHODS OF FLUID FLOW IN ROCK MASS 10 - 110

2.1 Introduction 10

2.2 Previous Works 13

2.3 Fluid Flow in Porous Media 18
- 2.3.1 Introduction 18
- 2.3.2 Saturated-unsaturated flow modeling 19
- 2.3.3 Quasi three-dimensional approach 24
- 2.3.4 Discussions 25

2.4 Two-dimensional Deformable Double Porosity Model 27
- 2.4.1 Introduction 27
- 2.4.2 Basic equations 28
- 2.4.3 Numerical analyses 38
- 2.4.4 Conclusions 52

2.5 Fluid Flow in Single Fracture Plane 54
- 2.5.1 Introduction 54
- 2.5.2 Modeling of channels 56
- 2.5.3 Results 62
- 2.5.4 Conclusions 69

2.6 Three-dimensional Discontinuous Model 72
2.6.1 Introduction 72
2.6.2 Verification of the joint network model 73
2.6.3 Three-dimensional mesh generator 78
2.6.4 Fracture flow with leakage form rock matrices 84
2.6.5 Examination of the influence of rock blocks 90
2.6.6 Conclusions 100

Chapter 3 COUPLING EFFECTS ON FLUID FLOW 111-204

3.1 Introduction 111

3.2 Previous Work 113

3.3 Two-dimensional Thermal-Hydraulic-Mechanical Coupling 117
3.3.1 Introduction 117
3.3.2 Basic theory 117
3.3.3 Verification of code 103
3.3.4 Effects of the dependence of the parameters on temperature and pressure 133
3.3.5 Effects on flow around an underground opening 155
3.3.6 Analysis of the Buffer mass test 160

3.4 Three-dimensional Thermal-Hydraulic-Mechanical Coupling 185
3.4.1 Introduction 185
3.4.2 Preconditioned conjugate gradient method 185
3.4.3 Comparison with analytical solutions 187
3.4.4 Analysis of a imaginary deep nuclear waste depository 190
3.4.5 Conclusions 196

Chapter 4 NUMERICAL METHODS OF SOLUTE TRANSPORT IN ROCK MASSES 206 - 283

4.1 Introduction 206

4.2 Previous Works 210

4.3 Two-dimensional Solute Transport Problem 217
4.3.1 Introduction 217
4.3.2 Upstream finite element method 218
4.3.3 Two-dimensional Eulerian and Lagrangian scheme 228
4.3.4 Conclusions and discussions 248

4.4 Transport Problem in Complex Geology 250
4.4.1 Introduction 250
4.4.2 Numerical models 252
4.4.3 Results 257
4.4.4 Conclusions 266

4.5 Three-dimensional Transport Model 270
4.5.1 Introduction 270
4.5.2 Basic theory 270
4.5.3 Examples 273
4.5.4 Conclusions 278

Chapter 5 APPLICATION OF SOLUTE TRANSPORT ANALYSES 284 - 341

5.1 Introduction 284

5.2 Transport in a Single Fracture Plane 286
5.2.1 Model description 286
5.2.2 Analyses results 292
5.2.3 Conclusions 297

5.3 Analyses of Field Tracer Test 302
5.3.1 Field tracer test 302
5.3.2 Model description 303

5.3.3 Results of the analyses 307
5.3.4 Discussions 313

5.4 Transport under Coupled Phenomena 319
5.4.1 Model description 319
5.4.2 Analysis method and strategy 323
5.4.3 Results 324
5.4.4 Conclusions 337

Chapter 6 CONCLUSIONS 342 - 349

List of Figures

Figure 2.1.1 Several types of rock interstices 12
(a) well-sorted sedimentary deposit having high porosity;
(b) poorly sorted sedimentary deposit having low porosity;
(c) well-sorted sedimentary deposit consisting of pebbles that are themselves porous, so that the deposit as a whole has a very high porosity;
(d) well-sorted sedimentary deposit whose porosity has been diminished by the deposition of mineral matter in the interstices;
(e) rock rendered porous by solution;
(f) rock rendered by fracturing
(after Meinzer(1923))

Figure 2.3.1 Definition of porosity and representative elementary volume (after Bear and verruijit(1987)) 19
U is a volume of a sphere centered at an arbitrary point, U_v is the volume of void space within U and U_0 is the REV

Figure 2.4.1 Double porosity modeling 29
The ground is modeled for two representative strata, S and C. In this case, the stratum St is omitted from the model.

Figure 2.4.2 Double porosity model of fractured rock mass 30

Figure 2.4.3 Comparison of analytical solution with numerical one with double porosity model (one-dimensional consolidation problem) 39

Figure 2.4.4 Comparison of experimental results with numerical ones with double porosity model (saturated-unsaturated seepage problem) 40

Figure 2.4.5 Schematic compression-time curve 41

Figure 2.4.6 Finite element model used in the analysis of secondary compression problem 42

Figure 2.4.7 Calculated compression-time curve with double porosity model 43

Figure 2.4.8 Mechanical analogue of secondary compression with double porosity model 43

Figure 2.4.9 Finite element mesh used in the Lugeon test simulation 46

Figure 2.4.10 Unsteady change of pressure head distribution obtained from the Lugeon test simulation with double porosity model (tf/m^2) 47

Figure 2.4.11 Finite element mesh used in the two-dimensional consolidation problem 48

Figure 2.4.12 Compression-time curve at point A in the two-dimensional consolidation problem 49

Figure 2.4.13 Unsteady change of ground water tables in the two-dimensional consolidation problem 51

Figure 2.4.14 Settlement at ground surface as a function of distance from center line in the two-dimensional consolidation problem 51

Figure 2.4.15 Lateral displacement at the C-C' section in the two-dimensional consolidation problem 53

Figure 2.5.1 Schematic view of channels on fracture plane 55

Figure 2.5.2 Schematic figure for the modeling of the channels 57
(a) Schematic finite element mesh and boundary conditions
(b) Schematic view of the channels included in one element

Figure 2.5.3 Calculated velocity distributions 63

Figure 2.5.4 Observed results in the migration test at the Stripa project 64

Figure 2.5.5 Comparison of real mechanical aperture (b_f) with theoretical smooth wall conducting apertures (b_r) (after Barton(1982) 68

Figure 2.5.6 Schematic view of fracture roughness trace 70

Figure 2.5.7 Distributions of apertures at the outlet boundary used in the analyses 70

Figure 2.6.1 Schematic view of the experiment about the seepage flow in the fracture rock mass 75

Figure 2.6.2 Fractured rock model used in the experiment 75

Figure 2.6.3 Measured aperture density distribution 77

Figure 2.6.4 Comparison of measured pressure change with numerical one with the joint element model 77

Figure 2.6.5 Convenient coordinate system 79

Figure 2.6.6 Flow of the mesh generating code for three-dimensional fractured medium 81

Figure 2.6.7 Fracture model of Case1 83

Figure 2.6.8 Fracture model of Case2 83

Figure 2.6.9 Fracture model of Case3 83

Figure 2.6.10 System in rectangular axes 86

Figure 2.6.11 Velocity and total head distribution of Case 1 (unit is 100tf.m2) at 7th day. 89
Solid lines are for fractures and dotted ones are for blocks

Figure 2.6.12 Sketch of CRNL ground water flow study site 91

Figure 2.6.13 Model used in the analyses 91

Figure 2.6.14 Drawdown versus log time response by conventional model using the data shown in Table 2.6.3 95

Figure 2.6.15 Drawdown versus log time response by modified double porosity model using the data shown in Table 2.6.3 (α=10^{-6}) 95

Figure 2.6.16 Drawdown versus log time response by conventional model such that the results agree with those from the field 96

Figure 2.6.17 Log drawdown versus log time response by conventional model such that the results agree with those from the field 96

Figure 2.6.18 Drawdown versus log time response by modified double porosity model using revised transmissivity (α=10^{-4}) 97

Figure 2.6.19 Log drawdown versus log time response by modified double porosity model using revised transmissivity (α=10^{-4}) 97

Figure 2.6.20 Drawdown versus log time response by modified double porosity model using revised transmissivity (α=2x10^{-4}) 99

Figure 2.6.21 Drawdown versus log time response by conventional model with isotropic permeability of rock blocks 99

Figure 2.6.22 Drawdown versus log time response by modified double porosity model with isotropic permeability of rock blocks 100

Figure 3.3.1 Coupled phenomena considered in THAMES 118

Figure 3.3.2 Comparison with the analytical solution of the one-dimensional consolidation problem 130

Figure 3.3.3 Comparison with the analytical solution of the stress-strain problem of a thick-walled circular cylinder subjected to uniform internal and external pressures 130

Figure 3.3.4 Comparison with the analytical solution of the thermal stress problem of a thick-walled circular cylinder subjected to a uniform temperature gradient 131

Figure 3.3.5 Comparison with the analytical solution of the one-dimensional heat conduction problem 131

Figure 3.3.6 Comparison with the experimental results of the coupled thermal and hydraulic problem (L is the length of the specimen, x is the distance from the top of the specimen, T_0 is the temperature of the injected water and T_l is the temperature of the water in the specimen at the initial state.) 132

Figure 3.3.7 Comparison with the experimental results of the saturated-unsaturated seepage problem 132

Figure 3.3.8 Relationships of Young's modulus to temperature for various kinds of granite (after Simooka (1983) and Heuze (1983))
E_0 is the Young's modulus at the temperature of 0°C 135

Figure 3.3.9 Relationships of Poisson's ratio to temperature for various kinds of granite (after Simooka (1983) and Heuze (1983)) 135

Figure 3.3.10 Relationships of thermal expansivity to temperature for various kinds of granite (after Simooka (1983) and Heuze (1983)) 137

Figure 3.3.11 Schematic of the variation of thermal linear expansion of granite at temperature and pressure (after Heuze (1983)) 137

Figure 3.3.12 Relationships of heat capacity to temperature for various kinds of granite (after Simooka (1983) and Heuze (1983)) 138
C_{v0} is the heat capacity at the temperature of 0°C

Figure 3.3.13 Relationships of thermal conductivity to temperature for various kinds of granite (after Simooka (1983) and Heuze (1983)) 140
K_{T0} is the thermal conductivity at the temperature of 0°C

Figure 3.3.14 Finite element model and temperature distribution as a function of time at the heat source temperature of 100°C 149

Figure 3.3.15 Relations between the temperatures at the heat sources and the temperatures at a depth of 1m under the heat source after 10^6 seconds from the beginning 151

Figure 3.3.16 Change process of the total head distribution at the heat source temperature of 30°C 151

Figure 3.3.17 Distribution of permeabilities after 10^6 seconds at the heat source temperature of 30°C 153

Figure 3.3.18 Effects of cyclic loading on permeability of tension fracture in granite with radial flow (after Iwai (1976)) 153
Q is outlet flow rate and Δh is the applied head difference

Figure 3.3.19 Change in the displacement at the upper boundary in setting the heat sources at 100°C 154

Figure 3.3.20 Relation between the displacement at the upper boundary and the temperature of the heat sources after 10^6 seconds 154

Figure 3.3.21 Model of macroscopic permeability test and observed and calculated water levels 157

Figure 3.3.22 Relation between the observed and calculated horizontal permeability at the middle height of the drift and the distance from the drift wall 157

Figure 3.3.23 Calculated vertical permeability distribution 159

Figure 3.3.24 Relations between pF, S_r and e of a weathered granite soil 163

Figure 3.3.25 Projected figure of Figure 3.3.24 on the pF-S_r plane 163

Figure 3.3.26 Projected figure of Figure 3.3.24 on the pF-lnS_r plane 164

Figure 3.3.27 Relation between ψ_{cr} and e 164

Figure 3.3.28 Finite element mesh used in the analysis of the Buffer mass test 171

Figure 3.3.29 Unsteady change in the distribution of a) porosity, b) the degree of saturation, c) thermal conductivity and d) permeability in the HCC 173

Figure 3.3.30 Unsteady change in the calculated temperature distributions 174

Figure 3.3.31 Unsteady change in the calculated porosity distributions 175

Figure 3.3.32 Unsteady change in the calculated water content distributions 176

Figure 3.3.33 Comparison of the numerical temperature distributions from Cases 1 and 2 with the experimental ones of the BMT 178

Figure 3.3.34 Calculated isothermal lines of Cases 1 and 2 after 0.9 years 178

Figure 3.3.35 Comparison of the calculated water contents distributions in the HCC with the observed ones 179

Figure 3.3.36 Comparison of measured iso-moisture contents in the HCC with the measured ones and the calculated iso-void ratiosa bout 10 months after the start 180

Figure 3.3.37 Comparison of the measured unsteady changes in pressure at the middle height of the heater hole wall with the calculated ones 182

Figure 3.4.1 Finite element mesh of consolidation problem 188

Figure 3.4.2 Comparison of numerical results with Terzaghi's solutions 189

Figure 3.4.3 Finite element mesh of thick-walled cylinder with a constant temperature gradient 190

Figure 3.4.4 Comparison of numerical results of thermal stress problem with analytical ones 191

Figure 3.4.5 Finite element mesh and boundary conditions for heat transfer problem 192

Figure 3.4.6 Comparison of numerical results of heat transfer problem with analytical ones 192

Figure 3.4.7 Finite element mesh and analysis conditions for three-dimensional model 193

Figure 3.4.8 Finite element mesh and analysis conditions for two-dimensional model 195

Figure 3.4.9 Displacement vector distribution at 100 years (two-dimensional analysis) 195

Figure 3.4.10 Displacement vector distribution at 100 years (three-dimensional analysis) 196

Figure 3.4.11 Relations between the elapsed time and the displacement from three-dimensional analysis 197

Figure 3.4.12 Velocity vector distribution at 10000 years 198

Figure 4.1.1 Modeling types for the geological structure (after Furuichi (1984)) 207

Figure 4.1.2 Types of adsorption isotherm modeling 207

Figure 4.2.1 Concept of the representative elemental volume (after Gillham and Cherry (1982)) 214

Figure 4.2.2 Concept of the scale effect of the dispersivity (after Gillham and Cherry (1982)) 214

Figure 4.2.3 Relationships between molecular diffusion and convective dispersion (after Pfannkuch (1963), Saffman (1960)) 216

Figure 4.3.1 Shape function (N) and weighting function (W) in a one-dimensional problem 219

Figure 4.3.2 Concentration distribution at time of 0.01 of the one-dimensional analysis (v=100, D=1.0, Δx=0.1, Δt=0.001, P_e=10, C_u=1) 223

Figure 4.3.3 Concentration distribution at time of 0.01 of the one-dimensional analysis (v=100, D=1.0, Δx=0.05, P_e=5, Δt is changed to arrange the Courant number) 225

Figure 4.3.4 Concentration distribution at time of 0.01 of the one-dimensional analysis (v=100, D=1.0, Δx=0.05, Δt=0.0005, P_e=5, C_u=0.1), "Modified" means the upstream method using a common technique to reduce the numerical dispersion, and " Upstream" means the convectional upstream method. 227

Figure 4.3.5 Concentration distribution at time of 0.01 of the one-dimensional analysis (v=100, D=1.0, Δx=0.1, Δt=0.0001, P_e=10, C_u=0.1), "Modified" means the upstream method using a common technique to reduce the numerical dispersion, and " Upstream" means the convectional upstream method. 227

Figure 4.3.6 Comparison of the concentration distributions 234
" another interpolation" means the results from equation (4.3.35)

Figure 4.3.7 Schematic representation of the process to find the four representative concentration point around the nodal point 236

Figure 4.3.8 Schematic representation of concentration plane around the nodal point 237

Figure 4.3.9 Comparison of the total head distributions 241

Figure 4.3.10 Comparison of the vertical downward velocity distributions 241

Figure 4.3.11 Comparison of two-dimensional problem 243
Numerical results are obtained from the Eulerian and Lagrangian method using the proposed interpolation method

Figure 4.3.12 Influences of the Peclet number on the relationships between the Courant number and the root mean square of the numerical errors 244

Figure 4.3.13 Comparison of analytical result and numerical result from the convectional method of characteristics 247

Figure 4.4.1 Schematic view of the heterogeneous model 258

Figure 4.4.2 Breakthrough curves of Case 1 of the heterogeneous model 259

Figure 4.4.3 Breakthrough curves of Case 2 of the heterogeneous model 259

Figure 4.4.4 Concentration distributions in the flow direction of a realization of Case 1 of the heterogeneous model at time of about 9×10^3 260

Figure 4.4.5 Concentration distributions at the center of each realization of Case 1 of the heterogeneous model at time of about 9×10^3 261

Figure 4.4.6 Breakthrough curve obtained from the double porosity model using the same parameters as those of both media in the analyses of the heterogeneous model 262

Figure 4.4.7 Concentration distribution in the flow direction of the double porosity model at time of about 9×10^3 263

Figure 4.4.8 Breakthrough curve obtained from the adjustment to the retardation factor of the very permeable medium of the double porosity model in order to obtain a continuously smooth curve 263

Figure 4.4.9 Breakthrough curve obtained from the two-site model of which $K_1 = 10^{-3}$, $K_2 = 10^{-6}$, $K_1' = 10^{-1}$ and $K_2' = 10^{-3}$ 265

Figure 4.4.10 Breakthrough curve obtained from the two-site model of which $K_1 = 10^{-3}$, $K_2 = 10^{-6}$, $K_1' = 0.05$ and $K_2' = 10^{-3}$ 265

Figure 4.4.11 Concentration distribution obtained from the two-site model of which $K_1 = 10^{-3}$, $K_2 = 10^{-6}$, $K_1' = 10^{-1}$ and $K_2' = 10^{-3}$ at time of about 9×10^3 266

Figure 4.4.12 Breakthrough curve obtained from the non-equilibrium of which $K_1 = 10^{-1}$ and $K_2 = 10^{-3}$ 267

Figure 4.5.1 Schematic view of the model 272

Figure 4.5.2 Schematic view of the first example problem 274

Figure 4.5.3 Comparison of the breakthrough curves 275
AD model is the advection-dispersion model, ADM model is the advection-dispersion model with matrix diffusion and ADML model is the new model. Γ of ADML model 1 is 0.0001 and Γ of ADML model 2 is 0.001.

Figure 4.5.4 Schematic view of the second example 276

Figure 4.5.5 Comparison of the concentration distributions at time 9.27. 276

Figure 5.2.1 Finite element mesh used in the analyses of flow and transport problem in a single fracture plane 292

Figure 5.2.2 Generated aperture distributions 293

Figure 5.2.3 Velocity vector distributions 293

Figure 5.2.4 Comparison between calculated breakthrough curves of the non-adsorbing tracer, Uranine, and measured ones 295

Figure 5.2.4 Comparison between calculated breakthrough curves of the non-adsorbing tracer, Uranine, and measured ones (continued) 296

Figure 5.2.5 Comparison between calculated breakthrough curves of the adsorbing tracer, Cesium, and measured ones 298

Figure 5.2.5 Comparison between calculated breakthrough curves of the adsorbing tracer, Cesium, and measured ones (continued) 299

Figure 5.3.1 Borehole layout and approximate extent of fracture zone 3
A solid line indicates an analysis region 304

Figure 5.3.2 Finite element mesh used in the flow analyses of CRNL tracer test 305

Figure 5.3.3 Calibration process of flow and transport analyses, in which n is the porosity in the fracture, T is the transmissivity in the fracture, α is the coefficient related to the leakage, D is the dispersion coefficient in the fracture, R_3 is the product of the porosity and the retardation factor in the rock matrix and β is the matrix diffusion coefficient. 308

Figure 5.3.4 Comparison between calculated and measured R.T.D. of Test 1 with the aperture of Case b 310

Figure 5.3.5 Comparison between calculated and measured R.T.D. of Test 1 with the aperture of Case c 310

Figure 5.3.6 Comparison between calculated and measured R.T.D. of Test 2 312

Figure 5.3.7 Comparison between measured and calculated R.T.D. of Test 3 obtained by using the same parameters as the ones in the analyses of Tests 1 and 2 314

Figure 5.3.8 Comparison between measured and calculated R.T.D. of Test 3 by using the parameters shown in Table 5.3.4 314

Figure 5.3.9 Distribution of the leakage rate for Test 1 317

Figure 5.3.10 Distribution of the leakage rate for Test 3 318

Figure 5.4.1 Schematic view of the imaginary depository and finite element mesh used for the coupled analyses 320

Figure 5.4.2 Heat generation from a vitrified waste 321

Figure 5.4.3 Temperature history at the center of the depository and the place at 100 m over the center of the depository 325

Figure 5.4.4 Temperature distribution of Case 1 326

Figure 5.4.5 Velocity distribution of Case 1 after 50 years from the beginning of the disposal 327

Figure 5.4.6 History of upward velocity at the place 100 m over the center of the depository 327

Figure 5.4.7 Deformation distribution of Case 1 328

Figure 5.4.8 History of upward deformation at the place 100 m over the center of the depository 329

Figure 5.4.9 Temperature distribution of Case 2 after 50 years from the beginning of the disposal 330

Figure 5.4.10 Velocity distribution of Case 2 after 50 years from the beginning of the disposal 330

Figure 5.4.11 Deformation distribution of Case 2 after 50 years from the beginning of the disposal 332

Figure 5.4.12 Concentration distribution of ^{137}Cs after 50 years from the disposal in Case 1 332

Figure 5.4.13 Concentration distribution of ^{137}Cs after 50 years from the disposal at the case in which the velocity is set at 100 times the one obtained from the coupled analysis of Case 1 333

Figure 5.4.14 Concentration distribution of ^{239}Pu after 500 years from the disposal in Case 1 333

Figure 5.4.15 Concentration distribution of ^{239}Pu after 500 years from the disposal at the case in which the velocity is set at 100 times the one obtained from the coupled analysis of Case 1 335

Figure 5.4.16 Concentration distribution of ^{239}Pu at the steady state in Case 1 335

Figure 5.4.17 Concentration distribution of ^{137}Cs after 50 years from the disposal in Case 2 336

Figure 5.4.18 Concentration distribution of ^{137}Cs after 50 years from the disposal at the case in which the velocity is set at 100 times the one obtained from the coupled analysis of Case 2 336

Figure 5.4.19 Concentration distribution of ^{137}Cs after 500 years from the disposal at the case in which the velocity is set at 100 times the one obtained from the coupled analysis of Case 2 338

Figure 5.4.20 Concentration distribution of ^{239}Pu after 500 years from the disposal in Case 2 338

Figure 5.4.21 Concentration distribution of ^{239}Pu after 50 years from the disposal at the case in which the velocity is set at 100 times the one obtained from the coupled analysis of Case 2 339

Figure 5.4.22 Concentration distribution of ^{239}Pu after 500 years from the disposal at the case in which the velocity is set at 100 times the one obtained from the coupled analysis of Case 2 339

Figure 5.4.23 Concentration distribution of ^{239}Pu at the steady state in Case 2 340

List of Tables

Table 1.2.1 Variables for each balance law 6

Table 2.2.1 Various methods solving initial boundary problems 14

Table 2.2.2 Previous works on saturated -unsaturated seepage analysis 15

Table 2.2.3 Previous works on joint elements (after Yashima (1985)) 17

Table 2.4.1 Data used in secondary compression analyses 41

Table 2.4.2 Data used in the Lugeon test analysis 46

Table 2.4.3 Data used in the two-dimensional consolidation problem 48

Table 2.5.1 Mean values for each cases 67

Table 2.6.1 Data for location of fractures 82

Table 2.6.2 Parameters used in the example problem 89

Table 2.6.3 Permeability and storage coefficient used in the analyses for field test at CRNL 93

Table 3.2.1 Previous main works for coupled hydraulic and mechanical problems 115

Table 3.3.1 Dynamic viscosity, μ, as a function of temperature 139

Table 3.3.2 Heat capacity of water, C_{vf}, as a function of temperature 142

Table 3.3.3 Degree of dependency of parameters on temperature and pressure 146

Table 3.3.4 Parameters at initial state 150

Table 3.3.5 Flow rate into the room at two different temperatures 159

Table 3.3.6 Unsaturated properties of swelling clay 167

Table 3.3.7 Approximate values of the pore pressure, and of the permeability, for Na bentonite at various bulk density (after Push and Borgesson (1985)) 167

Table 3.3.8 Permeability k in m/s versus bulk density of MX-80 (after Push and Borgesson (1985)) 167

Table 3.3.9 Unsaturated properties of buffer materials 169

Table 3.3.10 Swelling pressure P_s versus bulk density ρ of HCC at various temperature (after Push and Borgesson (1985)) 170

Table 3.3.11 Data of HCC used for analysis 171

Table 3.3.12 Comparison of the temperature at mid-height in heater hole no.1 recorded at BMT and calculated by numerical analysis 174

Table 3.4.1 Parameters used in the analysis of imaginary depository 193

Table 4.2.1 Comparison of Eulerian method and Lagrangian method (after Furuichi (1984)) 212

Table 4.4.1 Models used in the analyses 253

Table 4.5.1 Comparison of concentrations at distance of 1 at time 24.27 277

Table 5.3.1 Summary of tracer test conditions (after Raven,et al. (1988)) 303

Table 5.3.2 Parameters used in the seepage analyses 306

Table 5.3.3 Parallel plate openings determined from hydraulic tests (after Raven, et al (1988), unit is micrometers) 306

Table 5.3.4 Parameter values yield a good agreement with the observed results 311

Table 5.4.1 Parameters used in the coupled and transport analyses 322

Acknowledgement

This thesis is composed of research works for eight years by author who has been working as a researcher at the technical institute of Hazama corporation. After graduation from the Department of Agricultural Engineering at Kyoto University in 1982, he entered the Hazama corporation. The study mentioned in this thesis was started from the time when he had been a visiting scholar of the School of Civil Engineering in Kyoto University from 1985 to 1987.

Firstly, the author would like to thank Professor Toshihisa Adachi and Associate Professor Yuzo Ohnishi of the School of Civil Engineering at Kyoto University for their support and guidance throughout the course of this research. The academic atmosphere in their laboratory had been very stimulating him.

The author would like to express his very special thanks to Professor Takashi Hasegawa of the Department of Agricultural Engineering at Kyoto University and the staffs in his laboratory through which the author graduated from Kyoto University.

The author would like to acknowledge the kind support and constant encouragement given by the staffs of the technical institute of the Hazama corporation. Mr. Hiromi Kojo gave the author the chance to study at Kyoto University as the visiting scholar. Professor Keiichi Fujita of Tokyo Rika University, the former head of the technical institute of Hazama corporation, supported the study by the author. Mr. Yasuki Yamaguchi, the head of the technical institute, and Mr. Mutsuo Ohno, the director of the civil engineering division of the technical institute, have generously encouraged the author.

The author is also grateful to Associate Professor Yasuaki Ichikawa and Dr. Takashi Kyoya of Nagoya University, Associate Professor Tadashi Yamabe of Saitama University, Assistant Professor Ömer Aydan of Tokai university, Dr. Tadahiko Shiomi of Takenaka corporation, Mr. Masami Kamemura and Mr. Michito Shimo of Taisei corporation for their incentive discussions. Thanks are also due to Dr. Atsushi Iizuka of

Kanazawa University, Dr. Akira Murakami of Kyoto University. They have had a certain influence on the author.

Very sincere thanks are furthermore expressed to Mr. Ryo Yamashita for his important opinions and corporations for the transport analyses.

Special thanks are due to Ms. Heather Griswold for proofreading all of this thesis.

The author would like to express his heartfelt thanks to his wife Noriko and their sons, Masaru, Makoto and Manabu. Finally, the author is dedicating this thesis with affection to his parents, Shogo and Shirabe.

Chapter 1 INTRODUCTION

1.1 Background

In recent years, considerable attention has been focused on the storage of radionuclide waste in fractured rock. In such a storage system, fractures are the major conduits of both ground water and radionuclide leaking out of the repository. Hence, an accurate characterization of the hydrologic behavior of the fractured rock mass may be vital to the safety of such an operation. For the performance assessment of radioactive waste disposal systems, it is particularly important to predict how the radionuclide would be prevented from leaking through the natural ground.

In general, a numerical simulation is one of the most effective methods for predicting the behavior which will occur in the distant future. However, there are many unknown mechanisms involved with hydrologic and mechanical behavior in the natural ground, e.g., the fracture system and coupled behavior. To understand such difficult problems, in-situ and laboratory experiments have been carried out by many researchers under international cooperation, e.g., the Stripa project. Methods of numerical simulation have also been examined under international cooperation, e.g., HYDROCOIN and INTRAVAL, whose simulations are very useful to grasping the phenomena observed in in-situ and laboratory tests.

In the present study, the author will examine mass transport analysis methods and investigate the mass transport behavior in a rock mass by numerical approaches. Although a solute transport analysis is the most important subject of a safety assessment, the water flow has to be analyzed prior to the assessment. Since the concentration of radionuclide leaking out of a repository is generally not expected to grow very high, solute transport does not have any effect on the fluid flow behavior. Thus, the solute transport problem can be considered apart from the ground water transport problem.

The subjects investigated in this paper may be applied to other projects in addition to radioactive waste disposal systems. For example, the ground water flow analysis can be used for many types of projects in the field of civil engineering, e.g., dam construction and the excavation of underground openings. The coupled problems are also important to many projects because the real behavior is coupled with various phenomena. Moreover, the problem of solute transport is one of the most important subjects to be analyzed in regards to environmental pollution, since ground water pollution is becoming a serious problem in many situations.

1.2 Scope of Work

Based on the above-mentioned background, this paper may be divided into four parts. The first part, Chapter 2, is concerned with ground water flow analysis methods. The second part, Chapter 3, investigates the effects of the coupled mechanical and thermal behavior on the ground water flow. The third part, Chapter 4, focuses on solute transport analysis methods. Finally, in Chapter 5, transport analyses and ground water flow analyses are applied to real in-situ and laboratory experiments.

In Chapter 2, the fluid flow in a fractured rock mass is mainly investigated by numerical approaches. In order to do this, two simulation methods are proposed, i.e., one for the two-dimensional continuous approach and the other for the three-dimensional discontinuous approach. Using these approaches, real field tests and imaginary situations will be analyzed and the ground water flow behavior in various states of the ground will be examined. Moreover, the fluid transport in a fracture plane is investigated by numerical experiments, where transport is related to the channel flow in a fracture plane.

In Chapter 3, hydraulic, mechanical and thermal coupling problems are investigated. Firstly, the basic theory is introduced and then the effects of the change in the parameters on the coupled behavior by a numerical simulation are discussed. Granite is the material on which focus is placed in this examination. In addition, simulating the large scale permeability test and the Buffer mass test which were conducted in the Stripa project, the coupled behavior in the rock and buffer material is examined from various points of view. The three-dimensional approach is also presented, which uses the preconditioned conjugated gradient method to solve the coupled equations.

In Chapter 4, a few solute transport analysis methods are introduced, which use the velocity field obtained by the ground water flow analyses mentioned in the previous chapters. For two-dimensional schemes, the upstream and the coupled Eulerian and Lagrangian methods are examined. Moreover, the double porosity model and the non-equilibrium model are examined as the transport model through a complex geology. The

three dimensional model with plane joint elements is also introduced here. The methods of the numerical simulation of the solute transports are mainly investigated in this chapter.

In Chapter 5, the above-mentioned ground water flow analysis methods and the solute transport analysis methods are applied to a few real in-situ and laboratory tests. The validation of the models will be examined.

1.3 Perspective from Conservation Law

In this section, conservation equations are briefly discussed as background information for the mass transport process mentioned in this paper. By understanding a little of this information, each chapter will be seen in a better perspective.

A fundamental assumption of continuum mechanics is that average quantities are independent of the size of an averaging volume or area and are continuous over time and space. An average quantity is obtained by integrating a microscopic quantity over an averaging volume or area, whose averaging process yields a field of macroscopic quantities. In this filed of macroscopic quantities, the averaging volume represents and characterizes a physical point and may thus be referred to as an infinitesimal element of volume or a representative elementary volume as it is sometimes called. Based on the assumption that such a characteristic volume can be identified, the macroscopic balance equations are derived.

Hassanizadeh and Gray (1979) discussed the process of averaging in detail. They derived the following general forms for the macroscopic conservation equations of a typical thermodynamic property for multi-phase systems using the local volume averaging technique.

$$\frac{\partial}{\partial t}\left(\langle\rho\rangle_\alpha \overline{\psi}^\alpha\right) + \nabla\cdot\left(\langle\rho\rangle_\alpha \overline{v}^\alpha \overline{\psi}^\alpha\right) - \nabla\cdot\mathbf{i}^\alpha - \langle\rho\rangle_\alpha \bar{f}^\alpha - \langle\rho\rangle_\alpha e^\alpha(\rho\psi) - \langle\rho\rangle_\alpha \hat{I}^\alpha = \langle\rho\rangle_\alpha \overline{G}^\alpha \qquad in \quad V^+ + V^- \tag{1.3.1}$$

subject to :

$$\sum_\alpha \langle\rho\rangle_\alpha\left[e^\alpha(\rho\psi) + \hat{I}^\alpha\right] = 0 \qquad in \quad V^+ + V^- \tag{1.3.2}$$

and

$$[\langle\rho\rangle_\alpha \overline{\psi}^\alpha(\overline{v}^\alpha - \mathbf{u}) - \mathbf{i}^\alpha]\cdot\mathbf{N}^- = 0 \qquad on \quad \Sigma \tag{1.3.3}$$

where $\langle\rho\rangle_\alpha$ is the macroscopic mass density function, $\overline{\psi}^\alpha$ is the macroscopic property of phase α, $\overline{v}^\alpha$ is the macroscopic velocity field vector, $\mathbf{i}^\alpha$ and $\bar{f}^\alpha$ are the surface flux vector and the external supply of $\overline{\psi}^\alpha$, respectively. $e^\alpha(\rho\psi)$ and $\hat{I}^\alpha$ are the exchange of $\overline{\psi}^\alpha$ with other phases through phase changes and mechanical interactions, respectively. $\overline{G}^\alpha$ is the net production rate of $\overline{\psi}^\alpha$ and Σ is the surface of discontinuity which divides averaging volume V into V^+ and V^- and which moves with velocity $\mathbf{u}$. $\mathbf{N}^-$ is the unit vector normal to macroscopic surface Σ of space V^-. The summation in equation (1.3.2) is carried out over all phases.

The above equations consider an N-phase system, occupying space V and bounded by surface A, as the superposition of N continua which exchange thermodynamic properties through mechanical interactions and phase changes.

Equation (1.3.2) is the microscopic interfacial condition and asserts the conservation of thermodynamic property ψ for the whole body, while equation (1.3.3) is the general balance law across a macroscopic surface of discontinuity.

The individual balance laws for mass, momentum, angular momentum, energy and entropy are given by substituting the variables shown in Table 1.3.1 into equations (1.3.1)-(1.3.3).

Table 1.3.1 Variables for each balance law

Quality	ψ	$\mathbf{i}$	f	G
Mass	1	0	0	0
Linear momentum	v	t	g	0
Angular momentum	$r\times v$	$r\times t$	$r\times g$	0
Energy	$E+\frac{1}{2}v^2$	$t\cdot v+q$	$g\cdot v+h$	0
Entropy	S	φ	b	Γ

In this table, v is the velocity vector, t is the stress tensor, g is the external supply of momentum, r is the position vector, E is an internal energy density function, q is the heat flux vector, h is the external supply of energy, S is an internal entropy density function, φ is an entropy flux vector, b is the external supply of entropy and Γ is the net production of entropy.

The mass conservation law has to be obtained for all phases. When the mass conservation equation of a ground water flow is derived through coupling for a deformation problem, the mass conservation equation of a solid phase is closely related to that of a liquid phase (Yamagami (1979)), whose derivation process will be mentioned in Section 2.4 concerning the deformable double porosity modeling. The mass conservation law for ground water is used in all chapters in this paper. The mass balance equation of the solute transport, commonly called an advection-dispersion equation, will be discussed in Chapter 4.

A linear momentum balance equation is needed to define the motion of ground water flow, heat transport and solute transport. In general, Darcy's law is used as the equation of motion for ground water flow and Fourier's law and Fick's law are assumed to hold for heat transport and solute transport, respectively. The equilibrium equation is also derived from the linear momentum balance equation for a solid phase, but the acceleration term is omitted in this paper since dynamic problems are not considered.

The balance of angular momentum is reflected by the symmetric stress tensor, however, no extra discussion is carried out on this subject in the present paper.

An energy balance equation is the most important equation for defining the heat transfer. A coupled problem with temperature change is introduced in Chapter 3 of this paper, in which the equation is explicitly used. The entropy balance equation is used to obtain the governing equation of heat transport related to temperature. Although the process for obtaining the basic equation of heat transport will not be discussed in detail, the energy, the entropy conservation law and the equilibrium equation will be used to obtain the governing equation of heat transport used in Chapter 3. In this paper, since the

focus is placed on the only elastic deformation, the entropy balance equation is automatically introduced into the constitutive law of stress-strain relations.

To simulate a transport phenomenon of various properties, an appropriate representation of the velocity field is required. The macroscopic velocity obtained from the mass conservation equation of ground water flow is assumed to be available. The term "mass transport", used in the title of this paper, means that the various thermodynamic property transport systems mentioned above are discussed in this paper.

REFERENCES

M. Hassanizadeh and W. G. Gray: General conservation equations for multi-phase systems: 1 Averaging procedure, Adv. Water Res., 2, 131, (1979)

M. Hassanizadeh and W. G. Gray: General conservation equations for multi-phase systems: 2 Mass, momentum, energy, and entropy equations, Adv. Water Res., 2, 191, (1979a)

Yamagami, T.: Some consideration on the governing equations of flow through deformable porous media, Transaction of JSCE, No.304,pp.95-104, (1980)

Chapter 2 NUMERICAL METHODS OF FLUID FLOW IN ROCK MASS

2.1 Introduction

In this chapter, some methods of seepage analysis are introduced which give velocity fields used in transport analyses.

Ground water flow takes place through voids in geological media. The ground is often treated as a porous continuous medium and the equation of momentum for fluid flow in this porous medium is represented by Darcy's law. Although ground water is supposed to flow evenly through out the medium in such a treatment, the regime of the flow must be carefully observed in cases where the voids do not exist evenly. The equation of momentum for such a medium may not be represented by Darcy's law, for example, when the ground water flows through discontinuities in fractured rocks. The paths of the flow are constrained by the geometry of the fractures in the rock masses. Furthermore, the fluid may be transported unevenly on the fracture plane.

Figure 2.1.1 shows several types of rock interstices. Since interstices may range in size from huge limestone caverns to minute capillary openings, the nature of the fluid flow varies depending on the geological formation. It is important, therefore, to examine before calculation whether or not 1) the flow model presents the true nature of the flow and 2) the model is suitable for the object of the analysis .

The continuous approach has been used for many cases in the field of civil engineering. In particular, the saturated-unsaturated seepage analysis method has been most widely used. The main objectives of the calculation by this method are to evaluate the flow rate from a dam site or into an underground space, to know the pressure distribution for a mechanical analysis and so on. However, the velocity distribution has rarely been discussed seriously. In order to estimate velocity fields, the heterogeneity

and anisotropy of a ground are most important for the analyses and these properties are dependent on the rock interstices, as shown in Figure 2.1.1, and vary according to the scale of view.

On a microscopic level, there is velocity varying in both magnitude and direction across any pore cross section. It is very difficult, however, to predict such a phenomenon. This is due to the difficulties involved with identifying the parameter and modeling the geometry of the formation on a microscopic level.

Nevertheless, this phenomenon is important as far as the solute transport is concerned. It causes the spread of any initially close group of tracer particles. Although this spreading is not so much caused in a direction perpendicular to the average flow, the tracer particles are dispersed in a wide range normal to the direction of the flow because of molecular diffusion. The phenomenon of tracer particle movement can be explained as follows. The marked particles spread along each microscopic streamline occurring through velocity variations on a microscopic level. A concentration gradient of these particles is produced, molecular diffusion then produces a flux of tracers. The spreading caused by velocity variations on a microscopic level, enhanced by molecular diffusion especially in a direction transverse to the average flow, is referred to as mechanical dispersion. The separation between molecular and mechanical dispersions is not clear because it is artificial. The term hydrodynamic dispersion is used to denote the spreading which results from both diffusions.

In this chapter, the above-mentioned velocity on a microscopic level is not discussed. Rather, focus is placed on the average flow velocity as the other phenomenon by which solute particles are moved. Thus, the fluid flow is considered from a macroscopic point of view. The separation between micro and macro levels of velocity is very conventional, however, and is dependent on the modeling of the fluid flow. The velocity that affects the advection of a mass transport is considered.

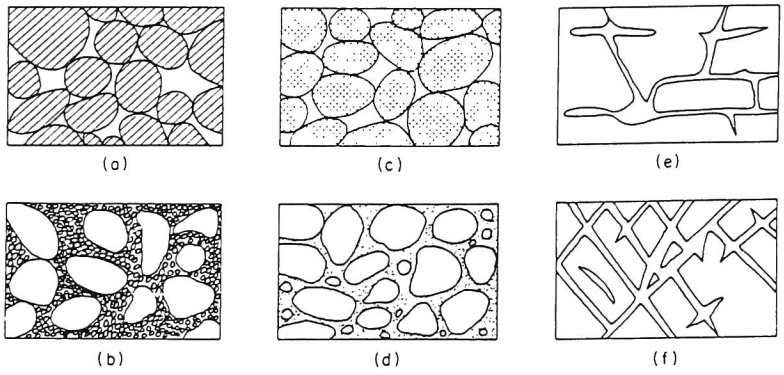


Figure 2.1.1 Several types of rock interstices
(a) well-sorted sedimentary deposit having high porosity;
(b) poorly sorted sedimentary deposit having low porosity;
(c) well-sorted sedimentary deposit consisting of pebbles that are themselves porous, so that the deposit as a whole has a very high porosity;
(d) well-sorted sedimentary deposit whose porosity has been diminished by the deposition of mineral matter in the interstices;
(e) rock rendered porous by solution;
(f) rock rendered by fracturing
(after Meinzer(1923))

A seepage analysis from a macroscopic point of view has been applied to both porous soil and fractured rock grounds. In this chapter, the method for an analysis of the porous media is firstly introduced. Then, the approach for fractured media is mentioned. The method for a porous medium has already been used in many civil engineering projects. Thus, only the theory for this method will be reviewed. On the other hand, the method for fractured media is being studied by many researchers at the present time. Both an equivalent continuum approach and a discrete approach are examined in this chapter.

2.2 Previous Works

Ground water flow is a movement of water in voids of the earth's crust. The materials of interest are soils, fractured rocks and so on. Although the nature of a ground water flow cannot be observed directly, Louis (1976) proposed that rock masses in which water flows might be divided into several groups, i.e., homogeneous porous media, porous jointed media, porous media containing impermeable barriers, porous media with small channels and karst media containing wide passages and caverns. Rock masses often occur as jointed porous media (Figure 2.2.1(f)). When considering the flow of water in a rock mass, the choice of a model for the medium is very significant. Either a continuous model or a discontinuous model may be chosen.

In the past,the continuous model has often been used to represent the rock mass in a seepage analysis, whereas focus has been placed on a discontinuous model for the safety assessment of high level radioactive waste disposal in a deep geology (e.g., Long(1989), Dershowitz (1985), Anderson (1986) and so on). This may be due to the fact that the vector of fluid velocity is more important for a mass transport analysis than the flow rate from a boundary and pressure distribution in a medium. However, the discontinuous modeling is less effective when a computer is applied than the continuous one. In addition, the discontinuous modeling is limited in the number of fractures which can be modeled quantitatively by this method. Whether a continuous or a discontinuous model is chosen is based on the relations between the spacing of joints and the size of the rock mass under consideration and the relations between the joints spacing and the dimensions of the structure or of its zone of influence.

The continuous model was firstly developed through use of the finite difference method(FDM) by Freeze and Witherspoon (1966). Although this method has many advantages due to the effects using a computer, it is limited in its geometric shape for a modeled region. At the present time, the finite element method(FEM) or boundary

element method(BEM) is often used for overcoming this limitation. Table 2.2.1 shows some important methods for solving boundary and initial value problems, which describe the ground water flow (refer to Huyakorn and Pinder(1983)).

Table 2.2.1 Various methods solving initial boundary problems

Analytical methods	Numerical methods
separation of variable	finite difference method
similarity solution	finite element method
complex variables techniques	collocation method
Fourier and Laplace transformation	method of characteristics
Green's function	boundary element method
perturbation method	
power series	

The most popular seepage analysis method in Japan is a saturated-unsaturated model by FEM. This has been used for many real projects.

Table 2.2.2 shows previous works on the analysis of seepage flow in a saturated-unsaturated ground. It is clear from this table that recently the finite element method has been used more often than the finite difference method.

The advantages of FEM are that it is easy to discretize the region to be analyzed and easy to apply nonlinear materials. Thus, a saturated-unsaturated analysis generally uses FEM. BEM has been used most effectively for solving the problem of ground water flow. This method holds promise for reducing computation effort through a reduction in problem dimensionality when the problem is of an elliptic type. When the problem is parabolic or has variable coefficients, however, the method loses many of its advantages.

Table 2.2.2 Previous works on saturated -unsaturated seepage analysis

Authors	dimension	numerical methods	hysteresis of unsaturated zone
Bredejeft(1970)	quasi three	FDM	NC
Freeze(1971)	two and three	FDM	C
Neuman(1973)	two	FEM	NC
Kamata et al.(1974)	quasi three	FDM	NC
Motokage et al.(1975)	quasi three	FDM	NC
Segol (1976)	three	FEM	NC
Akai et al.(1977)	two	FEM	C
Liggett(1977)	two	BEM	NC
Pinder et al.(1978)	two	Collocation methods	NC
Frind et al.(1978)	three	FEM	C
Komada et al.(1978)	three	FEM	NC
Akai et al.(1979)	three	FEM	C
Motojima(1981)	quasi three	FEM	NC
Gupta et al.(1984)	three	FEM	NC
Huyacorn(1986)	three	FEM	NC

C: considered, NC: not considered

A two-dimensional analysis has been most widely used in Japan. The quasi three-dimensional analysis has been carried out for large scale analyses. In particular, it has been used for analyses of settlements of the ground on a large scale by adding leakage from an aquitard. A three-dimensional analysis is very effective for the intricate geological structures built in Japan. Komada et al.(1978) indicated that an analysis of the seepage around a dam site by the three-dimensional method was a necessary process for the design of the dam.

On the other hand, studies on an analysis for fractured media have been conducted by many researchers during the past two decades. There are two approaches to analyzing the flow through a fractured medium. One of them is the discrete fracture approach. It regards a fractured medium as a continuum in which the discrete discontinuities exist. The joint element is a representative tool which explains the discontinuum. The previous main works concerning joint elements are introduced in Table 2.2.3, adding to Yashima's work (1985).

As shown in this table, joint elements are firstly used for the deformation analysis of media with discontinuities. Joint elements which consider coupled hydraulic and mechanical behavior have been developed by just a few researchers. Recently, a three-dimensional joint element network model has been used for the seepage analysis of fractured rocks. Although the discrete model requires much information on joints and involves high computation costs, it is a very effective way to examine the velocity distribution in rock masses. For this reason, the discrete fracture model is used to explain the flow field around a high level radioactive waste depository in a deep geology.

An alternative to the discrete fracture approach is an equivalent porous modeling approach. The advantage of this method is that average properties can be analyzed despite the fact that the details on the fracture geometry and simulation of the fluid flow within each fracture are not required. Several numerical studies based on the equivalent continuum approach have been developed. These include double porosity modeling by Barenblatt et al.(1960), crack tensor by Oda and Hatsuyama(1985) and equivalent porous modeling by Long et al.(1982). These approaches are similar to those mentioned above for porous media mentioned above.

Table 2.2.3 Previous works on joint elements (after Yashima (1985))

Authors	Dimension	Aperture*	Rotation	Dilatancy	Softening	Fluid flow
Goodman et al.(1968)	PS	NC	NC	NC	NC	NC
Mahtah et al.(1970)	three	NC	NC	NC	NC	NC
Heuze et al.(1971)	PS	NC	NC	NC	C	NC
Heuze et al.(1971)	PS	NC	NC	C	C	NC
Noorishad et al.(1971)	PS	NC	C	NC	NC	C
St. Jhon (1972)	PS three	NC	NC	NC	NC	NC
Royvray et al.(1972)	PS	NC	NC	C	C	NC
Goodman et al.(1972)	PS	NC	NC	C	C	NC
Ghaboussi et al.(1973)	C	NC	C	NC	NC	NC
Gale et al.(1974)	PS	NC	NC	NC	NC	C
Ngo (1975)	PS	NC	NC	NC	NC	NC
Sharma et al.(1976)	PS	C	NC	NC	NC	NC
Hilber et al.(1976)	PS	C	NC	NC	NC	NC
Goodman et al.(1977)	PS	NC	C	NC	NC	NC
Heuze(1979)	PS	NC	C	C	NC	NC
Xiurun(1981)	PS	NC	NC	C	NC	NC
Van Dillen et al.(1981)	PS three	C	NC	C	NC	NC
Heuze et al.(1982)	AS	NC	NC	C	NC	NC
Toki et al.(1982)	three	NC	C	NC	NC	NC
Ohnishi et al.(1982)	PS	NC	C	NC	NC	C
Matsumoto et al.(1983)	AS	NC	NC	NC	NC	C
Dershwitz (1984)	three	NC	NC	NC	NC	C
Herbert et al. (1989)	three	NC	NC	NC	NC	C

* Aperture of joint is not explained in the mesh information. Closing and opening of a joint is examined by constitutive law of the mechanical behavior of joints.
NC: not considered, C: considered, PS: plane strain, AS: axisymmetric

2.3 Fluid Flow in Porous Media

2.3.1 Introduction

In an aquifer, water flows through the complex network of pores and channels comprising the void space. The microscopic flow model cannot be verified, however, by measurements. On the other hand, the quantities can be measured and the boundary value problem can be solved at the macroscopic level. Thus, the continuum approach is adopted to describe the flow in porous media at this level.

Each phase (solid or liquid) in porous media is regarded as a continuum that fills up the entire arbitrary elementary volume in this approach. A set of overlapping continua is considered within every elementary volume. For each of these continua, average values are taken over the elementary volume and are assigned to its centroid. Thus, it is not necessary for the continuum porous model to specify the microscopic configuration of the individual phases.

For this approach, an appropriate size for the averaging volume must be selected. This averaging volume was introduced by Bear (1972) and is called the representative elementary volume (REV). To illustrate the determination of the size of REV, consider the void space configuration, the ratio U_v/U, in which U is a volume within a given porous medium domain and U_v is the volume of voids within U. Figure 2.3.1 shows variations of U_v/U as U increases. U_v/U with very small values for U is dependent on whether the point happens to fall in the void space or in the solid matrix. As U increases, large fluctuations occur due to the random distribution of voids and solids. As U is increased even further, however, these fluctuations gradually decay to above some volume $U=U_{min}$. If U is increased to beyond $U=U_{max}$, a trend or fluctuation may be observed due to the macroscopic heterogeneity of the porous media. The size of REV is in the range of $U_{min}<U<U_{max}$. Once REV has been determined, it is used to derive the macroscopic continuum description of the flow through use of averaging values. The process of averaging can be found in Hassanizandeh and Gray (1982).

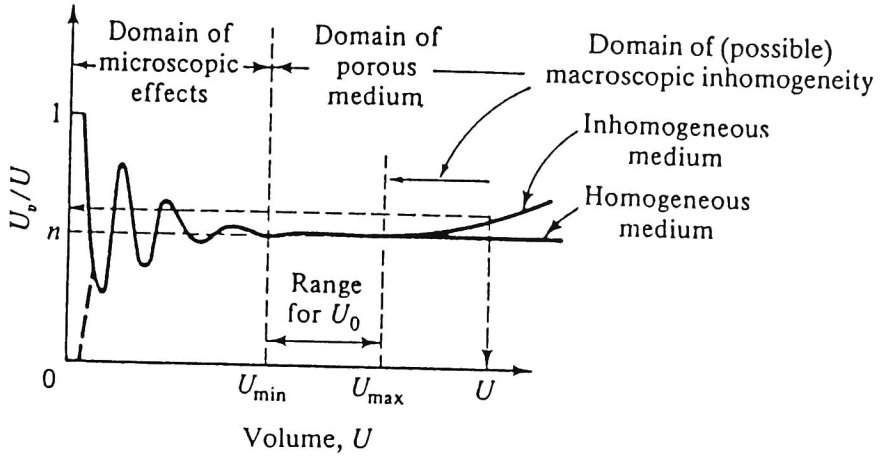


Figure 2.3.1 Definition of porosity and representative elementary volume (after Bear and verruijit(1987))
U is a volume of a sphere centered at an arbitrary point, U_v is the volume of void space within U and U_0 is the REV

In this section, it is assumed that REV can be selected for a domain. If REV is selected, the continuum approach can be used for the porous media. Soil, sand and extensively fissured rocks are examples of such media.

A saturated-unsaturated flow model has been used for many projects by assuming REV. In addition, the theory of this model is extensively used for other models mentioned in this paper. In this section, a saturated-unsaturated model and examples of the numerical approaches are introduced. The quasi three-dimensional model, which uses the transmissivity and storativity of media, is then introduced.

2.3.2 Saturated-unsaturated flow modeling

(1) Basic equation

The equation of continuity for ground water in a saturated-unsaturated zone is derived from Richards theory as follows:

$$\frac{\partial(\rho_f\theta)}{\partial t} = -(\rho_f v_i)_{,i} \qquad (2.3.1)$$

where ρ_f is the density of water, θ is the volumetric water content, t is time and v_i is the velocity vector.

The equation of motion for ground water may be explained by Darcy's law for both saturated and unsaturated porous regions. That is,

$$v_i = -k(\theta)_{ij} h_j \qquad (2.3.2)$$

in which $k(\theta)_{ij}$ is a permeability tensor, which is a function of θ, and h is a total head.

The total head can be expressed as the sum of pressure head ψ and elevation head z, namely,

$$h = \psi + z \qquad (2.3.3)$$

The volumetric water content is a function of the degree of saturation S_r and the porosity n, which is expressed as follows:

$$\theta = nS_r \qquad (2.3.4)$$

Substituting equations (2.3.2), (2.3.3) and (2.3.4) into equation (2.3.1), we obtain the following equation:

$$\{\rho_f k(\theta)_{ij}(\psi + z)_{,j}\}_{,i} = \frac{\partial}{\partial t}\rho_f n S_r \qquad (2.3.5)$$

Using a chain rule of differentiation, the right-hand side of equation (2.3.5) can be expanded to

$$\frac{\partial}{\partial t}(\rho_f n S_r) = n S_r \frac{\partial \rho_f}{\partial t} + \rho_f S_r \frac{\partial n}{\partial t} + \rho_f n \frac{\partial S_r}{\partial t} \quad (2.3.6)$$

The first term at the right-hand side represents a density change in the pore water. The second term means a deformation to the skeleton of a porous medium. The third term means a change in the saturation degree of an unsaturated medium.

Considering the compressibility of water, the density of water can be expressed as follows:

$$\rho_f = \rho_{f0}\left[1 + \beta_P (P - P_0)\right] \quad (2.3.7)$$

where P is the pore water pressure, ρ_{f0} is the reference density at $P=P_0$ and β_P is the compressibility of water. They are defined as

$$\beta_P = \left| \frac{1}{\rho_f} \frac{\partial \rho_f}{\partial P} \right| \quad (2.3.8)$$

Using Equation (2.3.7), the first term in equation (2.3.6) is given by

$$n S_r \frac{\partial \rho_f}{\partial t} = \rho_{f0} n S_r \beta_P \frac{\partial P}{\partial t} \quad (2.3.9)$$

Pressure head ψ is related to the pore water pressure as follows:

$$\psi = \frac{P}{\rho_f g} \quad (2.3.10)$$

Taking into account equations (2.3.3) and (2.3.10), equation (2.3.9) can be modified to

$$nS_r \frac{\partial \rho_f}{\partial t} = \rho_{fo}\, gnS_r \rho_f \beta_P \frac{\partial h}{\partial t} \qquad (2.3.11)$$

This equation indicates a density change in the pore water due to a change in the total head. If β_p is defined with water pressure ψ, $\rho_{f0}g$ is disregarded in equation (2.3.11).

For a one-dimensional consolidation problem, the second term on the right-hand side of equation (2.3.6) is expressed as follows (Narasimhan(1975)):

$$\rho_f S_r \frac{\partial n}{\partial t} \cong \frac{\rho_f S_r}{1+e} \frac{\chi C_c}{2.303\sigma'} \frac{\partial h}{\partial t} = \rho_f S_r \chi m_v \frac{\partial h}{\partial t} \qquad (2.3.12)$$

where e is the void ratio, χ is the parameter of effective stress in an unsaturated medium introduced by Bishop(1959), Cc is the compression index , σ' is the effective stress and m_v is the coefficient of volume compressibility.

Equations (2.3.11) and (2.3.12) indicate the effects of the compressibility of water and the deformation of solids on the fluid flow in porous media. The combined coefficient of equations (2.3.11) and (2.3.12) is called a specific storage, S_s.

On the other hand, the storage of an unconfined aquifer is related to the third term at the right-hand side of equation (2.3.6), which is rewritten as follows:

$$\rho_f n \frac{\partial S_r}{\partial t} \cong \rho_f \frac{\partial (nS_r)}{\partial t} = \rho_f \frac{\partial \theta}{\partial t} = \rho_f \frac{\partial \theta}{\partial \psi} \frac{\partial \psi}{\partial t} = \rho_f C(\psi) \frac{\partial h}{\partial t} \qquad (2.3.13)$$

This stands for the yield of an aquifer per unit area and unit drop of the water table. Thus, $C(\psi)$ is referred to as a specific yield and is defined by

$$C(\psi) = \frac{\partial \theta}{\partial \psi} \qquad (2.3.14)$$

Using equations (2.3.11)-(2.3.14), the governing equation for the ground water flow in saturated and unsaturated media is given by

$$\left\{\rho_f k(\theta)_{ij} h_j\right\}_{,i} - \rho_s S_s \frac{\partial h}{\partial t} - \rho_s C(\psi) \frac{\partial h}{\partial t} = 0 \qquad (2.3.15)$$

(2) Numerical approaches

Equation (2.3.15) can be used for any dimensional analysis. As shown in Table 2.2.2, a three-dimensional FEM has recently been the most widely used continuous approach. This is because the phenomenon of seepage through the underground occurs in a three-dimensional way, and therefore, it is difficult to explain the behavior by a two-dimensional method. In particular, the configuration of Japanese geology is too complicated to be expressed by a two-dimensional method. Thus, a two-dimensional analysis should be used not as a quantitative examination, but as a qualitative one.

Two methods of three-dimensional analysis exist. One is a method which can solve a three-dimensional equation directly. The other is a method which uses a quasi three-dimensional equation that is integrated in a vertical direction. The latter method has also been extensively conducted for the analysis of ground settlement in large areas.

A three-dimensional method that obtains a solution by solving a three-dimensional governing equation requires a large computer memory and is costly. Through the progress of computers, however, this problems have recently been solved. Freeze(1971) firstly carried out a three-dimensional saturated-unsaturated seepage analysis. He used the LSOR method and changed the time step interval to make a convergence of a solution. Segol (1976) firstly applied FEM to a three-dimensional analysis. Following, Frind et al.(1978) reported that a three-dimensional analysis was very effective for estimating a large scale fluid flow in the ground. To make the three-dimensional

approach more effective, Gupta et al.(1984) and Huyakorn and Springer(1986) attempted to use computers more effectively.

2.3.3 Quasi three-dimensional approach

(1) Basic theory

This method uses a two-dimensional governing equation by integrating it in a vertical direction with Dupuit assumptions, since seepage in a vertical direction can be ignored for analyses in large areas. Thus, the hydraulic conductivity is explained by

$$T = \sum_{i=1}^{N_s} K_i b_i \tag{2.3.16}$$

where T is the transmissivity, K_i is the permeability of the ith stratum, b_i is the thickness of the ith stratum and N_s is the number of strata.

The storativity can be defined as the summation of the product of the stratum thickness and the specific storage, namely,

$$S = \sum_{i=1}^{N_s} S_i b_i \tag{2.3.17}$$

where S is the storativity and S_i is the specific storage of the ith stratum.

The above explanations are for a confined aquifer. For an unconfined aquifer, the transmissivity and storativity are a function of a ground water table and reduce as the table goes down.

Using the above-mentioned transmissivity and storativity, the quasi three-dimensional analysis is carried out.

The quasi three-dimensional analysis, considering leakage from the aquitard, has also been performed for settlement problems on a large scale. Two methods of analysis

exist. One proposed by Bredehoeft and Pinder(1970) uses an analytical solution for the seepage flow in a vertical direction. The other uses the following equation:

$$V = K(h_u - h_o)/b_u \qquad (2.3.18)$$

where K and b_u are the permeability and thickness of the aquitard, respectively. h_u is the total head in the aquitard and h_o is the total head in the aquifer. The storativity of the aquitard is disregarded in equation (2.3.18).

(2) Numerical approaches

The quasi three-dimensional analysis, without leakage from an aquitard, has been carried out for many real projects in Japan. For example, Motokage and Minami(1975) examined the effects of a draw down of the water level in a lake on an adjoining rice field. Motojima(1981) predicted the seepage-out rate for the downstream area by filling water into a dam lake.

On the other hand, an analysis which considers the leakage from an aquitard has also been conducted for many cases, e.g. an examination of the relation between ground settlement and the discharge of ground water or the production of natural gas and an investigation of the role of a dam to the occurrence of ground water in the surrounding ground (Fujinawa (1977)).

2.3.4 Discussions

Table 2.2.2 indicates some representative studies about two, quasi three and three-dimensional seepage analyses. From this table, it is clear that quasi three-dimensional analyses have been carried out since 1970 and have had many substantial applications in Japan. While three-dimensional analyses have only been used for the past decade, they are expected to be applied to many projects in the future.

Unfortunately, there are problems with three-dimensional analyses, namely, the identification of parameters and economical aspects. The progress of computers will solve the latter problem, but further investigations and financial support are needed to identify the parameters since the areas considered are quite varied. Back analyses may be effective for solving this problem.

The basic equations mentioned in this section will be extensively used for other models in this paper. The concepts of transmissivity and storativity are used for the discontinuous seepage analysis in a fractured medium.

2.4 Two-Dimensional Deformable Double Porosity Model

2.4.1 Introduction

In this section, the continuous method is described in order to explain the seepage flow in a fractured medium. To simulate a more realistic phenomenon, the effects of ground deformation on the seepage flow are considered.

Currently there are two numerical approaches for analyzing the flow through a fractured porous medium, as mentioned in Section 2.2. One is the discrete fracture approach. The other is the equivalent continuum porous model. In this section, the double porosity model is applied to the flow through jointed porous media. This model was introduced by Barenblatt et al.(1960) and uses the concepts of statistical averaging, volume averaging and the theory of mixtures. This type of flow model was expounded by Huyakorn et al.(1983) and Warren and Root(1963). Sato et al.(1985) used the experimental approach with the realized double porosity model and showed how the effect of the permeability of a rock block on the entire permeability of a rock mass grows stronger with a decrease in fracture apertures.

On the other hand, studies on the numerical method for the analysis of coupled hydraulic and mechanical behavior have been performed on saturated porous media for a long time.Worth noting among the studies are those by Christian and Boehmer (1970) and Sandhu and Wilson (1969). A model which considers the elasto-plasticity or visco-plasticity of soils has recently been developed. Unlike studies on soils, however, studies on the coupled problem for fractured rocks have not been carried out for such a long time. The method that explicitly considers such fractures uses joint elements, as shown in Table 2.2.3. It is difficult, however, for this method to obtain the mechanical and hydraulic properties for each fracture. On the contrary, studies on the mechanical behavior that do consider the fractured medium as a continuum have been conducted by

many researchers (e.g., Oda(1986), Kyoya et al. (1985)). Their studies treat anisotropic properties induced by existing fractures.

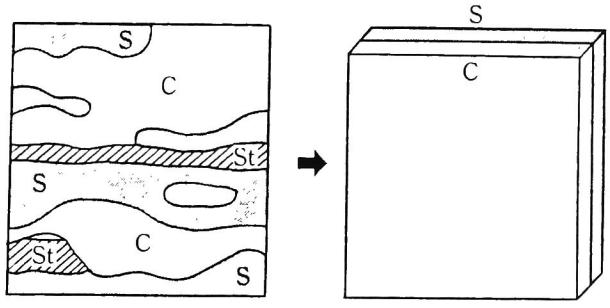
An extension of the double porosity model, which includes the coupling of flow and deformation, is also one of above-mentioned continuous approaches and was presented by Dugid and Lee (1973) and Wilson and Aifantis (1982). Dugid and Lee derived an equilibrium equations on one porosity medium of a pair. Willson and Aifantis derived an equilibrium equations based on both porosity media and applied the definition of effective stress proposed by Nur and Byerlee (1971) to the coupled term between flow and deformation in the equilibrium equation. These two approaches were developed for saturated jointed media. The approach that considers effective stress by two different pore water pressures, such as that by Wilson and Aifantis, can explain the various behavior.

In this chapter, the double porosity model for deformable saturated-unsaturated fractured rock masses is presented. Although the double porosity model has been developed in the field of oil engineering, the media of which are considered to be rock masses, this analogy can also be applied to clay that consists of different types of soil structures and soil foundations with many layers. For example, this model (see Figure 2.4.1) can be used for stratified media in spite of having to make a very fine finite element mesh to express the complicated inhomogeneity.

It is important to examine the phenomena occurring in a natural ground from many points of view. A few behavior of various media is examined with this newly developed model.

2.4.2 Basic equations

(1) Concept of double porosity model



(a) Typical geological profile (b) Double porosity modeling

Figure 2.4.1 Double porosity modeling
The ground is modeled for two representative strata, S and C. In this case, the stratum St is omitted from the model.

The double porosity model literally considers a medium by superposing two different porous media. In other word, two different water pressures are assumed to be at the same point in the medium and two continuous equations are formulated for both porous media.

Let p_1 be the average pressure of the fluid in one porous medium (referred to as the primary porosity medium) and p_2 be the average pressure of the fluid in the other porous medium (the secondary porosity medium). As an example of fractured porous media, p_1 represents the pressure in the rock block of a given point and p_2 represents the pressure in the fractures (see Figure 2.4.2). Because the permeabilities of the media are different, flow from one porous medium to the other is brought about by the difference between p_1 and p_2 at the same point. As mentioned above, two coupled equations are necessary to double porosity modeling. It is obvious that an analysis with this model has meaning for the transient state, since inhomogeneity of the ground is expressed by coupled terms in two continuous equations.

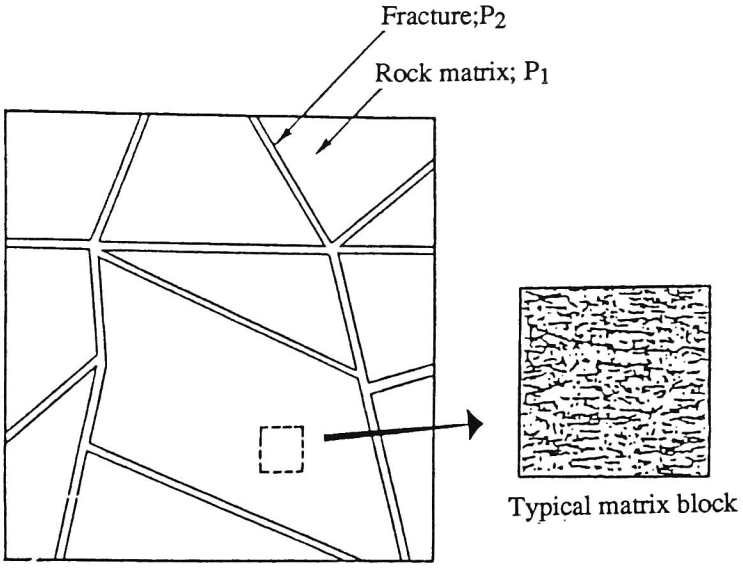


Figure 2.4.2 Double porosity model of fractured rock mass

There are two different water pressures at the same point in this model. Such a situation does not occur, however, in a real ground. Thus, this model is regarded not as a physical modeling, but as a mathematical modeling, and is deficient in that it is difficult to compare the calculated pressure values with the measured ones by this model. There do exist cases, however, where the measured values are not continuous. Thus, the pressures measured in the field have to be interpreted carefully.

In order to apply this model to a real field, a representative elementary volume (REV) needs to be considered. REV is a volume which includes two different porous media. It is large enough to exclude microscopic effects, yet small enough to keep the element homogeneous (see Figure 2.3.1). REV is also necessary to the analysis of a continuous porous medium. This is especially important in analyzing fractured rock masses with this model.

(2) Governing equations

The assumptions used to derive the governing equations are as follows:

1) The mechanical behavior of fractured media can be treated as a continuum.

2) Darcy's law is valid for the flow of water in saturated-unsaturated fractured media.

3) The fluid is slightly compressible and the solid grains (solid mass) are incompressible.

4) The deformation is considered in a field including both porous media. The water pressure related to an effective stress is assumed to be expressed by volumetric averaging of the two media.

5) The unsaturated flow in the primary porosity medium (e.g., the rock block) is calculated by the water retention curve. The unsaturated flow in the secondary porosity medium (e.g., fractures) is ignored.

Using the assumptions mentioned above and extending the governing equations derived by Huyakorn and Pinder (1983) to a saturated-unsaturated porous media (the above assumptions of 2) and 5)), we present the system of basic equations used in the model.

(a) Equilibrium equation

The total stress includes the effective stress and the fluid pressures for both porous media. After all, the governing deformation equation for a fractured medium is almost the same as that for conventional porous media. The equation can be written as follows by assuming that 1) the mechanical behavior is isotropically elastic, 2) the extensive stresses are positive and 3)the strains are infinitesimal:

$$F_i + (\lambda + G)\frac{\partial^2 u_j}{\partial x_j \partial x_i} + G\frac{\partial^2 u_i}{\partial x_j \partial x_j} - \alpha\frac{\partial p}{\partial x_i} = 0 \qquad (2.4.1)$$

where u_i is the deformation vector, F_i is the body force vector per unit volume of the medium, λ and G are Lame's constants and α is a pore pressure coefficient.

p is replaced by the weighted average of p_1 and p_2, i.e.,

$$p = \frac{S_{r1} n_1 p_1 + S_{r2} n_2 p_2}{n_1 + n_2} \tag{2.4.2}$$

where S_r and n are the degrees of saturation and porosity, respectively. Subscripts 1 and 2 represent the primary porosity medium and the secondary porosity medium, respectively.

Another definition of p in equation (2.4.1) was proposed by Wilson and Aifantis (1982), however, the values of water pressure calculated by their definition are mostly the same as those calculated by our definition.

Let n_1 be the volume of the porosity in the primary porosity medium divided by the total volume including both media. In the same way, let n_2 be the volume of the porosity in the secondary porosity medium divided by the total volume.

(b) Continuity equation

The continuity equation for a solid phase is given as

$$-\frac{\partial}{\partial x_i}\{(1 - n_1 - n_2)\rho_s v_{si})\} = \frac{\partial}{\partial t}\{(1 - n_1 - n_2))\rho_s\} \tag{2.4.3}$$

where ρ_s and v_{si} are the density and velocity vector of the solid phase, respectively.

Using a material derivative,

$$\frac{D}{Dt} = \frac{\partial}{\partial t} + v_{si}\frac{\partial}{\partial x_i} \tag{2.4.4}$$

and assuming that the solid phase is incompressible, equation (2.4.3) can be rewritten as

$$\frac{Dn_1}{Dt} + \frac{Dn_2}{Dt} = (1 - n_1 - n_2)\frac{\partial v_{si}}{\partial x_i} \quad (2.4.5)$$

The continuity of the flow in the primary pores is now considered. Let v_{1i} be the Darcy velocity through the primary porosity medium. Since Darcy's law is valid for the soil ground at rest, the relative velocity of the fluid can be defined as

$$v_{1i} = n_1 S_{r1}(v_{f1i} - v_{si}) \quad (2.4.6)$$

in which v_{f1i} is the real velocity of the fluid in the primary pores.

The continuity equation of flow in the primary medium can be written as:

$$-\frac{\partial}{\partial x_i}(n_1 S_{r1} v_{f1i}\rho_f) - \Gamma = \frac{\partial}{\partial t}(n_1 S_{r1}\rho_f) \quad (2.4.7)$$

where Γ is the flow rate transferred from the primary porosity medium to the secondary porosity medium. Introducing the substantial derivative and the average velocity v_i, equation (2.4.7) can be reduced to

$$-\frac{\partial}{\partial x_i}(v_{f1i}\rho_f) - \Gamma = n_1 S_{r1}\frac{D\rho_f}{Dt} + n_1\rho_f\frac{DS_{r1}}{Dt} + \rho_f S_{r1}\frac{Dn_1}{Dt} + \rho_f S_{r1} n_1\frac{\partial v_{si}}{\partial x_i} \quad (2.4.8)$$

Combining equations (2.4.5) and (2.4.8) and using the fluid compressibility relation $d\rho_f = \rho_{f0}\beta dp$ for the first term at the right-hand side of equation (2.4.8),

$$-\frac{\partial}{\partial x_i}(v_{f1i}\rho_f) - \Gamma = n_1 S_{r1}\rho_{f0}\beta\frac{Dp_1}{Dt} + n_1\rho_f\frac{DS_{r1}}{Dt} - \rho_f S_{r1}\frac{Dn_2}{Dt} + \rho_f S_{r1}(1-n_2)\frac{\partial v_{si}}{\partial x_i} \quad (2.4.9)$$

is obtained where ρ_{f0} is the reference density of the fluid, ρ_f is the density of the fluid and β is the compressibility of water.

According to the definition, n_2 is written as

$$n_2 = \frac{V_2}{V} \tag{2.4.10}$$

where V_2 is the volume of porosity for the secondary medium and V is the total volume. Differentiation of equation (2.4.10) with respect to time gives

$$\frac{Dn_2}{Dt} = \left(\frac{DV_2}{Dt} - n_2\frac{DV}{Dt}\right)/V \tag{2.4.11}$$

By definition,

$$V = V_1 + V_2 + V_s \tag{2.4.12}$$

where V_1 and V_s denote the volume of porosity in the secondary porosity medium and the bulk volume of the solid mass, respectively. Assuming the solid mass is incompressible,

$$\frac{Dn_2}{Dt} = \frac{DV_1}{Dt} + \frac{DV_2}{Dt}. \tag{2.4.13}$$

is obtained.

Substituting equation (2.4.13) into equation (2.4.11), the following is derived:

$$\frac{Dn_2}{Dt} = \left\{(1-n_2)\frac{DV_2}{Dt} - n_2\frac{DV_1}{Dt}\right\} / V. \tag{2.4.14}$$

Substituting the definition of the compressibility of fluid

$$-\left(\beta n_1 S_{r1} V\right)\frac{Dp_1}{Dt} = \frac{DV_1}{Dt}$$

$$-\left(\beta n_2 S_{r2} V\right)\frac{Dp_2}{Dt} = \frac{DV_2}{Dt} \tag{2.4.15}$$

into equation (2.4.14),

$$\frac{Dn_2}{Dt} = (1-n_2)\beta n_2 S_{r2}\frac{Dp_2}{Dt} + n_1 \beta n_2 S_{r1}\frac{Dp_1}{Dt} \tag{2.4.16}$$

is obtained.

Combining equations (2.4.16) and (2.4.9) yields

$$-\frac{\partial v_{1i}}{\partial x_i} - \frac{\Gamma}{\rho_f} = n_1 S_{r1}\beta(1-n_2 S_{r1})\frac{\partial p_1}{\partial t} + n_2 S_{r1} S_{r2}\beta(1-n_2)\frac{\partial p_2}{\partial t} + n_1\frac{\partial S_{r1}}{\partial t} + S_{r1}(1-n_2)\frac{\partial v_{si}}{\partial x_i} \tag{2.4.17}$$

where it is assumed that the fluid is slightly compressible and that $Dp_1/Dt \cong \partial p_1/\partial t$ and $Dp_2/Dt \cong \partial p_2/\partial t$.

Now let the following equation be valid:

$$n_1\frac{\partial S_{r1}}{\partial t} \cong \frac{\partial S_{r1} n_1}{\partial t} = \frac{\partial \theta_1}{\partial t} = \frac{\partial \theta_1 \partial p_1}{\partial p_1\ \partial t} \tag{2.4.18}$$

where θ_1 is the volumetric water content of the primary porosity medium.

Combining equations (2.4.18) and (2.4.17), the flow equation for the primary porosity medium is obtained taking into account the coupled effects of flow and deformation in the saturated-unsaturated medium. Its counterpart is the continuity equation for the secondary porosity medium. This is derived through a similar procedure to that given. The results are given by

$$-\frac{\partial v_{2i}}{\partial x_i}+\frac{\Gamma}{\rho_f}=n_2 S_{r2}\beta(1-n_1 S_{r2})\frac{\partial p_2}{\partial t}+n_1 S_{r1} S_{r2}\beta(1-n_1)\frac{\partial p_1}{\partial t}+\frac{\partial \theta_2 \partial p_2}{\partial p_2\ \partial t}+S_{r2}(1-n_1)\frac{\partial v_{si}}{\partial x_i}$$

(2.4.19)

(2.4.19)

To obtain the final form of the two equations, Darcy's law is used, namely,

$$v_{li}=\frac{k_{lij}}{\mu}\left(\frac{\partial p_l}{\partial x_j}+\rho_f g_j\right) \qquad l=1,2 \tag{2.4.20}$$

where k_{1ij} and k_{2ij} are the permeability tensors of the primary and secondary porosity media, respectively. μ is the kinematic viscosity and g_i is the ith component of the gravitational acceleration.

The required flow equations take the form

$$\frac{\partial}{\partial x_i}\left\{\frac{k_{lij}}{\mu}\left(\frac{\partial p_l}{\partial x_j}+\rho_f g_j\right)\right\}\pm\frac{\Gamma}{\rho_f}=$$

$$n_l S_{rl}\beta(1-n_{\hat{l}} S_{r\hat{l}})\frac{\partial p_l}{\partial t}+n_{\hat{l}} S_{r\hat{l}} S_{rl}\beta(1-n_{\hat{l}})\frac{\partial p_{\hat{l}}}{\partial t}+\frac{\partial \theta_l \partial p_l}{\partial p_l\ \partial t}+S_{rl}(1-n_{\hat{l}})\frac{\partial v_{si}}{\partial x_i}$$

$(\hat{l}=2,\ if\ i=1.\ \hat{l}=1,\ if\ l=2)$ (2.4.21)

(c) Leakage term Γ

The formula describing fluid transfer between the primary porous medium and the secondary porous medium is derived by the dimensional analysis in Barenblatt's model(Barenblatt et al.(1960)). As an alternative to this approach, a more elaborate approach that estimates transient fluid transfer rates has been developed by Huyakorn et al.(1983). In their model, the primary porosity medium (rock blocks) is idealized as a series of equal-sized spheres or prismatic blocks, and the flow through the rock blocks into the fractures (the secondary porosity model) is solved using the convolution integral of the analytical solution or finite differences. Dugid and Lee (1973), on the other hand, presented an approach whereby the flow rate between the primary and secondary

porosity media is obtained by the analytical solution of the one-dimensional transient heat transfer equation. Comparing the results obtained by the analytical solution of the transient equation with those of the steady equation, Dugid and Lee concluded that the approach which applies the analytical solution of the steady heat conduction equation yields sufficiently accurate results.

The rate of flow transfer between two different pressures at a steady state is presented as

$$\Gamma = \frac{k_1}{\mu} \frac{4 n_2 \rho_f}{\pi c \zeta} (p_1 - p_2) \tag{2.4.22}$$

where ζ is the block characteristics' length (e.g., the half length of a crack in the primary porosity medium) and c is the void aperture. Since it is difficult in many cases to identify ζ, c and n_2, it is useful to rewrite equation(2.4.22) as follows:

$$\Gamma = \tilde{\alpha} \frac{k_1 \rho_f}{\mu} (p_1 - p_2) \tag{2.4.23}$$

where $\tilde{\alpha}$ is a dimensionless parameter related to ζ, c, n_2 and the specific surface of fractures. The leakage rate can be adjusted with this parameter.

(d) Initial and boundary conditions

There are initial and boundary conditions that should be considered. They can be expressed as:

Initial conditions

$$u_i(\vec{x},t) = u_i^0(\vec{x},0)$$

$$p_l(\vec{x},t) = p_l^0(\vec{x},0) \qquad l = 1,2, \tag{2.4.24}$$

Boundary conditions

$$u_i(\vec{x},t) = \hat{u}_i(\vec{x},t)$$

$$\tau_{ij}(\vec{x},t) = \widehat{S_{ij}}(\vec{x},t)$$

$$p_l(\vec{x},t) = \hat{p}_l(\vec{x},t)$$

$$\left\{\frac{k_{lij}}{\mu}\left(\frac{\partial p_l}{\partial x_j} + \rho_f g_j\right)\right\} n_j = \widehat{Q}_l(\vec{x},t) \qquad l = 1,2 \tag{2.4.25}$$

where $\vec{x}$ is a position vector, τ_{ij} is the surface traction, $\hat{S}_{ij}$ is the prescribed surface traction, $\hat{Q}$ is the prescribed flux. The notation ^ denotes the prescribed values.

(e) Finite element discretization

The Galerkin method is used here to formulate the finite element discretization. A linear quadrilateral isoparametric element is employed in the code. The system of algebraic equations derived from finite element approximation is nonlinear due to the dependency of permeability in the unsaturated primary porous medium on suction. Thus, it is necessary to employ an iterative method to obtain a solution.

2.4.3 Numerical analyses

The numerical procedures described in the foregoing sections have been implemented into a computer code capable of simulating the coupled flow and deformation behavior in a fractured porous medium. In order to demonstrate the function and utility of this code, some example problems will now be solved with this code.

(1) Comparison of numerical results with analytical and experimental results

To verify the numerical solution algorithm and assess its accuracy, the code is applied to simulate two problems, namely, a seepage problem in a saturated-unsaturated porous medium and a one-dimensional consolidation problem in a saturated ground. The results of the consolidation analysis are compared with Terzaghi's theoretical solution. A comparison of the degrees of consolidation is presented in Figure 2.4.3. It shows a good agreement between the analytical and numerical solutions. To calculate this problem, the water in the secondary porosity medium and the water flow between both media are set not to flow. Thus, the overburden pressure is taken by the water pressure of the primary porosity medium immediately after loading. The effective stress increases due to a decrease in the water pressure in the primary porosity medium during consolidation.

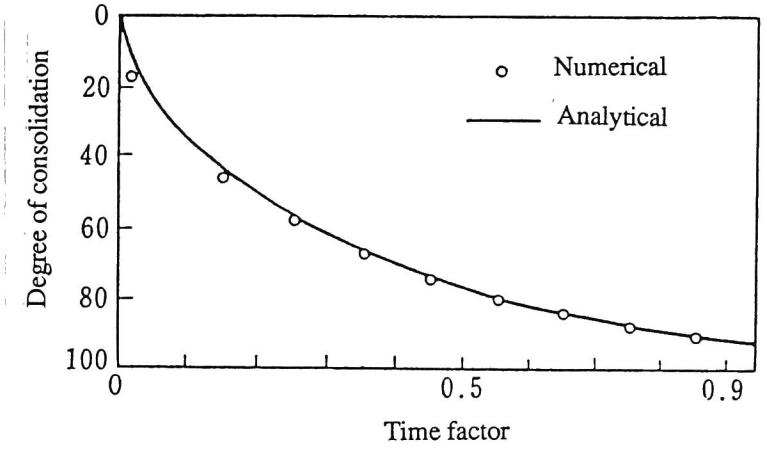


Figure 2.4.3 Comparison of analytical solution with numerical one with double porosity model (one-dimensional consolidation problem)

The saturated-unsaturated flow problem is analyzed by setting the deformation and water pressure of the secondary porosity medium to be zero. A comparison between the

numerical and the experimental results obtained by Akai and Uno (1966) shows a good agreement between the two sets of results (Figure 2.4.4).

From the above-mentioned results, the basic functions of this code seem valid.

(2) Secondary compression problem

The analysis of the secondary compression problem is mostly performed with the visco-elastic model. The author will now try to analyze this problem with the double porosity model using the theory whereby the primary consolidation is caused by a change in the effective stress, which in turn is brought about by the dissipation of excess pore water pressure from the macro pore, and the secondary compression is due to the dissipation of water pressure from the micro pore (see Figure 2.4.5).

Let the primary porosity be the micro pore, and the secondary porosity be the macro pore. The permeability of the primary porosity is set to be different from that of the secondary porosity. Figure 2.4.6 shows the one-dimensional model used in the calculation. The properties of macro and micro pores are given in Table 2.4.1. Figure 2.4.7 indicates the results of the compression as a function of time. "Single porosity",

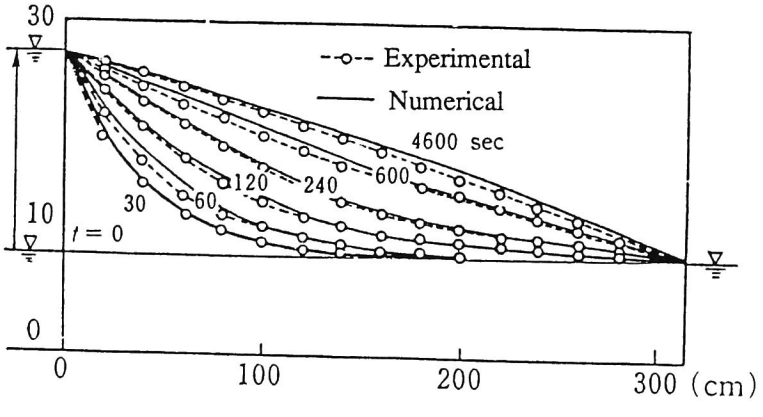


Figure 2.4.4 Comparison of experimental results with numerical ones with double porosity model (saturated-unsaturated seepage problem)

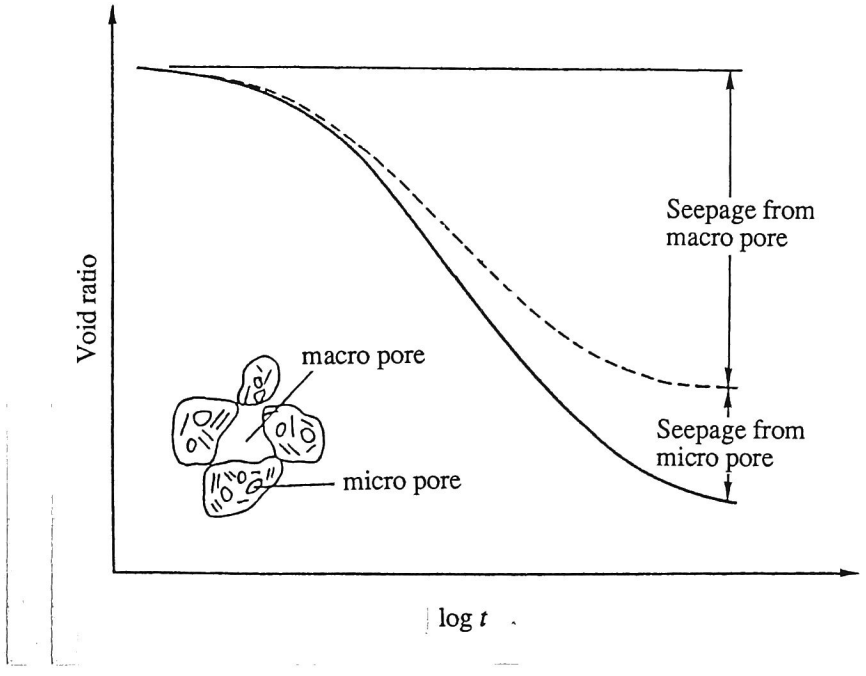


Figure 2.4.5 Schematic compression-time curve

Table 2.4.1 Data used in secondary compression analyses

Properties	Values
Permeability of micro pore	1.0×10^{-12} m/s
Porosity of micro pore	0.2
Permeability of micro pore	1.0×10^{-9} m/s
Porosity of micro pore	0.5
Young's modulus	100 tf/m^2
Poisson's ratio	0.3
Void aperture	0.025 m
Matrix characteristic length	0.015 m

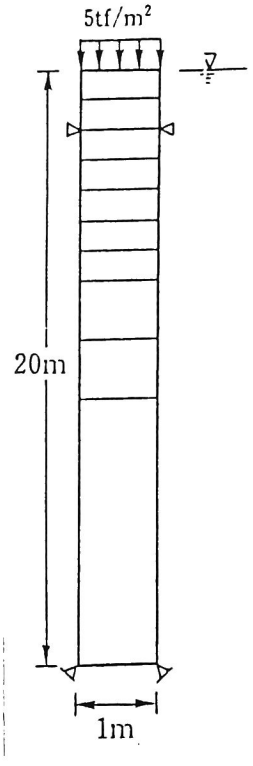


Figure 2.4.6 Finite element model used in the analysis of secondary compression problem

indicated by the solid line in this figure, is the result of applying the model without dissipation of the water pressure in the micro pore.

The compression calculated with the double porosity model, using the constant Young's modulus, is delayed more than the compression calculated with the single porosity model. This is due to a delay in the increase of the effective stress by the slow dissipation of the water pressure in the micro pore. After consolidation, the final settlements of both models are the same because Young's modulus of the single porosity model is the same as that of the double porosity model.

To express a secondary compression, it is necessary to consider the change in Young's modulus of the ground due to the compression in the micro pore. Using the mechanical analogue shown in Figure 2.4.8, the following equilibrium equation is introduced:

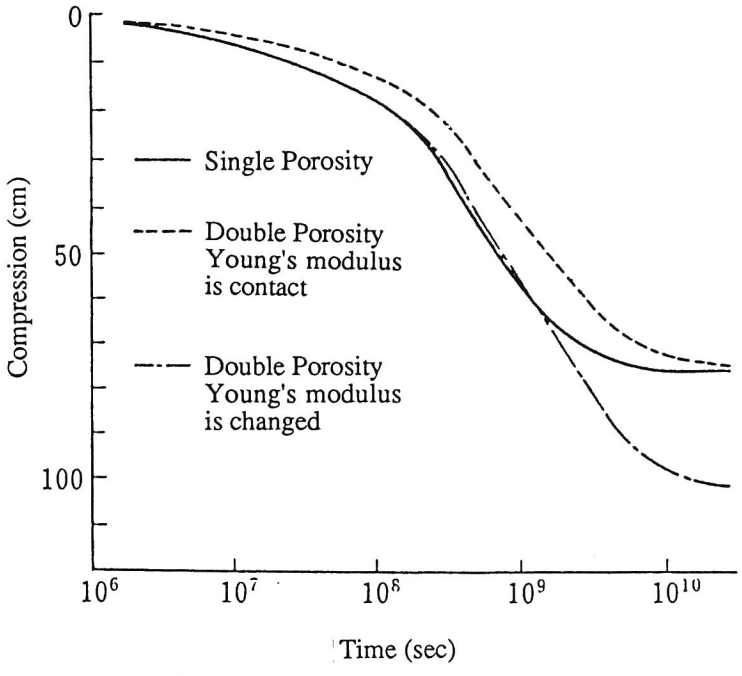


Figure 2.4.7 Calculated compression-time curve with double porosity model

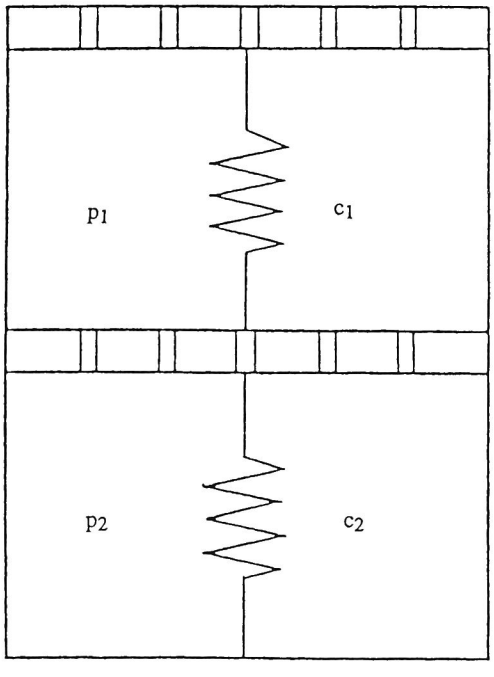


Figure 2.4.8 Mechanical analogue of secondary compression with double porosity model

$$(c_1^{-1} + c_2^{-1})^{-1}\varepsilon - (c_1^{-1} + c_2^{-1})^{-1}(c_1^{-1}p_1 + c_2^{-1}p_2) = \sigma \qquad (2.4.26)$$

where c_1 is the elastic constant of the primary porosity medium (micro pore) and c_2 is the elastic constant of the secondary porosity medium (macro pore). c_2 is the parameter of the soil's skeleton structure and is assumed to be constant as in Terzaghi's theory .

Since the micro pore medium is expected to become hard due to drainage, Young's modulus of the primary medium is assumed to increase according to the following exponential function:

$$E_1 = E_{10}\, exp(\Delta p_1^0 - \Delta p_1) \qquad (2.4.27)$$

where Δp_1^0 is an increment of the excess water pressure of the primary porosity medium immediately after loading. In this case, Δp_1^0 equals 5 tf/m^2. Δp_1 is the excess water pressure of the primary porosity medium during consolidation and E_{10} is Young's modulus at the initial state.

Applying equation (2.4.25), Young's modulus of the soil involving both media is obtained as

$$E_1 = \frac{E_1 E_2}{E_1 + E_2}. \qquad (2.4.28)$$

The results calculated by setting the initial Young's modulus of both media at 100 tf/m^2 are given by the dot-dash line in Figure 2.4.7. The analysis using the double porosity model with the assumptions mentioned above can represent the tendency of the secondary compression.

To represent the secondary compression, using the theory that the secondary compression occurs due to drainage from the micro pore, it is necessary to consider the mechanical properties, taking account of the deformation of the micro pore medium. Although the nonlinear function is used, equation (2.4.26) in this chapter, the problem

of how to identify such a mechanical parameter remains to solved.

(3) Simulation of the Lugeon test

To examine the transport of water pressure in a fractured rock mass, the Lugeon test is simulated with the double porosity model.

The finite element mesh and boundary conditions used in the problem are shown in Figure 2.4.9. Table 2.4.2 gives the data used in the analysis. Figure 2.4.10 indicates the distribution of the water pressure head as a function of time. Because the permeability of the rock blocks is larger than that of the fractures, the transport of the water pressure in the rock block is much slower than that in the fractures.

The double porosity model can represent the discontinuous situation between rock blocks and fractures, as shown in Figure 2.4.10. The pressure in the rock matrix in Figure 2.4.10 corresponds to the pressure P_1 in Figure 2.4.2, and the one in the fracture corresponds to the pressure P_2 in Figure 2.4.2. In the double porosity model, the field of the P_1 is superposed on that of the P_2, and the two pressures exist at the same point. The interation between both pressure fields are considered at an unsteady state. Figure 2.4.10 shows such a unsteady change of both pressure fields. On the contrary, a conventional continuous method can not express such a discontinuous pressure fields because one pressure field is modeled in the model. It is also difficult for the model using joint elements to express the discontinuous pressure at the fracture, because the pressure at the joint element is shared by the adjoining solid elements which discretize the rock mass field.

The real phenomenon for fractured sedimentary rocks seems to be the same as these results. The water flows rapidly through a fracture and the pressure in the fracture is reduced. On the other hand, the water pressure in a rock block remains high and the water is supplied into the adjoining fractures. This kind of phenomenon and the analysis method will be discussed in more detail in a later chapter.

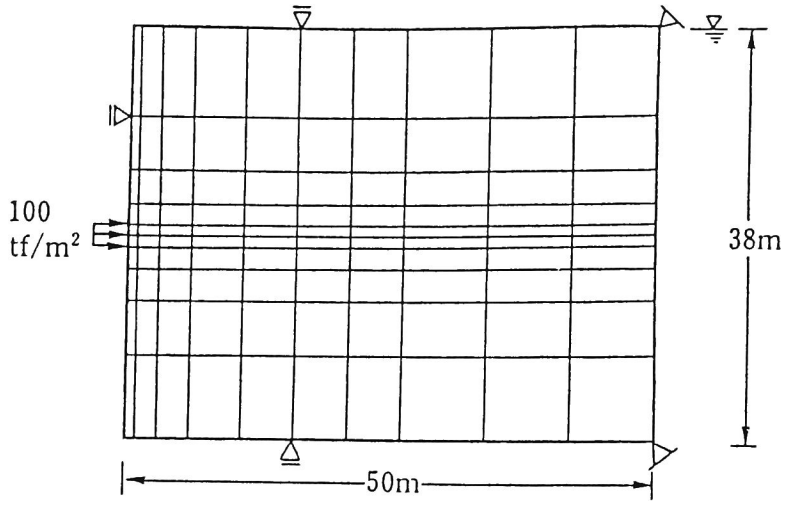


Figure 2.4.9 Finite element mesh used in the Lugeon test simulation

Table 2.4.2 Data used in the Lugeon test analysis

Properties	Values
Permeability of rock matrix	1.0×10^{-11} m/s
Porosity of rock matrix	0.2
Permeability of fracture	1.0×10^{-4} m/s
Porosity of fracture	0.05
Young's modulus	1.0×10^{4} tf/m^2
Poisson's ratio	0.3
Fracture aperture	0.001 m
Matrix characteristic length	0.5 m

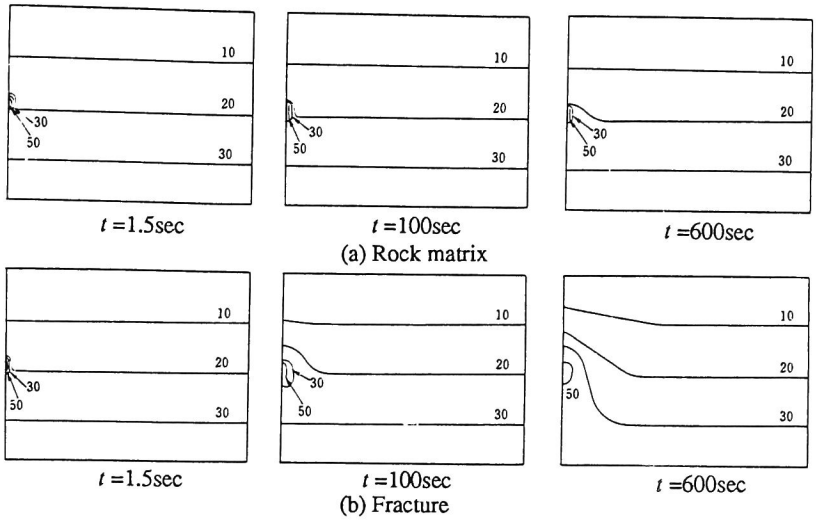


Figure 2.4.10 Unsteady change of pressure head distribution obtained from the Lugeon test simulation with double porosity model (tf/m^2)

(4) Two-dimensional consolidation problem

A two-dimensional consolidation problem is analyzed using the finite element model and boundary conditions shown in Figure 2.4.11. Two cases are examined: One is a saturated case in which the ground water table corresponds to the ground level. The other is a saturated-unsaturated case in which the ground water table is located at a depth of 5 m from the ground level. For the saturated case, the upper boundary is set at a zero hydraulic pressure condition, and the other boundaries are set at a no-flow condition. All the all boundaries are set at a no-flow condition for the saturated-unsaturated case.

Table 2.4.3 gives the data used in the analysis. Since Young's modulus is assumed to be constant in this analysis, the secondary compression presented in the Section (1) of this chapter does not appear. The difference between the double porosity model and the conventional consolidation model is the nature of the effective stress change. In this

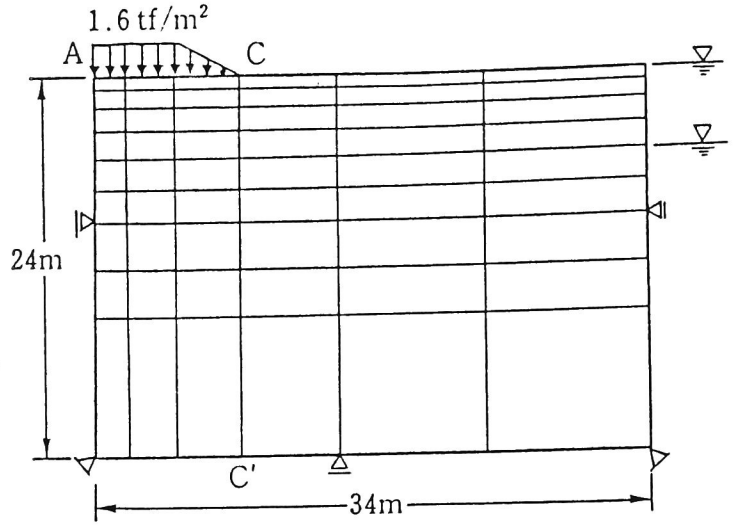


Figure 2.4.11 Finite element mesh used in the two-dimensional consolidation problem

Table 2.4.3 Data used in the two-dimensional consolidation problem

Properties	Values
Permeability of rock matrix	1.0×10^{-12} m/s
Porosity of rock matrix	0.2
Permeability of fracture	1.0×10^{-9} m/s
Porosity of fracture	0.5
Young's modulus	1.0×10^{2} tf/m^2
Poisson's ratio	0.33
Void aperture	2.0×10^{-2} m
Matrix characteristic length	5.0×10^{-2} m

analysis, let the primary porosity be the undeformable micro pore of the clay and the secondary porosity be the macro pore.

In order to make a comparison with the conventional method, the results calculated with the Sandhu type consolidation model (single porosity model), which uses the linear quadrilateral isoparametric element for the water pressure and the quadratic quadrilateral element for the displacement, are given with the results from an analysis using our double porosity model.

Figure 2.4.12 shows the settlement as a function of time at point A. The compression calculated by the double porosity model is delayed more than that calculated by the single porosity model because of the slow increase in effective stress. The compression at an early stage after loading in the saturated-unsaturated case is larger than that in the

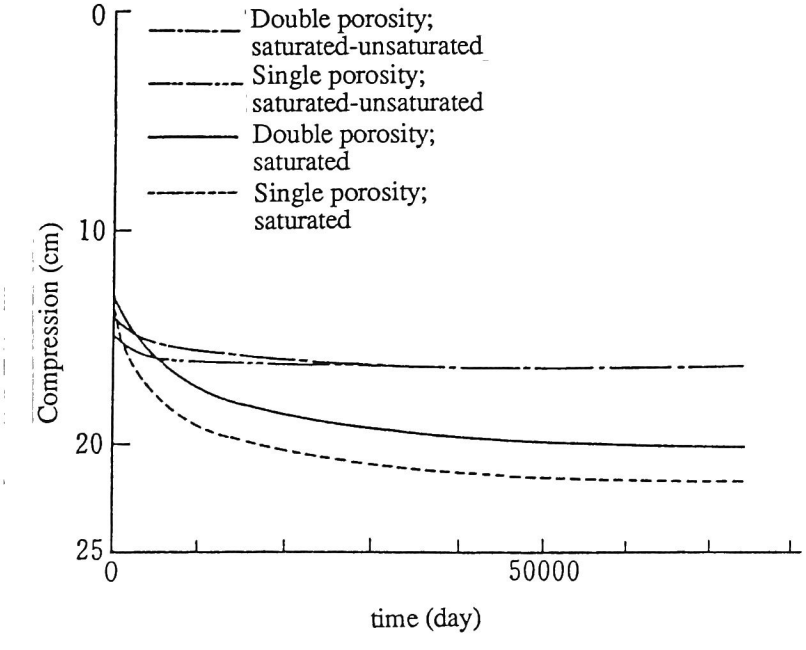


Figure 2.4.12 Compression-time curve at point A in the two-dimensional consolidation problem

saturated case. Further more, the completion of consolidation in the saturated-unsaturated case occurs earlier than that in the saturated case.

The settlement after consolidation in the saturated-unsaturated case is smaller than that in the saturated case. This is probably due to the fact that the elastic compression immediate after loading becomes large, and the settlement by consolidation becomes small, as the load is burdened at the unsaturated part.

Figure 2.4.13 indicates the ground water tables as functions of time in the saturated-unsaturated case. The change in the ground water table obtained by the single porosity model analysis is slight. On the other hand, the change by the double porosity model analysis is complicated. The water pressure under the loading part of the primary porosity, for which the permeability is low, is larger than the water pressure of the secondary porosity, for which the permeability is high. The water pressure in the other part of the primary porosity medium is lower than that of the secondary one. The water table finally reaches an equilibrium state in which the pressure distribution is lower than that of the single porosity model.

Figure 2.4.14 shows the settlement at the ground surface as a function of the distance from the center line. Immediately after loading, the settlement calculated by the single porosity model is larger than that calculated by the double porosity model. This is because the water pressure obtained by the single porosity analysis is lower than the water pressure of the secondary porosity by the double porosity model analysis. The pressure of the secondary porosity is more efficient on the deformation than the pressure of the primary one. However, the settlement after consolidation, obtained by the single porosity analysis, is smaller than that obtained by the double porosity analysis. This is due to the fact that the water pressure distribution by the double porosity model analysis is lower than that by the single porosity analysis.

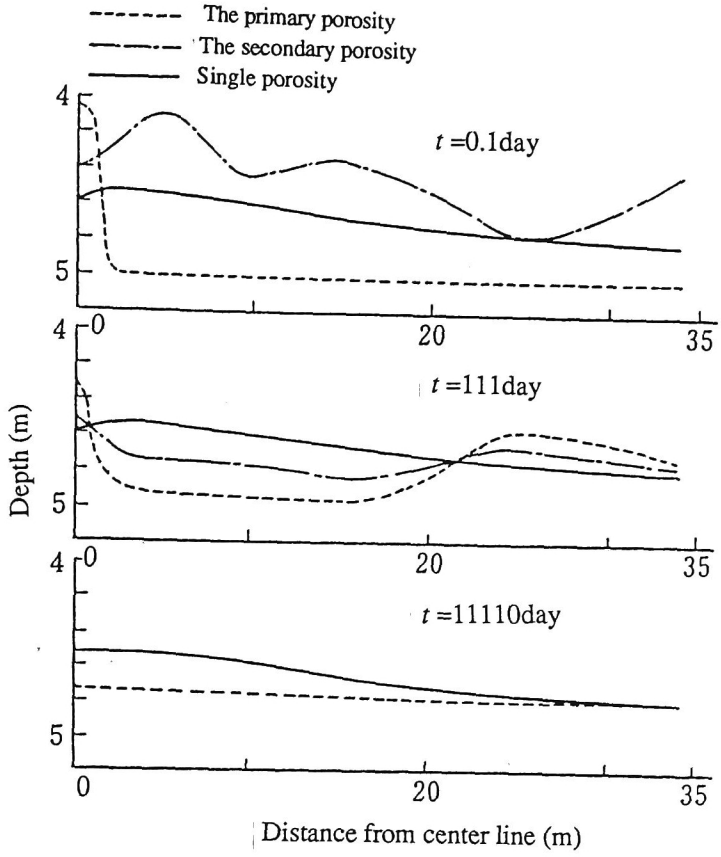


Figure 2.4.13 Unsteady change of ground water tables in the two-dimensional consolidation problem

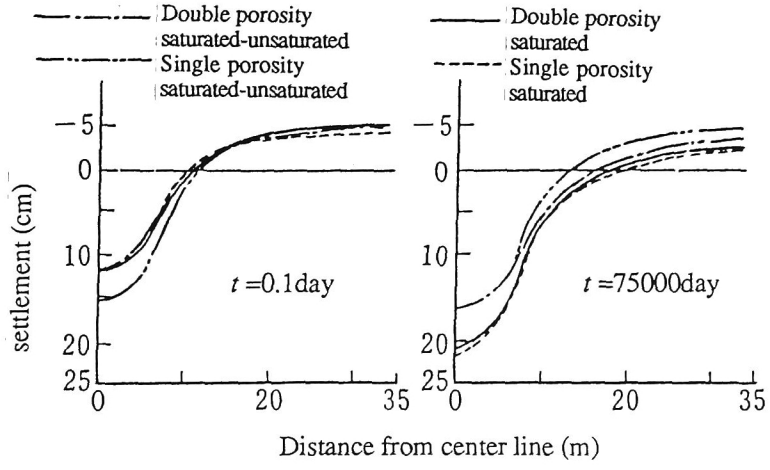


Figure 2.4.14 Settlement at ground surface as a function of distance from center line in the two-dimensional consolidation problem

Figure 2.4.15 shows the distribution of the lateral displacement at the C-C' section. The lateral displacement immediately after loading in the saturated-unsaturated case is smaller than that in the saturated case. On the other hand, the lateral displacement after consolidation in the saturated-unsaturated case is larger than that in the saturated case. The difference between the double porosity analysis and the single porosity analysis is slight for the saturated case. In the saturated-unsaturated case, however, displacement at the shallow part calculated by the double porosity model is larger than that calculated by the single porosity model immediately after loading. After consolidation by the double porosity analysis, displacement at the deep part is smaller than that by the single porosity analysis.

As mentioned above, the double porosity analysis can represent the behavior whereby the load applied at the ground surface is not transferred to the deep part due to the existence of the upper unsaturated part.

2.4.4 Conclusions

The work presented here provides a technique for the investigation of the coupled mechanical-hydraulic behavior of saturated-unsaturated fractured rock masses. The work is based on the double porosity modeling proposed by Barenblatt et al.(1960) and the saturated-unsaturated seepage analysis method developed by Neuman (1973).

In this chapter, the method is applied to the analysis of the secondary compression problem, the Lugeon test simulation and the two-dimensional consolidation problem with a free surface.

From the studies in this chapter, the following conclusions can be drawn:

1) The basic function of this newly developed code is recognized as being accurate by comparing the numerical results with the analytical and experimental results.

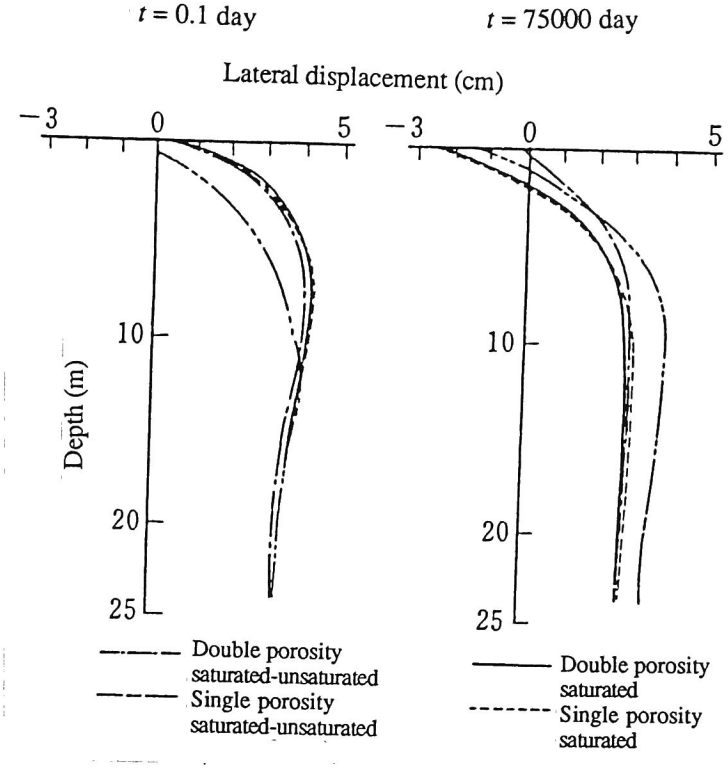


Figure 2.4.15 Lateral displacement at the C-C' section in the two-dimensional consolidation problem

2) To represent the secondary compression with the double porosity model, it is necessary to consider an elastic constant which can account for the deformation caused by the dissipation of water from the micro pore. The use of such a method, in addition to that of a visco-elastic analysis, is expected to aid in the understanding of the mechanism of the secondary compression.
3) This method can be applied to discontinuous phenomena, such as the flow through a fractured medium, that cannot be explained by the conventional continuous method.
4) This method can reflect the effect of the unsaturated part on the total ground deformation more dramatically than the conventional method.

2.5 Fluid Flow in a Single Fracture Plane

2.5.1. Introduction

The modeling a flow in a single fracture plane is one important subject for the analysis of flows in fractured rock masses.

Since Snow (1969) idealized water movement in a single fracture as a laminar flow between smooth parallel plates separated by a constant aperture, referred to as the Cubic law, many researchers have adopted this assumption to their analyses of flows in fractured media. For an analysis using the Cubic law, the aperture of the fracture is the important parameter and it is assumed to be constant in one fracture plane.

A recent study at the Stripa mine by Abelin et al. (1985), however, indicated that fractures were closed in some parts and opened in others, and that the openings might vary considerably over the fracture plane. Thus, they supposed that there were channels on the fracture plane and that the fluid flowed along these channels. Stagnant zones were also supposed to exist in the fractures, as shown in Figure 2.5.1.

The extent, width and aperture of the channels are presently unknown. Tsang and Tsang(1987), however, assumed the width to be 0.2 times the channel length and the aperture to be distributed according to the Gamma function.They then assumed that each channel was independent and did not intersect. Rasmuson and Neretnieks (1986) also assumed that the cylindrical channel did not intersect with other channels. Moreno et al. (1988) used the fracture plane divided by a rectangular grid into nodes with different apertures. They assumed that the aperture density distribution was lognormal. Tsang and Tsang (1990) and Stratfoed et al. (1990) idealized the channel flow with a variation of the fracture aperture on the plane. Both of them also used a lognormal distribution as the aperture density distribution. Kobayashi and Yamashita (1989) analyzed the solute migration in a single fracture by representing the fracture as a rectangular array of representative elements of which the aperture was constant. They used the Gamma

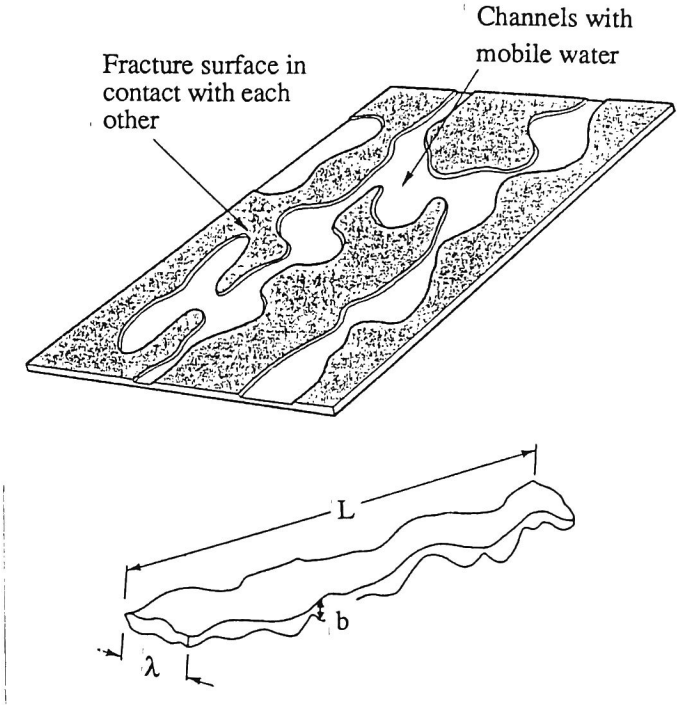


Figure 2.5.1 Schematic view of channels on fracture plane

function as the probability density distribution of the aperture, but their results showed that the probability distribution for the aperture might not be the Gamma function.

The reason why some probability distribution ought to be used for the aperture has been derived from observed results by several other researchers. However, the apertures have not always been observed on a fracture plane. In many cases, the aperture was measured for the intersections between fractures and planes like outcrops or boreholes. Some influences might exist from the excavation or cutting of the ground on the aperture distribution observed from such conditions.

The aperture distribution needed for an analysis is what contributes to the fluid flow in a fracture. However, these are very difficult to measure directly. Thus, it is necessary to

examine the aperture distribution used for an analysis before applying the results observed by many other researchers.

In this chapter, the author tries to examine which probability distribution is most suitable for the real phenomena using the numerical approach. The functions to be examined are the Gamma, exponential and lognormal ones.

The calculated results are compared with these of the migration test in a single fracture at the Stripa project.

2.5.2 Modeling of channels

(1) Inhomogeneous permeability field

Channels are generally imaged as line structures. If joint elements are used as a way to express such structures, the direction and length of the joint elements would have a large effect on the calculated results. Since there is no information about them, however, an ordinary two-dimensional finite element method is used in which elemental permeabilities vary at random. Figure 2.5.2 shows the schematic figure for the modeling of the channels on a plane.

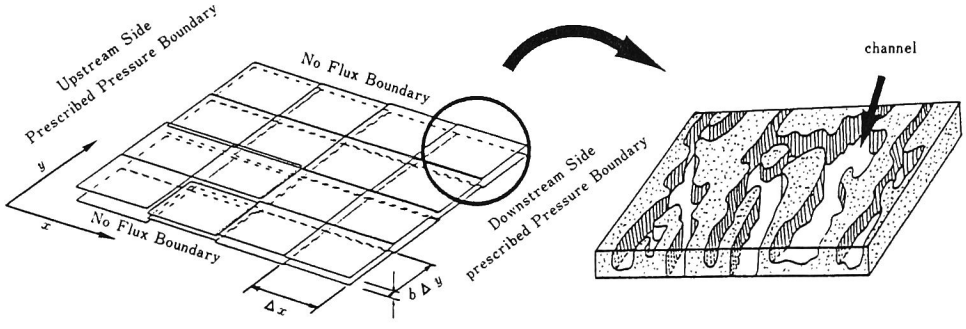
The assumptions used for the modeling are as follows:

1) Length L, width λ and aperture b of the channels are assumed to be constant in each element.

   This means that each element has a representative elementary volume for the channels.

2) The width, λ, is assumed to be in proportion to the length according to the following equation:

$$\lambda = 0.2\ L. \qquad (2.5.1)$$



(a) Schematic finite element mesh and boundary conditions

(b) Schematic view of the channels included in one element

Figure 2.5.2 Schematic figure for the modeling of the channels

Although the width of the channel has never been observed and its quantities and tendency are unknown at the present time, the above relation was assumed by Tsang and Tsang(1987). According to this assumption, the longer channel has the larger width. A similar tendency can often be observed for the relation between the aperture and the length of the fracture in rock masses.

3) The volume of the channels are assumed to be 10% of that of the fracture.

Although this ratio may be dependent on the field, it is reported to be 5 - 20 % in the Stripa project.

4) The permeability in each element is calculated by the following equation:

$$k_e = 0.1\frac{b^3}{12\mu} \qquad (2.5.2)$$

in which μ is the viscosity of the groundwater. This equation is derived from the following processes:

The flow ratio is obtained by

$$Q^e = \frac{\lambda b^3}{12\mu} J \qquad (2.5.3)$$

where J is a hydraulic gradient.

On the other hand, the relationships between channel length L and mesh spaces Δ x and Δy can be calculated by considering that the areal ratio of the channel to the fracture at the outlet boundary section is the same as the volumetric ratio in a fracture.

Using the volumetric ratio of the channel to the fracture (10%), channel length L for the x-direction is obtained by the following equation:

$$\frac{b\lambda}{b\Delta y} = 0.2\frac{L}{\Delta y} = 0.1 \qquad (2.5.4)$$

Thus, the next relation is obtained:

$$L = 0.5\Delta y \qquad (2.5.5)$$

The results for the y-direction are derived with same process as follows:

$$L = 0.5\Delta x. \qquad (2.5.6)$$

From equations (2.5.1), (2.5.3), (2.5.5) and (2.5.6), the apparent permeability of each element is given by

$$K_x^e = \frac{0.2Lb^3}{12\mu} \times \frac{1}{b\Delta y} = \frac{0.1b^2}{12\mu}$$
$$K_y^e = \frac{0.2Lb^3}{12\mu} \times \frac{1}{b\Delta x} = \frac{0.1b^2}{12\mu} \qquad (2.5.7)$$

The transmissivity is formulated by multiplying this permeability by aperture b.

5) The aperture is assumed to be distributed according to a given probability density function.

In this chapter, we examine the following three functions:

• Gamma function

$$n(b) = \frac{1}{b_p^2} b e^{-b/b_p} \qquad (2.5.8)$$

where b_p is the aperture at the peak of distribution. Note that $b_0=2b_p$ in which b_0 is the mean aperture.

• Exponential distribution

$$n(b) = \frac{1}{b_0} e^{-(1/b_0)b} \qquad (2.5.9)$$

• Lognormal distribution

$$n(b) = \frac{1}{\zeta(2\pi)^{1/2} b} e^{\frac{\ln b - \beta}{2\zeta}} \qquad (2.5.10)$$

where $\zeta^2 = \ln(1+(\sigma/b_0)^2)$, $\beta=\ln b_0 - 0.5\zeta^2$ and σ is the standard deviation of the aperture of the channels.

Using the assumptions mentioned above, the inhomogeneous permeability field is derived. The elementary transmissivity is given according to the above probability density functions (PDFs) for the apertures.

In order to generate the apertures with the Gamma function and the exponential distribution, the following equation is used:

$$\int_0^{\eta} n(b)\, db = R \qquad (2.5.11)$$

where R is a uniform random number from 0 to 1 generated by a computer. η for the Gamma function is obtained by the intermediate value theorem because it cannot be directly obtained from the above integration.

The aperture generated with the lognormal function is calculated with ζ and β by the following:

$$X_1 = \beta + \zeta\,(-2ln\,R_1)^{1/2}\,cos(2\pi R_2)$$
$$X_2 = \beta + \zeta(-2ln\,R_2)^{1/2}\,cos(2\pi R_1) \qquad (2.5.12)$$

in which R_1 and R_2 are independent random numbers. Using these X_i, apertures with the lognormal PDF are obtained by the next equations:

$$b_i = exp(X_i)\ (i = 1,2\ ). \qquad (2.5.13)$$

(2) Conditions and calculation cases

We carry out steady seepage analyses with the inhomogeneous permeability fields obtained from equation (2.5.2) and the stochastic models of the above-mentioned apertures. The results obtained from our analyses are compared with those obtained by the migration test on a single fracture in the Stripa project (Abelin et al. (1985)).

In the Stripa project, tracers were injected into a single fracture which had a natural water flow towards the experimental drift. Migration distances of 5 and 10 m were used. Hydraulic gradients applied in the aperture calculation were 4 and 7.47.

Flow from the injection point might have been radial symmetry. However, the results examined by Abelin et al. did not indicate much difference between radial symmetry and a one-dimensional flow.

Generally speaking, the estimation of apertures is independent of the boundary conditions. Thus, apertures obtained from experiments have to be independent of the kind of experiments conducted. Furthermore, it is very difficult to grasp the real water flow conditions around caverns. For these reasons, the flow field calculated in this analysis is set at a simpler one. The model used in the analysis focuses on the flow in the fracture plane and has a two-dimensional inhomogeneous permeability field. The boundaries parallel to the flow direction are set at no-flux conditions and the inlet and outlet sides are set to have constant total pressures such that the hydraulic gradient is 2×10^{-4}, as shown in Figure 2.5.2. The value for this hydraulic gradient is not related to the measurement in the Stripa project. To compare the characteristics of the aperture obtained by this analysis with those obtained in the Stripa project, the non-dimensional values related to the aperture are used.

The analysis is carried out for the steady state and the cases to be examined are as follows:

1) The basic case: The space in the x-direction of an element , Δx, is constant at 10 cm, while the one in the y-direction , Δy, is constant at 50 cm. The x-direction is the same as the flow direction, as shown in Figure 2.5.2. The total number of elements is 2000. The region is divided into 100 elements in the x-direction and 20 in the y-direction. The scale is 10 m x 10 m. The apertures in the region, b, are given by the Gamma distribution.
2) Δy is changed according to the exponential distribution. This means that the distribution of length for the channels varies in the y-direction. The apertures are given by the Gamma function.

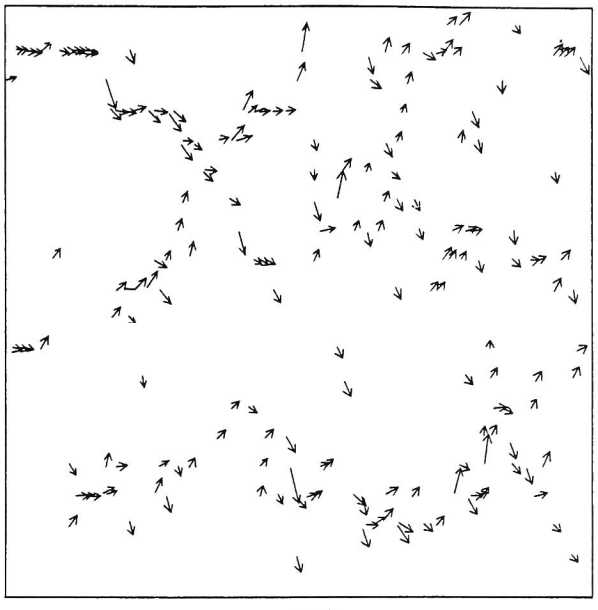
3) Δx and Δy are set according to the exponential distribution. The apertures are given by the Gamma function.
4) The spaces in the x and y-directions are the same as for the basic case. The apertures are given by the exponential distribution.
5) Δx and Δy are the same as for the basic case. The apertures are given by the lognormal distribution of which standard deviation, σ, is 0.004.
6) Δx and Δy are the same as for the basic case. The apertures are given by the lognormal distribution of which the standard deviation, σ, is 0.01.

For all the above cases, the mean aperture, b_0, is 0.02 cm, the maximum aperture is 1.0 cm, the mean length of the channel, L_0, is 25 cm and the maximum length is 110 cm. A few patterns for each case are calculated by the different initial values of random numbers.

2.5.3 Results

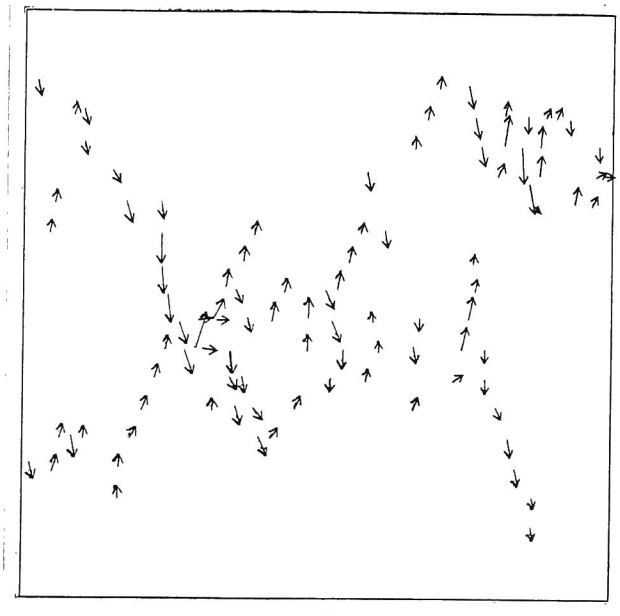
(1) Velocity distributions

Figure 2.5.3 shows one of the velocity vector distributions for Cases 1 and 6. Velocities under 25% of the maximum velocity are omitted in order to emphasize the main flow paths in these figures. It is clear from these figures that the water flows selectively on the higher permeable paths. Hence, the water does not flow out homogeneously at the outlet boundary. This is the same tendency as that observed in the migration test conducted in a single fracture at the Stripa project, as shown in Figure 2.5.4. Thus, the nature of the flow on the fracture plane simulated in this analysis is expected to be similar to the real one.



5.08×10^{-5} (cm/s)

(a) Case1



3.62×10^{-7} (cm/s)

(b) Case 6

Figure 2.5.3 Calculated velocity distributions

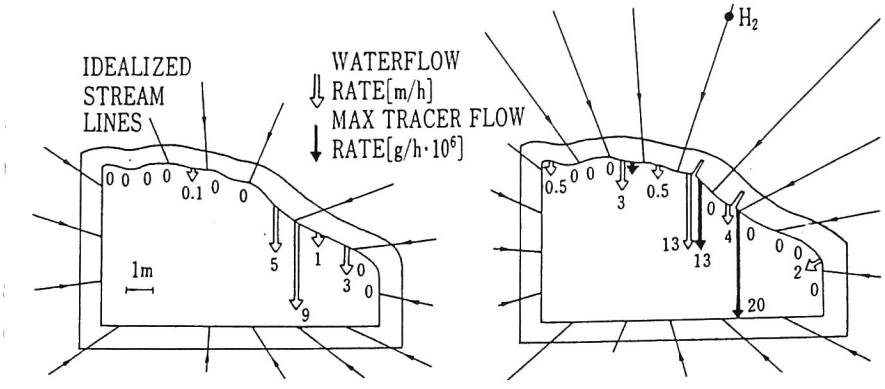


Figure 2.5.4 Observed results in the migration test at the Stripa project

(2) Aperture of channels

In this section, the distribution of channel apertures is examined with reference to the report presented by Abelin et al. in the Stripa project. They calculated the apertures by the following three methods:

1) Mass balance fracture width b_f

This is determined by the flow rate from the fracture, Q , and the residence time of the water, T_w,

$$QT_w = L_f b_f B \qquad (2.5.14)$$

where L_f is the flow path length and B is the total length of the outlet boundary. b_f is a real physical aperture which can be measured directly by the law of mass conservation.

2) Frictional loss fracture width b_l

This is given by the water velocity obtained by the mean residence time and the flow path length:

$$L_f/T_w = \frac{b_f^2\, gJ}{12\mu} \qquad (2.5.15)$$

in which J is the hydraulic gradient.

3) Cubic law fracture width, b_r

This is given by the flow rate and the pressure drop,

$$Q/B = \frac{b_r^3\ 12\ gJ}{12\mu} \qquad (2.5.16)$$

The latter two apertures are based on the assumption that the laminar flow pressure drops in a slit. The total water flow rate at the outlet boundary is obtained from the product of the velocity perpendicular to the boundary and the length at the outlet boundary line, $\Delta y|_{x=Lf}$, of each element:

$$Q = \sum \Delta y/_{x=Lf} \times u \qquad (2.5.17)$$

where it should be noted that the unit of u is $[L^2T^{-1}]$ because transmissivity is used for u.

The mean residence time is obtained by dividing the distance, L_x (=L_f), in the flow direction by the mean velocity at the outlet boundary, U:

$$T_w = L_x/U$$
$$U = Q/(\sum \Delta y/_{x=Lf} \times b\ ). \qquad (2.5.18)$$

Thereby, the apertures mentioned above can be obtained as follows:

$$b_f = QT_W/L_fB = (\sum \Delta y|_{x=L_f} \times b)/B$$

$$b_l = (Q12\mu/gJ\sum \Delta y|_{x=L_f} \times b)^{1/2}$$

$$b_r = (Q12\mu/BgJ)^{1/3}. \qquad (2.5.19)$$

Using the ratios of the above apertures, b_l/b_f and b_r/b_f, the aperture distribution of the channels on the real fracture plane is investigated. The physical meaning of the former ratio is the rate of the contribution of the fractional loss to the real physical aperture and the physical meaning of the latter ratio is the rate of the contribution of flow rate to the physical aperture.

Table 2.5.1 shows the mean values for each case, as well as the results obtained by Abelin, et al.. For b_r/b_f, the reciprocal of it is indicated in the table for the following discussion. It is clear from this table that the ratio given by the lognormal distribution with the large standard deviation has the best agreement with the ratio in the Stripa project. Furthermore, the lognormal distribution with the smaller standard deviation does not result in a good agreement. It is also clear from Cases 2 and 3 that a variation in the channel length does not have much influence on the flow along the fracture plane.

Although such results are omitted in Table 2.5.1, the results by other distributions (including the lognormal one with the small standard deviation) result in a good agreement if a percentage under 1% of the channel volume in the fracture is used. This is too small for a percentage of the channel volume, and therefore, it can be inferred from these results that the fluid flows through the limited part of a fissure plane. Figure 2.5.3 b) also shows limited paths of fluid transport.

Barton et al.(1985) have investigated the b_f/b_r. Their examination is related to the relationships between b_f/b_r and b_r, namely, the physical aperture and the theoretical smooth wall aperture, as shown in Figure 2.5.5.

Table 2.5.1 Mean values for each cases

Case	b_r	b_l	b_f	b_f/b_r	b_l/b_f	JRC
Δx,Δy; basic case	66	33.5	228	3.45	0.145	14
b; Gamma distribution						
Δy; exponential distribution	64	35	215	3.33	0.164	14
b; Gamma distribution						
Δx,Δy; exponential distribution	68	44	238	3.57	0.160	15
b; Gamma distribution						
Δx,Δy; basic case	55	30	188	3.57	0.160	13
b; exponential distribution						
Δx,Δy; basic case	61	29	280	4.55	0.109	18
b; lognormal distribution ($\sigma^2 = 0.004$)						
Δx,Δy; basic case	1.7	0.8	77	50.0	0.01	26
b; lognormal distribution ($\sigma^2 = 0.01$)						
Stripa project	7	1.65	140	20.0	0.01	24

They emphasized that the estimation made with the theoretical smooth wall assumption was erroneous due to the joint roughness of the real fractures. They considered that a mismatch between the real mechanical aperture and the theoretical one had been caused by flow losses due to tortuosity and surface roughness. The following equation was given as an appropriate model of the data trends shown in Figure 2.5.5:

$$b_r = JRC^{2.5}(b_f/b_r)^2 \qquad (2.5.20)$$

where *JRC* is the Joint Roughness Coefficient that Barton et al.(1977) introduced. The theoretical and real mechanical apertures are rewritten as b_r and b_f, respectively, in this section. The theoretical smooth wall aperture corresponds to the Cubic law fracture width b_r, and the real mechanical aperture corresponds to the mass balance fracture width b_f.

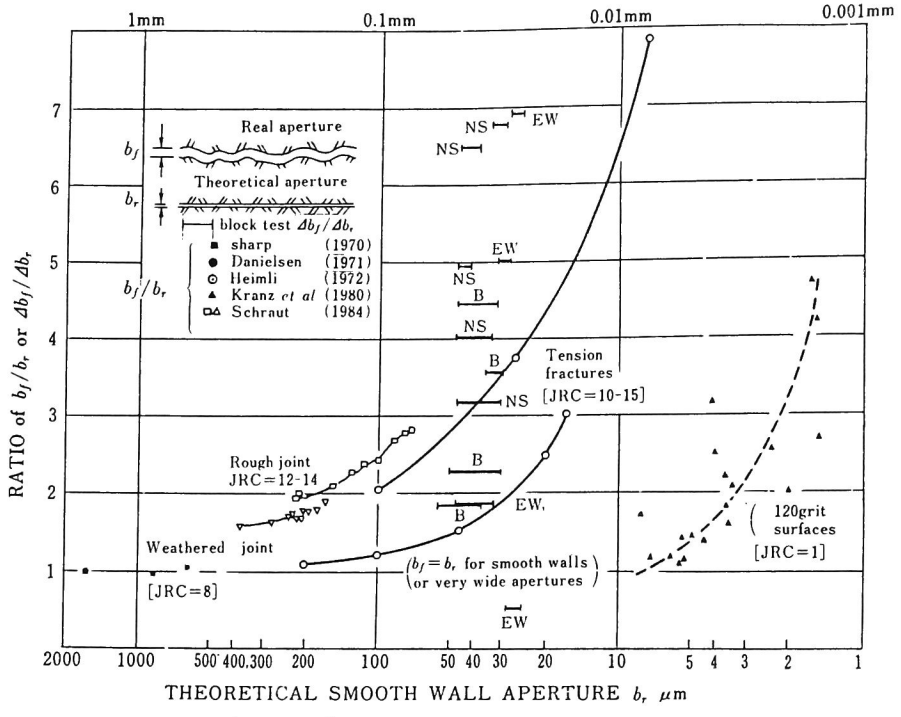


Figure 2.5.5 Comparison of real mechanical aperture (b_f) with theoretical smooth wall conducting apertures (b_r) (after Barton(1982)

The *JRC* was calculated by substituting b_f and b_r ,obtained by the above analyses, into equation (2.5.20). Table 2.5.1 indicates the calculated *JRC*. The value of *JRC* in Case 6, of which results are most agreeable to those in the Stripa project, is 26. This is a very high value. The other cases have values between 14 and 18. The *JRC* obtained by the Stripa single fracture migration test results comes to 24. This also is a very high value, as Barton et al. considered the highest *JRC* to be 20.

Figure 2.5.5 was derived from six sources. The range of b_f/b_r was between 1 and 8 in their investigation, while the value of b_f/b_r in Case 6 is 50.

The roughness of the fracture is a deviation from the planar surfaces. Ordinarily, when the deviation from planarity is under 1 mm, it is referred to as roughness. If it is over 1 mm, that is called waviness. They are judged from observations at an outcrop or a borehole wall, and thus, the roughness is the geometric information of the fracture.

Meanwhile, channels are the paths of fluid flow on the fracture plane and the channel aperture is the hydrodynamic information of the fracture. Thus, the *JRC* from equation (2.5.20) using b_f and b_r may have to be distinguished from the *JRC* originally introduced by Barton et al. because b_f was not measured but inferred from the fluid transport phenomena.

The values of the *JRC* indicated in Table 2.5.1, however, seem to show a certain degree of scattering for the aperture of the channels.

A schematic view of fracture roughness traces is shown in Figure 2.5.6. These are aspects from a small scale of view. However, the length of a single element at the outlet boundary, Δ y, is 50 cm for this basic case. Thus, we cannot directly compare the shape of the fracture traces. The nature of fracture traces at the outlet boundary for our analysis must be seen from a large scale of about 10 m. Figure 2.5.7 illustrates one of the distributions of apertures at the outlet boundary in our examination. Figures 2.5.7a) and b) are for Case 1 and 6, respectively. The apertures are plotted for the logarithms of cm in those figures. As can be seen in Figure 2.5.7, the apertures plotted by the lognormal distribution with a large standard deviation vary more widely than those plotted by the Gamma distribution.

The results mentioned above infer that the deviation of the channel apertures on a fracture plane is larger than that of the roughness observed at the outcrops and that the ground water flows along limited paths.

2.5.4 Conclusions

The flow in a single fracture was calculated in order to examine the character of channel apertures. The channels were simulated by the inhomogeneity of permeability on a fracture plane. The permeability of each element constituting a fracture plane is the

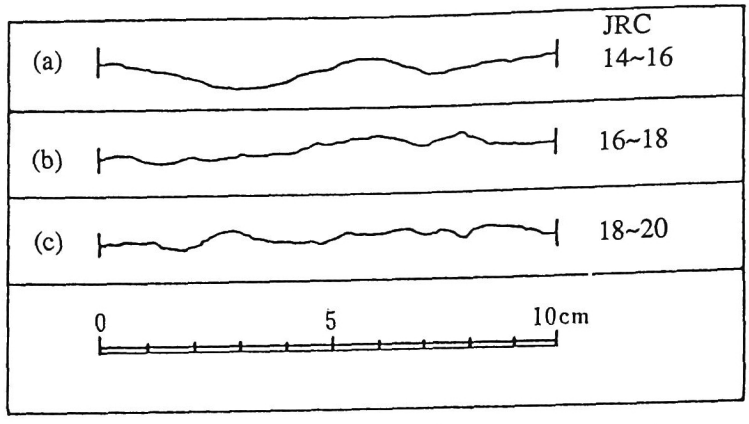
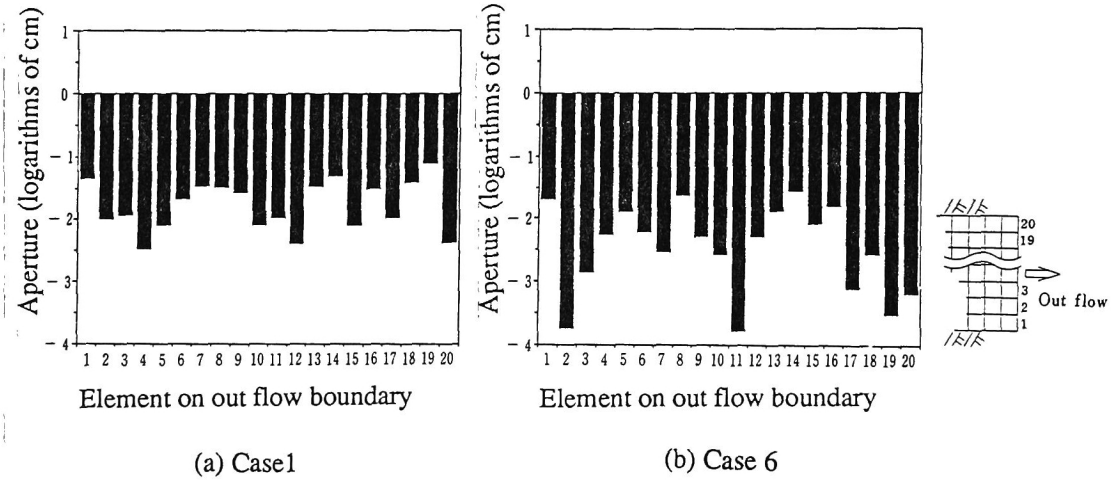


Figure 2.5.6 Schematic view of fracture roughness trace



(a) Case1 (b) Case 6

Figure 2.5.7 Distributions of apertures at the outlet boundary used in the analyses

function of the channel apertures and the apertures were obtained by given probability density functions.

An examination was carried out using three apertures of a fracture, i.e., a mass balance aperture, b_f, a frictional loss aperture,b_l and a Cubic law aperture, b_r. The dimensionless ratios, b_r/b_f and b_l/b_f , are compared with those obtained from the migration test on a single fracture in the Stripa project.

Barton et al. derived the equation related to the real mechanical aperture and a theoretical one using *JRC*. The characteristics of the channel apertures were examined by that equation.

The conclusions of this chapter are summarized as follows:

1) The real aperture distribution of a fracture in the Stripa mine may be the lognormal distribution with a large standard deviation. Thus, the apertures of channels vary widely on a single fracture plane.
2) The fluid on a fracture plane flows along the more permeable regions and the area of paths is very small for that of the plane.
3) The *JRC* from equation (2.5.20), using b_f and b_r, is different from that introduced by Barton et al., yet it does have the ability of an index for channel aperture characteristics.
4) The deviation of channel apertures on a fracture plane may be larger than that of the roughness observed at the outcrops.

The channeling experiments were conducted in phase 3 of the Stripa project. A simulation of the experiment will be carried out to examine the character of the channel flow. The numerical simulation techniques are very useful for investigating the phenomena because of their ability for consideration from various points of view.

2.6 Three-Dimensional Discontinuous Model

2.6.1 Introduction

In this section, the three-dimensional discontinuous flow model is introduced. The discontinuous approach is a method in which the analysis is performed by explicitly applying data on the locations, orientations, shapes and material properties of the fractures. A shortcoming of this approach is the need for much data on the fractures in the rock mass. A complete description of the fractures is difficult to obtain because of their three-dimensional nature and their limited exposure in outcrops, boreholes and tunnels. It is common, therefore, to use a statistical approach to describe the fracture system. If the modeling is limited to large fractures and fault systems, this method may deterministically express the large fracture network by conducting concentrated observations and field experiments.

On the other hand, the continuous approach is not appropriate for the examination of the velocity vector of flow through the fracture network because the fluid mainly flows through the fracture network in the rocks. This kind of approach should be used for the flow rate estimation.

For the above-mentioned reasons, the discontinuous model approach seems to be better suited to analyzing the flow path in a fractured rock mass than the continuous model approach. However, conventional analyses using the discontinuous approach are carried out to examine the statistical aspect of the flow rate at the outlet boundary (e.g., Herbert and Gale (1989)). This may be due to difficulties involved with the exact modeling of fracture systems.

For the application of the discontinuous method to the rock masses in Japan, discontinuities existing in an ordinary ground are too numerous to represent with a discrete model. Hence, the fractures must be classified into large ones that have great effects on the fluid flow in the rock mass and other small ones. Accordingly, it may be

most substantial for real problems that the major fractures be explicitly analyzed and the minor ones be treated by the statistical continuum modeling.

In this method, the large fracture zones or faults are considered as the main paths of the fluid flow.The rock blocks, including other small cracks, are analyzed for their influences on the flow in those main paths.

However, the network model by joint elements without solid elements of rock blocks is often used. It is dependent on ground conditions and the scale of the point of view, whether influences of the rock blocks on the flow in a fracture are considered or not. Approaches that do not consider rock blocks are suitable for media in which the rock blocks can be considered impermeable. Nevertheless, the flow in rock blocks has to be considered when it includes many small joints and has significant permeability. The role of rock blocks does not seem negligible, especially at an unsteady state.

In this section, the joint element network model is firstly verified by the results obtained in the laboratory. Then, an automatic generator of a three-dimensional finite element mesh is presented which can define the closed blocks surrounded by randomly distributed fracture planes. This kind of generator is very useful for an analysis which considers the permeability of rock blocks. Furthermore, the new seepage analysis method with a extended double porosity model, that can express the discontinuous pressure field, is introduced. Lastly, the influence of seepage in rock matrices on the flow in the fractures is examined using the extended double porosity model and conventional FEM with joint elements. The joint elements used in the conventional FEM share nodes with the adjoining rock block elements. Thus, the permeability of the contacted rock blocks has an influence on the flow in the fractures, and the discontinuous pressure distribution at the fracture cannot be expressed.

2.6.2 Verification of the joint network model

(1) Laboratory experiment

Laboratory experiments were conducted to examine the seepage flow in a three-dimensional fractured rock mass. An imitation of the rock mass was made from polystyrene foam. 4 x 4 x 4 cm cubic blocks of the polystyrene foam were used as the rock blocks. Each block was bonded to a small area of the block surface. All the apertures of the vertical fractures observed at each horizontal section were measured by a crack scale while the fractured rock model was being made. The horizontal apertures were measured at the surface of the imitation rock after making it.

The number of polystyrene foam blocks that imitated fractured rocks was 1000 (10 x 10 x 10 pieces, about 40 x 40 x 40 cm). Each cubic block was coated with waterproof paint to prevent water from seeping into the block.

The artificial fractured rock mass was set in a water basin, as shown in Figure 2.6.1. The water table was set to be 2 cm beneath the top of the rock.

The pipe, with a radius of 0.5 cm,was set from the center of the top to the middle depth of the artificial fractured rocks, as shown in Figure 2.6.2. This pipe had many open holes about 10 cm from the bottom. The upper and lower surfaces of the artificial rock are covered with silicone caulking to keep both surfaces in a no-flux condition.

Water was injected from the water tank under a constant rate during a given interval; then the valve was shut down in an instant. Thus, the test was carried out like a pulse constant flow test. The change in pressure at the injection zone was measured by the manometer.

(2) Numerical approach and modeling

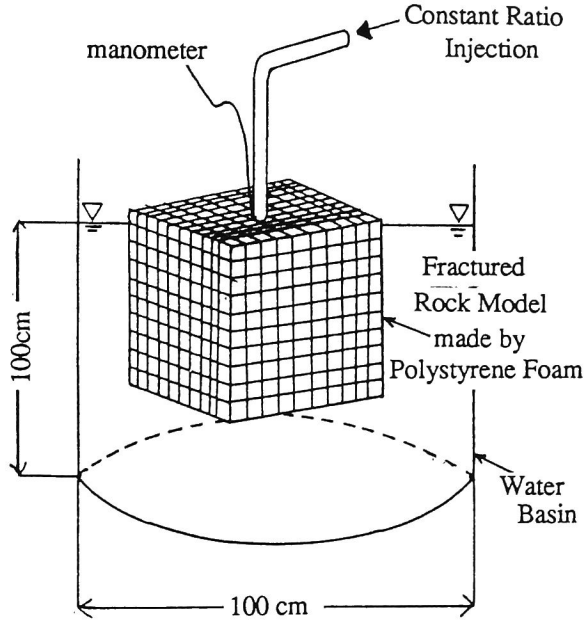


Figure 2.6.1 Schematic view of the experiment about the seepage flow in the fracture rock mass

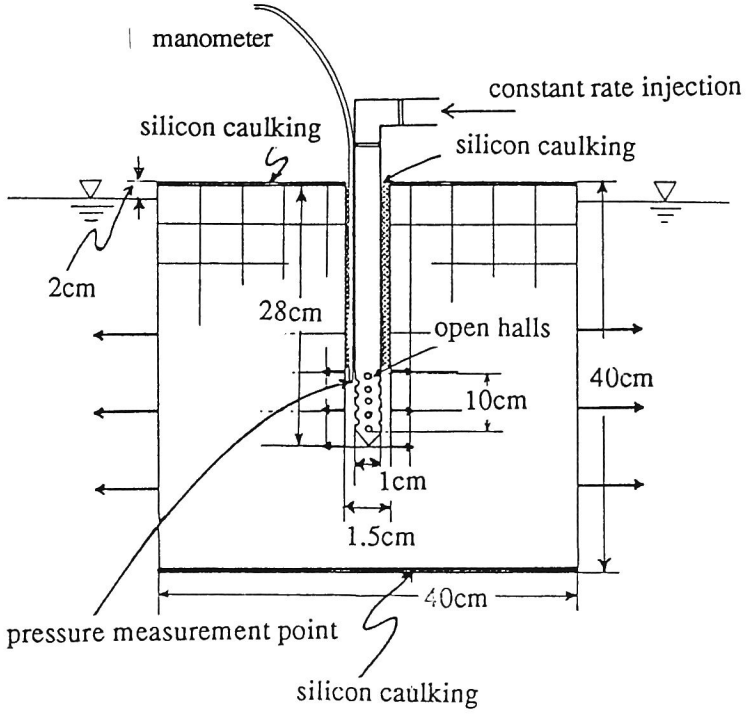


Figure 2.6.2 Fractured rock model used in the experiment

Since each block had been coated with waterproof paint, the seepage flow in the blocks could be ignored. The three-dimensional fracture plane network approach (referred to as the joint element model) was used.

All apertures of the vertical fractures were measured with a crack scale. The permeability of each fracture was obtained by the Cubic law and these apertures. The horizontal apertures were measured only at the surfaces of the artificial rocks. Those of the inner part could not be observed. The data taken at the surfaces indicates that the probability density function of the apertures is approximated by the lognormal distribution, as shown in Figure 2.6.3. According to this distribution function, the apertures in the inner part of the artificial fractured rocks are inferred by a computer.

Storativity of the fracture network is assumed as

$$S_s = nS_r\beta_P \qquad (2.6.1)$$

where S_r is the degree of saturation, n is the aperture of a fracture and β_p is the compressibility of water. Thus, the storativity of a fracture is given by a constant value for each fracture in this analysis.

(3) Results

The analyses were carried out for five cases with different horizontal aperture distributions. The results are shown in Figure 2.6.4. It is clear from this figure that the calculated pressures are less than the measured ones. This is because the points at which the pressures were measured do not correspond to the points estimated in the analyses.

Except for pressure values, the calculated pressure changes agree with the measured pressure change. It is clear from these results that the joint element model can simulate the real phenomena if the geometric condition of the fracture network is known well. However, it should be noted that the effects of the permeability of the rock blocks on the flow in a fracture network were not considered in the experiment.

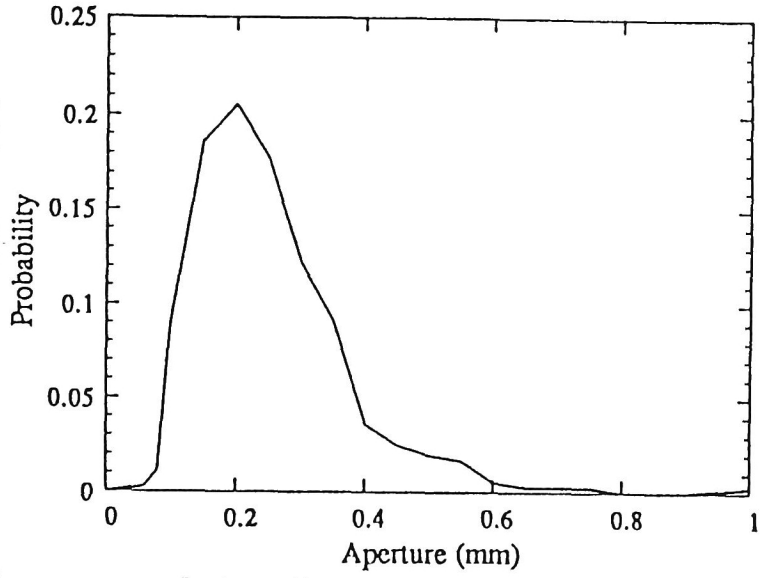


Figure 2.6.3 Measured aperture density distribution

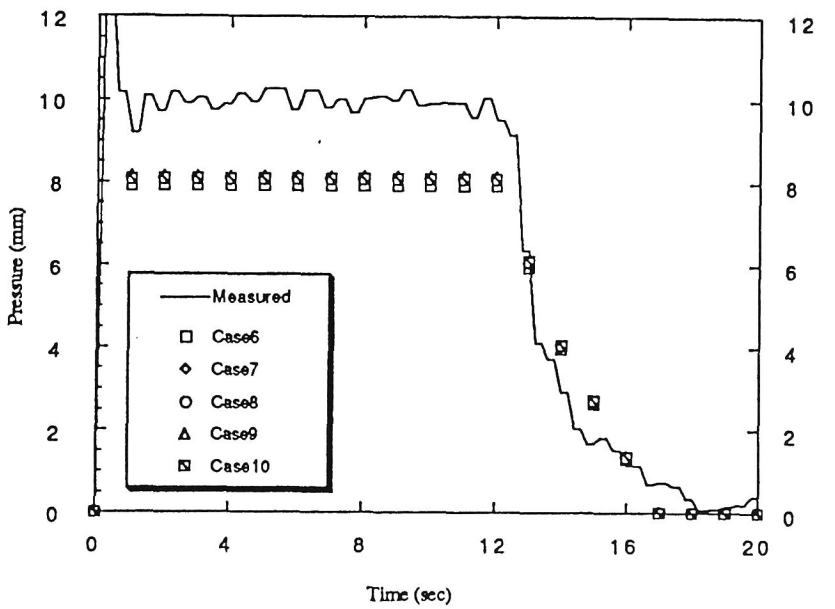


Figure 2.6.4 Comparison of measured pressure change with numerical one with the joint element model

2.6.3 Three-dimensional mesh generator

(1) General remarks

Many three-dimensional fracture models have been developed, for example, the orthogonal model defined by three sets of unbounded orthogonal joints (Snow (1965)), the Baecher model expressed by circular or elliptical joints (Baecher et al. (1978)), the Veneziano model based on the Poisson planes (Dershowitz et al. (1988)), the Dershowitz model (Dershowitz (1979)), the Mosaic model (Ambarcumjan (1974)) and so on. Long et al. (1987) created the fractured rock mass model with geostatistics.

Some of these models have been used for seepage analyses, the aim of which in many cases has been to examine the statistic aspects of the flux at the outlet boundaries, not to obtain the deterministic distributions of the velocity or pressures. Moreover, these models do not consider the fluid flow in the rock blocks.

The mesh generator introduced in this section is for analyses which consider the seepage flow in rock blocks and can define the closed blocks surrounded by randomly distributed fracture planes.

When transport analyses are conducted after an examination of the seepage flow for the safety or environmental assessment of a high level radioactive waste disposal project, the matrix diffusion phenomenon is one of the most important subjects to be examined. This mesh generator is expected to be useful for such analyses.

(2) Methodology

The probability density functions of fracture properties are needed for a conventional fracture modeling because fractures are generated by statistical methods. Concern lies in the fact that large conspicuous fractures may come to be the main paths of the fluid flow. Those fractures have to be deterministically distributed according to the field

measurement results. Hence, it is assumed that much information on such fractures is obtained by field investigations.

The necessary geometric information on the fractures is limited to the location of the following:

1) the normal vector of each fracture

2) the coordinates of a given point for each fracture

in which we assume that each fracture is a plane. The normal vector of a fracture is given by the two angles shown in Figure 2.6.5. The fracture planes can be distributed deterministically in the three-dimensional medium from the above information.

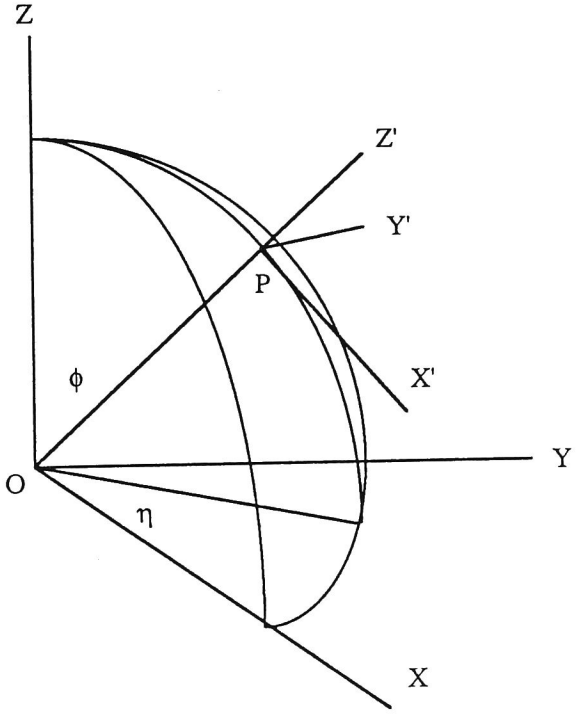


Figure 2.6.5 Convenient coordinate system

Sequentially, the closed block surrounded by those planes is defined. Figure 2.6.6 shows the procedure. The detailed treatment is mentioned in the following, in which each number coincides with the one in Figure 2.6.6:

1. In the" Do" loop for each fracture plane, the intersections between the new plane and each plane are firstly obtained; then the cross points between those intersections and each plane are treated as the new nodal points.
2. Each nodal point is defined by three planes and this information is registered.
3. Each point is examined to discover whether it exists over or under each plane, and this judgement is registered. In this procedure, the points just on the plane are recorded as belonging to both groups of points (over and under the plane).
4. Whether the closed block surrounded by the planes exists or not is examined.
   The number of over-and-under combinations of all planes is 2^{NPL} in which NPL is the number of planes. The number of nodal points is counted for each over-and-under combination. A block is defined for the group of points amounting to more than three. A group of nodal points which amounts to more than three can form a three-dimensional block. The maximum possible number of blocks generated by NPL planes is 2^{NPL}.
5. Planes that define the closed block are obtained; then the block is divided into tetrahedrons. This procedure is the same as that performed in the Block theory introduced by Goodman and Shi (1985).

As mentioned above, a closed block surrounded by any generated planes can be defined.

A fracture plane is firstly generated as an infinite plane in the analysis region, which is divided into polygonal regions by many intersections of the other planes. A portion of these divided polygons can be randomly marked as joints. This portion corresponds to "Persistence". Any hydraulic characteristics can be set to arbitrary polygons to generate a more realistic fractured rock model.

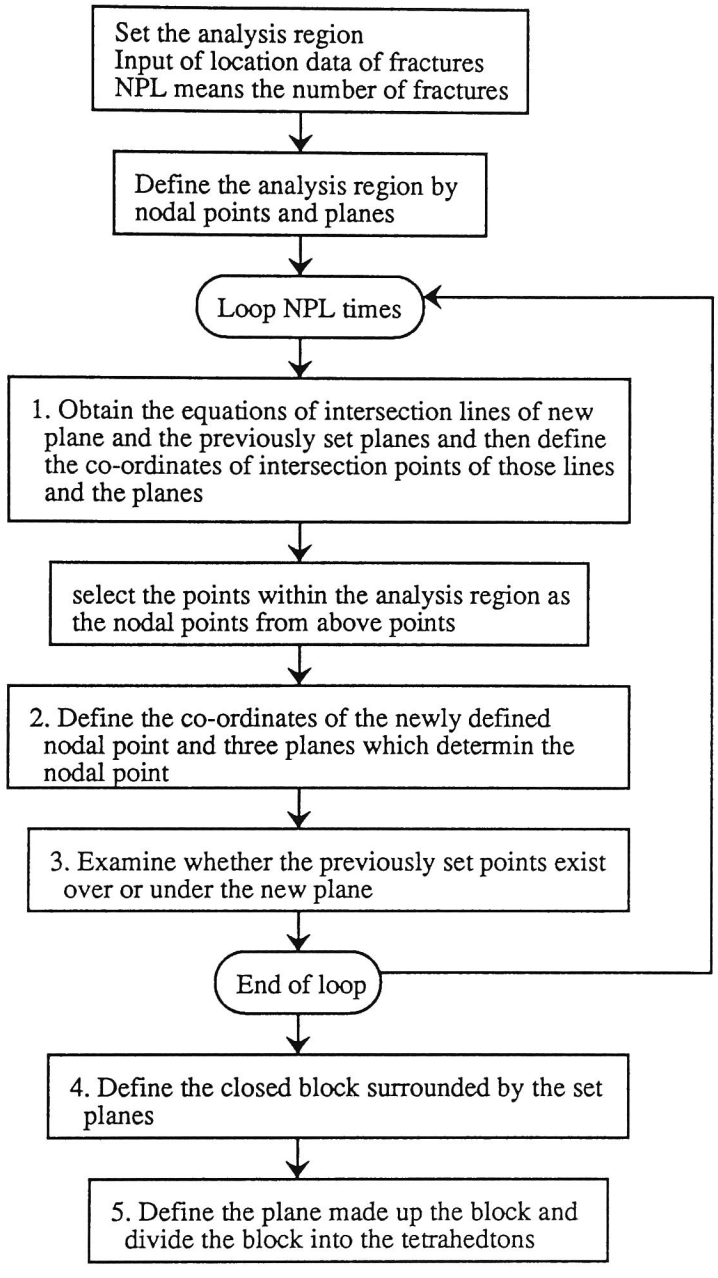


Figure 2.6.6 Flow of the mesh generating code for three-dimensional fractured medium

For the fractured rock model mentioned above, the discrete fractures are the large ones which have a significant permeability. Hence, we assume the information on those fracture planes, for example, the location, persistence and hydraulic characteristics, is established well before the analysis. The object of generating a rock model is to get a realistic model. Accordingly, there is no need to carry out a Monte Carlo simulation for the fractured rock models.

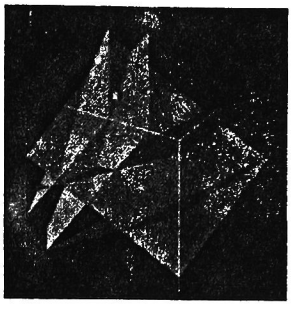
(3) Examples

Figure 2.6.7- 9 show examples of generated fracture models by the above method. Table 2.6.1 provides information on the fracture locations. For all examples, the region is 1000 x 1000 x 1000 m and the number of fractures is 5. Case 3 has bounded fractures and was generated by randomly selecting open fractures from Case 2.

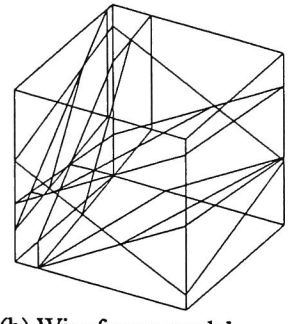
Table 2.6.1 Data for location of fractures

Case 1	Center of plane			Normal Vector	
	x	y	z	η	ϕ
	120	940	370	30	60
	340	450	530	-30	60
	900	100	420	60	-60
	10	10	670	60	-60
	10	710	230	-30	80

Case 2,3	Center of plane			Normal Vector	
	x	y	z	η	ϕ
	120	940	370	45	30
	340	450	530	-30	45
	900	100	420	25	-60
	10	10	670	60	55
	30	700	470	30	-12

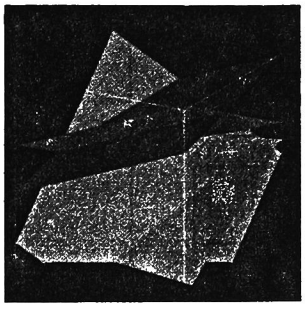


(a) Surface model

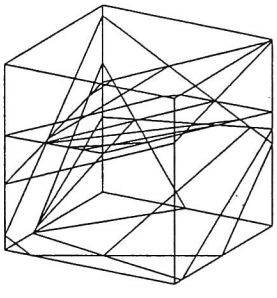


(b) Wire frame model

Figure 2.6.7 Fracture model of Case1

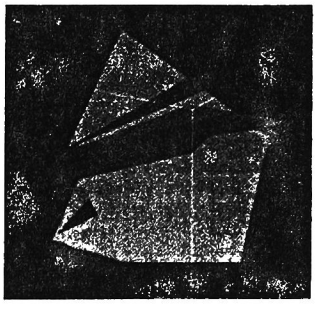


(a) Surface model

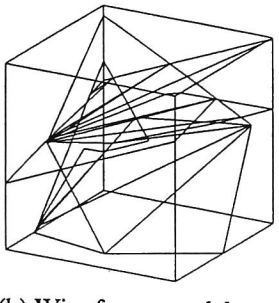


(b) Wire frame model

Figure 2.6.8 Fracture model of Case2



(a) Surface model



(b) Wire frame model

Figure 2.6.9 Fracture model of Case3

2.6.4 Fracture flow with leakage from rock matrices

(1) General remarks

The double porosity model was introduced by Barenblatt (1960). In this model, a medium is considered by superposing two different continuous porous media. In other words, two different water pressures are assumed to exist at the same point in a medium, and fluid transport from one medium to another occurs at the transient state because of the difference between the two water pressures. Thus, this model can consider the discontinuous flow situation between a rock matrix block and a fracture. In this section, the secondary porosity medium (i.e., the fracture) is represented by joint plane elements distributed in a three-dimensional medium, and the primary medium (the rock block) is expressed by ordinary three-dimensional solid elements. Hence, this new model considers a fractured rock mass by superposing a continuous porous medium and discontinuous planes. The geometry and properties of the set of joints have to be known in this model as well as in the conventional discrete fracture approach.

(2) Governing equations

The double porosity model for a deformable saturated-unsaturated medium is introduced in Section 2.4. The equation obtained by subtracting the term for deformation from the governing equations for fluid flow is given by

$$\frac{\partial}{\partial x_i}\left\{\frac{k_{1ij}}{\mu}\left(\frac{\partial p_1}{\partial x_j}+\rho_f g_j\right)\right\} = (n_1 S_{r1}\beta_P + C_{c1})\frac{\partial p_1}{\partial t} - \frac{\Gamma}{\rho_f} \qquad (2.6.2)$$

where p is the water pressure, n is the porosity, S_r is the degree of saturation, μ is the kinematic viscosity of water, ρ_f is the density of water, g is the gravitational acceleration, β_P is the compressibility of water, C_{c1} is the specific moisture capacity defined as $\partial\theta/\partial p$,

θ is the volumetric water content and Γ is the rate of fluid mass transferred from the rock block to the fracture. Subscript 1 stands for the primary porosity media.

Leakage term Γ is written by the following:

$$\Gamma=\dot{\alpha}\frac{k_1\rho_f}{\mu}(p_1 - p_2) \tag{2.6.3}$$

where $\dot{\alpha}$ is a dimensionless parameter related to the average length in the rock block from the fracture plane and the specific surface of the fractures. The leakage rate can be adjusted with this parameter.

The continuity equation for the fracture plane is represented for the two-dimensional medium. Thus, the governing equation for fluid flow is given by

$$\frac{\partial}{\partial\xi_i}\left\{\frac{k_{2ij}}{\mu}\left(\frac{\partial p_2}{\partial\xi_j}+\rho_f g_j\right)\right\}=S_2\frac{\partial p_2}{\partial t}+\frac{\Gamma}{\rho_f} \tag{2.6.4}$$

where ξ_i is the local two-dimensional coordinate defined on the fracture plane, S_2 is the storativity and k_{2ij}/μ is the transmissivity of a fracture.

(3) Finite element discretization

The Galerkin method was used to formulate the finite element discretization. The standard method can be applied to the equation for the rock block. However, the equation for a fracture written with two-dimensional local coordinate has to be transformed to one written with the global three-dimensional coordinate.

Suppose that OX, OY, OZ, which is a system of rectangular axes, and OX', OY', OZ', which is another set of rectangular axes whose direction cosines relative to OXYZ, are ($cos\ \alpha_x$, $cos\ \alpha_y$, $cos\ \alpha_z$), ($cos\ \beta_x$, $cos\ \beta_y$, $cos\ \beta_z$) and ($cos\ \gamma_x$, $cos\ \gamma_y$, $cos\ \gamma_z$), respectively, as shown in Figure 2.6.10. Thereby, transformation matrix [T] can be written as

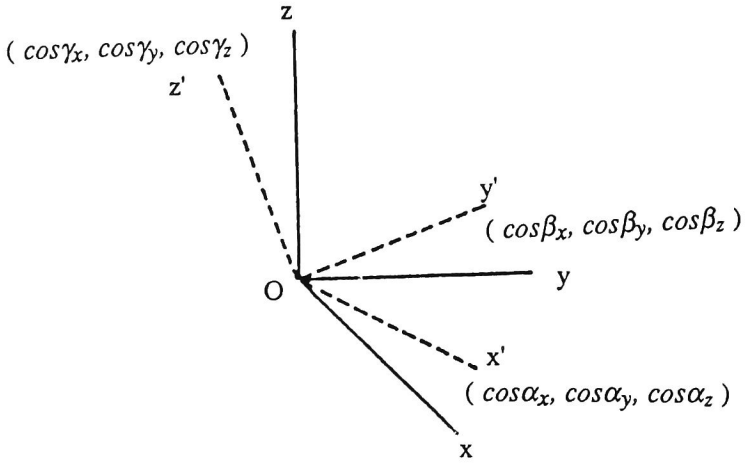


Figure 2.6.10 System in rectangular axes

$$[T]=\begin{bmatrix} cos\ \alpha_x & cos\ \alpha_y & cos\ \alpha_z \\ cos\ \beta_x & cos\ \beta_y & cos\ \beta_z \\ cos\ \gamma_x & cos\ \gamma_y & cos\ \gamma_z \end{bmatrix} \qquad (2.6.5)$$

where α_i is the angle between axis i in XYZ system and axis X', β_i is the angle between axis i and axis Y' and γ_i is the angle between axis i and axis Z'.

Jaeger and Cook(1969) show more convenient expressions of transformation matrix components for practical usage. The direction is frequently specified by its longitude η and zenith angle ϕ, as shown in Figure 2.6.5.

The axes associated with these coordinates are radial PZ', PX' in plane OPZ and associated with ϕ, and PY' chosen to make a right-handed system in the direction of η increasing. The direction cosines shown in equation (2.6.5) can be expressed in terms of η and ϕ as follows:

$$[T]=\begin{bmatrix} \cos\phi\cos\eta & \cos\phi\sin\eta & -\sin\phi \\ -\sin\eta & \cos\eta & 0 \\ \sin\phi\cos\eta & \sin\phi\sin\eta & \cos\phi \end{bmatrix} \qquad (2.6.6)$$

Angles ϕ and η can be obtained from the strike and dip of a fracture.

Let $[k_{x'i}]$ be the permeability tensor on the X'Y' plane, i.e., the fracture plane. Those components are transformed to global coordinates by $[T]$ in the following way:

$$[K_{xi}]=[T]^t[k_{x'i}][T] \qquad (2.6.7)$$

where $[k_{xi}]$ is the permeability tensor of a fracture in a global coordinate. The matrix with superscript t indicates a transposed one.

Hydraulic gradients are transformed in the same way, namely,

$$\left\{\frac{\partial p}{\partial x_i}\right\}=[T]^t\left\{\frac{\partial p}{\partial x'_i}\right\} \qquad (2.6.8)$$

Using the above transformation, equation (2.6.4) is discretized to a three-dimensional medium.

Two unknown variables, i.e., the potentials of the rock block and the fracture, are calculated on the fracture plane from the formulations mentioned above. One unknown variable, that of the rock block, is obtained from the rock blocks without the fracture plane.

(4) An unsaturated flow

An unsaturated flow in porous media may be estimated with a water retention curve. Such a hydraulic parameter in an unsaturated zone has been obtained for many types of soils. Nishigaki, et al.(1982) obtained the water retention curve for mudstone. That for

other kinds of rocks has not, however, been investigated very thoroughly. Despite such a situation, the permeability in the unsaturated zone in the rock matrix is conveniently assumed to change according to the k-θ relationships in which θ is a function of suction.

The mechanism of an unsaturated flow in fractures has not been investigated much either. Evans(1983) concluded that the unsaturated flow in a fracture was ignorable, because the rate of the unsaturated flow in a joint was less than that of saturated flow in a rock matrix. We assume that the unsaturated permeability in a fracture is zero.

(5) Numerical analyses

In order to demonstrate the function of the above-mentioned extended double porosity model, an example problem is solved using the fracture model generated in Case 1 of the previous section.

For boundary conditions, the total water head is set at 2000 tf/m^2 for the inlet boundary and at 1000 tf/m^2 for the outlet boundary. The initial condition is set at 1000 tf/m^2 for the total water head over the entire region. Table 2.6.2 indicates the parameters used for the analysis.

Figures 2.6.11a)–c) show the distribution of the velocity vectors and total water heads for each plane on the 7th day. There are two kinds of water heads on the plane, i.e., one for the fracture and the other for the rock block adjoining the fracture. It is clear from these figures that the velocity vectors on the fracture plane are influenced by the intersecting fractures and that the head distribution is discontinuous at the fracture plane in the rock mass.

Figure 2.6.11d) indicates all the velocity vectors calculated in this analysis. It is understood from this figure that the fluid flow according to the fracture system is very complicated. This phenomena cannot be simulated by a continuous approach.

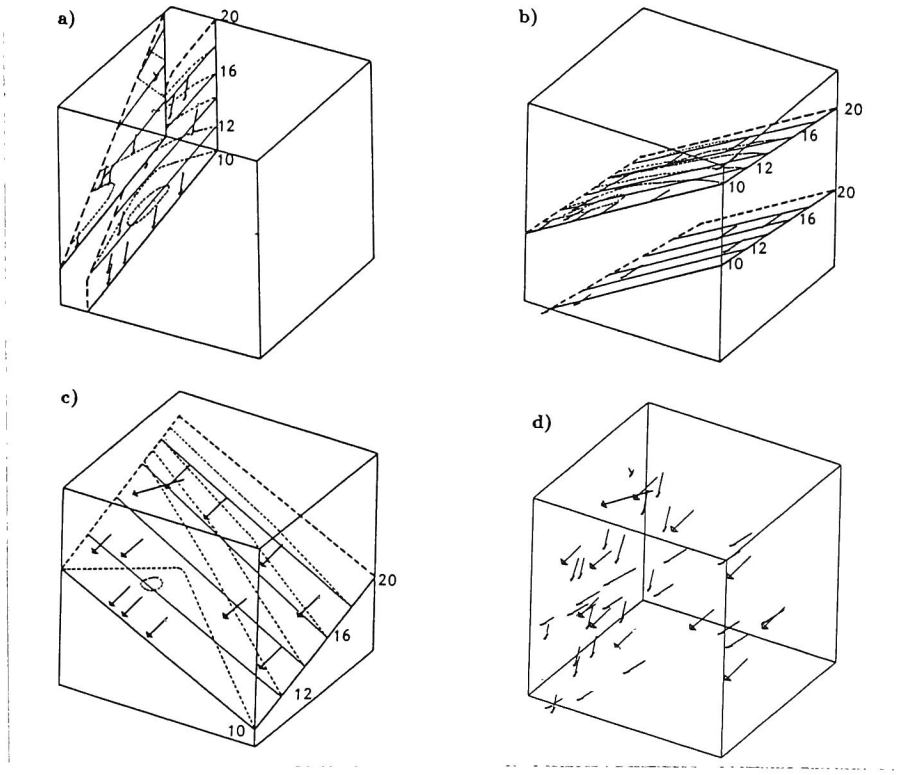


Figure 2.6.11 Velocity and total head distribution of Case 1 (unit is 100tf.m2) at 7th day.
Solid lines are for fractures and dotted ones are for blocks

Table 2.6.2 Parameters used in the example problem

Parameters	Values
Permeability of rock blocks	10^{-7} m/s
Permeability of fractures	10^{-4} m/s
Porosity of rock blocks	0.05
Porosity of fractures	0.002

2.6.5 Examination of the influence of rock blocks

(1) Field experiment at Chalk River Nuclear Laboratories

The field experiment to be analyzed is a hydraulic characterization test conducted by Chalk River Nuclear Laboratories (CRNL). This is test problem No. 3 for HYDROCOIN level 2. This site is located 200 kilometers northwest of Ottawa in Ontario, Canada.

The site is underlain by rocks in the Grenville Province of the Canadian Shield and has a well-exposed upthrown rock mass bounded on three and possibly four sides by faults or major fracture zones.

Four major fracture zones of high permeability (Nos. 1 through 4) were identified at the site. The locations of the fracture zones are shown together with the study-site boreholes in Figure 2.6.12. Geological information and the results of the hydraulic characterization test are introduced in detail by Raven(1985).

In this section, we analyze the hydraulic interference test on fracture No. 1. This zone is a narrow subhorizontal fracture intersected by eight test intervals (FS 5-1, 7-3, 8-2, 9-2, 10-1, 15-1, 16-2 and 17-1) at depths of from 33 to 50 m. Two pump tests were conducted at borehole FS-10. The test in which the water was discharged at a constant rate of 9.0 l/m on August 20-27, 1982, is examined here.

The model used in the analysis is shown in Figure 2.6.13 together with the initial and boundary conditions. The initial water table is assumed to be 5 m under the ground level for the whole area. A no-flux boundary condition is set except for at the northern vertical boundary. This boundary has a constant head whose value is the same as the initial value.

The water is discharged at the node corresponding to the intersection of FS-10 and fracture No. 1. The behavior of the water pressure at each borehole is analyzed.

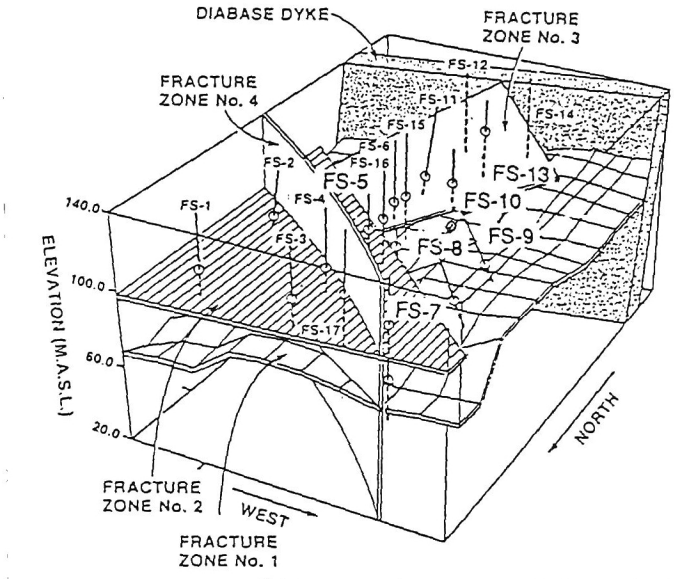


Figure 2.6.12 Sketch of CRNL ground water flow study site

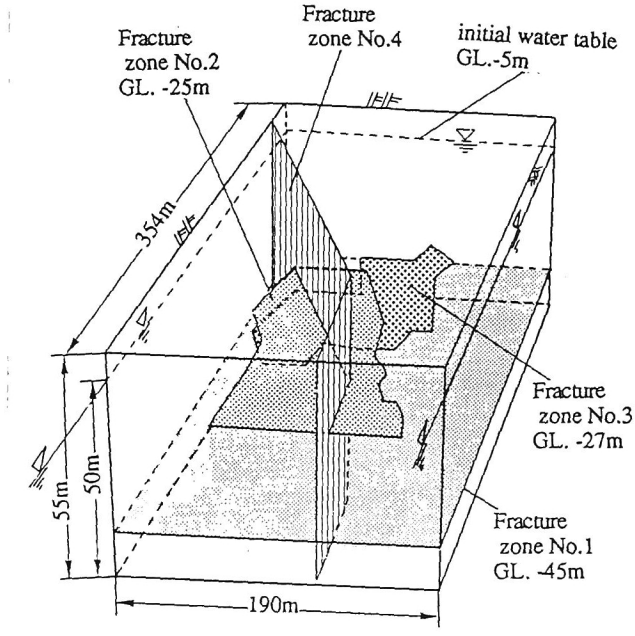


Figure 2.6.13 Model used in the analyses

We examine this field test by applying the extended double porosity model (called the extended model in this section) and the conventional finite element model with joint elements (called the conventional model). The latter model corresponds to the former one with leakage at the equilibrium state. The joint elements used in the conventional model share nodes with the adjoined rock block elements. Thus, the total water heads in the fractures equal those at the fracture wall and the discontinuous pressure distribution at the fracture cannot be expressed. On the other hand, the extended model supposes an unsteady state where there is the difference between the water heads in the fractures and those at the fracture wall. The flow rate from the rock blocks to the fractures is adjusted by parameter $\dot{\alpha}$. Thereby, the contribution of rock blocks to the flow in the fracture network is more diversely presented by the extended model

(2) Results

Table 2.6.3 shows the permeability and storage coefficient used in the analyses. The permeability of each rock bock is determined by calculating the log-mean of permeabilities estimated from straddle-packer injection tests by Raven (1985). The principal direction relative to three geographic reference axes is defined by three direction cosines (i.e., l_1, m_1 and n_1 for K_1). Geographic reference axes (one south, two east and three down) were used in the report by Raven. Table 2.6.3 also uses this reference. The anisotropic permeability obtained from this information is then transformed to our coordinate system (x is east, y is north and z is upward) for the analyses. The principal direction shown in Table 2.6.3 is the average for ones obtained by Raven.

The specific storage of the rock matrices were not obtained. Hence, the specific storage was assumed as shown in the table from the water compressibility and supposed porosity of the rock blocks.

The transmissivity of each fracture is derived with the Cubic law from the aperture shown in Table 2.6.3, which is estimated from the interference test by Raven. The storativity of each fracture zone is also obtained by the interference test.

Table 2.6.3 Permeability and storade coefficient used in the analyses for field test at CRNL

Zone	Principal Permeability(m/sec)			Storativity	Principal direction*		
	K_1	K_2	K_3	S	l_1	l_2	l_3
					m_1	m_2	m_3
					n_1	n_2	n_3
Rock matrices					-0.100	-0.128	-0.058
over fracture N0.1	9.13×10^{-9}	7.03×10^{-9}	1.40×10^{-9}	5×10^{-7}	-0.298	0.066	-0.160
					-0.060	-0.223	0.223
Rock matrices					-0.330	-0.040	-0.360
under fracture	9.99×10^{-9}	8.62×10^{-9}	5.76×10^{-9}	5×10^{-7}	-0.340	-0.420	-0.030
No.2.&3					0.230	0.470	0.510
Rock matrices					-0.077	-0.097	-0.018
under fracture	9.17×10^{-8}	7.25×10^{-8}	2.79×10^{-8}	5×10^{-7}	-0.026	-0.265	0.128
No.1					0.294	0.341	0.594

Fracture	Transmissivity (m^2/sec)	Storativity	Aperture(μm)
Fracture No.1	1.75×10^{-6}	2×10^{-5}	280
Fracture No.2	8.05×10^{-7}	7×10^{-5}	100
Fracture No.3	3.05×10^{-6}	1×10^{-5}	155
Fracture No.4	1.78×10^{-7}	5×10^{-5}	60

*Direction cosines relative to geographic reference axes.

Figure 2.6.14 shows the results calculated by the conventional model using the data shown in Table 2.6.3, which is a draw down versus log time response in observation boreholes intersecting fracture zone No. 1. The measured values at the observation wells are shown by a dotted chain line in the figure. Figure 2.6.15 shows the results of the draw down versus log time by a extended model, with $\dot{\alpha} = 10^{-6}$, using the same data. It is clear from these figures that the draw down by the conventional model is faster than that shown in the results observed in the field. On the other hand, since the extended model can adjust the flow rate from the rock blocks to the fractures, the draw down is well simulated using the parameters obtained by the field test. Thus, in order to express the phenomena observed in the field by the conventional model, it is necessary to adjust the transmissivity.

Figure 2.6.16 shows the results calculated by the conventional model such that the results agree with those from the field. The transmissivity used in this analysis is 4.2 x 10^{-7} m^2/s (aperture of 80 μm). Figure 2.6.17 indicates the log draw down versus log time response for the same results. Figure 2.6.18 shows the results of the draw down versus log time by extended double porosity model with $\dot{\alpha} = 10^{-4}$ using revised transmissivity. Figure 2.6.19 is the log -log plot of it.

When the permeability is set to be low in the extended model, the flow rate must be adjusted to be faster by increasing $\dot{\alpha}$. Moreover, the differences in draw down between observation wells grows larger than those by the conventional model. This is because the leakage rate from rock blocks near the discharge point may be larger than that far from the discharge point in the extended model.

It is also found from Figure 2.6.17 and 2.6.19 that the extended model expresses the upward convex shape of the log-log plot and the small draw down at an early stage. This means that the apparent storativity in the fractures at the early stage become larger than the measured one, and that more water is supplied from the rock blocks at the middle stage. On the contrary, the apparent storativity at the early stage and the flow supply from

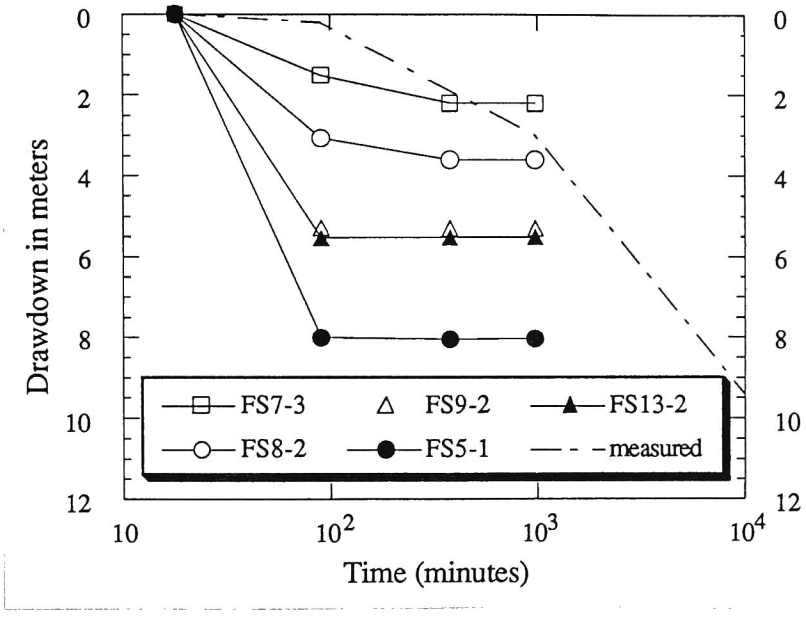


Figure 2.6.14 Drawdown versus log time response by conventional model using the data shown in Table 2.6.3

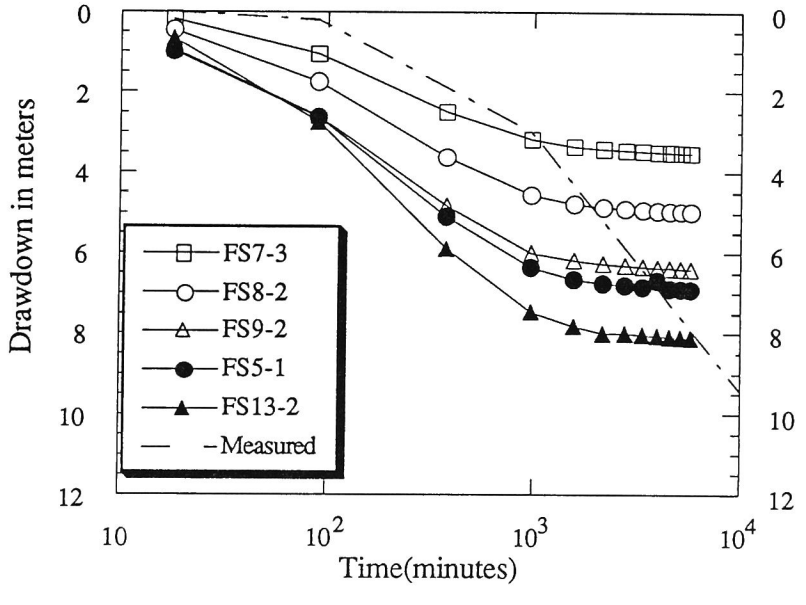


Figure 2.6.15 Drawdown versus log time response by modified double porosity model using the data shown in Table 2.6.3 (α=10^{-6})

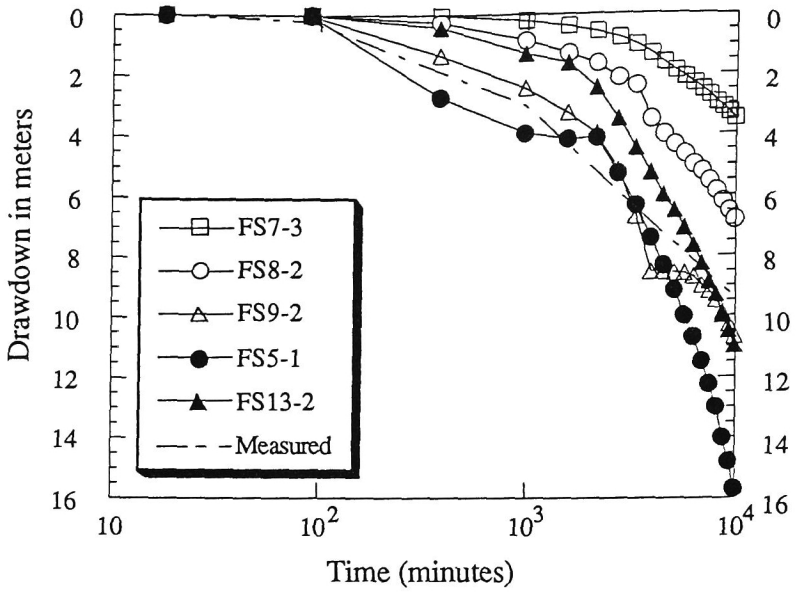


Figure 2.6.16 Drawdown versus log time response by conventional model such that the results agree with those from the field

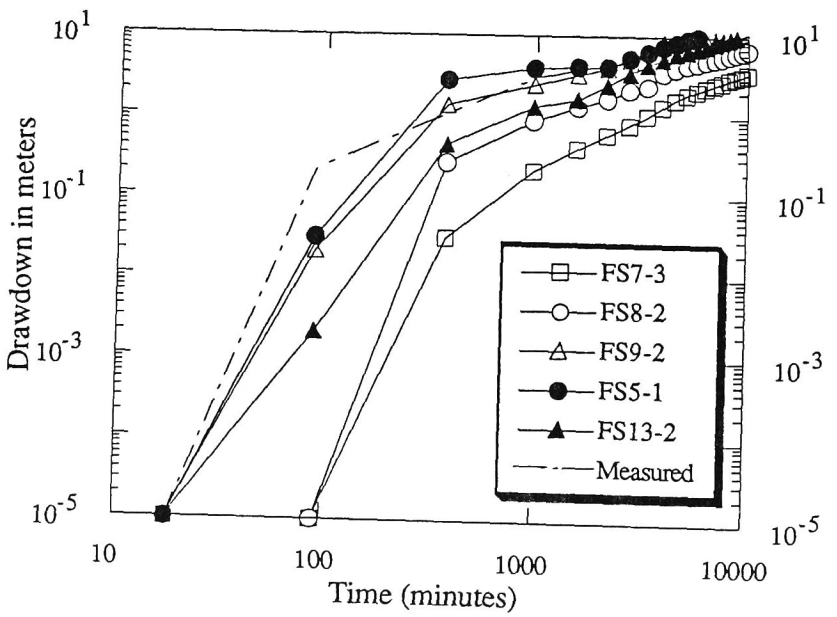


Figure 2.6.17 Log drawdown versus log time response by conventional model such that the results agree with those from the field

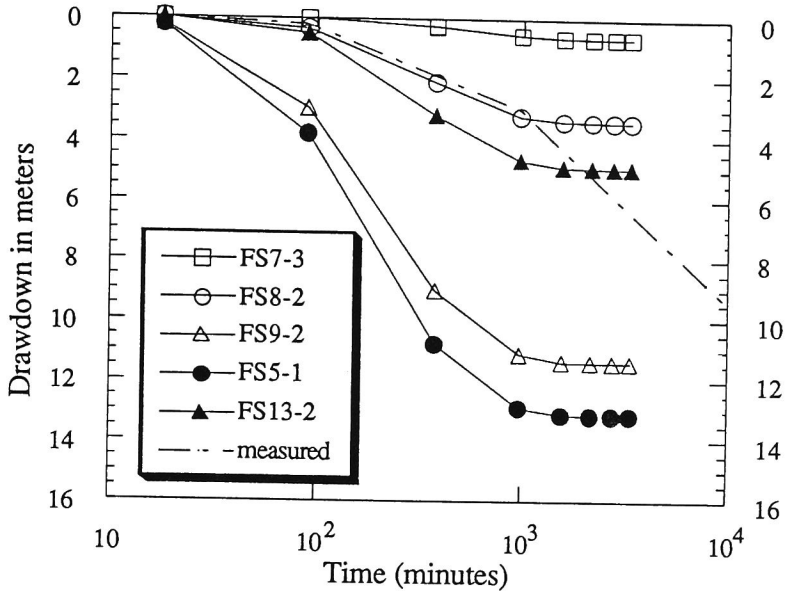


Figure 2.6.18 Drawdown versus log time response by modified double porosity model using revised transmissivity (α=10^{-4})

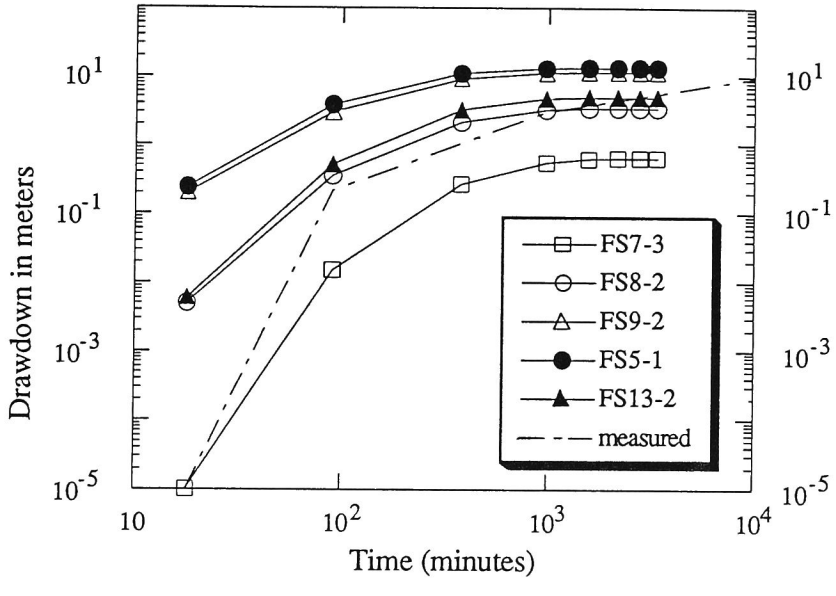


Figure 2.6.19 Log drawdown versus log time response by modified double porosity model using revised transmissivity (α=10^{-4})

the rock blocks at the middle stage, explained by the conventional model, are smaller than those measured in the field.

Parameter $\dot{\alpha}$ is set at 10^{-4} in the analysis shown in Figure 2.6.18. The results using $\dot{\alpha}$ as $2\text{x}10^{-4}$ are shown in Figure 2.6.20. When the leakage rate is higher, the draw down rate is lower and the time it takes to reach the steady state is shorter. In addition, the difference between observation wells becomes smaller. It is found from these results that the solution by the extended model is very dependent on parameter $\dot{\alpha}$. In other words, these results infer that leakage from the rock blocks may have a large effect on the flow in fractures at a real field.

Figure 2.6.21 indicates the results obtained by the conventional model with the isotropic permeability of rock blocks. The isotropic permeability is obtained by averaging the principal permeabilities in Table 2.6.3. It is clear by comparing Figure 2.6.21 and 2.6.16 that the draw down aspect simulated with the isotropic property is very different from the one which considers the anisotropy of rock blocks. When the isotropic permeability of rock blocks is used, the draw down curve is not smooth but has two phases, namely, the small draw down at the middle stage and the sudden large draw down after that. Such a tendency of the draw down curve is found at FS5-1 in Figure 2.6.16 and is emphasized in Figure 2.6.21.

Figure 2.6.22 shows the results from the extended model with the isotropic permeability of rock blocks. Rapid and large draw downs at all observation wells have occurred in this case.

It can be concluded from these results that the influence of the anisotropy of rock blocks to the flow in the fractures at the CRNL site is very great. In addition to the large anisotropy of the rock blocks at this site, the flow in the fracture No. 1 may be affected by the existence of other fracture zones and the boundary conditions.

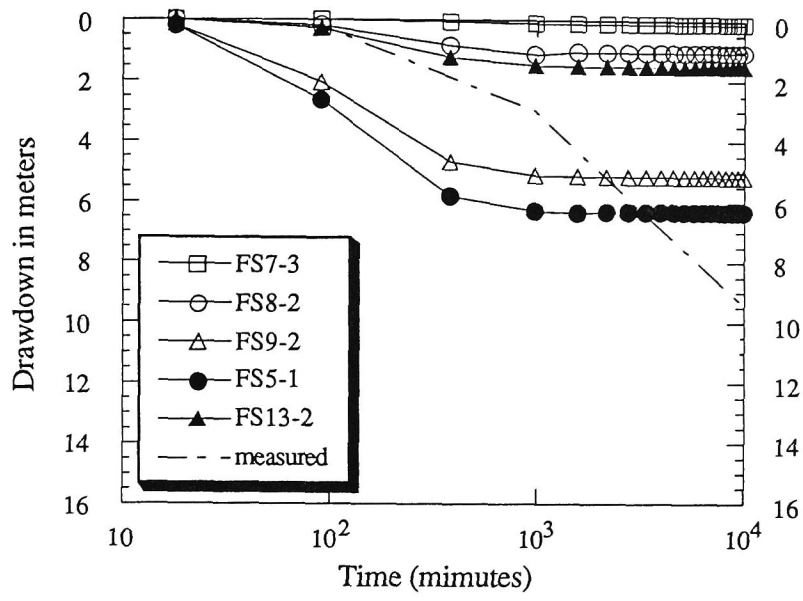


Figure 2.6.20 Drawdown versus log time response by modified double porosity model using revised transmissivity (α=2x10^{-4})

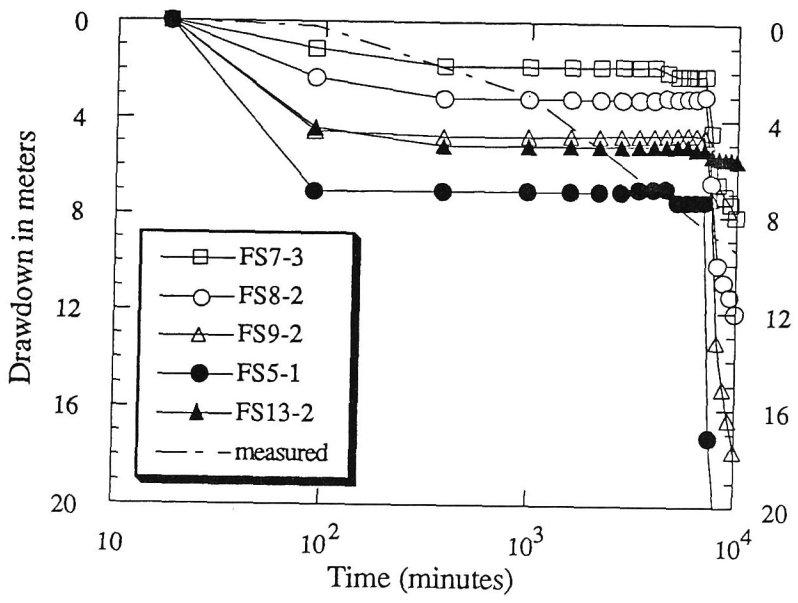


Figure 2.6.21 Drawdown versus log time response by conventional model with isotropic permeability of rock blocks

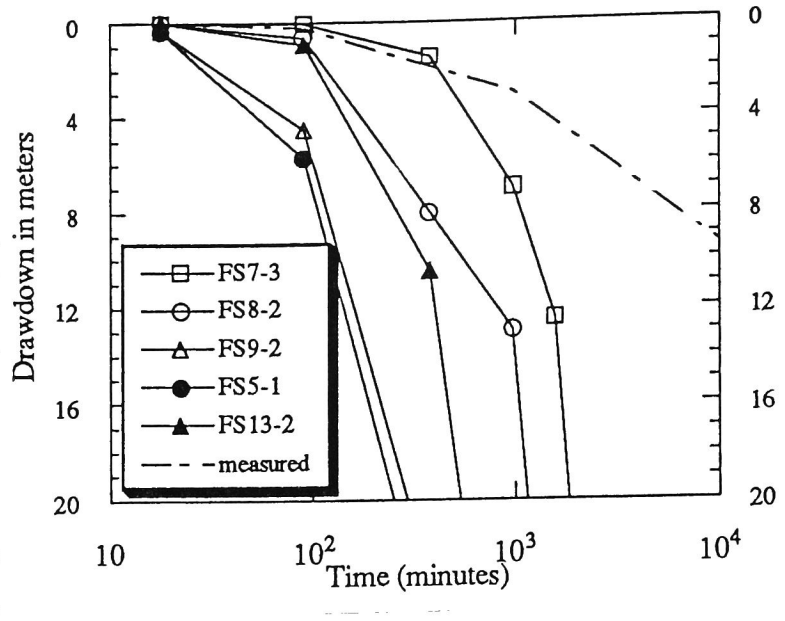


Figure 2.6.22 Drawdown versus log time response by modified double porosity model with isotropic permeability of rock blocks

Although measured values at all observation wells are almost the same as those shown by the dotted chain line, the calculated ones vary with the distance from the pumping point in all cases. This may be because a high permeable path exists in the fracture zone of the real field. To simulate this phenomena, it is necessary to introduce the inhomogeneity of permeability in the fracture plane element in the analysis. The inhomogeneity can be introduced by changing the permeability of each element of the fracture, while it is very difficult to obtain the information of the inhomogeneity from the field observation and to verify the structure model of the heterogeneous fracture plane.

2.6.6 Conclusions

Firstly, the propriety of a joint network analysis was examined in this section. Secondly, the mesh generator system was presented, in which the closed block surrounded by an arbitrary fracture network system could be defined. Thirdly, the new

seepage analysis method (the extended model) was introduced, in which the discontinuous pressure distribution at the fracture plane could be simulated. Finally, the influence of rock matrices on the flow in fractures was examined by the conventional continuous finite element method with joint plane elements (conventional model) and the extended model.

Although many problems remain to be solved in the discontinuous approach, this method is very useful for inferring the main velocity vectors in a rock mass. The conventional discontinuous approaches, however, have been used to examine the statistical aspect at the outlet boundary. This may be due to the difficulties of complete rock fracture modeling. If the modeled fractures are limited to large ones, however, we may make a more realistic model by concentrating on observations and experiments for those fractures.The selection of fractures, considered to be the main paths of the fluid flow, before the analysis, is very important for such a modeling.

There are many fields in Japan where small faults exist as the main paths in a rock mass. It would be easy to identify such paths in many Japanese fields. Thus, a combination of the discontinuous and continuous approaches is considered by the author to be very effective for the analysis of a seepage flow in an ordinary Japanese rock mass.

In addition, the modeling is also dependent on the scale of view of the analysis. The one mentioned above is for an analysis of relatively large scale in which relatively large fractures can be distinguished from many existing discontinuities. On the other hand, it may be difficult to distinguish them on a small scale. For such a case, the fracture network model without seepage in the rock blocks may be effective.

Conclusions for this section can be summarized as follows:

1) For fractured rocks, whose rock blocks have a very small permeability, the joint element network model is effective if the geometric and hydraulic conditions of the fractures are well established.

2) Since it is difficult for the Japanese rocks to model all fractures by joint elements, however, a discontinuous fracture modeling has to be applied to the possible main paths of the ground water. The rock blocks in such a model have many small cracks and fissures and their permeability is not negligible. For such a model, the mesh generator introduced in this section would be useful for the analysis.

3) The newly developed model (extended model) can simulate the discontinuous pressure distribution at the fracture plane. Moreover, the contribution of rock blocks to the flow in a fracture network is more diversely presented by this model.

4) For adjusting the leakage rate from the adjoined rock block to the fracture by the conventional model, it is necessary to change the transmissivity of the fracture. In addition, it is difficult to simulate the draw down aspect by the conventional model, even if the transmissivity is adjusted.

5) For fractured media with permeability and water storage in their rock blocks, the numerical results are strongly dependent on the way in which the leakage from the blocks to the fractures is explained. In other words, the influence of leakage on the flow in the fracture may be large in real fields.

6) The anisotropy of rock blocks has a great influence on the flow in a fracture for media with a large anisotropy. In particular, for models in which the rock blocks have many small cracks, the equivalent permeability may be anisotropic.

7) The main paths with a large permeability may exist in the fracture zone. To simulate the flow in such a field by the model mentioned above, it is necessary to introduce the inhomogeneity of the permeability on the fracture plane elements.

REFERENCES

Abelin, H., Neretnieks, I., Tunbrant, S. and Moreno, L.: Final report of the migration in a single fracture -Experimental results and evaluation-, Stripa project 85-03, SKB, (1985).

Akai, K. and T. Uno: Study on the quasi-one-dimensional, non-steady seepage flow through soil, Transaction of JSCE, No. 125, pp.14-22, (1966)

Akai, K., Y. Ohnishi and M. Nishigaki: Finite element analysis of saturated-unsaturated seepage in soil, Transaction of JSCE, Vol.264, pp.87-96, (1977)

Akai, K., Y. Ohnishi and M. Nishigaki: Finite element analysis of three-dimensional flows in saturated-unsaturated soil, 3rd Int.Conf. on Numerical Methods in Geomech., Archen, (1979)

Ambarcumjan, R.V.: Convex polygons and random tessellations, In Harding, E.F., Kendall, D.G.(eds), Stochastic geometry, pp 176--191. John Wiley & Sons, New York, (1974)

Andersson, J. and R. Thunvik: Predicting mass transport in discrete fracture networks with the aid of geometrical field data, Water Resour. Res., Vol.22, No.13, pp.1941-1950, (1986)

Baecher, G.B., Lanny, N.A. and Einstein, H.H.: Trace length biases in joint surveys, Proc. of the 19th U.S. symposium on rock mechanics, Vol. 1, pp 56-65, (1978).

Barenblatt, G.I., I.P. Zheltov and I.N. Kochika: Basic concepts in the theory of seepage of homogeneous liquids in fissured rocks (strata), PMM, Vol.24, 852, pp.286-1303, (1960)

Barton, N. and V. Choubey: The shear strength of rock joints in theory and practice, Rock Mech. 10, pp. 1-54, (1977).

Barton, N., S. Bandis and K. Bakhtar: Strength, deformation and conductivity coupling of rock joints, Int. J. Rock Mech, Min, Sci. & Geomech. Abstr. Vol. 22, No. 3, pp. 121-140, (1985)

Bear, J.: Dynamics of fluids in porous media, American elsevier, New York, (1972)

Bishop, A.w.: The principle of effective stress, Tek. Ukeblad, Norway, No.39, (1959)

Bredehoeft, J.D. and G.F. Pinder: Digital analysis of areal flow in multi-aquifer groundwater systems: A quasi three-dimensional model, Water Resour. Res., 6(3), pp.883-888, (1970)

Christian, J.T. and J.W. Boehmer: Plane strain consolidation by finite elements, J. Soil Mech. and Foundation Div. ASCE, SM 4, pp.1435-1457, (1970)

de Royvray, A.L. and R.E. Goodman: Finite element analysis of crack intiation in a block model experiment, Rock Mechanics, Vol.4, pp.203-223, (1972)

Dershowitz, W.S. and H.H. Einstein: Characterizing rock joint geometry with joint system models, Rock mechanics and rock engineering, Vol. 21, pp 21-51, (1988).

Dershowitz, W.S.: Rock joint systems, Ph.D. Thesis, Massachusetts Institute of Technology, Cambridge, Massachusetts, (1979).

Duguid, J.O. and P.C.Y. Lee: Flow in fractured porous media, Research Report No. 73 WR-1, Princeton University, (1973)

Evans, D.D.: Unsaturated Flow and Transport through Fractured Rock -Related High Level Waste Repositories, NUREG/CR-3206, (1983).

Freeze, R.A. and P.A. Witherspoon: Theoretical analysis of regional groundwater flow; 1. Analytical and numerical solutions to the mathematical model, Water Resour. Res. 2, pp.641-656, (1966)

Freeze, R.A.: Three-dimensional, transient, saturated-unsaturated flow in a groundwater basin, Water. Resour. Res., 7(2), pp.347-366, (1971)

Frind, E.O. and M.J. Verge: Three-dimensional modeling of groundwater flow systems, Water Resour. Res., Vol.14, No.5, pp.844-856, (1978)

Gale, J.E., R.V. Taylor, P.A. Witherspoon and M.S. Ayatollahi: Flow in rocks with deformable fractures, Finite Element Methods in Flow Problem, Ed. by Oden, J.T.,

O.C. Zienkiewicz, R.H. Gallagher and D. Taylor, Univ. Alabama at Huntsville Press, Huntsville, Alabama, pp.583-598, (1974)

Ghaboussi, J., E.L. Wilson and J.Isenberg: Finite element for rock joints and interfaces: Proc. ASCE, Vol.99, No. SM10, pp.833-848, (1973)

Goodman, R.E. and J.J. Dubois: Duplication of dilatancy in analysis in jointed rocks, Proc. ASCE, Vol. 98, No. SMR, pp.399-422, (1972)

Goodman, R.E. and St. John: Finite element analysis for discontinuous rocks, Numerical methods in geotechnical engineering, Ed by Desai, C.S. and J.T. Christian, McGraw-Hill, New York, pp. 148-175, (1977)

Goodman, R.E., R.L. Taylor and T.L. Brekke: A model for the mechanics of jointed rock, ASCE, Vol.14, No. SM5, pp.637-659, (1968)

Goodman, R.E., Shi, G-H.: Block theory and its application to rock engineering, Prentice--Hall, Englewood Cliffs, N.J.(1985).

Gupta, S.K., C.R. Cole and G.F. Pinder: A finite-element three-dimensional groundwater (FE3DGW) model for a multiaquifer system, Water Resour. Res., Vol.20, No.5, pp.553-563, (1984)

Hassanizadeh, M. and W. G. Gray: General conservation equations for multi-phase systems: 1 Averaging procedure, Adv. Water Res., 2, 131, (1979)

Herbert, A.W. and J.E. Gale: Fracture flow modeling of the test site characterization and validation area in the Stripa mine - Draft - , Stripa symp., Stockholm, (1989).

Heuze, F.E. and R.E. Goodman: Finite element studies of pile driver tunnels including considerations of support requirements, Univ. California Berkeley, Report to U.S. Corps of Engineers, Omana, Neb., Contract DACA 45-71-C0031, (1971)

Heuze, F.E. and T.G. Barbour: New models for rock joints and Interfaces, Proc. ASCE, Vol. 108, No. GT5, pp.757-776, (1982)

Heuze, F.E., R.E. Goodman and A. Bornstein: Joint perturbation and no tension finite element solutions, Rock Mechanics, Vol.3, No.1, pp.13-24, (1971)

Heuze, F.E.: Dilatant effects of rock joints, Proc. 4th Cong. ISRM, Montreux, Switzerland, Vol.1, pp.169-175, (1979)

Hilber, H.M. and R.L. Taylor: A finite element model of fluid flow in systems of deformable fractured rock, SESM Report No.76-5, Univ. California, Berkeley, (1976)

Huyakorn, P.S. and E.P. Springer: A three-dimensional finite-element model for simulation water flow in variably saturated porous media, Water Resour. Res., Vol.22, No.13, pp.1790-1808, (1986)

Huyakorn, P.S. and G.F. Pinder: Computational methods in subsurface flow, Academic Press, New York, (1983)

Huyakorn, P.S., B.H. Lester and C.R. Faust: Finite element techniques for modeling groundwater flow in fractured aquifers, Water Resources Research, Vol. 19. No. 4, pp.1019-1035, (1983)

Jaeger, J.C. and N.G.W. Cook: Fundamentals of Rock Mechanics, Methuen & CO LTD, (1969).

Kobayashi, A. and R. Yamashita: Preliminary results on case 9 -by using the non uniform velocity distribution-, The third INTRAVAL work shop, Helsinki, (1989).

Kobayashi, A. and R. Yamashita: Three-dimensional flow model in fractured rock mass, Rock Joints, Barton & Stephansson (eds), pp. 639-646, (1990).

Komada, H. and T. Ohmachi: Three-dimensional seepage analysis of fill dam, Large Dams, No.86, J. of the Japanese national committee on large dams, pp.1-15, (1978)

Kyoya, T., Y.Ichikawa and T. Kawamoto: A damage mechanics theory for discontinuous rock mass, Proc. 5th Int. Conf. Numer. Mech. in Geomech., Vol. 1, A.A. Balkema, pp.469-480, (1985)

Liggett, J.A.: Location of free surface in porous media, ASCE J. Hydraul. Div., 103(HY4), pp.353-365, (1977)

Long, J.C.S., D.M. Billaux: From field data to fracture network modeling; an example incorporating spatial structure, Water Resources Research, Vol. 23, No. 7, pp.1201 1216, (1987).

Long, J.C.S., J.S. Remer, C.R. Wilson and P.A.Witherspoon: Porous media equivalents for networks of discontinuous fractures, Water Resources Research 18, No. 3, pp.645-658, (1982)

Long, J.C.S., J.S. Remer, C.R. Wilson and P.A.Witherspoon: Porous media equivalents for networks of discontinuous fractures, Water Resources Research 18, No. 3, pp.645-658, (1982)

Long, J.C.S., K. Karasaki, A. Davey, J. Peterson, M. Landsfeld, J. Kemeny and S. Martel: Preliminary prediction of inflow into the D-holes at the Stripa mine, Stripa symp., Stokholm, (1989)

Louis, C.: Introduction à l'hydraulique des roches, Ph.D. Thesis, Paris, (1976)

Mahtab,M.A, and R.E. Goodman: Three-dimensional finite element analysis of jointed rock slopes, Proc. 2nd Cong. ISRM, Belgrade, Vol.3, (1970)

Matsumoto,T., H. Sekiguchi and Y. Nishida: Effects of end restraint of the triaxial sample on its isotropic consolidation behavior, The 18th Japan National Conf. on Soil Mech. and Foundation Engineering, pp.227-228, (1983)

Moreno, L., Y. Tsang, C.F. Tsang, I. Neretnieks: Flow and solute transport in a single fracture. A two-dimensional statistical model, SKB Technical report 88-03, (1988).

Motokage,I and I. Minami: Simulation of underground water in the Echigawa delta area, Transaction of JSIDRE, Vol.58, pp.14-20, (1975)

Motozima, I.: On seepage flow through fill dams and its foundations located on permeable bed, Technical Report of Central Research Institute of Electric Power Industry, No. 381011, (1981)

Narashimhan, T.N.: A unified numerical model for saturated-unsaturated groundwater flow, Ph.D. Dissertation, Department of Civil Engineering, Univ. of California, Berkely, (1975)

Neuman, S.P.: Saturated-unsaturated seepage by finite elements, ASCE J. Hydral. Div., 99(HY12), pp.2233-2251, (1973)

Ngo, D. : A network topology approach to the finite element analysis of progressive crack growth in concrete members, SESM Report No. 75-6, Univ. California, Berkeley, (1975)

Nishigaki, M., Kagitomi, J. and Shimo, M.: The Applicability of the Instantaneous Profile Method for the Measurement of the Water Retention Character of the Mud Stone, The 17th Japan National Conference on Soil Mechanics and Foundation Engineering, pp. 2385 - 2388 (in Japanese), (1982).

Noorishad, T.N., P.A.Witherspoon and T.L. Brekke: A method for coupled stress and flow analysis of fractured rock masses, Geotechnical Engineering Publication No. 71-6, University of California, Berkeley, (1971)

Nur, A. and J.D. Byerlee: An exact effective stress law for elastic deformation of rock with fluids, J.G.R., Vol. 76, No. 26, pp.6414-6419, (1971)

Oda, M. and M. Hatsuyama: Permeability tensor for jointed rock masses, Proc. of the Int. Symp. on Fundamentals of Rock Joints, pp.303-312, Bjorkiden, (1985)

Ohnishi, Y., H. Kagimoto and K.Nishino: Estimation of discontinuity characteristics and its application to rock hydraulics analysis, Transaction of JSCE, pp.241-248, (1986)

Ohnishi, Y.and H. Ohtsu,: Coupled stress flow analysis of discontinuous media by finite elements, Transaction of the JSCE No. 322, pp.111-120, (1982)

Pinder, G.F., E.O. Frind and M.A. Celia: Groundwater flow simulation using collocation finite elements, Proc. of the 2nd Int. Conference on Finite Elements in Water Resour., pp.1.171-1.185, (1978)

Rasmuson, A. and I. Neretnieks: Radionuclide transport in fast channels in crystalline rock, Water Resour. Res., Vol. 22, No. 8, pp. 1247-1256, (1986).

Raven K.G.: Hydraulic characterization of a small groundwater flow system in fractured monzonitic gneiss, The fourth HYDROCOIN Work shop, (1985).

Sandu, R.S. and E.L. Wilson: Finite element analysis of seepage in elastic media, J. Eng. Mech. Div. ASCE, EM 3, pp.641-652, (1969)

Sato, K., T. Shimizu and Y. Ito: Fundamental study on permeability and dispersion in double porosity rock masses, Fifth International Conference on Numerical Methods in Geomechanics, Nagoya, pp.657-664, (1985)

Segol, G.: A three-dimensional Galerkin-finite element model for the analysis of contaminant transport in saturated-unsaturated porous media, Proc. of the First Int. Conference on Finite Elements in Water Resour., pp.2.123-2.145, (1976)

Sharma, H.D..et al.: Generalization of sequential nonlinear analysis, A study of rockfill dam with joint elements, Proc. 2nd Int. Conf. Num. Meth. in Geo., Blacksburg, Va., Vol.2, pp.662-685, (1976)

Snow, D.T.: A parallel plate model of fractured permeable media, Ph. D. Dissertation, University of California, Berkeley, (1965).

Snow, D.T.: Rock fracture spacings, openings and porosities, Jour. Soil Mech. and Found. Division, ASCE, Vol. 94, No. 1, pp. 73-91, (1968).

St. John, C.M.: Finite element analysis of two and three-dimensional jointed structures-Computer programs, Rock Mechanics Research Report No. 13, Imperial College, London, (1972)

Stratford, R.G., A.W. Herbert and C.P. Jackson: A parameter study of the influence of aperture variation on fracture flow and the consequences in a fracture network, Rock Joints Barton & Stephansson (eds), pp. 413-422, (1990)

Toki, K., F. Miura and T. Ohtake: Non-linear seismic response analysis of soil-structure interaction system by 3-dimensional joint element, Transaction of JSCE, Vol.322, pp.51-62, (1982)

Tsang, Y.W. and C.F. Tsang: Channel model of flow through fractured media, Water Resour. Res., Vol. 23, No. 3, pp. 467-479, (1987).

Tsang, Y.W. and C.F. Tsang: Hydrological characterization of variable aperture fracture, Rock Joints Barton & Stephansson (eds), pp. 423-431, (1990)

Van Dillen, D.E. and R.D. Ewing: BMINES, A finite element code for rock mechanics applications, Proc. 22th Sympo. on Rock Mech., MIT Publishing, Cambridge, Mass., pp.353-358, (1982)

Warren, J.E. and P.J. Root: The behavior of naturally fractured reservoirs, Soc. of Petroleum Engineers Journal, pp.245-255, (1963)

Wilson, R.K.and E.C.Ainfantis: On The Theory of Consolidation with Double Porosity, Int. J. Engng. Sci. Vol. 20, No. 9, pp.1009-1035, (1982)

Xirun, G.: Non-linear analysis for joint element and its application in rock engineering, Int. J. Num. Meth. in Geo., Vol.5, pp.229-245, (1981)

Yashima, A.: Study on the mechanical characteristics of a discontinuous rock mass and the application to the tunnel excavation problem (in Japanese), Doctoral Dissertation, Kyoto Univ., (1985)

Chapter 3 COUPLING EFFECTS ON FLUID FLOW

3.1 Introduction

In this chapter, the effects of coupled phenomena on ground water flow are discussed. Coupled behavior occurring in a rock mass is one of the most complicated phenomena studied in the field of rock mechanics. This subject has to be examined not only through experiments and measurements, but also with powerful numerical analyses because it is difficult to understand the mechanism of such a complicated phenomenon only through experiments.

High level radioactive waste disposal in a deep geology is expected to create a particularly complicated situation, because the radioactive decay of high level radioactive waste affects the host rock thermally and a repository is planed to be constructed in a very deep ground. An assessment of the performance of a nuclear waste repository involves the evaluation of the combined effects of mechanical, hydraulic and thermal processes in the complex geological system.

Under such complicated conditions, the transport problem is also a problem to be solved for the assessment. It is commonly assumed that the concentration of solute does not have any influence on the behavior of the ground water flow, because the amount of radionuclides leaking out of the repository is not expected to be so great, while the mechanical behavior may affect the permeability of the ground and change the velocity distributions of the ground water. Although the solute transport is affected by a changed velocity, it is not affected directly by the mechanical behavior. The temperature change in the ground will change the chemical condition, which in turn influences the solute transport behavior. However, it seems difficult at the present time to make a mathematical model of the transport phenomenon considering the effects of thermal change, because sufficient data related to such a phenomenon does not exist. It may be appropriate,

therefore, to treat the thermal effects on the solute transport problem as the dependency of the retardation factor on temperature.

For the above-mentioned reasons, it is commonly assumed that the solute transport problem can be considered apart from the hydraulic, mechanical and thermal problems for the performance assessment of radioactive waste disposal projects.

In this section, the two-dimensional coupled hydraulic, mechanical and thermal problems is examined. Firstly, the basic theory is introduced; secondly, the effects of variable parameters on the coupled behavior are examined through numerical experiments; thirdly, the ground water flow around the opening is investigated under conditions where the temperature is changed; and finally, the coupling phenomena occurred in a buffer material are examined in comparison to the results of the Buffer mass test conducted in the Stripa project. Subsequently, the three-dimensional problem is examined. Because this kind of coupled problem has many unknown variables, large capacity of computer is needed for the analysis of a practical problem. To save computer storage and calculation time, the preconditioned conjugate gradient method is introduced into the code. Using the newly developed code, the three-dimensional results are compared with the two-dimensional ones for a imaginary deep nuclear waste depository.

3.2 Previous Works

Many coupled analyses have been performed on pairs of hydraulic, mechanical and thermal phenomena. And for a long time, solution techniques for these coupled problems lagged behind analytical solutions and were restricted to simple geometries. The recent development of computers has advanced the numerical techniques drastically in the field of coupled analysis.

For the coupled hydraulic and mechanical problems of saturated porous media, the consolidation problem of clay has been studied for quite some time and notable among these are studies by Christian and Boehmer (1970) and Sandhu and Willson (1969). Recently, a model considering the elasto-plasticity or visco-plasticity of soils has been developed. On the other hand, many problems related to the hydraulic and mechanical analyses for fractured rock still exist. One of them is the modeling of a fractured medium in which the deformation and the ground water flow are strongly influenced by the geometry of the fractures. Moreover, whether or not the principle of effective stress can be applied is not yet understood well. As a matter of fact, the behavior of fractured rock cannot be predicted very well at the present time because of the unresolved problems mentioned above. The state of the art of studies on the various coupled processes for rock joints has been introduced by Tsang (1990).

In such a situation, it seems important to examine whether the model used for the analysis is suitable for the object of the evaluation or not and to understand what limitations and assumptions exist in the model. For a thorough understanding of the model, we have to consider the results of the analyses, after which the phenomena that may occur in the future can be predicted.

Currently, there are a few approaches for fractured porous medium. One is the discrete fracture approach, which regards the fractured medium as a continuum in which discrete discontinuities exist (Noorishad et al. (1971) and Ohnishi and Ohtsu (1982)). The other approach is the equivalent continuous model which models the anisotropic properties

produced by the existing fractures (Oda (1986)). In addition, the distinct element method (DEM),which considers the pore water pressure, is used for many projects (Barton (1988) and Fairhurst and Hart (1987)). Table 3.2.1 shows the previous works for coupled hydraulic and mechanical problems, adding to Iizuka's work (1988).

For coupled thermal and mechanical problems, there are many studies which apply classical mechanics with numerical calculation techniques that are based on continuum mechanics. In these studies, Duhamel-Neuman's equation is often used for an equilibrium equation to introduce thermal stress. In such analyses, the medium is treated as an elastic one. On the other hand, the influence of the mechanical behavior on energy conservation is often ignored, and thus, fully coupled thermal and mechanical analyses have rarely been carried out. In some cases, thermal stress is treated as an initial stress is and is obtained separately before solving the mechanical problems (e.g., Shimooka (1982)).

When plastic deformation by thermal stress has to be considered, the yield function is needed as a function of the temperature in addition to stress. Such a treatment is rarely conducted, however, for analyses in the geotechnical field. In many cases, the plastic deformation is conventionally considered apart from the thermal stress (Utsugida (1985), Hamajima et al. (1987)).

For fractured rock masses, DEM has recently been used for assessing the performance of the natural barrier of a radioactive waste repository (Shen and Stephansson (1990)).

There are many engineering problems related to coupled hydraulic and thermal behavior. Geothermal and freezing soil problems are representative of problems existing in the geotechnical field. The modeling for these coupled problems is dependent on the temperature range considered. Vaporization has to be considered for the geothermal problem because of the high temperature and high pressure under ground (Marcer and Faust (1975), Witherspoon et al. (1975)). In contrast, the frost action is intensively studied for the freezing soil problem. Such a phase change behavior is very complicated and involves many unknown mechanisms. When a complex phenomenon such as vapor-

Table 3.2.1 Previous main works for coupled hydraulic and mechanical problems

Author	Published Year	Mechanical Property	Hydraulic Region	Object
Sandhu et al.	'69	E	S	Soil
Christian et al.	'70	E	S	Soil
Yokoo et al.	'71	E	S	Soil
Noorishad et al.	'71	E*	S	Rock
Ghaboussi et al.	'73	E	S	Soil
Simpson	'73	EP	S	Soil
Cundall et al.	'74	VE	S	Rock
Ohta et al.	'75	EP	S	Soil
Small et al.	'75	EP	S	Soil
Lewis et al.	'76	EP	S	Soil
Akai et al.	'78	EP	S	Soil
Carter et al.	'79	EP	S	Soil
Shibata et al.	'80	EP	S	Soil
Ohnishi et al.	'80	E	SU	Soil
Matsui et al.	'81	EP	S	Soil
Nakagawa et al.	'82	E	SU	Soil
Ohnishi et al.	'82	E*	SU	Rock
Nakai et al.	'83	EP	S	Soil
Oda	'86	E	S	Rock

E: Elastic, EP: Elasto-plastic, E*: Elastic for rock matrices and Elasto-plastic for fractures, VE: Visco-elastic, S: Saturated, SU: Saturated-unsaturated

ization or freezing is analyzed, limitations and assumptions of the numerical model must be well understood before examining the numerical results.

On the other hand, the coupled problem related to high level radioactive waste disposal in a deep geology has also been intensively studied recently. The effect of increasing temperatures due to the radioactive decay of waste on the ground water flow around a repository has been studied by many researchers (e.g., Hodgkinson (1980), Wang et al. (1981)). The models used in their analyses are dependent on the ground conditions at which the repository is assumed to have been constructed. In cases where the repository will be constructed in an unsaturated region (e.g., tuff in the U.S.A.), vaporization is the

most important phenomenon to be analyzed. On the contrary, when the repository will be constructed in deep crystalline rock, the convection induced by increasing temperatures is the most important matter for assessment.

In more recent studies, the problems of coupled hydraulic, mechanical and thermal phenomena have been studied. Beer and Carapcioglu (1981) derived basic equations which describe the thermoelastic behavior of a ground due to hot water injection into confined and leaky aquifers. Hart (1981) presented a model which fully describes coupled thermal, mechanical and hydraulic behavior in nonlinear porous geologic systems and which calculates the model by an explicit finite difference method. Noorishad et al. (1984) applied a finite element method with joint elements to fully coupled phenomena for a saturated fractured rock mass. Ohnishi et al. (1985) developed a finite element code to handle the problems of coupled hydraulic, thermal and mechanical behavior of a saturated-unsaturated geologic medium.

3.3 Two-dimensional thermal-hydraulic-mechanical coupling

3.3.1 Introduction

A numerical analysis code is developed to examine fully coupled thermal, hydraulic and mechanical phenomena. This code supposes a high level radioactive waste disposal in a deep geology. The temperature range assumed in this code is under 100 °C, and thus, vaporization is not considered. Using this code, we examine the effects of variable parameters on the coupled phenomena and the influence of changes in the permeability of rock on the fluid flow in a rock mass due to temperature changes. Moreover, the phenomenon of water movement occurring in the complicated situation near the radioactive waste package is investigated. These examinations are very important for the performance assessment of radioactive waste disposal.

THAMES (Thermal, Hydraulic And MEchanical System analysis) is a finite element code designed to simulate fully coupled thermal, hydraulic and mechanical behavior in a saturated-unsaturated geologic medium. The mathematical formulation for the model utilizes Biot's theory, with the Duhamel-Neuman's form of Hooke's law, and the energy balance equation. The governing equations are derived with the fully coupled thermal, hydraulic and mechanical relationships, as shown in Figure 3.3.1. The three coupled equations are solved simultaneously.

3.3.2 Basic theory

(1) Assumptions

The governing equations are derived under the following assumptions:

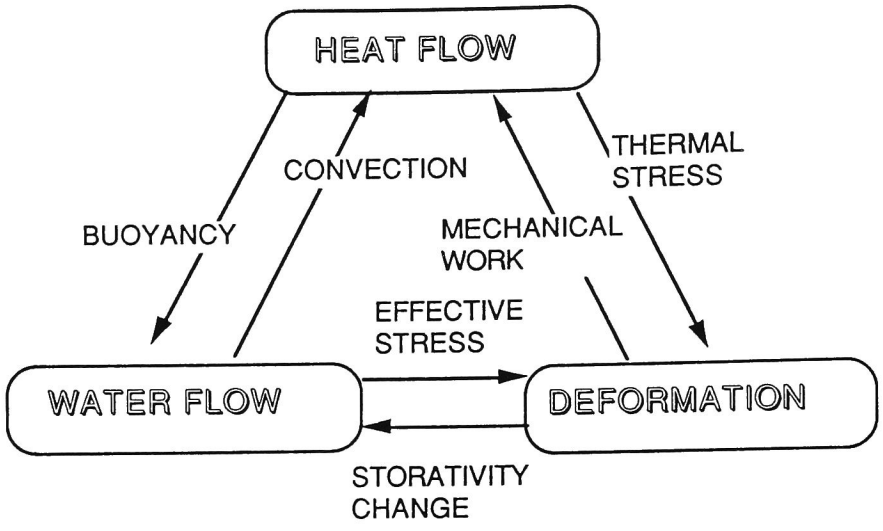


Figure 3.3.1 Coupled phenomena considered in THAMES

1) The medium is poro-elastic.

2) Darcy's law is valid for the flow of water in a saturated-unsaturated medium.

3) Heat flow occurs only in solid and liquid phases.

The phase change of water from liquid to vapor is not considered.

4) Heat transfer among three phases (solid, liquid and gas) are disregarded.

5) Fourier's law holds for heat flux.

6) Water density varies depending upon temperature and the pressure of water.

(2) Equilibrium equation

The equation of motion for a medium in a static case is known as an equilibrium equation. It is written in a total stress expression as

$$\sigma_{ij,j} + \rho b_i = 0 \qquad (3.3.1)$$

where σ_{ij} is stress, ρ is the density of a soil-water mixing medium and b_i is the body force.

Terzaghi defined the effective stress principle. Bishop and Blight (1963) extended his definition and proposed the following equation for a saturated-unsaturated medium:

$$\sigma_{ij} = \sigma'_{ij} + \chi \delta_{ij} \rho_f \psi \qquad (3.3.2)$$

where σ'_{ij} is the effective stress, δ_{ij} is Kronecker's delta, ρ_f is the unit weight of water and ψ is the pressure head. Subscript f means "fluid". Parameter χ is defined as

$$\chi = \begin{cases} 1 & \text{saturated zone} \\ \chi(S_r) & \text{unsaturated zone} \end{cases} \qquad (3.3.3)$$

χ is a nonlinear function of S_r (the degree of saturation).

The validity of equation (3.3.2) is not definite and is still under debate even now. However, here it is assumed that equation (3.3.2) holds and that χ is approximately equal to S_r.

Substituting equation (3.3.1) for equation (3.3.2), we obtain the equilibrium equation for the effective stress in a saturated-unsaturated geologic medium.

$$\left(\sigma'_{ij} + \chi \delta_{ij} \rho_f \psi \right)_{,j} + \rho b_i = 0 \qquad (3.3.4)$$

where $(\chi \delta_{ij} \rho_f \psi)$ is a term which means that changes in the pressure head influence the equilibrium equation.

The effects of temperature can be implemented in a constitutive law for a solid medium. For an isotropic linear elastic material, Duhamel-Neuman's relationship can be used and the following constitutive law is obtained:

$$\sigma'_{ij} = C_{ijkl} \varepsilon_{kl} - \beta \delta_{ij} (T - T_0) \qquad (3.3.5)$$

where $\beta=(3\lambda+2\mu)\alpha_T$. C_{ijkl} is an elastic matrix, ε_{kl} is the strain tensor, T is temperature, λ and μ are Lamé's constants and α_T is the thermal expansivity coefficient. Subscript 0 means that the parameter is in a reference state.

The Infinitesimal strain-deformation relationship is

$$\varepsilon_{kl} = \frac{1}{2}(u_{k,l} + u_{l,k}) \qquad (3.3.6)$$

where u_i is the deformation vector.

Substituting equations (3.3.5) and (3.3.6) into equation (3.3.4), the stress equilibrium equation is obtained which takes into account the effects of temperature and pore pressure change,

$$\left[\frac{1}{2} C_{ijkl}(u_{k,l} + u_{l,k}) - \beta\delta_{ij}(T - T_0) + \chi\delta_{ij}\rho_f\psi\right]_j + \rho b_i = 0 \qquad (3.3.7)$$

$(-\beta\delta_{ij}(T-T_0))_j$ is a term which stands for the influence of heat transfer on the equilibrium equation.

(3) Continuity equation for ground water

The equation of continuity for ground water in a saturated-unsaturated zone is derived from Richards' theory as follows:

$$\frac{\partial(\rho_f\theta)}{\partial t} = -(\rho_f v_i)_{,i} \qquad (3.3.8)$$

where θ is the volumetric water content, t is time and v_i is the velocity vector.

The equation of motion for ground water can be explained by Darcy's law. That is,

$$v_i = - k(\theta)_{ij} h_j \qquad (3.3.9)$$

in which $k(\theta)_{ij}$ is a permeability tensor that is a function of θ. h is the total head.

The total head can be expressed as the sum of pressure head ψ and elevation head z, namely,

$$h = \psi + z \qquad (3.3.10)$$

The volumetric water content is a function of the degree of saturation S_r and porosity n, which is expressed as

$$\theta = nS_r \qquad (3.3.11)$$

Substituting equations (3.3.9), (3.3.10) and (3.3.11) into equation (3.3.8), we obtain the following equation:

$$\left\{\rho_f k(\theta)_{ij} (\psi + z)_{,j}\right\}_{,i} = \frac{\partial}{\partial t} \rho_f n S_r \qquad (3.3.12)$$

The right-hand side of equation (3.3.12) is expanded to

$$\frac{\partial}{\partial t}(\rho_f n S_r) = n S_r \frac{\partial \rho_f}{\partial t} + \rho_f S_r \frac{\partial n}{\partial t} + \rho_f n \frac{\partial S_r}{\partial t} \qquad (3.3.13)$$

The first term at the right-hand side represents a density change in the pore water. The second term means a change in the skeleton of the porous medium. The third term stands for a change in the degree of saturation in an unsaturated region.

Considering the compressibility and thermal expansivity of water, the density of water can be expressed as

$$\rho_f = \rho_{f0}\left[\, 1 - \beta_T (T - T_0) + \beta_P (P - P_0) \right] \qquad (3.3.14)$$

where P is the pore water pressure and ρ_{f0} is the reference density at $P=P_0$ and $T=T_0$.

β_T and β_P are the thermal expansivity and compressibility of water, respectively, and are defined as

$$\beta_T = \left| -\frac{1}{\rho_f}\frac{\partial \rho_f}{\partial T} \right| \cdots (P = constant) \qquad (3.3.15)$$

and

$$\beta_P = \left| \frac{1}{\rho_f}\frac{\partial \rho_f}{\partial P} \right| \cdots (T = constant) \qquad (3.3.16)$$

Eaton (1983) assumed that buoyancy could be ignored in an unsaturated zone due to the insignificant effect on the fluid flow. Adopting this assumption, we set $\beta_T=0$ in an unsaturated zone.

A combination of the first terms in equations (3.3.13) and (3.3.14) yields

$$nS_r \frac{\partial \rho_f}{\partial t} = \rho_{fo} nS_r \left(-\beta_T \frac{\partial T}{\partial t} + \beta_P \frac{\partial P}{\partial t} \right) \qquad (3.3.17)$$

Pressure head ψ is related to the pore water pressure as follows:

$$\psi = \frac{P}{\rho_f g} \qquad (3.3.18)$$

Taking into account equations (3.3.10) and (3.3.18), equation (3.3.17) can be modified to

$$nS_r \frac{\partial \rho_f}{\partial t} = \rho_{fo} n S_r \left(- \beta_T \frac{\partial T}{\partial t} + \rho_{fg} \beta_P \frac{\partial h}{\partial t} \right) \tag{3.3.19}$$

Assuming that the strain is infinitesimal, the second and third terms at the right-hand side of equation (3.3.13) are expressed as

$$\rho_f S_r \frac{\partial n}{\partial t} \equiv \rho_f S_r \frac{\partial\, u_{i,i}}{\partial t}$$
$$\rho_f n \frac{\partial S_r}{\partial t} \equiv \rho_f \frac{\partial (nS_r)}{\partial t} = \rho_f \frac{\partial \theta}{\partial t} = \rho_f \frac{\partial \theta}{\partial \psi} \frac{\partial \psi}{\partial t} \tag{3.3.20}$$

Equation (3.3.12) is modified by using equations (3.3.19) and (3.3.20) as follows:

$$\left\{ \rho_f k(\theta)_{ij} h_j \right\}_{,i} - \rho_{fo} n S_r \rho_{fg} \beta_P \frac{\partial h}{\partial t} - \rho_s C(\psi) \frac{\partial \psi}{\partial t} - \rho_f S_r \frac{\partial u_{i,i}}{\partial t} + \rho_{fo} n\, S_r \beta_T \frac{\partial T}{\partial t} = 0 \tag{3.3.21}$$

where $C(\psi)$ is the specific water content and is defined as

$$C(\psi) = \frac{\partial \theta}{\partial \psi}. \tag{3.3.22}$$

Equation (3.3.21) is an equation of continuity for ground water which takes into account the compressibility of the ground and changes in density by temperature change.

(4) Energy conservation law

In general, the ground consists of materials with three phases, i.e., solid, liquid and gas. It is not easy to understand the behavior of heat transfer through such a composite material, because the way in which heat is transported is different for each phase and a heat transfer may occur between phases. However, the state of the gaseous phase in a ground is too complicated to be modeled. For simplicity, a pore in a porous medium is assumed to be filled with only a liquid phase in this section. This means that the ground water does not change in phase from liquid to gas or vise versa and the thermal conductivity of the gaseous phase is disregarded. Since the heat conductivity of the gaseous phase is smaller than that of the liquid and solid phases, the heat conductivity of the composite material is not affected much by the volume of the gaseous phase.

An energy conservation law, based upon the process proposed by Bear and Carapcioglu (1981), is derived from the above assumptions without the effect of viscous dissipation for ground water.

Considering the existence of an unsaturated zone, the equation of energy conservation is written as

$$nS_r\rho_f C_{vf}\left(\frac{\partial T_f}{\partial t} + V_f \nabla T_f\right) = -\nabla \cdot nS_r J_f - \left(\frac{\partial P}{\partial T_f}\right)_{\rho_f} nS_r T_f \nabla V_f \qquad (3.3.23)$$

where C_v is a specific heat and J is the heat flux by conduction. In equation (3.3.23), the first term at the left-hand side shows the time dependency of energy, the second term shows the change in energy due to heat convection. The first terms at the right-hand side expresses the change in energy by heat conduction and the second term shows a reversible energy change caused by compression.

Similarly, the energy conservation law for a solid phase is written as

$$(1-n)\rho_s C_{vs}\left(\frac{\partial T_s}{\partial t} + V_s \cdot \nabla T_s\right) = -\nabla(1-n)J_s - (1-n)\beta T_s \frac{\partial \varepsilon_s}{\partial t} \qquad (3.3.24)$$

where subscript s means "solid". In equation (3.3.24), the second term at the right-hand side indicates the reversible energy change caused by deformation.

Faust and Mercer (1979) proposed that the movement of water through porous media is so slow and the surface areas of all phases are so large that it is reasonable to assume that a local thermal equilibrium among phases is achieved instantaneously. This means that the heat transfer between phases in the ground can be disregarded. If this assumption is permitted, the following equation is then valid:

$$T = T_s = T_f. \tag{3.3.25}$$

Using this assumption, equations (3.3.23), (3.3.24) and (3.3.25) can be combined and an equation of energy conservation for the ground can be obtained by

$$\{ nS_r\rho_f C_{vf} + (1\text{-}n) \rho_s C_{vs} \} \frac{\partial T}{\partial t} + \{ nS_r\rho_f C_{vf} V_f + (1\text{-}n) \rho_s C_{vs} V_s \} \cdot \nabla T$$
$$= - \nabla \cdot \{ \{ nS_r J_f + (1\text{-}n) J_s \} \} - nS_r T \left(\frac{\partial p}{\partial T} \right)_{\rho f} \nabla V_f - (1\text{-}n) T\beta \frac{\partial \varepsilon_s}{\partial t} \tag{3.3.26}$$

When it is assumed that Fourier's law is valid for heat conduction, the following equations are given:

$$J_f = - K_{Tf} \nabla T$$
$$J_s = - K_{Ts} \nabla T \tag{3.3.27}$$

where K_T is the coefficient of heat conduction.

The term $\partial P/\partial T$ in equation (3.3.26) can be modified by applying equations (3.3.15) and (3.3.16) as follows:

$$\left(\frac{\partial P}{\partial T}\right)_{\rho f} = \left|\frac{\beta_T}{\beta_P}\right|_{\rho f = constant} \qquad (3.3.28)$$

Ignoring the velocity of a solid, equation (3.3.26) is rewritten using equations (3.3.6), (3.3.9), (3.3.27) and (3.3.28) in the following form:

$$(\rho C_v)_m \frac{\partial T}{\partial t} + ns_r \rho_f C_{vf} V_{f\,i} T_{,i} - K_{Tm} T_{,ii} + ns_r T \frac{\beta_T}{\beta_P} k(\theta)\, h_{,ii} + \frac{1}{2}(1-n)\beta T \frac{\partial}{\partial T}(u_{i,j} + u_{j,i}) = 0 \qquad (3.3.29)$$

where $(\rho C_v)_m$ and K_{Tm} are expressed as follows:

$$(\rho C_v)_m = ns_r \rho_f C_{vf} + (1-n)\rho_s C_{vs} \quad \text{and} \qquad (3.3.30)$$

$$K_{Tm} = ns_r K_{Tf} + (1-n) K_{Ts}. \qquad (3.3.31)$$

Equation (3.3.29) is an energy conservation law in which the effects of stress-deformation and ground water flow are considered. The first, second and third terms at the right-hand side express changes in energy due to heat conduction, pore water pressure and reversible energy caused by solid deformation, respectively.

(5) Governing equations

Equations (3.3.7), (3.3.21) and (3.3.29) represent the governing equations for coupled thermal, hydraulic, mechanical problems. We use these equations by means of total head expression such as

$$\left[\frac{1}{2} C_{ijkl}(u_{k,l} + u_{l,k}) - \beta \delta_{ij}(T - T_0) + \chi \delta_{ij} \rho_f h\right]_{,j} + \overline{\rho_s} b_i = 0$$

$$\left\{ \rho_f k(\theta)_{ij} h_{,j} \right\}_{,i} - \rho_{fo} n S_r \rho_f g \beta_P \frac{\partial h}{\partial t}$$

$$- \rho_f C(\psi) \frac{\partial h}{\partial t} - \rho_f S_r \frac{\partial u_{i,i}}{\partial t} + \rho_{fo} n S_r \beta_T \frac{\partial T}{\partial t} = 0$$

$$(\rho C_v)_m \frac{\partial T}{\partial t} + n s_r \rho_f C_{vf} V_{f\,i} T_{,i} - K_{Tm} T_{,ii}$$

$$+ n s_r T \frac{\beta_T}{\beta_P} k(\theta) h_{,ii} + \frac{1}{2}(1\text{-}n)\beta T \frac{\partial}{\partial T}(u_{i,j} + u_{j,i}) = 0 \qquad (3.3.32)$$

where $\overline{\rho_s} = (1\text{-}n)(\rho_s - S_r \rho_f)$ and ρ_s is the density of a solid phase.

It is necessary to establish the following initial and boundary conditions in order to solve equation (3.3.32).

Initial conditions:

$$u_i(\tilde{x}, t) = \hat{u}_i(\tilde{x}, 0)$$

and

$$h(\tilde{x}, t) = \hat{h}(\tilde{x}, 0) \qquad (3.3.33)$$

Boundary conditions:

displacement:

$$u_i(\tilde{x}, t) = \hat{u}_i(\tilde{x}, t)$$

or traction:

$$\sigma_{ij}(\tilde{x}, t)\, n_j(\tilde{x}) = \hat{T}_i(\tilde{x}, t),$$

total head:

$$h(\tilde{x}, t) = \hat{h}(\tilde{x}, t)$$

or flow rate:

$$\{ k(\theta)\, h_{,i} \}\, n_i = -\hat{Q}(\tilde{x}, t),$$

temperature:

$$T(\tilde{x}, t) = \hat{T}(\tilde{x}, t)$$

or heat flow:

$$K_{Tm} T_{,i} n_i = -\hat{Q}_T(\tilde{x}, t). \qquad (3.3.34)$$

where $\tilde{x}$ is a position vector, n_j is the unit normal vector, $\hat{u}$ is the known displacement, $\hat{h}$ is the known head, $\hat{T}_i$ is the known surface traction, $\hat{Q}$ is the prescribed flow rate and $\hat{Q}_T$ is the prescribed heat flow.

(6) Numerical techniques

The Galerkin type finite element technique is employed to formulate a finite element discretization. In order to obtain stable solutions, linear isoparametric elements are used to represent the behavior of total head h and temperature T. Quadratic isoparametric elements are used to express displacement u_i. In order to integrate time derivatives, a time

weighting factor is introduced, and thus, any type of finite difference scheme may be applied.

3.3.3 Verification of code

THAMES has to be verified for fully coupled hydraulic, mechanical and thermal problems. However, these problems can not be solved analytically at the present time. Therefore, the code is verified with the available analytical and experimental results.

The problems considered in the verification are as follows:

(1) A one-dimensional consolidation problem: An analytical solution to this problem can be found in Terzaghi (1925).

(2) The stress-strain problem of a thick-walled circular cylinder subjected to uniform internal and external pressures: An analytical solution to this problem can be found in Timoshenko and Goodier (1951).

(3) The thermal stress problem of a thick-walled circular cylinder subjected to a uniform temperature gradient: An analytical solution to this problem can be found in Boley and Weiner (1960).

(4) A one-dimensional heat conduction problem: An analytical solution to this problem can be found in Smith (1965).

(5) A coupled thermal and hydraulic problem: Experimental results can be found in Sato (1982). He experimented with hot water seepage in a saturated sand sample.

(6) A saturated-unsaturated seepage problem: A quasi one-dimensional, non-steady seepage flow through a sand box was examined by Akai and Uno (1966).

An excellent agreement was achieved between the finite element solutions by THAMES and the analytical and experimental solutions. The numerical results are presented in Figures 3.3.2 - 3.3.7. From these calculations, we suppose that THAMES is verified for the fundamental functions of it.

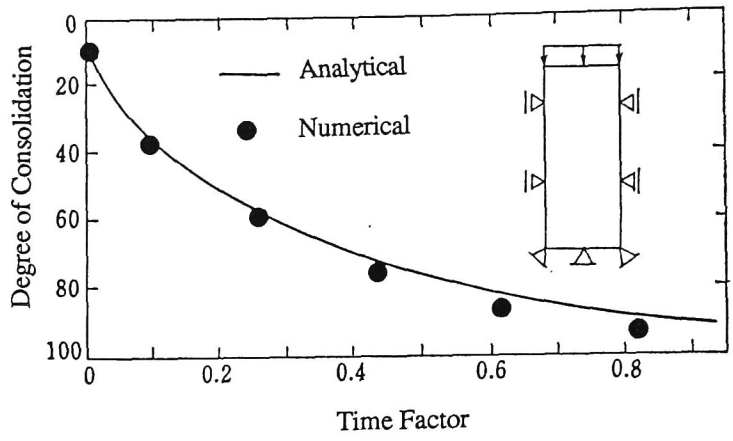


Figure 3.3.2 Comparison with the analytical solution of the one-dimensional consolidation problem

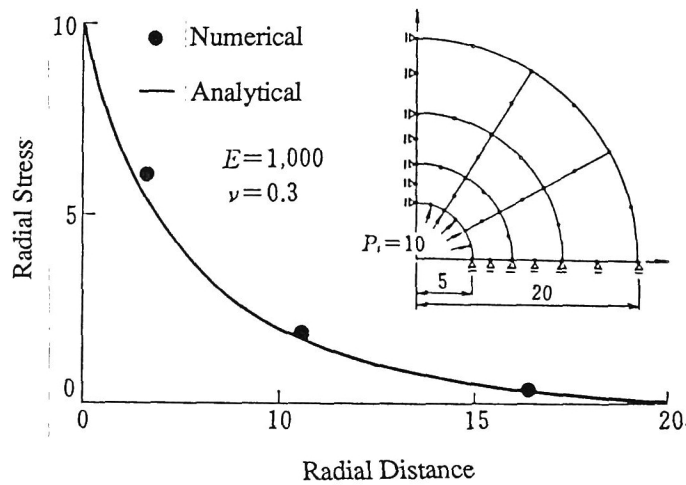


Figure 3.3.3 Comparison with the analytical solution of the stress-strain problem of a thick-walled circular cylinder subjected to uniform internal and external pressures

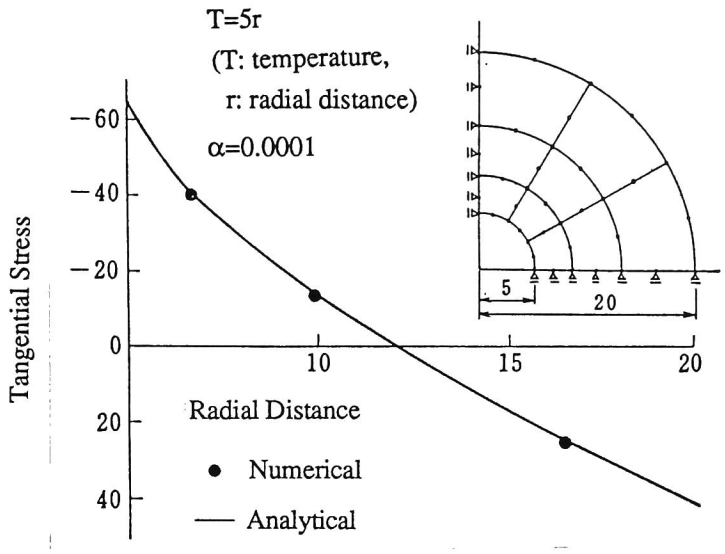


Figure 3.3.4 Comparison with the analytical solution of the thermal stress problem of a thick-walled circular cylinder subjected to a uniform temperature gradient

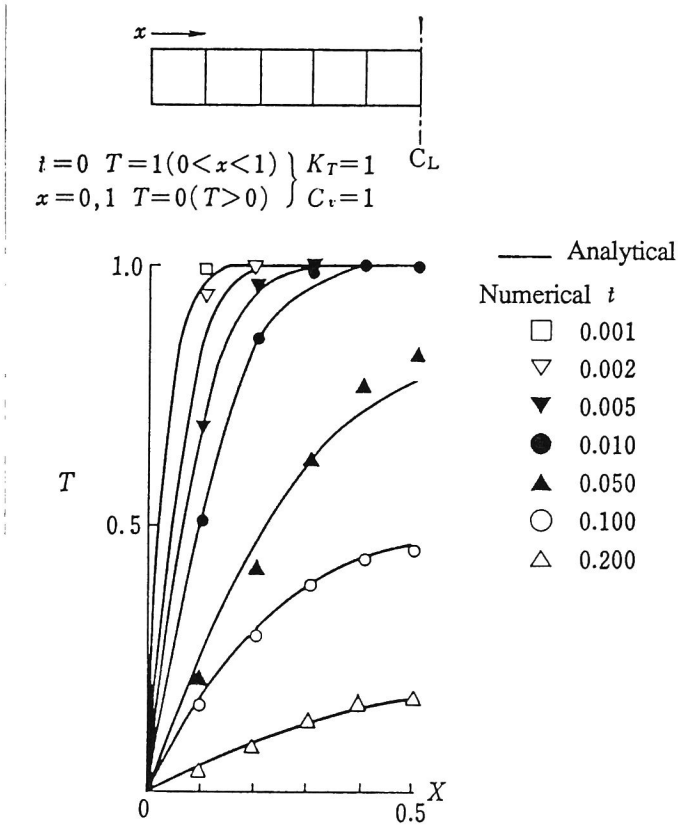


Figure 3.3.5 Comparison with the analytical solution of the one-dimensional heat conduction problem

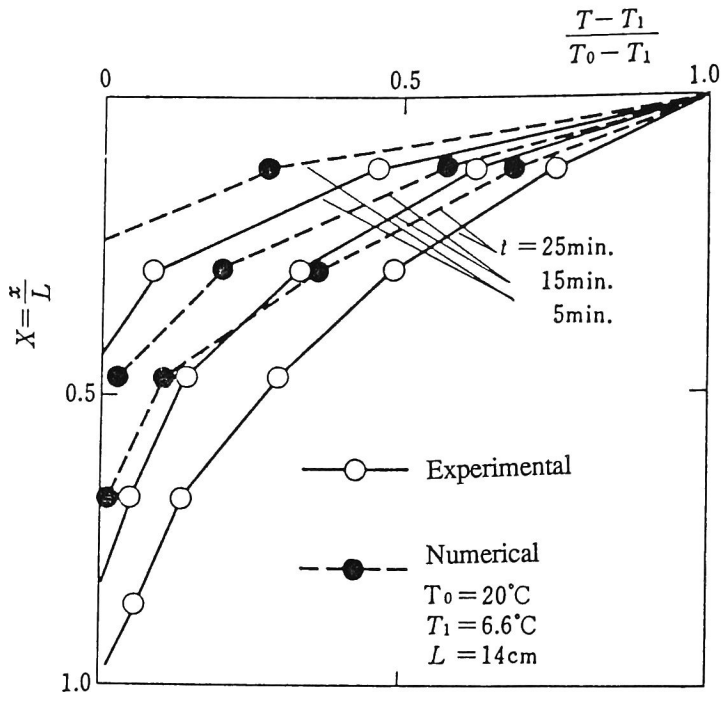


Figure 3.3.6 Comparison with the experimental results of the coupled thermal and hydraulic problem (L is the length of the specimen, x is the distance from the top of the specimen, T_0 is the temperature of the injected water and T_1 is the temperature of the water in the specimen at the initial state.)

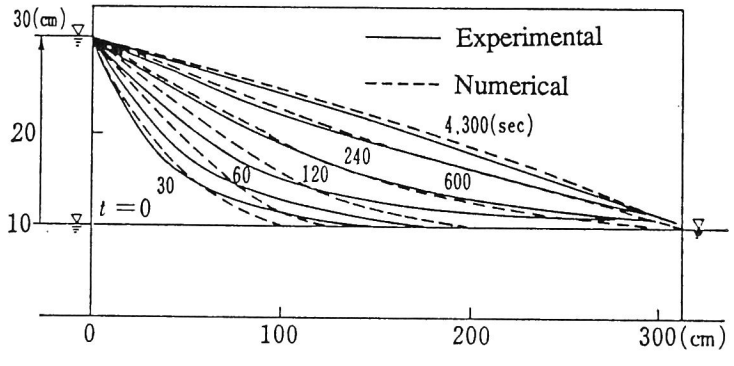


Figure 3.3.7 Comparison with the experimental results of the saturated-unsaturated seepage problem

3.3.4 Effects of the dependence of the parameters on temperature and pressure

(1) General tendency of the dependence of the parameters

To solve the basic equations mentioned in Section 3.3.2 with the finite element method, the following parameters are needed:

1) Young's modulus
2) Poisson's ratio
3) Thermal expansivity of solids
4) Thermal expansivity of fluids
5) Heat capacity of solids
6) Heat capacity of fluids
7) Thermal conductivity of solids
8) Thermal conductivity of fluids
9) Permeability
10) Relation between permeability and water content
11) Compressibility of fluids
12) Initial porosity
13) Density of solids
14) Reference density of fluids

The dependence of the above parameters of water and granite rock mass on temperature and pressure are all investigated, except for 12) and 14), which present the initial state of the ground. The reason why granite is selected as a solid phase is that investigations for granite have been carried out most often and a great deal of data can be used.

The effects of the variable parameters on the phenomena are not examined by the experimental method. This kind of examination is an example in which the effects of the numerical approach are represented.

1) Young's modulus, E

The E of crystalline rock generally decreases as the temperature increases. The following are considered to be the reasons for this phenomenon:

a) changes in the E of a mineral,

b) the effects of a release of stress at the boundary between minerals.

As examples of a), the E of quartz and plagioclase decreases with an increase in temperature. The released stress mentioned in b) are expected to be the one which is released by yielding cracks at the boundary between minerals; cracks are caused by the anisotropic thermal expansion of the minerals. On the contrary, the isotropic thermal expansion of hyaline rock causes E to increase (Shimooka et al. (1983)). Figure 3.3.8 shows the relations of E to temperature for various kinds of granite. In general, the decrement of E decreases with increases in the confining pressure. This is probably because the effect of b) decreases (Heuze (1983)). In the isothermal case, E generally decreases with an increase in the confining pressure.

When a rock is cooled after being heated, a plastic strain occurs by thermal history (Shimooka et al. (1983)).

Moreover, E is dependent of the geometry and characteristics of fractures existing in a rock. The mechanical properties for fractures have been studied by many researchers (e.g., Goodman (1976)). However, the method for applying the information on fractures to the model of a whole rock, including both fractures and rock blocks, may involve many problems which are yet to be solved. In general, the E of a rock has anisotropic characteristics induced by the geometry of existing discontinuities.

2) Poisson's ratio, ν

Figure 3.3.9 shows the relations of ν to temperature for various kinds of granite. The ν of some granite decreases with an increase in temperature while that of some other granite does not change. The dependence of ν on temperature may be slight.

On dependence on stress, it has been reported that ν does not change in the stress region under the yield stress (Heuze (1983)).

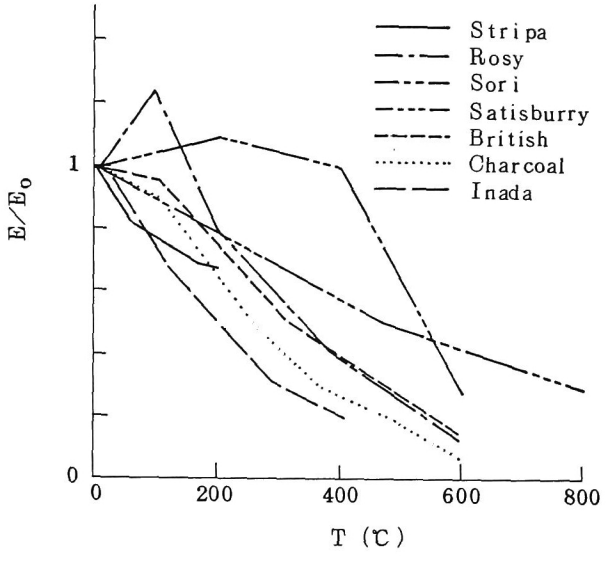


Figure 3.3.8 Relationships of Young's modulus to temperature for various kinds of granite (after Simooka (1983) and Heuze (1983)) E_0 is the Young's modulus at the temperature of 0°C

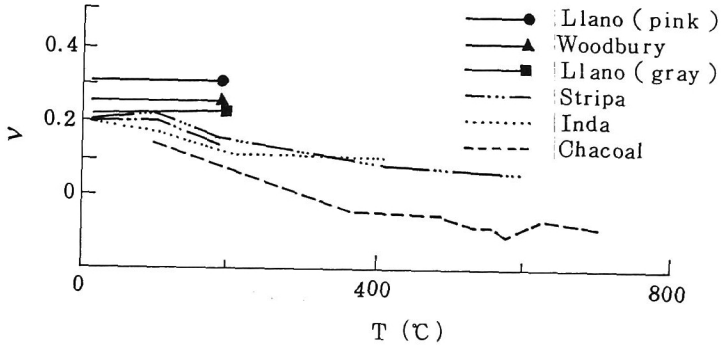


Figure 3.3.9 Relationships of Poisson's ratio to temperature for various kinds of granite (after Simooka (1983) and Heuze (1983))

3) Thermal expansivity of solids, α_s

The coefficient of the linear thermal expansion of many minerals increases with an increase in temperature. Thus, that of a rock consisting of those minerals will also increase with temperature (Shimoka, et al. (1983)). Figure 3.3.10 shows the relations of α_s to temperature for various kinds of rock. Among the various types, granite has a large thermal dependency on α_s. The α_s of granite increases rapidly below the temperature at which the α-β phase change of quartz occurs (, i.e., 573°C under an atmospheric air pressure). Over that temperature, α_s decreases.

In cases where the granite is confined, the mechanical dependency of α_s is small, below 500°C, because the occurrence of cracks at the boundary between minerals is prevented. Under conditions over 500°C, the maximum value of α_s, observed at a temperature in which an $\alpha-\beta$ phase change of quartz occurs, decreases with an increase in pressure, while the critical temperature increases with pressure (see Figure 3.3.11 (Heuze (1983)).

The anisotropy of the α_s of crystalline rock is small because many kinds of minerals make up this rock, and because the direction of the axis of crystals is arbitrary (Shimooka et al. (1983)).

4) Thermal expansivity of fluids, β_T

The density of water increases with temperatures from 0 to 3.98°C and reaches its maximum value at 3.98°C under an atmospheric air pressure. The dependency of the density of the water on temperature and pressure is given by equation (3.3.14). Thus, β_T is negative between 0 and 3.98°C and positive over 3.98°C under an atmospheric air pressure.

β_T increases with pressures under 4000 kg/cm^2 at 0°C. This dependency of β_T on pressure decreases with an increase in temperature and β_T is independent of the pressure at 40°C and increases with pressure over 40°C.

5) Heat capacity, C_v

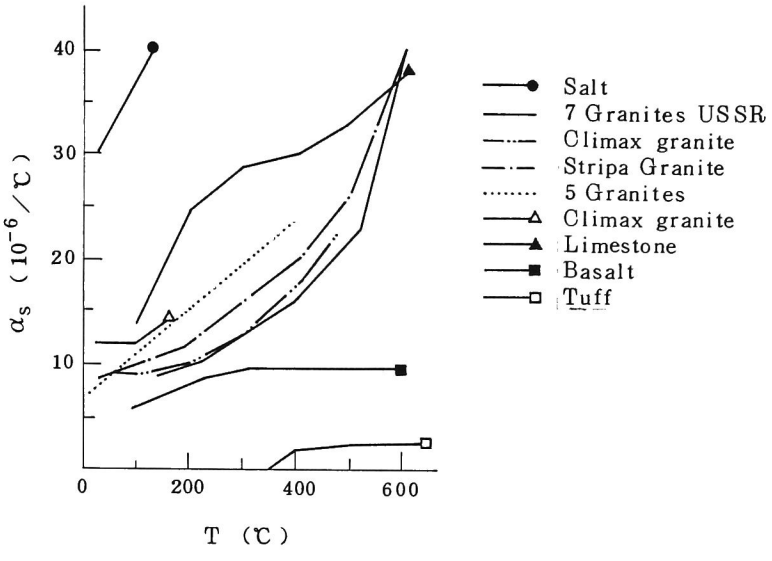


Figure 3.3.10 Relationships of thermal expansivity to temperature for various kinds of granite (after Simooka (1983) and Heuze (1983))

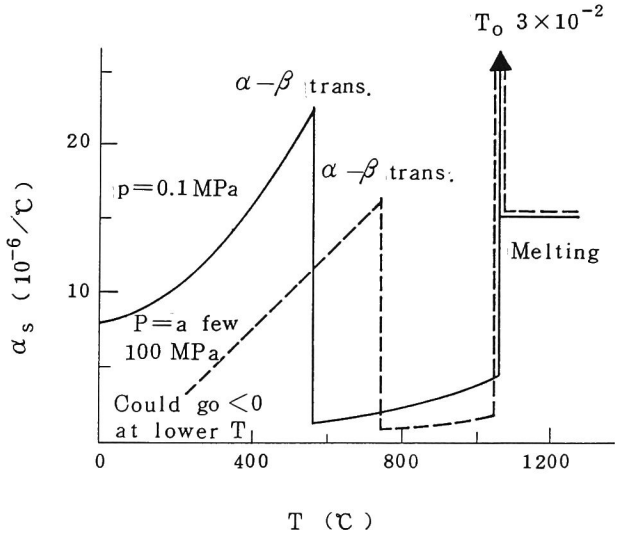


Figure 3.3.11 Schematic of the variation of thermal linear expansion of granite at temperature and pressure (after Heuze (1983))

(a) Heat capacity of solids, C_{vs}

Since the C_{vs} of many minerals increases with temperature, that of many types of rock also increases with temperature. The range of C_{vs} for many minerals is between 700 and 1000 J/kg°C. Thereby, the difference in the C_v between various types of rock is small. Figure 3.3.12 shows relations of C_v to temperature for various types of granite, in which the C_v means the heat capacity of the granite including pore water and the rock matrices.

While detailed data has not been obtained, C_{vs} is generally expected to decrease with an increase in pressure since C_{vs} decreases with an increase in density.

(b) Heat capacity of fluids, C_{vf}

The heat capacity of water decreases with an increase in temperature and has a minimum value at 37.5°C, as shown in Table 3.3.1. On the other hand, the mechanical dependency of C_{vf} has not yet been measured. Nevertheless, Hodgkinson et al. (1983) estimated $(1/C_{vf})(\partial C_{vf}/\partial P) = 6x10^{-2}m^2N^{-1}$ from thermodynamic relations.

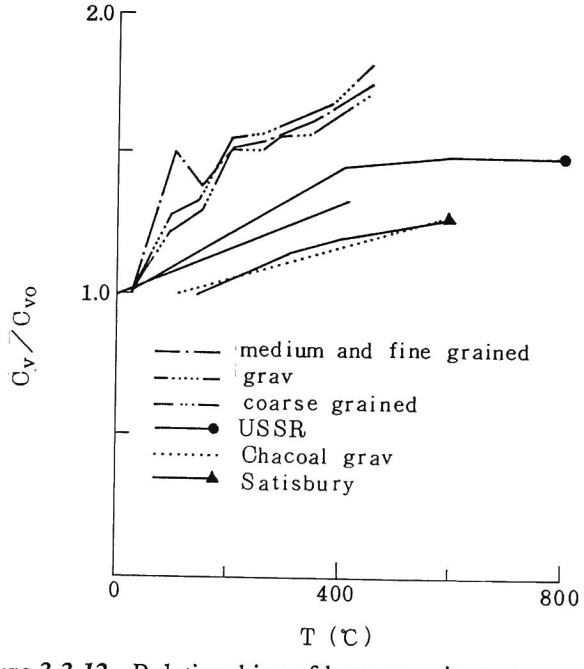


Figure 3.3.12 Relationships of heat capacity to temperature for various kinds of granite (after Simooka (1983) and Heuze (1983)) C_{v0} is the heat capacity at the temperature of 0°C

Table 3.3.1 Heat capacity of water, C_{vf}, as a function of temperature (J/g°C)

℃	C_{vf}	℃	C_{vf}	℃	C_{vf}	℃	C_{vf}
0	4.2174	25	4.1793	50	4.1804	75	4.1925
5	4.2019	30	4.1782	55	4.1821	80	4.1961
10	4.1919	35	4.1779	60	4.1841	85	4.2002
15	4.1855	40	4.1783	65	4.1865	90	4.2048
20	4.1816	45	4.1792	70	4.1893	95	4.2100

6) Thermal conductivity, K_T

(a) Thermal conductivity of solids, K_{Ts}

In many cases, it seems difficult to measure the thermal conductivity of only the solid phase of a porous composite material. Hence, many previous works for granite have been carried out for a material which is constituted from solid, liquid and gas phases.

The K_T of a granite including all three phases decreases with temperature increases below 200°C. The following experimental equation has been proposed (Heuse (1983)).

$$K_T = 6.3\times10^{-3}\times\left(6.7\times10^{-6}T\right) + \left(3.41\times10^{-9}T^2\right)\ cal/cm\cdot s\cdot deg \qquad (3.3.35)$$

From many previous studies, the decrement of the K_T the granite with an increase in temperature can be estimated as $(1/K_T)(\partial K_T/\partial T) = 10^{-3}K^{-1}$. Figure 3.3.13 shows the relations of K_T to temperature for various types of granite.

The K_{Ts} of the crystalline minerals decreases with an increase in temperature. On the contrary, that of the hyaline minerals increases with temperature. The effect of the micro-pore in the matrices on the thermal nonlinearity of the K_T is dependent

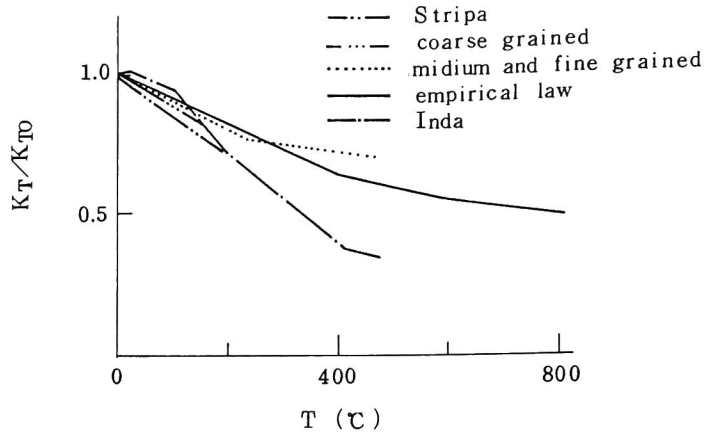


Figure 3.3.13 Relationships of thermal conductivity to temperature for various kinds of granite (after Simooka (1983) and Heuze (1983)) K_{T0} is the thermal conductivity at the temperature of 0°C

on the degree of crystallization of the minerals (Shimooka et al. (1983)). The above-mentioned decreasing tendency of granite is derived from complicated phenomena in the micro-level.

For the mechanical dependency of K_T, it was reported by Heuze (1983) that K_T increased 10% with a 90MPa increment of pressure. However, this is probably because the volume of the gas phase, whose thermal conductivity is very small, became small by a decrease in the void volume due to compression.

(b) Thermal conductivity of fluids, K_{Tf}

K_{Tf} increases with temperature. The nonlinearity of K_{Tf} for changes in pressure has not been investigated thoroughly.

7) Permeability, k

In general, the permeability of the ground is written as

$$k = \frac{k_0}{\eta}\rho_f g = \frac{k_0}{\mu} g \qquad (3.3.36)$$

where k_0 is the intrinsic permeability whose dimension is $[L^2]$, η is the viscosity of the fluid whose dimension is $[ML^{-1}T^{-1}]$ and μ is the kinematic viscosity of the fluid whose dimension is $[L^2T^{-1}]$. Using a gravitational unit, the general permeability is given as

$$k \equiv \frac{k_0}{\mu} \qquad (3.3.37)$$

Thereby, the permeability can be examined for k_0 and μ. It should be noted that the permeability used in this code is that for a whole ground including both rock blocks and fractures.

(a) Intrinsic permeability, k_0

The void existing in a rock mass consists of micro-cracks in the rock matrix and fractures. The ground water flows mainly through the fractures. The minerals in a rock matrix expand by thermal expansion and the rock matrix also expands due to the relatively small volume of micro-cracks in it. On the other hand, fractures between rock matrices are closed by the expansion of rock matrices. In many cases, the intrinsic permeability of the rock mass decreases with an increase in temperature due to the closing of the fractures.

In other words, the phenomenon means the decrease of an effective porosity and is caused by the stress induced by the thermal stress. Hence, this change in the permeability is dependent on the stress state in a rock mass.

(b) Kinematic viscosity, μ

The μ of water decreases with temperature, as shown in Table 3.3.2. On the other hand, the mechanical dependency of μ has not yet been quantitatively investigated. The viscosity of a general fluid increases with pressure, while that of water behaves strangely under 30°C. The viscosity of water decreases with an

increase in pressure, and then it increases after giving a minimum value to the viscosity under 30°C. The pressure which gives the minimum value to the viscosity decreases with an increase in temperature, and the minimum value of the viscosity disappears over 30°C. The viscosity of the water increases with temperatures over 30°C (Kauzmann and Eisenberg (1969)). In general, the mechanical dependency of the viscosity of water, η, is expressed by $(1/\eta)(\partial\eta/\partial P)=10^{-9}m^2N^{-1}$ (Hodgkinson et al. (1983)).

Table 3.3.2 Kinematic viscosity, ν, as a function of temperature (x $10^{-6}m^2s^{-1}$)

℃	ν	℃	ν	℃	ν
0	1.792	40	0.658	80	0.365
10	1.307	50	0.554	90	0.326
20	1.0038	60	0.475	100	0.295
30	0.801	70	0.413		

(c) Permeability, *k*

With an increase in temperature, both k_0 and μ decrease. Thus, the effects of temperature on the permeability cancel each other out. It is reported, however, that a permeability decreased from ten to four times with a temperature increase in some field tests (Heuze (1983)) and the permeability increased slightly with temperature in other tests. This is probably dependent on the method of the test. In a test where water is injected at a high pressure, such as a Lugeon test, the high water pressure prevents the closing of fractures induced by the thermal expansion of the rock matrices. After all, the injection rate increases due to a decrease in the viscosity of the water, and the permeability seems to increase with temperature. In contrast, the macro-permeability test conducted in the Stripa project indicated a decrease in the permeability with an increase in temperature. In this test, the flow rate into the

underground opening and the water pressure around the opening were measured under a natural hydraulic gradient; then, the permeability was calculated from this data.

From the above-mentioned observed results, it seems that the permeability decreases with temperature under a natural water pressure state because the decrement of k_0 is larger than that of the viscosity of the water with an increase in temperature.

The mechanical dependency of k is dependent on that of k_0 due to the small dependency of the viscosity of water.

8) Relation between permeability and water content, $k(\theta)$

The unsaturated property of mudstone has been obtained by laboratory experiments (Nishigaki et al. (1982)). That of crystalline rock, however, has not been obtained. In addition, many unknown mechanisms exist for the unsaturated flow in a fracture.

On the other hand, studies on the unsaturated properties of soil have been carried out by many researchers through experimental and analytical methods. The permeability of a soil in an unsaturated region is dependent on the viscosity of the water, the shape, the size, the tortuosity and the connectivity of the void, the surface activity of the soil particles and the water content. The permeability of various types of rock in an unsaturated region are expected to have similar dependencies.

Rock interstices are related to the intrinsic permeability and the viscosity of water, both mentioned in Section (5). The water content is expected to change with temperature due to evaporation. The aspects of this phenomenon, however, have not been observed much for either rock or soil. The surface activities in a rock matrix and a fracture are dependent on the nature of the water retention. However, not many studies on the water retention curve for rock have been conducted.

It can be concluded at the present time, therefore, that neither the water flow in an unsaturated region of rock nor the nonlinearity of the unsaturated properties of the rock are not understood well. However, in numerical analyses, the conventional

treatment for evaporation in an unsaturated rock has been carried out with relations between the density and the internal energy of water (Pruess and Wang (1984)). In the field of soil science, changes in water content with temperature are examined by considering the suction, which is a function of temperature, and the volumetric water content.

9) Compressibility of fluids, β_p

Under an atmospheric air pressure, β_p decreases with an increase in temperature from 0 to 46°C and has a minimum value at 46°C. The decrement between 0 and 46°C becomes smaller with an increase in pressure and disappears at an atmospheric air pressure of about 3000 (Eisenberg and Kauzman (1969)).

Moreover, β_p increases with pressure. β_p at an atmospheric air pressure of 1000 is 1.3 times as much as that at an air atmospheric air pressure (Science chronological table (1990)).

10) Density of solids, ρ_s

The density for a solid phase, ρ_s, is generally a function of temperature T and pressure P, such that

$$d\rho_s = \frac{\partial \rho_s}{\partial P} dP + \frac{\partial \rho_s}{\partial T} dT \qquad (3.3.38)$$

The $(1/\rho_s)(\partial \rho_s/\partial P)$ of granite is $10^{-10}m^2N^{-1}$ and the $(1/\rho_s)(\partial \rho_s/\partial T)$ of it is $3\times10^{-5}K^{-1}$. Thus, the dependences of the density of granite on temperature and pressure are expected to be very slight.

(2) Treatment of the dependency of the parameters on temperature and pressure in the code

Table 3.3.3 shows the degree of dependency for the investigated parameters in the previous section. In this table, parameters whose rate of dependency is more than $|10^{-3}|$ per unit temperature change or unit stress change (N/M^2) are intrinsic permeability, k_0, dynamic viscosity, μ, heat capacity, C_v, thermal conductivity, K_T and thermal expansivity, α_s. These all have a relatively stronger dependency for temperature change than for stress change.

The mechanical dependencies of C_{vs}, β_T, α_s and K_{Tf} are not understood quantitatively. In addition, although the dependency of Young's modulus, E, of the rock matrices on temperature and stress is large, it is necessary to make a model of the rock mass including rock matrices and fractures for the analyses. However, the change in Young's modulus of the rock masses is greatly dependent on the characteristics and geometry of the fractures in it. The modeling method for the mechanical properties of a discontinuous material is being studied by many researchers at the present time, but an authorized one has not yet been established. Moreover, in cases where the dependency of E on temperature is considered, the thermal stress is dependent on temperature through a change in E in addition to the dependency of α_s on temperature. This makes it difficult to estimate the effects of the thermal dependence of thermal expansion and the permeability of the rock. Therefore, the E of the rock is assumed to be constant in this section.

We shall try to examine the effects of the dependencies of the parameters on the coupled behavior by introducing those dependencies into the THAMES analysis. Let us show how the above-mentioned dependencies of the parameters are treated in the next sections.

1) Treatment of the thermal dependency of μ, C_{vf}, K_{Tf}, K_{Ts} and α_s.

The μ,K_{Tf} and C_{vs} of granite decrease or increase simply by an increase in temperature. The changing rates are shown in Table 3.3.3. The K_{Ts} and α_s of granite also decrease and increase, respectively, simply a with temperature increase below the temperature at which the α-β phase change of a quartz has occurred. On the other hand, C_{vf} has a minimum value in the process where the temperature increases.

Table 3.3.3 Degree of dependency of parameters on temperature and pressure

	Young's Modulus E	Poisson's ratio ν	thermal expansivity		density		permeability
solid/fluid	solid	solid	solid α_s	fluid β_T	solid ρ_s	fluid ρ_f	-
Unit	kg/cm^2	-	K^{-1}	K^{-1}	g/cm^3	g/cm^3	cm/s
Typical Value	10^5-10^6	0.2 - 0.3	$6x10^{-6}$	$5x10^{-4}$	2.6 - 2.7	1	10^{-10}-10^{-12}
Thermal dependency	-10^{-3}	10^{-5}-10^{-6}	10^{-3}-10^{-4}	-10^{-4}	$-3x10^{-5}$	$-5x10^{-4}$	0.2
Mechanical dependency	? *1	10^{-11}-10^{-10}	?	? *2	10^{-10}	$5x10^{-10}$	-10^{-8}

	Intrinsic permeability	Dynamic viscosity μ	Compress-ibility β_p	Heat capacity		Thermal conductivity	
solid/fluid	solid	fluid	fluid	solid C_{vs}	fluid C_{vf}	solid K_{Ts}	fluid K_{Tf}
Unit	m^2	m^2/s	cm^2/kgf	J/kgK	J/kgK	W/mK	W/mk
Typical value	10^{-16}-10^{-18}	10^{-6}	10^{-4}	800-1000	4200	2.9	$6x10^{-1}$
Thermal dependency	-10^{-2} *3	-10^{-2}	? *2	$5x10^{-4}$	$\|10^{-3}\|$	-10^{-3}	10^{-3}
Mechanical dependency	-10^{-8}	?	$3x10^{-9}$	-10^{-11}	?	$5x10^{-9}$	?

*1 : There are unknown factors for rock mass although the dependency is great.
*2 : Complicated nonlinearity is found.
*3 : Obtained from $\frac{E}{1-2\nu}\cdot\alpha\cdot 1$ = 1 MPa
? : Qualitative examination cannot be carried out due to lack of data
The dependency of a parameter, H, on temperature, T and pressure, P is obtained from $-\frac{1}{T}\frac{\partial H}{\partial T}\times 100$ and $-\frac{1}{P}\frac{\partial H}{\partial P}\times 100$, respectively. The unit of T is °C and that of P is N/m^2.

In this section, the dependency of μ and C_{vf} with changes in temperature is considered by linearly interpolating the values shown in Tables 3.3.1 and 3.3.2. The K_{Tf}, K_{Ts}, C_{vs} and α_s are assumed to change by the rates indicated in Table 3.3.3.

2) Treatment of the thermal and mechanical dependency of k_0

The permeability mentioned in this section is related to the fluid flow through a rock mass, including both fractures and matrices.

The dependency of the permeability of granite masses, including many fractures, on the stress change has been investigated by many researchers. The permeability changes are induced by the stress-state change occurring from not only the loading forces exerted on the medium, but also from the thermal stress induced by changes in temperature.

Iwai (1976) conducted many experiments on the relation between the permeability of fractures and the cyclic load, σ_e, normal to the fracture plane. He pointed out that the coefficients introduced in the proposed permeability-stress relation equations by Louis (1969) and Gangi (1975) were not obtained as constants. He then proposed the following relation by using the stress-aperture relation introduced by Goodman (1976):

$$\frac{k_d}{k_{d,0}} = \frac{1}{\left\{1 + A\left(\frac{\sigma_e}{\zeta}\right)^{t'}\right\}^3} \qquad (3.3.39)$$

where $k_{d,o}$ is k_d in the initial state; k_d is the transmissivity obtained by dividing the outlet flow rate by the difference in the total heads at the inlet and outlet boundaries. A, ζ and t' are constants. He reported that this equation expressed the phenomena observed in his experiments well and the coefficients became constant. Moreover, Kelsall et al. (1984) simulated the Macro permeability test conducted in the Stripa project by application of this equation and obtained a good agreement with the experimental results.

From the above-mentioned results and the small dependency of μ on the stress, it can be concluded that equation (3.3.39) expresses the relation between the permeability and the normal stress to the fracture at the isothermal condition well. Thus, this equation is used as the dependency of intrinsic permeability k_0 on the stress, including the thermal stress.

Firstly, in the same way as it was used by Kelsall, the following equation is introduced from equation (3.3.39):

$$\frac{k_e}{k_{0d}} = \frac{\left\{1 + A\left(\frac{\sigma_{e0}}{\zeta}\right)^{t'}\right\}^3}{\left\{1 + A\left(\frac{\sigma_e}{\zeta}\right)^{t'}\right\}^3} \qquad (3.3.40)$$

where k_e is the k_0 at the normal stress to the fracture, σ_e, and k_{0d} is the k_0 at the reference stress, σ_{e0}. σ_e and σ_{e0} are the effective stresses normal to the direction of k_e, namely, the effective stress normal to the fracture plane. For example, k_{0d} is the k_0 in the position at which the in-situ hydraulic test is carried out and σ_{e0} is the stress at that location. In the model, k_{od} and σ_{eo} are assumed to be known, and σ_e and σ_{e0} are the effective stresses normal to the principal direction of permeability and are used to introduce the anisotropic hydraulic situation. Thereby, k_{eii} of the intrinsic permeability is changed by equation (3.3.40) according to changes in σ_{eii}. The permeability is then obtained from equation (3.3.37).

It should be noticed that the use of this dependency of the permeability of granite rock masses on the stress change is limited to the fractured medium in which ground water flows mainly through the fractures. This is because the permeability of the rock matrix blocks is not considered in equations (3.3.39) and (3.3.40). In addition, this dependency is limited to the rocks for which the cubic law holds, because Iwai assumed the cubic law in equation (3.3.39).

(3) Examination of the effects of the dependency the parameters on the behavior

Using the variable parameters mentioned in the above section, the effects of thermal and mechanical dependency of materiel on the coupled behavior in granite rock masses is examined. In particular, the dependencies on temperature are examined because the dependencies of all parameters on stress are smaller than those on temperature.

The model used for the investigation is one dimensional, as shown in Figure 3.3.14. The boundary conditions are also indicated in this figure. The parameters in the initial state are shown in Table 3.3.4. The calculations for the investigation are carried out for seven cases, i.e., five cases in which each dependency of the five parameters is considered, a case in which the dependencies of all parameters are considered and a case in which no dependency is considered. For each case, the temperature is set at 30, 40, 50 and 100°C at the heat sources and the initial temperature is set at 20°C.

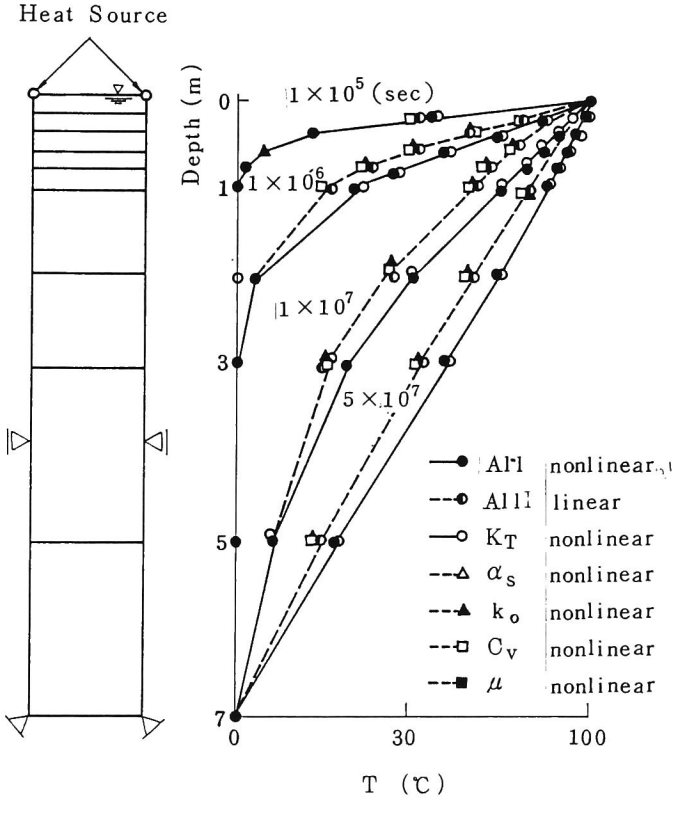


Figure 3.3.14 Finite element model and temperature distribution as a function of time at the heat source temperature of 100°C

Table 3.3.4 Parameters at initial state

Parameter	Value	Parameter	Value	Parameter	Value
E	5×10^{6} tf/m^2	ν	0.33	k_0	1×10^{-6} m^2
C_{vs}	837J/kg°C	K_{Ts}	3×10^{-8} kJ/m·s·°C	α_s	8×10^{-6}
A	0.0276	ζ	0.00217	t'	0.728

1) Effect on heat transfer

Figure 3.3.14 shows the temperature distribution as a function of time at the heat source temperature of 100°C. It is found that K_T has the most effect on the temperature distribution and C_v does not have so much effect, while the degrees of dependency of K_T and C_v are basically the same. Figure 3.3.15 shows the relations between the temperatures at the heat sources and the temperatures at a depth of 1 m under the heat sources after 10^6 seconds from the beginning of the calculation. It is found from this figure that the differences among all the dependencies of the parameters become clear when the temperatures at the heat sources are high. In cases where the dependencies of all parameters are considered, the temperature is 3% higher than that for cases in which no dependency is considered, in setting the heat sources at 100°C.

2) Effects on pressure distribution

Figure 3.3.16 shows the change process for the total head distributions when the heat sources are set at 30°C. Although an effect on the temperature distribution occurs at a heat source temperature of 100°C, the effect on the pressure distribution has already take place when the heat sources are set at 30°C. This sensitive effect on the pressure distribution is due to the dependency of the intrinsic permeability, k_0, on

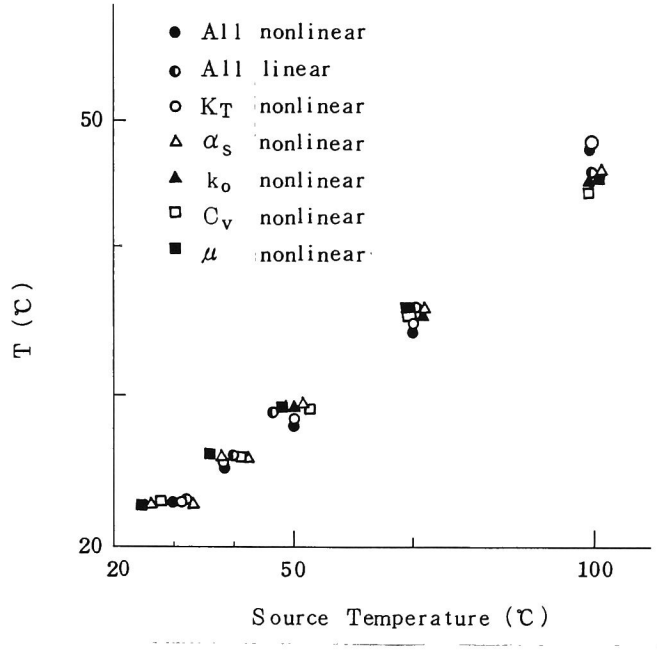


Figure 3.3.15 Relations between the temperatures at the heat sources and the temperatures at a depth of 1m under the heat source after 10^6 seconds from the beginning

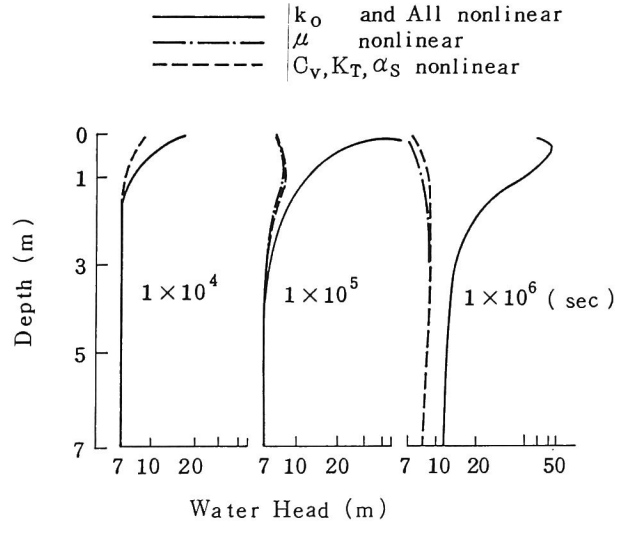


Figure 3.3.16 Change process of the total head distribution at the heat source temperature of 30°C

temperature. k_0 decreases through thermal expansion near the heat sources which are located at the outlet flow boundary of this model. The high pressure near the upper boundary is caused by the fact that the upward flow, induced by buoyancy, is prevented at the region near the boundary where the permeability decreases. Figure 3.3.17 indicates the distribution of permeabilities after 10^6 seconds when setting the heat sources at 30°C. It is found from this figure that the permeability changes drastically near the heat sources in the cases when the dependencies of the only intrinsic permeability and all the parameters are considered. Equation (3.3.40), proposed by Iwai (1976), is the relation between k_0 and stress and is more sensitive at a low stress than at a high stress, as shown in Figure 3.3.18. The stress levels in the analyses range from the initial one, 0.01MPa, to the maximum one, about 6MPa; the stress change is caused by thermal stress. This stress level coincides with the stress level at which a large change in permeability occurs in Figure 3.3.18. This is the reason for the sensitive effect of k_0 on the pressure distribution. The permeability in cases where all the dependencies are considered, reduces to 99% of the permeability in cases where no dependency is considered. In addition, the effect of μ is found to be slight for permeability changes, while it is not found at all in pressure distribution changes.

3) Effects on deformation

Since no external force is exerted in this model, the deformation is caused only by the thermal stress. Figure 3.3.19 shows the change in the displacement at the upper boundary in setting the heat sources at 100°C. It is found from this figure that the thermal expansivity, α_s, has the greatest effect on thermal expansion. The deformation is intensified by α_s which increases with temperature. Moreover, k_0 also has a slightly larger effect than the other parameters. This is also found in Figure 3.3.20 which shows the relation between the displacement at the upper boundary and the temperature of the heat sources after 10^6 seconds. In particular, it can be noted that the effect of k_0

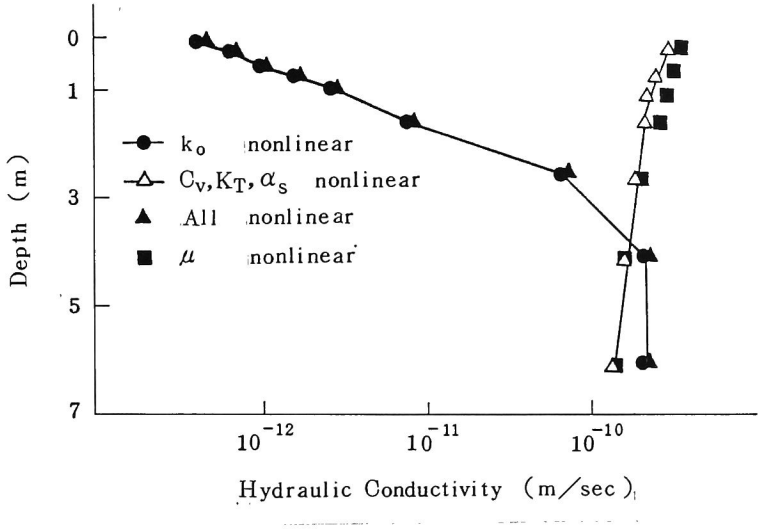


Figure 3.3.17 Distribution of permeabilities after 10^6 seconds at the heat source temperature of 30°C

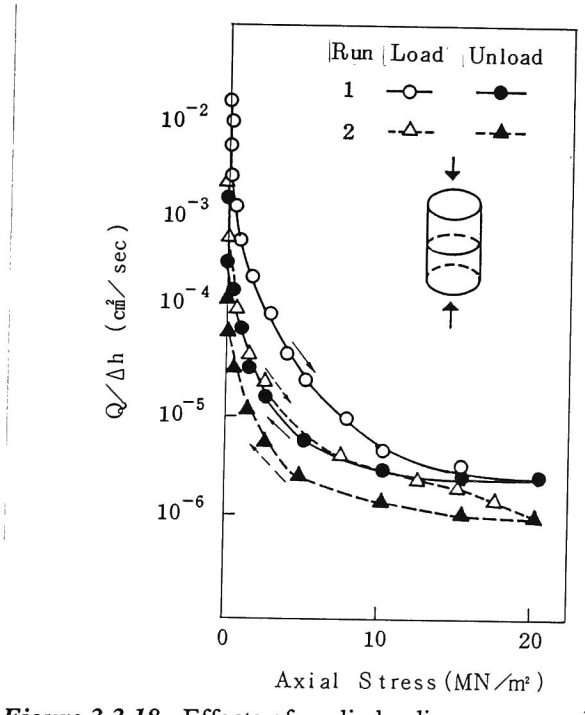


Figure 3.3.18 Effects of cyclic loading on permeability of tension fracture in granite with radial flow (after Iwai (1976))

Q is outlet flow rate and Δh is the applied head difference

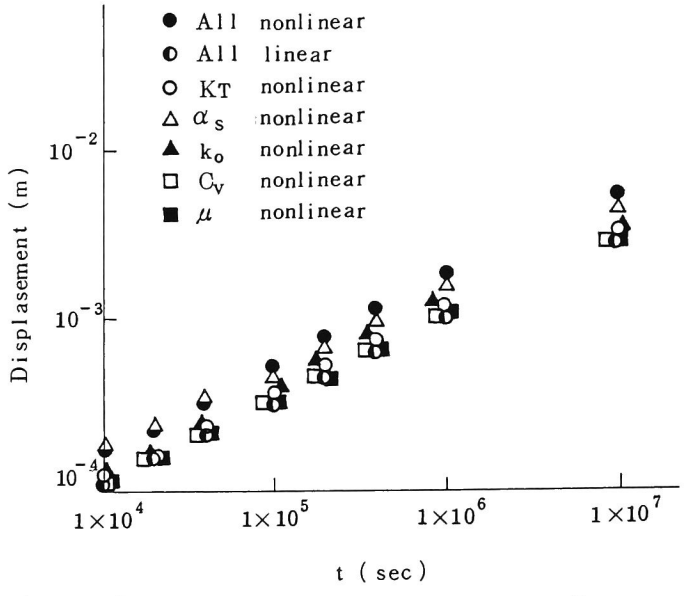


Figure 3.3.19 Change in the displacement at the upper boundary in setting the heat sources at 100°C

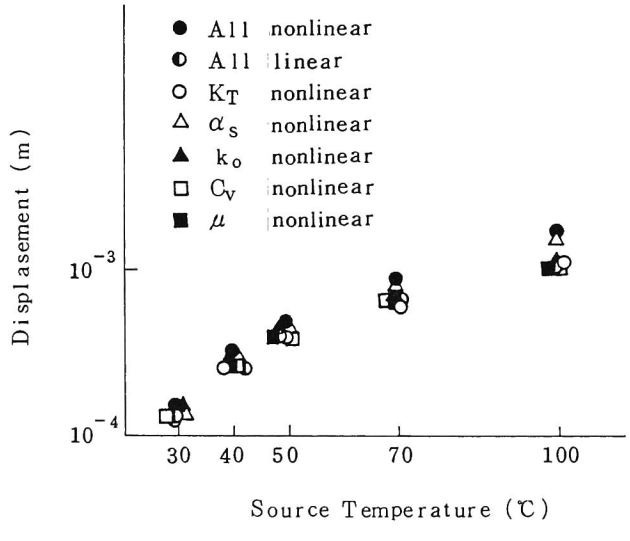


Figure 3.3.20 Relation between the displacement at the upper boundary and the temperature of the heat sources after 10^6 seconds

occurs at a low heat source temperature. This is because of the high pore-water pressure induced by the decreasing k_0.

At a heat source temperature of 100°C, the deformation is about 60% larger when all the dependencies are considered than when no nonlinearities are considered.

(4) Conclusions

In this section, after investigating the dependency of the parameters used in the THAMES code on temperature and stress, whose dependency has an effect on the coupled phenomenon, is examined with the numerical analyses. The investigated parameters are related to granite and water. The conclusions are summarized as follows:

1) The thermal conductivity, specific heat, thermal expansivity and permeability of granite have a greater dependency on temperature than the other parameters. The dependency of permeability on temperature is mainly caused by changes in the fracture aperture caused by the thermal expansion of adjoining rock matrix block.
2) For the coupled behavior of granite, the dependency on the temperature of thermal conductivity has the greatest effect on heat transfer, that of the permeability has the greatest effect on the fluid flow and that of the thermal expansivity has the greatest effect on thermal expansion. The other nonlinearities do not affect the coupled phenomena.
3) Among those sensitive dependencies, the changes of the permeability is the most significant. The permeability very much depends on the low stress level, and its nonlinearity has much influence on the coupled behavior. The second most important dependency is that of the thermal expansivity on temperature. That of the thermal conductivity is very small.

3.3.5 Effects on flow around an underground opening

In this section, by comparing the results of in-situ tests conducted in the Stripa project, the ground water flow around an underground opening is examined under temperature changes.

(1) Model description

At the Stripa mine in Sweden, a macroscopic permeability test was conducted in the Stripa project (Nelson and Wilson (1980)). The ventilation drift, 5 x 5 x 30 m in size, was sealed off and equipped with a ventilation system whose temperature was controlled to evaporate all the water seeping into the room. The water seepage was determined by measurements of the mass flow rate and the difference in the humidities of entering and existing streams. The pressure gradients in the rock mass were measured in holes that radiate out from the sealed room. The geology is a granite and the drift exists 335 m below ground level.

For a coupled finite element analysis, the rock cavern is simply modeled as shown in Figure 3.3.21. The parameters in the initial state are set as shown in Table 3.3.4. The initial temperature is set at 20°C for all regions and the initial water table is set at the top of the region. The water head is fixed at the initial state at the right side vertical boundary and at a zero pressure head at the drift wall. The heat flux is set at zero for all boundaries. Excavation of the underground space is simulated by unloading the initial stress.

To examine the behavior occurring around the opening, the changes of the parameters mentioned in the previous section are considered.

(2) Results

The relation between the calculated horizontal permeability at the middle height of the drift and the distance from the drift wall is shown in Figure 3.3.22 in comparison with the ob-

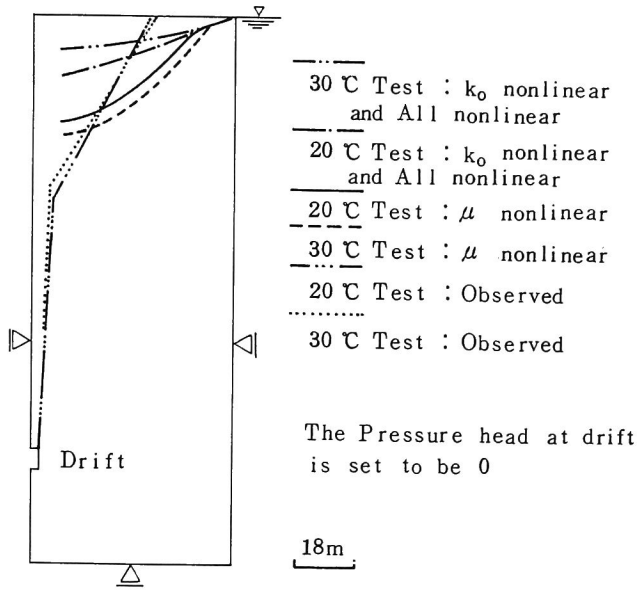


Figure 3.3.21 Model of macroscopic permeability test and observed and calculated water levels

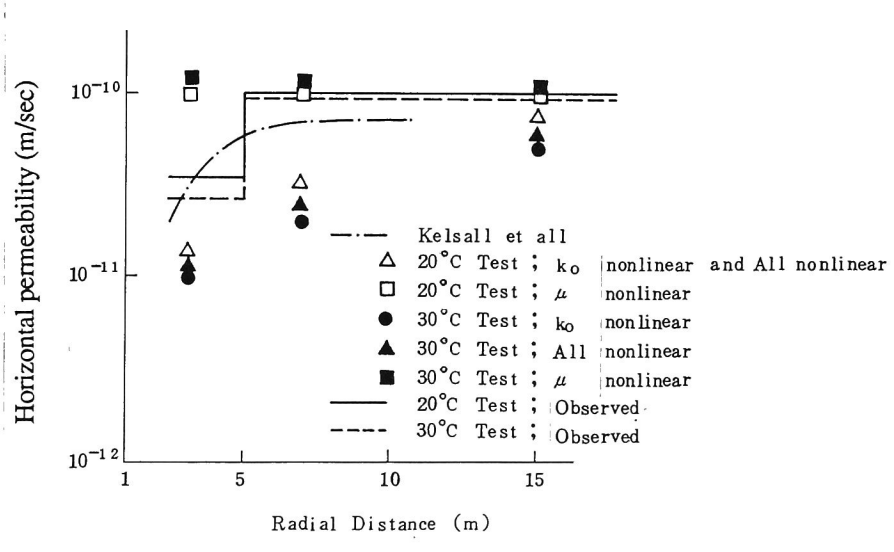


Figure 3.3.22 Relation between the observed and calculated horizontal permeability at the middle height of the drift and the distance from the drift wall

served results. Except for the results from the case in which only the change of μ is considered, a reduction in permeability near the drift is found in the numerical results at a room temperature of 20°C. This is because of the closing of the fractures brought about by an increasing tangential stress.

Moreover, when the room temperature rises to 30°C, the rock matrix block expands and the fractures close. Thus, the permeability of the rock mass reduces with an increase in temperature, as shown in Figure 3.3.22, while the viscosity of the water decreases. This tendency is similar to that of the observed phenomena. The reduction in permeability around the opening causes the water level to be high, as shown in Figure 3.3.21, but the height of the calculated water table is different from the measured one.

In considering only the k_0 change, the permeability of the rock near the drift decreases to 29% from the initial state with an increase in temperature. This decrement is roughly the same as that estimated by Kelsall et al. (1984)). In a case where all the dependencies are considered, the decrement becomes 20% due to the effect of the increase in μ. This value is approximately the same as the one observed in the in-situ tests, i.e., 22%.

The calculated flow rate seeping into the room at the two different temperatures is shown in Table 3.3.5, but a quantitative comparison is difficult to make because of uncertainties of the hydraulic boundary conditions. In a case where only the thermal and mechanical dependency of k_0 is considered, the reduction rate of the water inflow at a room temperature of 30 to 20°C, is 39.4%, while the reduction rate is 32.9% in the case where all the dependencies are considered. This is due to the effect of the increase in μ. It is found from these results, therefore, that a change in the inflow rate is considerably influenced by the temperature dependency of the kinematic viscosity, μ.

Figure 3.3.23 shows the calculated vertical permeability distribution. It is expected from this figure that the high permeable zone, which corresponds to a loosened area, exists to the depth of 7 m from the wall surface.

(3) Conclusions

Table 3.3.5 Flow rate into the room at two different temperatures

Parameter considering thermal dependency	flow rate into room (ml/min) room temperature 20°C	room temperature 30°C
k_0	31	18.8
μ	58.5	63.3
all parameters	31	21
observed at Stripa	50	42

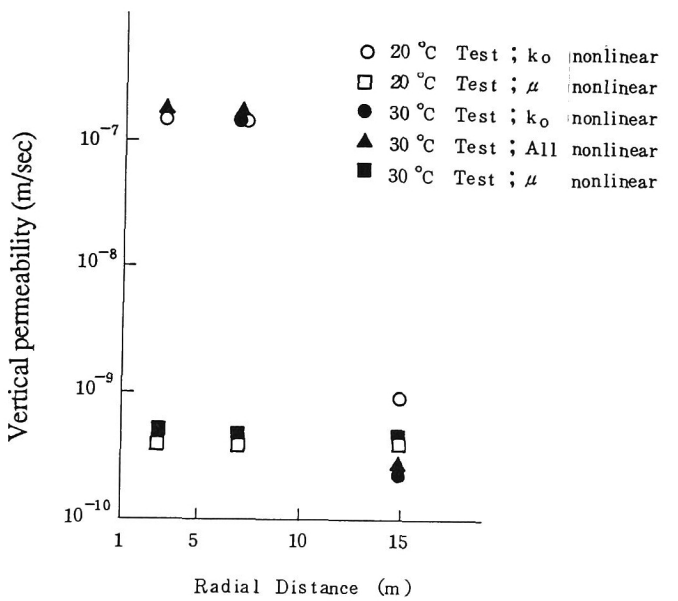


Figure 3.3.23 Calculated vertical permeability distribution

Using THAMES and considering the material dependencies on temperature and stress, the ground water flow around an underground opening was examined. The conclusions are summarized as follows:

1) Considering the dependency of the permeability on stress changes, the flow rate seeping into the underground opening is estimated well qualitatively. It is found from this examination that a decrease in the flow rate into the opening is caused by an increase in the tangential stress around the opening which is induced by the excavation. In addition, when the temperature is increased, the permeability around the opening decreases due to a closing of the fracture apertures induced by the thermal expansion of adjoining rock matrix blocks.
2) In cases where the temperature is changed, the dependency of the kinematic viscosity, μ, on temperature has a great influence on the flow rate change into the opening. When only the dependency of the intrinsic permeability, k_0, on stress is considered, the decrement of the flow rate into the opening induced by temperature change is overestimated. Otherwise, in the isothermal state, an analysis which only considers the change of k_0 can express well the phenomena occurring around the opening, as mentioned above.
3) The decreasing permeability in the tangential direction around an opening may represent the loosened area. This decrease is caused by the opening of the fractures in the tangential direction; the opening is induced by the excavation.

3.3.6 Analysis of the Buffer mass test

(1) General description

In this section, the Buffer mass test conducted in the Stripa project will be examined by THAMES.

The general objective of the Buffer mass test (BMT) was to check the functions of highly compacted Na-bentonite as a buffer material around a canister or an overpack and

the functions of sand/bentonite mixtures as a tunnel backfill. The test arrangement consisted of six large boreholes, for setting electrical heaters, surrounded by blocks of the highly compacted sodium bentonite. The power of the heater simulated the heat production of waste canisters. The holes were covered by the sand/bentonite backfill that was compacted on site in a tunnel 340 m below the ground surface. The temperature, swelling pressure and water content of the buffer materials were measured. The BMT involved the analysis of temperature distributions, moisture distributions and swelling pressure developments in the heater holes; the analyses were performed by Push and Borgesson (1985) and Knutsson (1983). Their calculation techniques seem too simple, however, to examine the influence of such a complicated coupled behavior as that which occurs in the buffer materials. In order to understand this phenomenon, it seems necessary to investigate it with a more realistic model which can simulate the phenomena occurring in the BMT well.

Among such complicated coupled phenomena, an effort is made to understand the behavior of the highly compacted bentonite in the heater holes in this section by using THAMES. Since the unsaturated properties of the highly compacted clay were not examined so well in the Stripa project, however, the water retention curve (dependent on the porosity change caused by swelling) has to be assumed in a feasible way. In this section, a method to estimate the unsaturated properties of the buffer materials is firstly presented. Then, the coupled behavior of the BMT is investigated through a comparison of the numerical results and the measured ones.

(2) Unsaturated properties of swelling clay

1) Introduction

A highly compacted clay (called HCC in this section) was used as a buffer material in the heater holes in the BMT. The HCC was made of highly compacted Na-bentonite which has a high swelling capacity. It is assumed that it took up water from the

surrounding rock and swelled. This resulted in a tight contact with the confining rocks and an embedded waste canister. To analytically investigate the function of the HCC as an artificial barrier, it is necessary to know the characteristics of the unsaturated permeability change in the HCC during the swelling process. The unsaturated properties in the HCC were not intensively investigated, however, in the Stripa project program. Here, the author proposes equations to estimate the hydraulic conductivities dependent on the void ratio, e, the suction, ψ and the degree of saturation, S_r , and then the water retention curve of the HCC.

2) Relationships between volumetric water content, θ and suction, ψ

Figure 3.3.24 shows the relations between $pF(= \ln \psi)$, S_r and e of a weathered granite soil, whose figure indicates that the relation between S_r and pF is dependent on the void ratio. Figure 3.3.25 is the projected figure of Figure 3.3.24 on the pF-S_r plane. Figure 3.3.26 is the projected figure of it on the pF-ln S_r plane. It is found from both figures that the relation between ψ and S_r may be determined independently of e, if the critical capillary head, ψ_{cr}, is dependent on the void ratio. Figure 3.3.27 indicates ln ψ_{cr} as a linear function of e, which is obtained from the above-mentioned test results on weathered granite soil. Consequently, the following equations are derived by using the relations between ln ψ_{cr} and e and ψ and S_r proposed by Farrel and Larson (1972) and Brooks and Corey (1966), respectively:

$$\psi = exp(\omega \cdot e + \upsilon) \cdot exp(\gamma(1-S_r)) \qquad (3.3.41)$$

and

$$\psi = exp(\omega \cdot e + \upsilon) \cdot S_r^{-1/\lambda} \qquad (3.3.42)$$

where ω and υ are the gradient and the intercept of the relation between ln ψ_{cr} and e, respectively, as shown in Figure 3.3.27. γ is the constant relating ψ to S_r , whose

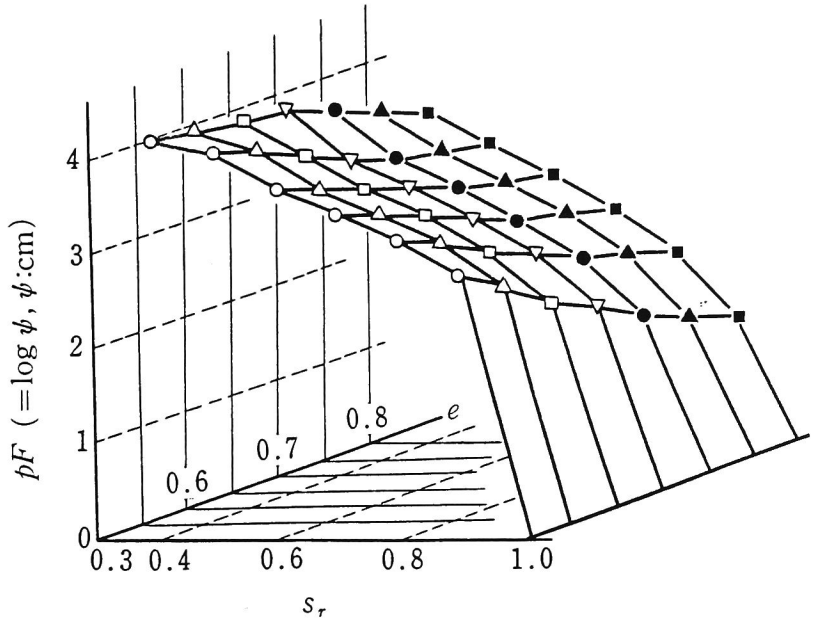


Figure 3.3.24 Relations between pF, S_r and e of a weathered granite soil

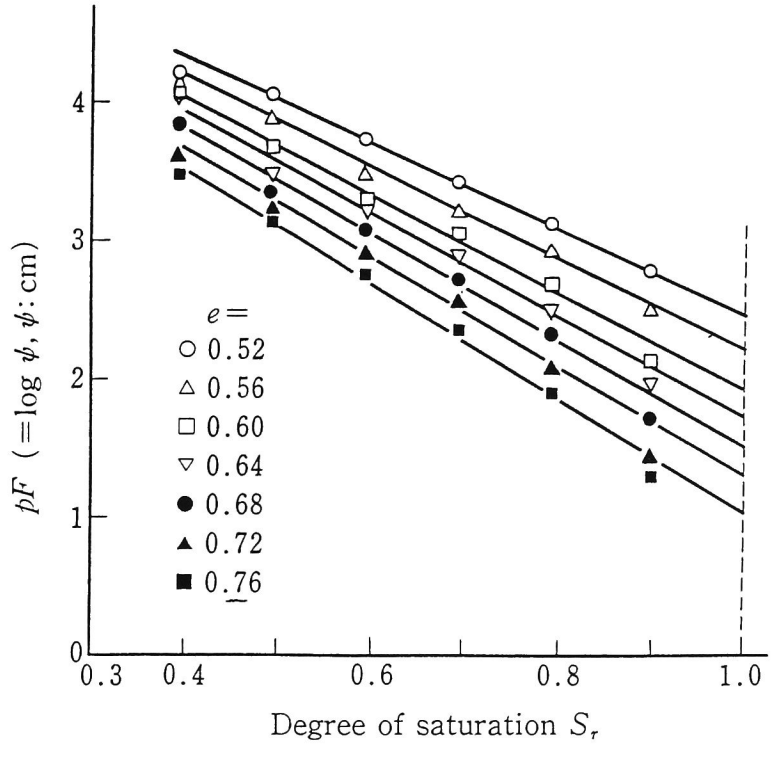


Figure 3.3.25 Projected figure of Figure 3.3.24 on the pF-S_r plane

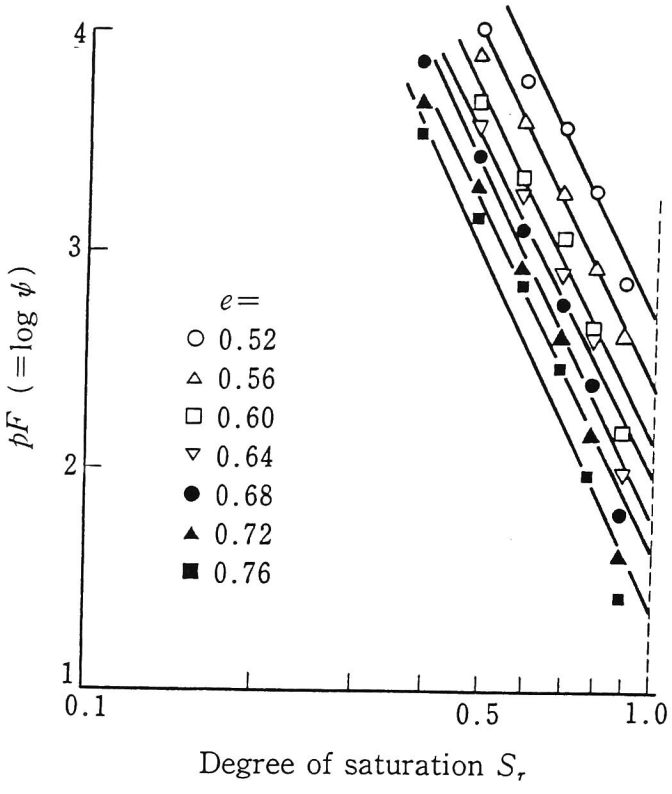


Figure 3.3.26 Projected figure of Figure 3.3.24 on the pF-lnS_r plane

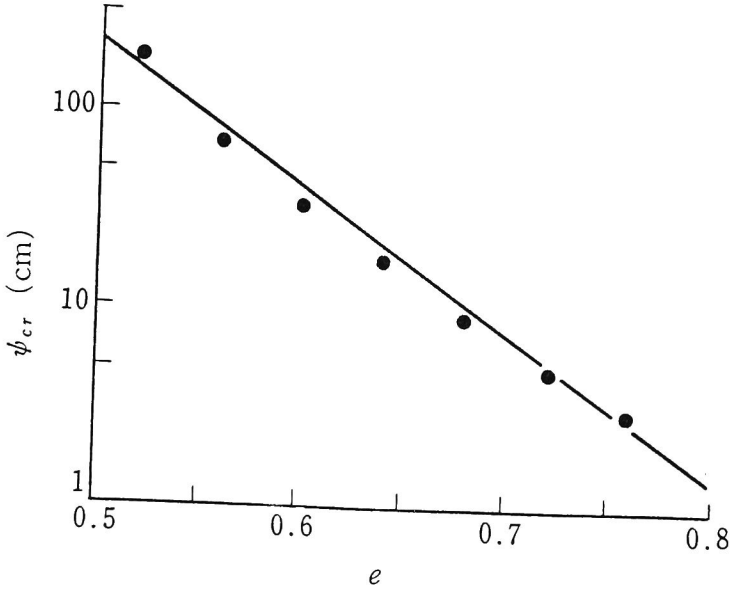


Figure 3.3.27 Relation between ψ_{cr} and e

relation was proposed by Farrel and Larson (1972). λ is the constant proposed by Brooks and Corey (1966).

3) Relationships between relative permeability, k_r and volumetric water content, θ

There are many proposed empirical relations between k_r and S_r. The most popular formula among them is the one proposed by Irmay (1954); it is written as

$$k = k_{sat}(S_r)^{\varphi} \tag{3.3.43}$$

where φ is a constant and k_{sat} is the permeability coefficient in a saturated medium.

Hillel and Gardner's formula (1970) is suitable for a clay soil with a high degree of saturation; it is given as

$$k_r = exp(\pi (S_r - 1)) \tag{3.3.44}$$

where π is a constant.

The dependency of the permeability on the void ratio was studied by Terzaghi as early as 1925. Experimental work by numerous researchers in the field of soil mechanics has shown that soil permeability is indeed an exponential function of a void ratio (Lambe and Whiteman (1969)) such as

$$log\ k_{sat} = \delta \cdot e + \xi \tag{3.3.45}$$

where δ and ξ are constants.

Combining equations (3.3.45) and (3.3.43), we obtain

$$k = exp(\delta \cdot e + \xi) \cdot (S_r)^{\varphi} \tag{3.3.46}$$

Combining equations (3.3.45) and (3.3.44), we also obtain

$$k = exp(\delta \cdot e + \xi) \cdot exp(\pi (S_r - 1)) \qquad (3.3.47)$$

Nakano et al. (1986) have experimented about the nature of swelling clays. Table 3.3.6 shows the calculated values of constants φ and ξ from their experimental data. It is found that φ is dependent on the void ratio and π is basically independent of it. Hence, it is expected that equation (3.3.47) is much more suitable for the swelling clays used in their experiments than equation (3.3.46).

4) Unsaturated properties of highly compacted clay, HCC

The hydraulic properties of the HCC investigated in the Stripa project are shown in Tables 3.3.7 and 3.3.8 (Push and Borgesson (1985)). To obtain the unsaturated properties of the HCC from this data and the formulas mentioned above, it is necessary to assume a degree of saturation for each value of suction shown in Table 3.3.7 and the relation between ψ_{cr} and e.

In this section, it is assumed that equation (3.3.46) can be applied to examine the seepage flow in the unsaturated HCC, using the equation about φ and k_{sat} which will be mentioned in the next section. Moreover, equation (3.3.42) is used for the relation among S_r, ψ and e, applying the experimental results by Mualem (1978).

a) Relations between k, S_r and e

The relative permeability k_r for each density is calculated by dividing k, shown in Table 3.3.7, by k_{sat}, the permeability for 70 °C in Table 3.3.8. Constant φ in equation (3.3.46) is obtained from the following equation proposed by Nishigaki (1985):

$$k = 0.69\text{-}1.31 \cdot log(k_{sat}) \qquad (k_{sat}: cm/sec) \qquad (3.3.48)$$

Table 3.3.6 Unsaturated properties of swelling clay

k(cm/day)	k_{sat}(cm/day)	S_r	e	φ	π
4×10^{-5}	2.9×10^{-4}	0.84	2.45	11.4	12.3
8×10^{-6}	2.6×10^{-4}	0.72	2.23	10.6	12.5
2×10^{-6}	2.4×10^{-4}	0.59	2.13	9.1	11.8
8×10^{-7}	2.3×10^{-4}	0.45	2.03	7.1	10.6

Table 3.3.7 Approximate values of the pore pressure, and of the permeability, for Na bentonite at various bulk density (after Push and Borgesson (1985))

ρ (t/m^3)	ψ (MPa)	k (m/s)
1.7	–0.3	10^{-12}
1.8	1 – 3	5×10^{-13}
1.9	3 – 7	1.5×10^{-13}
2.0	7 – 10	8×10^{-14}
2.1	15 – 40	2×10^{-14}

Table 3.3.8 Permeability k in m/s versus bulk density of MX-80 (after Push and Borgesson (1985))

ρ t/m^3	k (m/s)	
	Room Temp. very low gradients	70°C gradient 10^{-4} to 10^{-3}
2.1	1.5×10^{-14}	1.5×10^{-13}
2.0	2×10^{-14}	2×10^{-13}
1.9	3×10^{-14}	5×10^{-13}
1.8	5×10^{-14}	8×10^{-13}
1.7	8×10^{-14}	10^{-12}

The S_r is obtained from equation (3.3.43) using the constant φ which was calculated with equation (3.3.48). The void ratio for each density can be derived from S_r and the corresponding density. Table 3.3.9 shows the calculated values of k_r, φ, S_r and e of the HCC for various void ratios. It is concluded that Irmay's formula is valid for the buffer materials since φ can be regarded as being independent of e.

On the other hand, the relation between k_{sat} and e is given from the values in Table 3.3.9 as

$$k_{sat} = 10^{-13} \times 10^{(e-0.26)/(1.09)} \quad (m/s). \qquad (3.3.49)$$

Combining equations (3.3.46) and (3.3.49) and the average value of the constant φ shown in Table 3.3.9, the equation which represents the unsaturated permeability dependent on the void ratio and the degree of saturation is obtained as

$$k = 10^{-11} \times S_r^{14.27} \times exp\left[(e-0.26) \times 2.30/1.09\right] \quad (cm/s). \qquad (3.3.50)$$

b) Relations among S_r, ψ and e

As mentioned above, the degree of saturation as a function of suction ψ and void ratio e were not obtained in the Stripa project. In order to proceed with a calculation using equation (3.3.42), it is necessary to firstly assume constant λ in equation (3.3.42). Mualem (1978) experimentally examined λ for 50 kinds of soils. Averaging λs for the clay soil in Mualem's study, λ is assumed to be 0.367 as a material constant of the HCC in this section. Subsequently, ψ_{cr} as a function of e is calculated with the following three parameters, i.e., S_r shown in Table 3.3.9, ψ shown in Table 3.3.7 and the empirical formula proposed by Brooks and Corey (1966). The relation between ψ_{cr} and e of the HCC is consequently given as

$$\ln\left(|\varphi_{cr}|\right) = -1.76 \cdot e + 7.0 \qquad (3.3.51)$$

Table 3.3.9 Unsaturated properties of buffer materials

ρ (t/m^3)	k_r	φ	S_r	e
1.7	1.0	13.8	1.00	1.43
1.8	0.6	13.9	0.97	1.08
1.9	0.3	14.2	0.92	0.81
2.0	0.4	14.6	0.94	0.66
2.1	0.1	14.9	0.87	0.49

The equation which represents the suction dependent on the void ratio and the degree of saturation is obtained from equations (3.3.42) and (3.3.51) as

$$\varphi = exp(-1.76 \cdot e + 7.0) \cdot S_r^{-2.7} \qquad (3.3.52)$$

Equations (3.3.50) and (3.3.52) are the mathematical expressions of the unsaturated properties of the HCC. It should be noted that these equations do not take the evaporation effect into consideration.

(3) Kinematic viscosity and swelling pressure

1) Kinematic viscosity

Kinematic viscosity, μ, is obtained by the interpolation of Table 3.3.1 in which it is shown as a function of temperature.

2) Swelling pressure

In the finite element computation, the swelling pressure, P_s, is treated as nodal force. While the degree of saturation, S_r, is less than 100%, P_s is assumed to be equal to ψ and while S_r is 100%, P_s is obtained by interpolating the values shown in Table

3.3.10 as functions of temperature and density. It should be noted that this treatment of the swelling pressure is very conventional. Properly speaking, the swelling mechanism should be considered in the constitutive law. However, a proper model for swelling does not exist. In particular, the behavior in the unsaturated zone has not been observed well. For these reasons, the above-mentioned conventional treatment is used in the analyses.

Table 3.3.10 Swelling pressure P_s versus bulk density ρ of HCC at various temperature (after Push and Borgesson (1985))

ρ (t/m^3)	P_s (tf/m^2)		
	20°C	70°C	90°C
2.15	4592.	4082.	3571.
2.10	3061.	2041.	1735.
2.05	1531.	1020.	816.
2.00	714.	510.	408.
1.95	459.	306.	255.

(4) Analyses of the Buffer mass test

The axisymmetric finite element mesh, shown in Figure 3.3.28, is used for the numerical analyses. The model contains a slot between the HCC and the rocks. Three cases are calculated in this section, i.e., Case 1 in which bentonite powders are placed in the slot, Case 2 in which water is placed in the slot, and Case 3 in which bentonite powders are placed in the slot without considering the thermal expansion of the HCC. Material properties of the HCC used in the analyses are given in Table 3.3.11. The electric heater is set at 600 W.

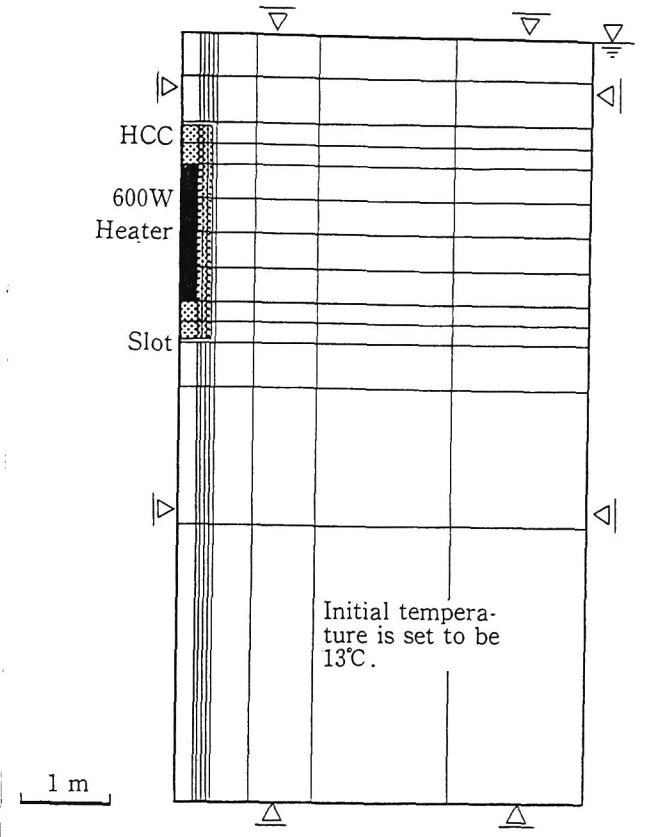


Figure 3.3.28 Finite element mesh used in the analysis of the Buffer mass test

Table 3.3.11 Data of HCC used for analysis

Property	Value
mass density	2.15 t/m^3
porosity	0.42
Young's modulus	1.0×10^6 tf/m^2
Poisson's ratio	0.3
thermal expansion coef.	6.0×10^{-6} °C^{-1}
specific heat	1220 J/kg°C
thermal conductivity	1.46×10^{-3} kJ/ms°C
intrinsic permeability	10^{-19} m^2

The following subjects are thoroughly investigated:

1) changes in the heat transport phenomena in the HCC with seepage and expansion
2) changes in the water flow phenomena in the HCC with seepage and expansion
3) the effects of thermal expansion on heat transport and expansion in the HCC
4) the effects of materials placed in the slots on heat transfer, seepage and expansion in the HCC.

in which the term "expansion" means the coupled behavior of swelling and thermal expansion.

1) Changes in the heat transport phenomena in the HCC during seepage and expansion

Figure 3.3.29 shows the unsteady changes in the distribution of porosity n, the degree of saturation S_r, heat conductivity K_T and permeability k in the HCC, whose results are obtained from Case 1. The distances shown in these figures are the radial distances from the heater.

Figure 3.3.29 a) shows that n increases with time in the HCC. On the other hand, Figure 3.3.29 b) indicates that S_r increases to 100% after one reduction; its property is dependent on n and the state of the seepage. K_T decreases gradually with an increase in n as shown in Figure 3.3.29 c), in which K_T is a function of n and S_r.

Hence, it is found that the distribution of K_T is influenced by n more effectively than by S_r.

On the other hand, Figure 3.3.30 shows unsteady changes in the calculated temperature distributions. In Case 1, although Figure 3.3.29 c) shows that the distribution of K_T after 3 weeks is different from the one after 4 months, Figure 3.3.30 a) shows that the temperature distribution after 3 weeks is the same as the one

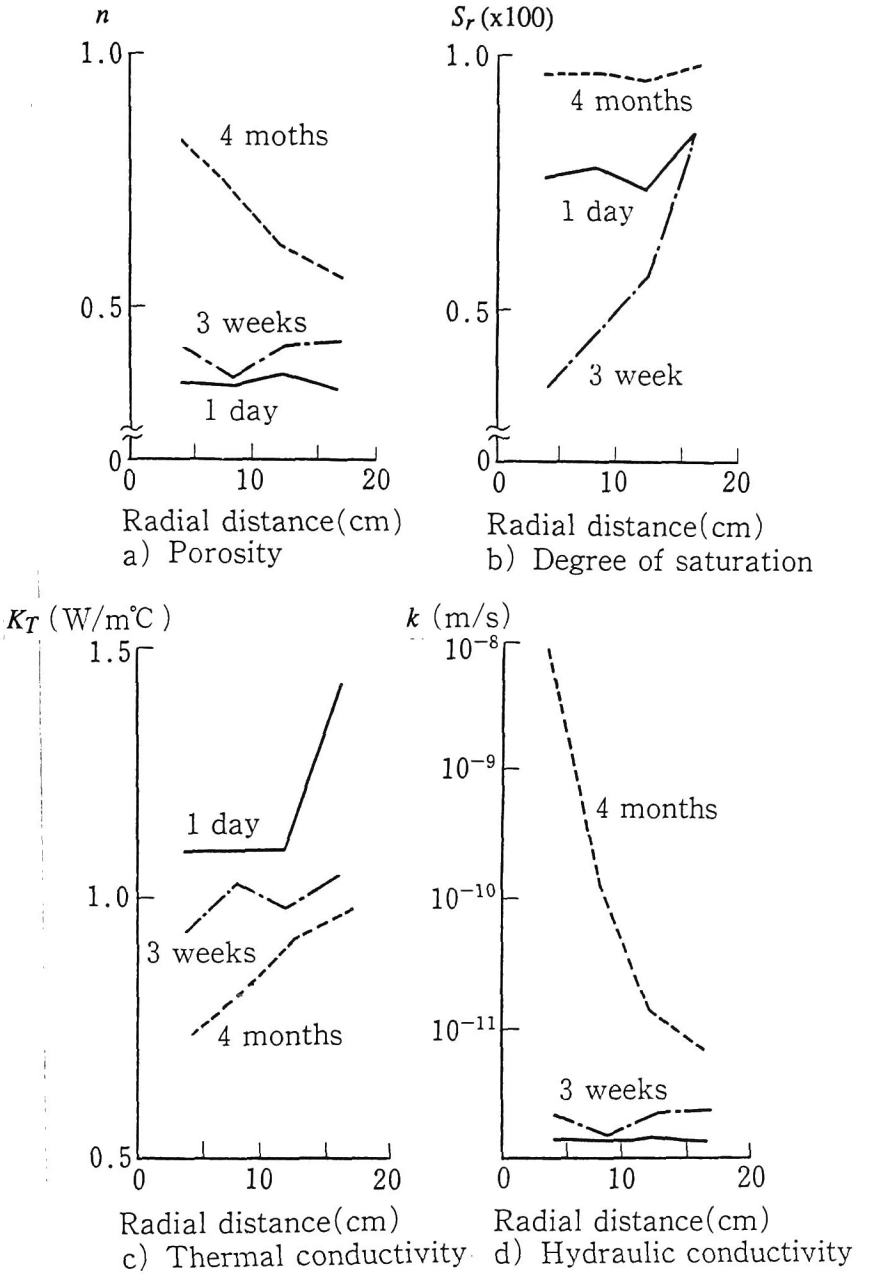


Figure 3.3.29 Unsteady change in the distribution of a) porosity, b) the degree of saturation, c) thermal conductivity and d) permeability in the HCC

after 4 months. It is found, therefore, that the temperature distribution is not very dependent on the distribution of K_T.

Moreover, Figure 3.3.30 a) shows that the temperature increases in the early stages and settles down to a steady state after a small peak near the heater at the 7th week. This tendency is similar to the real phenomena shown in Table 3.3.12, in which a comparison of calculated temperature changes and measured ones is given. The reason for this unsteady temperature change is considered to be as follows.

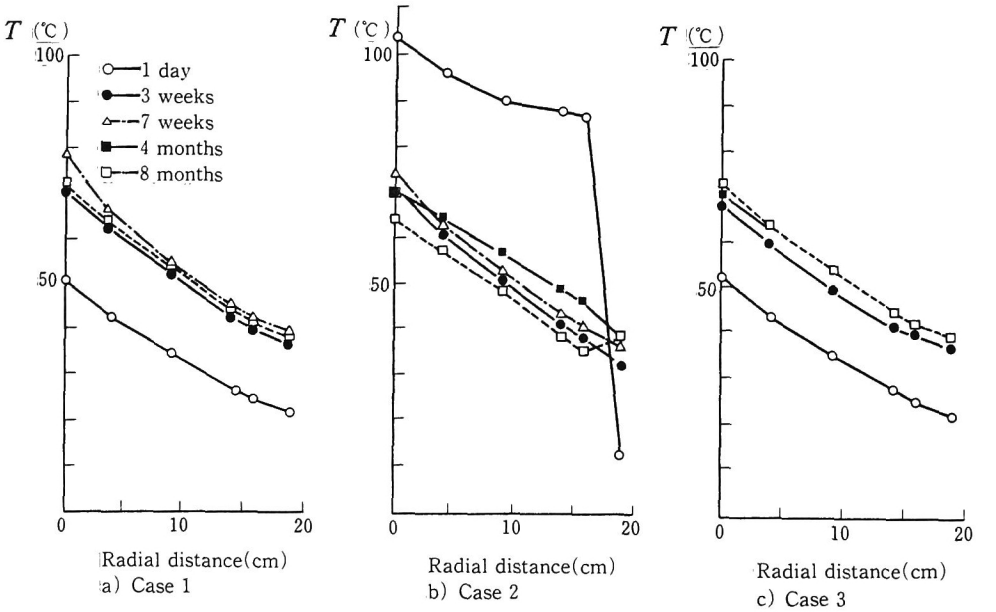


Figure 3.3.30 Unsteady change in the calculated temperature distributions

Table 3.3.12 Comparison of the temperature at mid-height in heater hole no.1 recorded at BMT and calculated by numerical analysis (°C)

Time	Heater surface		Rock/HCC interface	
	Observed	Numerical	Observed	Numerical
1 week	66	64.8	32	31.2
10 weeks	70	78.6	33	38.8
1 year	65	73	34	39.9
2.4 years	65	73.9	35	39.9

It is found from Figures 3.3.31 a) and 3.3.32 a), in which the unsteady change of the calculated distribution of porosity, n, and the unsteady change of the calculated distribution of water content, w, are presented, respectively, that the w near the heater increase slightly from the 3rd to the 7th week, while the n increases drastically near the heater during this period. The radial distance in these figures is the distance from the heater. This slow increase in w near the heater may be due to the slow supply of water from the surrounding rocks. Hence, that the K_T of the HCC near the heater is expected to decrease temporarily from the 3rd to the 7th week, and thus, the temperature increases during this period.

In other words, the temperature distribution may be dependent on the change rate of the K_T.

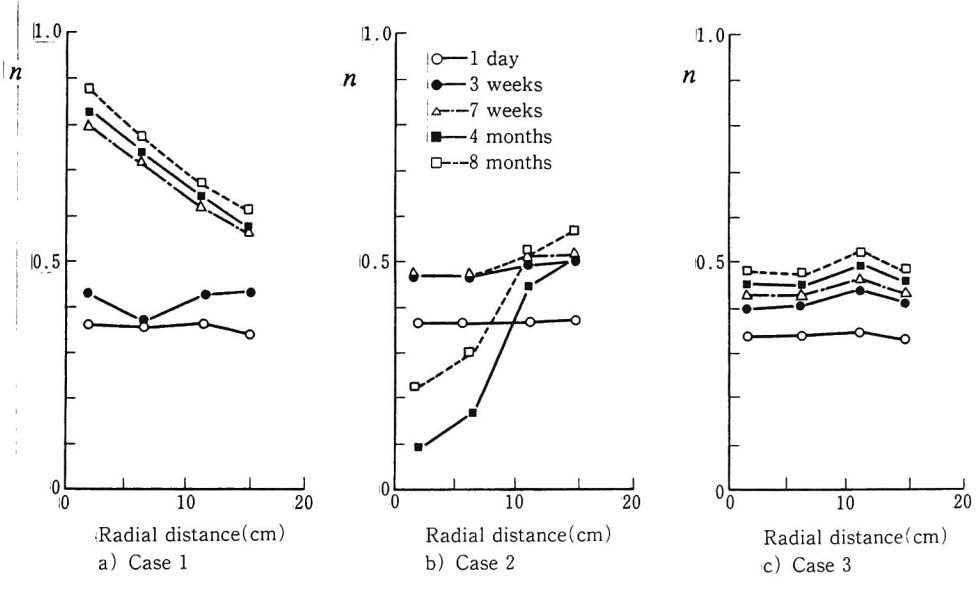


Figure 3.3.31 Unsteady change in the calculated porosity distributions

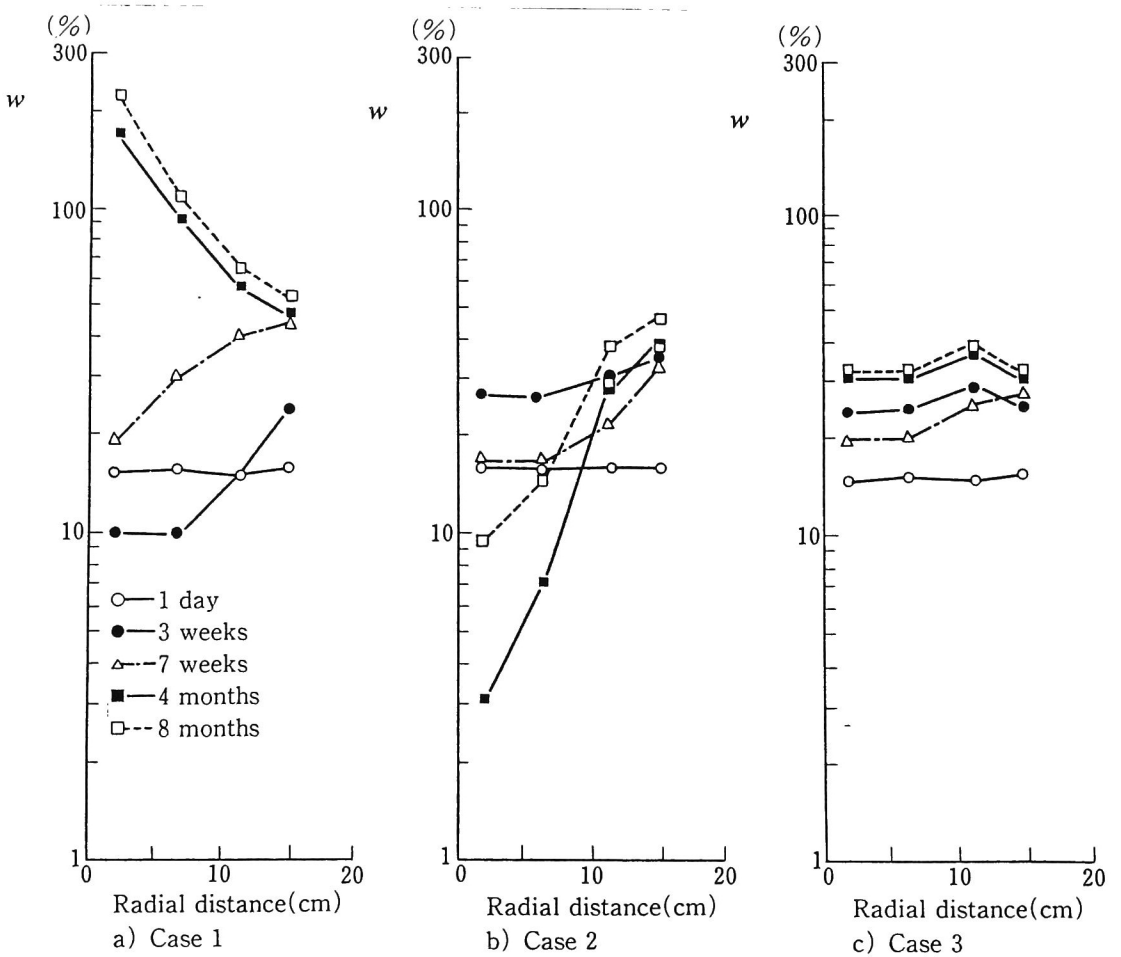


Figure 3.3.32 Unsteady change in the calculated water content distributions

While complex changes in heat transport phenomena are inferred, as mentioned above, the temperature distribution is well simulated through these calculations, as shown in Figure 3.3.33, where a comparison of the numerical results from Cases 1 and 2 with the experimental results of the BMT is given. In addition, Figure 3.3.34 indicates the calculated isothermal lines surrounding the heater hole after 0.9 years (about 11 months).

2) Changes in the water flow phenomena in the HCC during seepage and expansion

The k in the HCC is calculated with equations (3.3.50) and (3.3.52), which are functions of e and S_r. It is found from Figures 3.3.29 a), b) and d) that the distribution of k is influenced more by n than by S_r, and that k increases with an increase in n. Figure 3.3.29 d) also shows that the distribution of k in the HCC is not uniform. This is because the distribution of n is not uniform by the partial expansion.

The complicated unsaturated seepage behavior in Case 1 is assumed from Figures 3.3.31 a) and 3.3.32 a). S_r, which is given as $wG_s(1-n)/\rho_f n$, is inferred to temporarily decrease near the heater at the 7th week due to the abrupt increase in n by thermal expansion and the slow increase in w. This phenomena is found in the 3rd week from Figure 3.3.29 b). After that, the HCC is expected to be saturated gradually with the increase of k.

Figure 3.3.35 shows a comparison of the calculated distributions for w in the HCC and the measured ones. It indicates that the calculated distributions of w are higher than the measured ones. This difference may be possibly due to the evaporation of water which is ignored in our analyses.

Figure 3.3.36 indicates the measured iso-moisture contents in the HCC surrounding the heater, the calculated ones and the calculated iso-void ratios. It is seen that the measured iso-moisture contents are quite different from the computed ones, and that the calculated iso-moisture contents seem to correlate with the iso-void ratios.

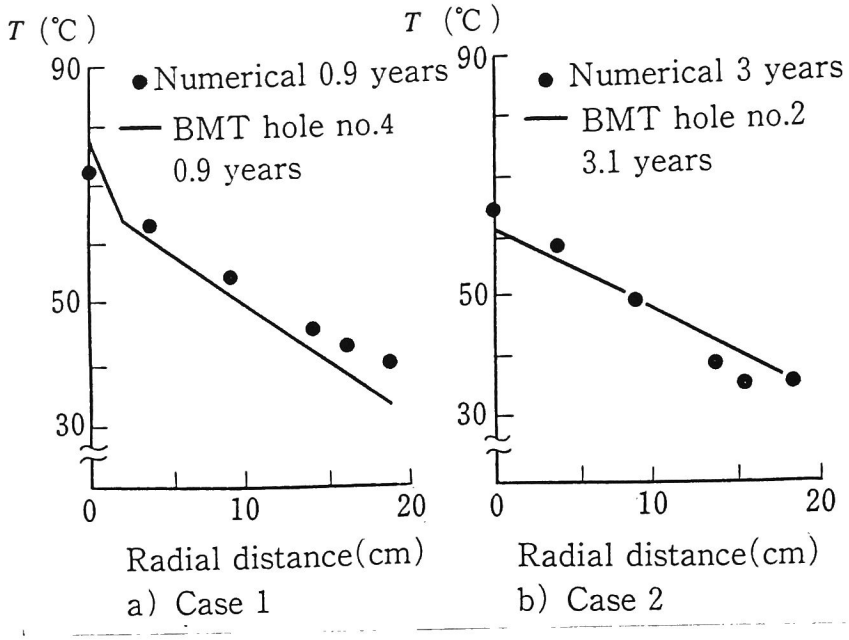


Figure 3.3.33 Comparison of the numerical temperature distributions from Cases 1 and 2 with the experimental ones of the BMT

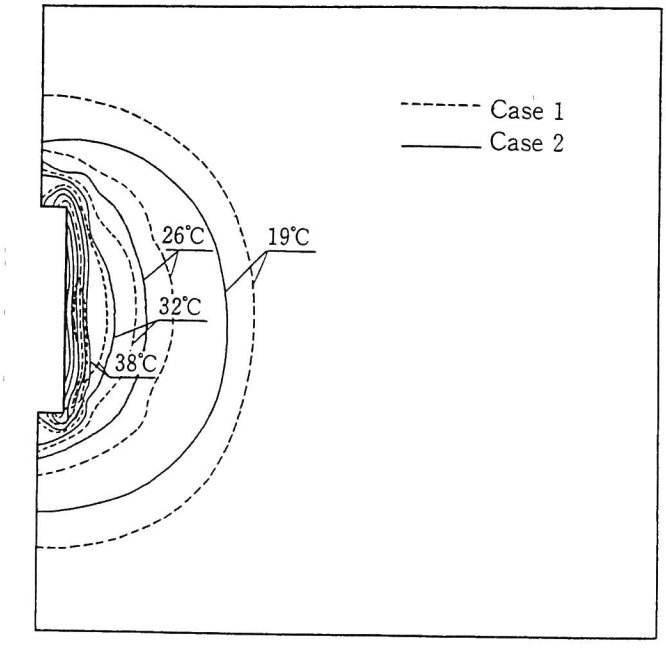


Figure 3.3.34 Calculated isothermal lines of Cases 1 and 2 after 0.9 years

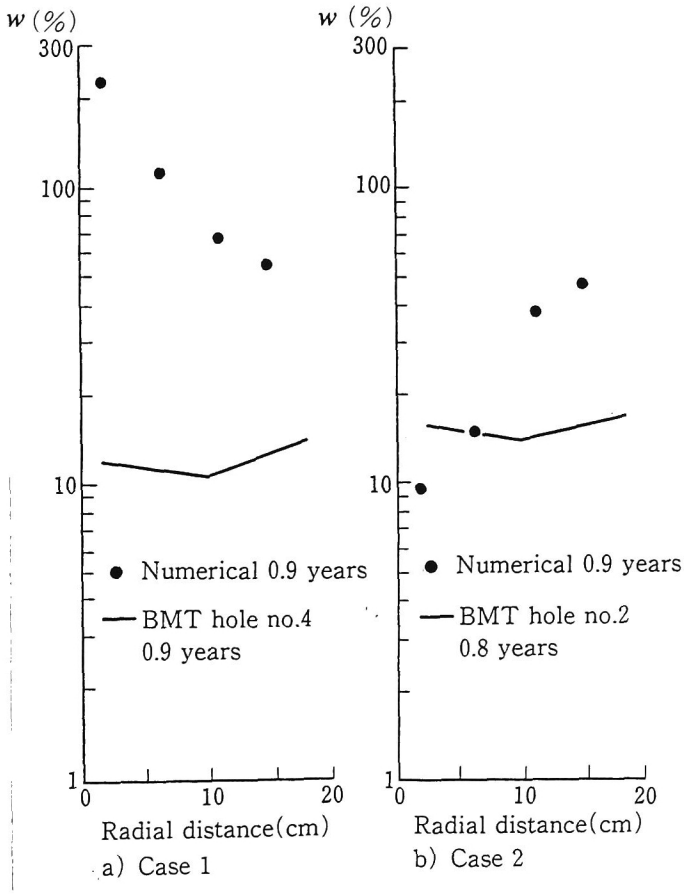
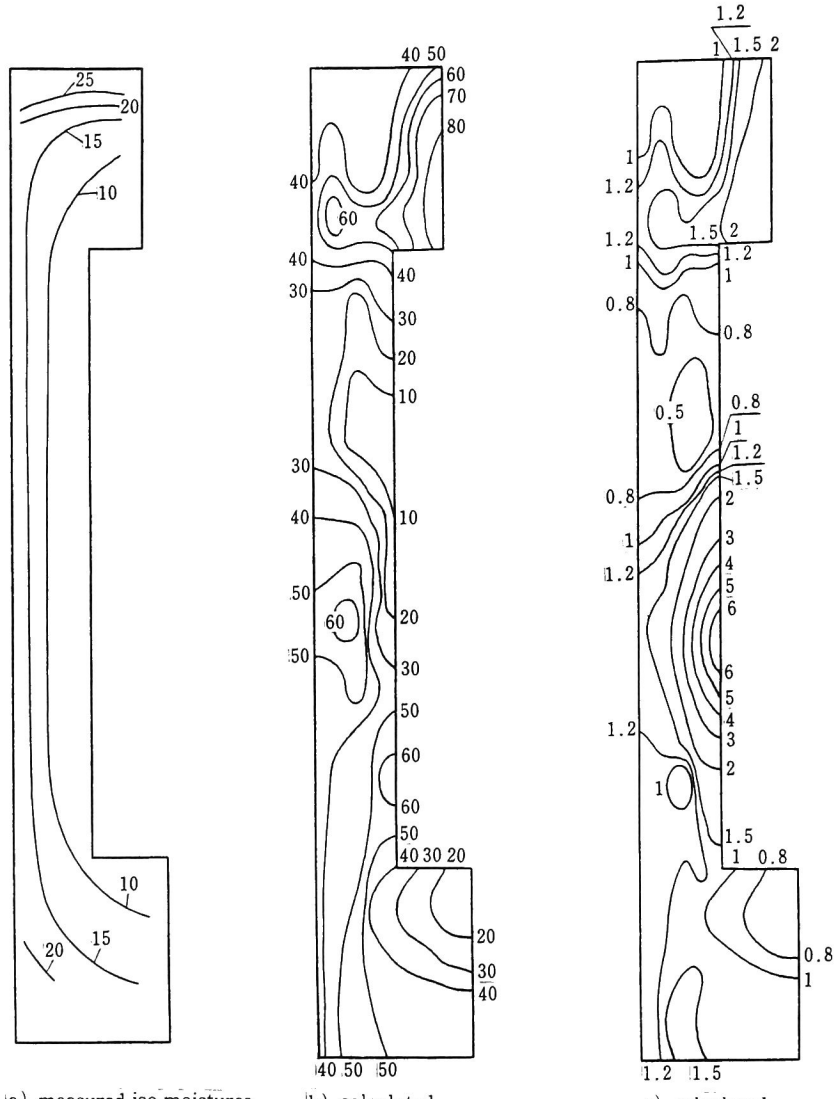


Figure 3.3.35 Comparison of the calculated water contents distributions in the HCC with the observed ones



a) measured iso-moistures in heater hole no.4 (%)

b) calculated iso-moistures(%)

c) calculated iso-void ratios

Figure 3.3.36 Comparison of measured iso-moisture contents in the HCC with the measured ones and the calculated iso-void ratiosa bout 10 months after the start

From these results, it seems reasonable that the real distribution of w in the HCC may be influenced more strongly by water movement due to evaporation than by changes in the void ratio due to expansion.

It is concluded that since k is very much dependent on n, the seepage behavior is influenced by the complicated state of expansion. Moreover, the real behavior is expected to be even more complex with the effect of additional evaporation.

3) Effects of thermal expansion on heat transport and expansion

Figures 3.3.31 a) and c) indicate that the HCC expands near the heater more than near the rock in Case 1, while it expands uniformly near both in Case 3. It may be expected, therefore, that the nonuniformity of the distribution of n in the HCC is caused by thermal expansion, since the swelling due to seepage occurs uniformly, as shown in Case 3, in which thermal expansion is not considered.

Figures 3.3.30 a) and c) show that the temperature distribution at the 8th month in Case 1 is basically the same as the one in Case 3, and that the temperature does not increase near the heater temporarily at the 7th week in Case 3. This is probably because K_T would not decrease much at that time in Case 3, since w does not increase very much, as shown in Figure 3.3.32 c). Hence, changes in K_T, induced by thermal expansion, may have influence on the temperature distribution in the HCC.

Figure 3.3.37 shows a comparison of the measured unsteady changes in pressure at the middle height of the heater hole wall and the calculated ones. It is found from Figure 3.3.37 a) that the expansion pressure induced by both swelling by seepage and thermal expansion (Case 1) is about twice that induced by only the swelling due to seepage (Case 3). Thermal expansion, therefore, may have a great effect on the expansion behavior occurring in the HCC.

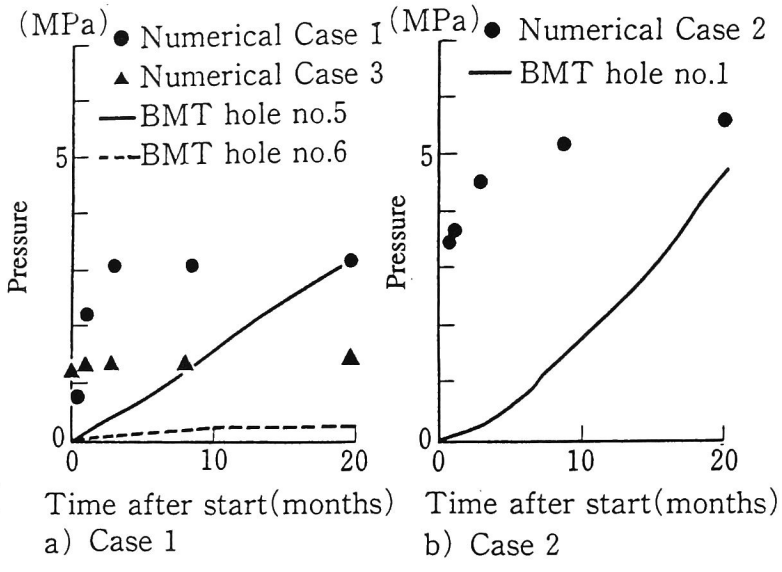


Figure 3.3.37 Comparison of the measured unsteady changes in pressure at the middle height of the heater hole wall with the calculated ones

Figure 3.3.37 also shows that the calculated expansion pressure is greater than the measured one at the early stage and that it arrives at a steady state earlier than the measured one. This is caused by the fact that the suction and the temperature distribution reach the steady state at an early stage of the computation. There is not much difference in the measured temperature distribution, however, between after 0.9 years and after 3 years, as shown in Figure 3.3.33, although the measured heater holes are different. Thus, the increase in pressure at the heater hole wall after 1 year may be caused by the swelling due to seepage.

It may be concluded that the assumption related to the swelling process in an unsaturated region is not appropriate for the behavior occurring in the HCC, the assumption being that the swelling pressure is the same as the suction.

4) Effect of material placed in the slot on heat transfer, seepage and expansion

Figures 3.3.30 a) and b) indicate that the temperature in Case 1 rises up gradually, while the temperature settles down to a steady state after an increase on the first day in Case 2. This high temperature on the first day is possibly because the heat is confined in the HCC due to the effect of the high heat capacity of water in the slot. After a while, the temperature in the HCC decreases by conducting the heat through the water to the adjoining rocks. Figure 3.3.34 indicates that temperature spreads farther in Case 1 than in Case 2 after 0.9 years due to this effect at the early stage.

Figure 3.3.31 b) shows that n is smaller near the heater than near the slot after 4 months in Case 2. This is probably because the HCC is compressed near the heater by the swelling induced by the seepage from the surrounding rock. In other words, the swelling due to seepage from the slot is larger than the thermal expansion due to a temperature increase of the heater. This phenomenon is different from that occurring in Case 1. Thus, it is assumed that the expansion behavior in the HCC is dependent on the material filled in the slot.

Figure 3.3.32 b) shows that the w of the HCC decreases near the heater after 7 weeks. The tendency of the unsteady change in the distribution of w is similar to that of n shown in Figure 3.3.31 b). This is probably because the delayed supply of water to the part near the heater from the surrounding rock at the 7th week, as shown in Case 1, does not occur in Case 2.

(4) Conclusions

This section described the application of the coupled thermal, hydraulic and mechanical analysis methods to the Buffer mass test conducted in the Stripa project.
The conclusions are summarized as follows:

1) The distributions of heat conductivity and permeability are affected more by porosity changes than by water content changes, and they become nonuniform with the process of expansion.
2) The temperature distribution is not so much dependent on the complicated heat conductivity distribution in the HCC as on the change rate of heat conductivity.
3) The assumption related to the swelling process in an unsaturated region might not be appropriate for the behavior occurring in the HCC, the assumption being that the swelling pressure is the same as the suction.
4) Evaporation may have a serious effect on the water content distribution in the HCC.
5) Thermal expansion has much influence on the expansion behavior in the HCC.
6) When water is placed in the slot between the HCC and the surrounding rock, the temperature rises in the HCC the first day after the canister has been set up and then decreases afterwards.
7) The expansion process is influenced by the material placed in the slot.

Although these analyses were carried out through use of many assumptions, the results are helpful for understanding the phenomena observed at the site. The phenomena will be better understood by refined experiments based on the results of these analyses.

Problems remain with the unsaturated properties, depending on void ratio changes such as those in equations (3.3.50) and (3.3.52), and the constitutive law which includes swelling due to seepage.

3.4 Three-dimensional Thermal-Hydraulic-Mechanical Coupling

3.4.1 Introduction

For the assessment of the high level radioactive waste disposal and the understanding of the phenomena which occurred at the site, coupled thermal, hydraulic and mechanic behavior has to be examined as exactly as possible. In the previous section, the two dimensional coupling code was introduced for this purpose and a few field experiments were examined. The geometry of the depository is, however, three dimensional and that effect is not negligible. Thus, we developed the new analysis code for three dimensional coupled thermal, hydraulic and mechanic phenomena in the saturated-unsaturated fields, which is called THAMES3D. This code takes advantage of preconditioned conjugate gradient method in order to save the computer storage and calculation time.

In this section, the method of this code and verification results are presented, and then two example problems are solved and the three dimensional results are compared with the ones obtained from the two dimensional analysis.

3.4.2 Preconditional conjugate gradient method

The equations mentioned in the previous section are discretized to finite element with the Galerkin method and then the matrix form, $Gx = f$, is constructed, where G is the global matrix, x is the unknown vector and f is the nodal force vector.

Gauss Elimination method (GE method) is often used for solving the matrix form. GE method is very useful for solving the matrix of which band width is not large. The band width of the matrix is dependent on the number of unknown variables and the connectivity of the elements. It is generally very difficult to number nodes so as to make the band width small for three dimensional mesh. Furthermore five unknown variables have to be considered (displacements of X-Y-Z directions,total water head,

temperature) in this three-dimensional coupled analysis. Thus a rather large band width of the global matrix is often produced for the analysis in this code. Large memory storage of computer and calculation time are needed if GE Method is applied for the examination with this code. From these reasons, we have to use the more effective method to solve the matrix.

THAMES3D takes advantage of the Preconditioned Conjugate Gradient Method (PCG method). In this iteration method only the relations between the neighboring nodes are considered. Thereby, the memory needed is smaller than in the case of the GE method.

The algorithms of PCG method can be explained as follows:

(1) First Step (initial state)

$$r_0 = b\text{-}Ax_0, \quad P_0 = B\, r_0 \tag{3.4.1}$$

in which A is G^TG. Superscript T means transposed matrix, b is G^Tf, P is a correction vector, r_i is the error at the ith iteration and subscript 0 means the initial set. B is a preconditioner.

(2) Iteration Calculus

Firstly, we get the magnitude of correction,

$$\alpha_k = \frac{(P_k,\, r_k)}{(P_k,\, AP_k)} \tag{3.4.2}$$

where (P,r) is the inner product of P and r, α is the magnitude of correction, subscript k is the iteration number. Then the unknown vector is corrected with the next equation.

$$x_{k+1} = x_k + a_k P_k \tag{3.4.3}$$

Using this unknown vector, the error at the (k+1)th iteration is calculated by the following equation.

$$r_{k+1} = r_k - \alpha_k A P_k \qquad (3.4.4)$$

Sequentially, the correction vector at (k+1)th iteration is obtained like the followings.

$$\beta_k = -\frac{(r_{k+1}, AP_k)}{(P_k, AP_k)}, \qquad P_{k+1} = r_{k+1} + \beta_k P_k \qquad (3.4.5)$$

This iteration continues until P_k becomes zero. At this point, r_k also becomes zero and then, x_k becomes exact . B is called a preconditioner which reduces the iteration cycles. In this case only the diagonal of global matrix A is involved in the preconditioner B.

3.4.3 Comparison with analytical solutions

In order to verify the functions of THAMES3D, theoretical solutions for the mechanical-hydraulic, mechanical-thermal and hydraulic-thermal problems are compared with the ones calculated with the THAMES3D. This code has to be verified for the fully coupled hydraulic, mechanic and thermal problem. This problem is, however, not solved analytically at the present.

As to the comparison of the mechanical behavior with the hydraulic behavior, a one dimensional consolidation problem was investigated. Figure 3.4.1 illustrates the finite element mesh and the loading condition. The upper boundary is set to be a drainage condition and the other boundaries are set to be a no-flux condition. Displacement is allowed for the z-direction (vertical direction) only. The numerical results are compared with Terzaghi's solutions as shown in Figure 3.4.2. As can be seen in this figure, the calculated results agree with the theoretical ones very well.

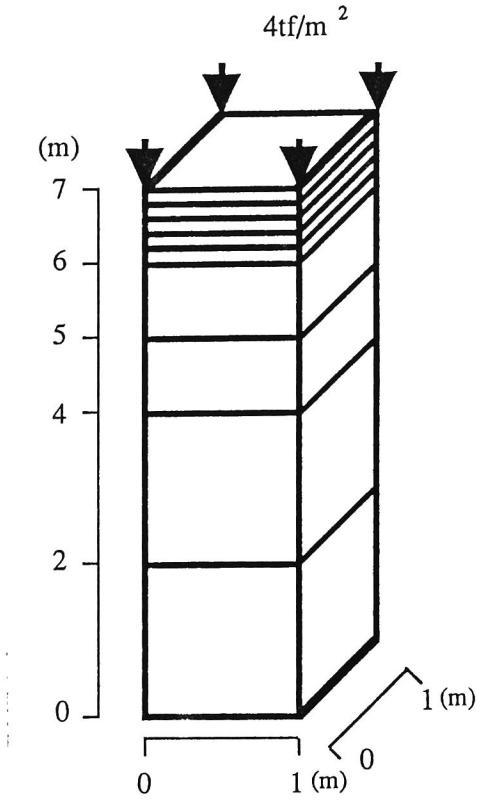


Figure 3.4.1 Finite element mesh of consolidation problem

The mechanical-thermal analysis is applied to a two dimensional thermal stress problem as shown in Figure 3.4.3. This simulates the thermal stress induced in the thick walled cylinder with a constant temperature gradient. The horizontal and vertical boundaries are fixed and the inner and outer ones allow a displacement. The temperature distribution is given by $t = 5°C/r$ in which r is the radial distance and t is the temperature. The comparison of numerical results with analytical ones are shown in Figure 3.4.4. It is found from this figure that the calculated radial and tangential stresses agree with the analytical ones very well.

The heat transfer in moving groundwater field is the third problem to be considered for the THAMES3D verification analysis. The fluid flows to x-direction only with the

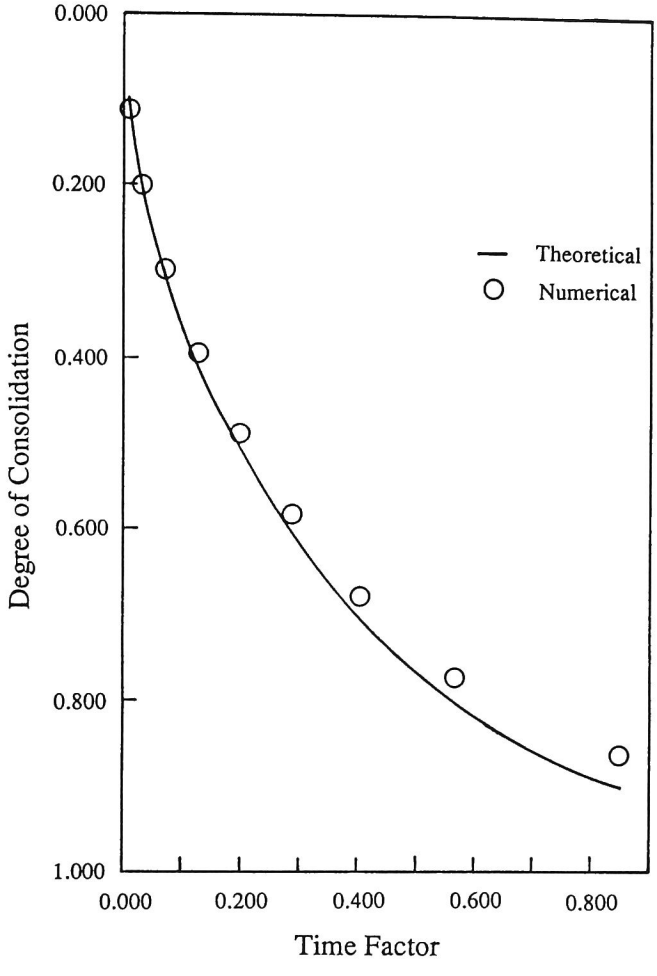


Figure 3.4.2 Comparison of numerical results with Terzaghi's solutions

constant velocity; 0.05m/s.The temperature is fixed at 1 °C at the upstream boundary and 0 °C at the downstream boundary as shown in Figure 3.4.5. The results are shown in Figure 3.4.6. As can be seen in the figure, the theoretical results coincide with the numerical results very well. This type of advection-dispersion problem is difficult to solve for the advection dominate. The nature of the advection-dispersion equation can be conveniently characterized by the Peclet number. In this case it is 0.25. If the problem has the higher Peclet number, the THAMES3D will not solve the problem well.

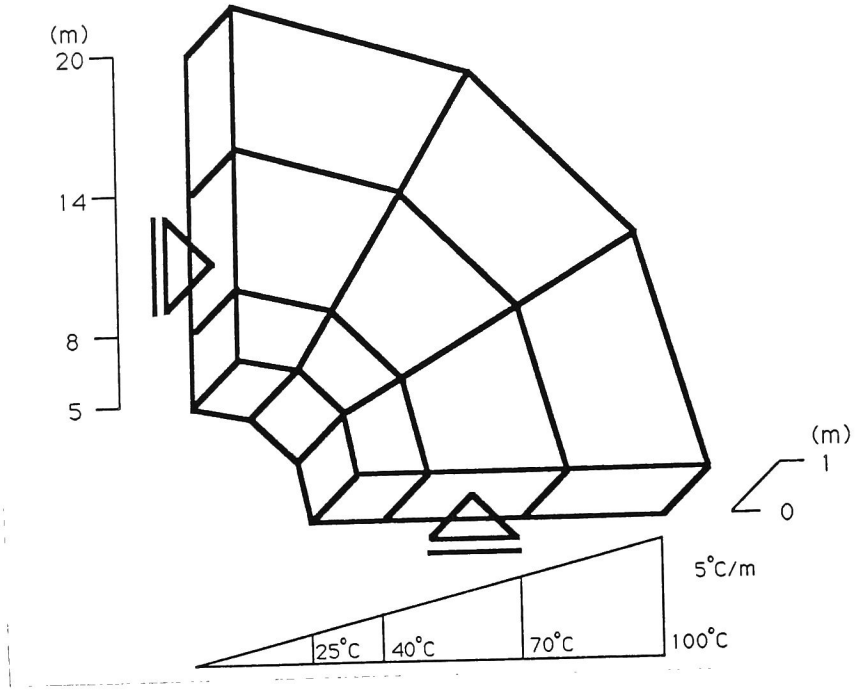


Figure 3.4.3 Finite element mesh of thick-walled cylinder with a constant temperature gradient

However, the problem treated for the high level radioactive waste disposal has the very low velocity field. Thus, this does not appear to be a problem for practical purpose.

3.4.4 Analysis of a imaginary deep nuclear waste depository

High-level radioactive wastes are planed to be disposed in deep geological formations after a interim storage. In our model calculations, the region is considered having an area of 2000 x 2000 m and a height of 1500 m as shown in Figure 3.4.7. The geology is supposed as granite. The depository is assumed to be located within a 500 m times 500 m square at the depth of 1000 m. Table 3.4.1 gives the properties of the rock mass considered.

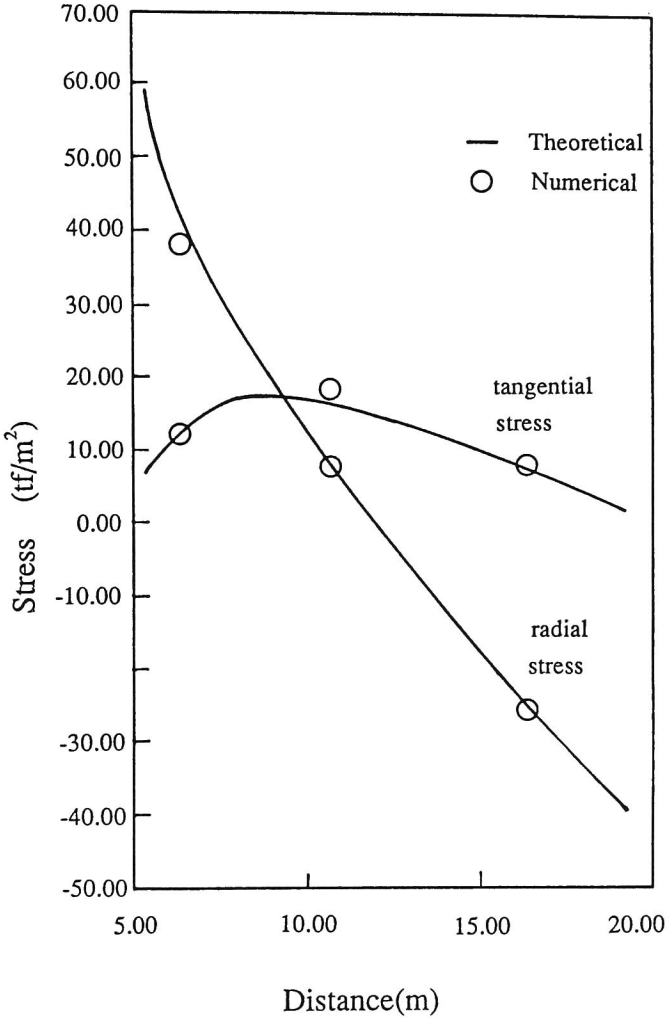


Figure 3.4.4 Comparison of numerical results of thermal stress problem with analytical ones

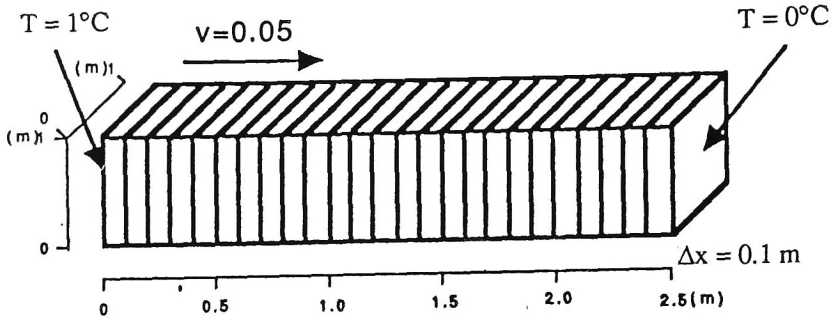


Figure 3.4.5 Finite element mesh and boundary conditions for heat transfer problem

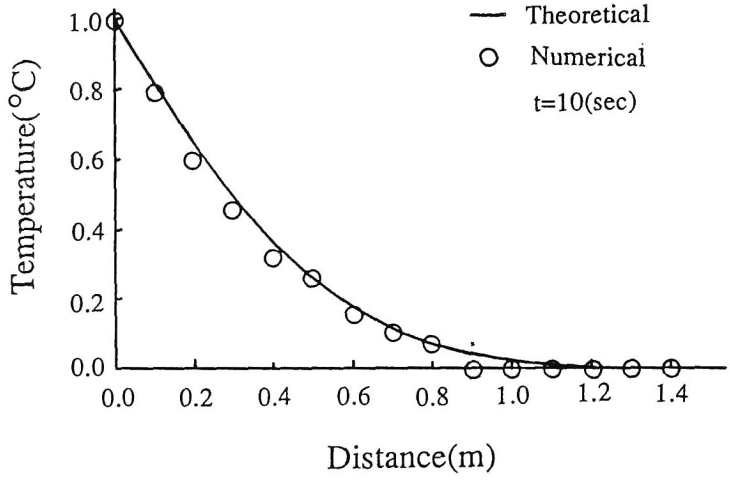


Figure 3.4.6 Comparison of numerical results of heat transfer problem with analytical ones

Table 3.4.1 Parameters used in the analysis of imaginary depository

Parameters	Values
Young's Modulus	500000tf/m^2
Poisson's Ratio	0.3
Unit Weight	2.7t/m^3
Initial Void Ratio	0.02
Intrinsic Permeability (x-direction)	10^{-12} m^2
(y-direction)	10^{-12} m^2
(z-direction)	10^{-12} m^2
Specific Heat of Soil	42.6 m/ C
Heat Conductivity of Fluid	$6.12x10^{-5}$tf/ °Cs
Heat Conductivity of Soil	$6.12x10^{-5}$tf/ °Cs
Thermal Expansion Coefficient	$6.0x10^{-6}$ 1/ °C

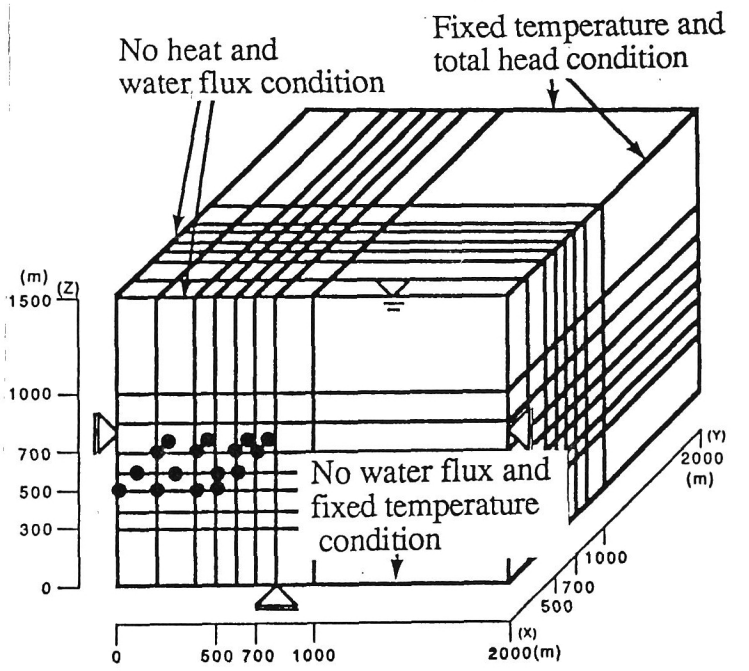


Figure 3.4.7 Finite element mesh and analysis conditions for three-dimensional model

This model is analyzed by using the two-dimensional code,THAMES and the three-dimensional code, THAMES3D. Figure 3.4.8 is the schematic figure of two dimensional model and Figure 3.4.7 is that of three dimensional one. The depository is simulated by the heat sources indicated by circles in Figures 3.4.7 and 3.4.8. The heat source is set at 100°C during the analyses. The temperature in the initial state is a function of the depth, D_{ep},

$$t = 20 + 3xD_{ep}/100 \qquad (°C) \qquad (3.4.6)$$

Therefore, the temperature at the depository (= GL. -1000m) is 50°C.

The permeability is also assumed to be the function of the depth. We use the following equation proposed by Iwai (1976).

$$\frac{k_e}{k_{od}} = \frac{\{1 + A(\sigma_{eo}/\zeta)^{t'}\}}{\{1 + A(\sigma_e/\zeta)^{t'}\}} \qquad (3.4.7)$$

where k_e is the intrinsic permeability under the stress, σ_e and k_{od} is the one under the reference stress, σ_{eo}. A, ζ and t' are the constants.

Total water head is constant for all regions in the initial state. The boundary conditions are indicated in Figures 3.4.7 and 3.4.8.

The distribution of displacement vectors at y = 0 (frontal profile) due to thermal stress after an elapsed time of 100 years is shown in Figure 3.4.9 and Figure 3.4.10. The three dimensional analysis gives similar results as the two dimensional one at the vicinity of the heat source. However, with increasing distance from the heat source the three dimensional analysis yields smaller displacements. The reason for the divergence of the results is due to the assumption of plane strain condition in the two-dimensional case. The thermal stress are isotropic and the depository has the finite length for y-direction in Figure 3.4.7.

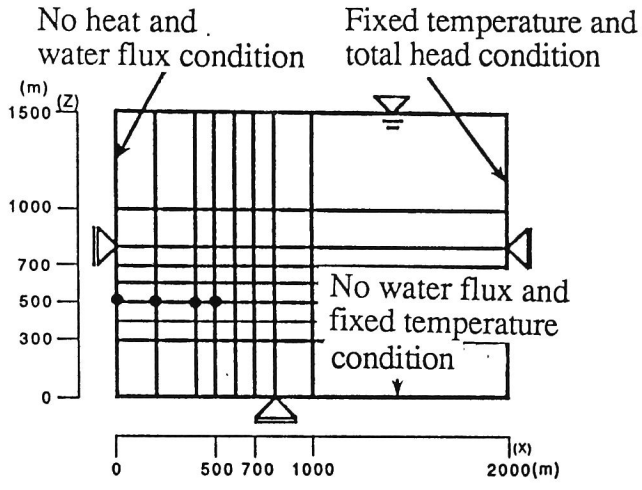


Figure 3.4.8 Finite element mesh and analysis conditions for two-dimensional model

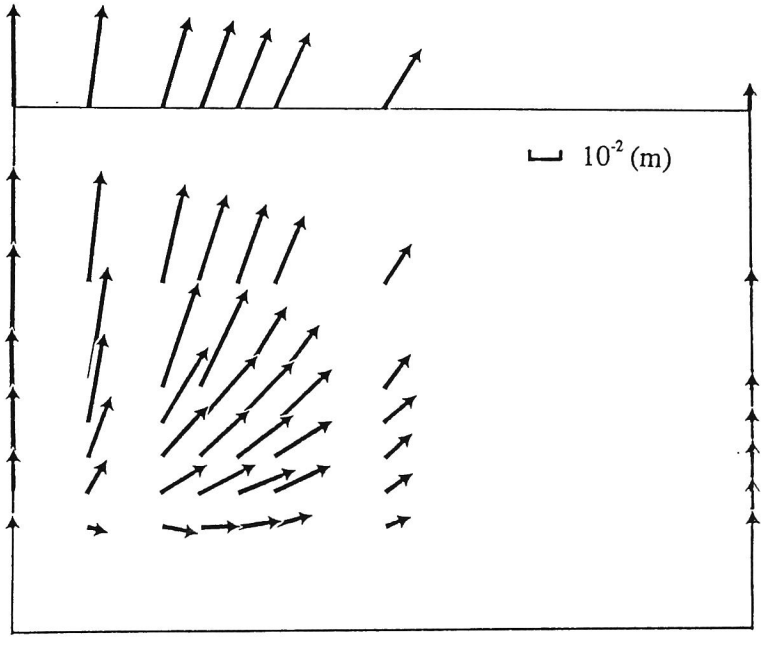


Figure 3.4.9 Displacement vector distribution at 100 years (two-dimensional analysis)

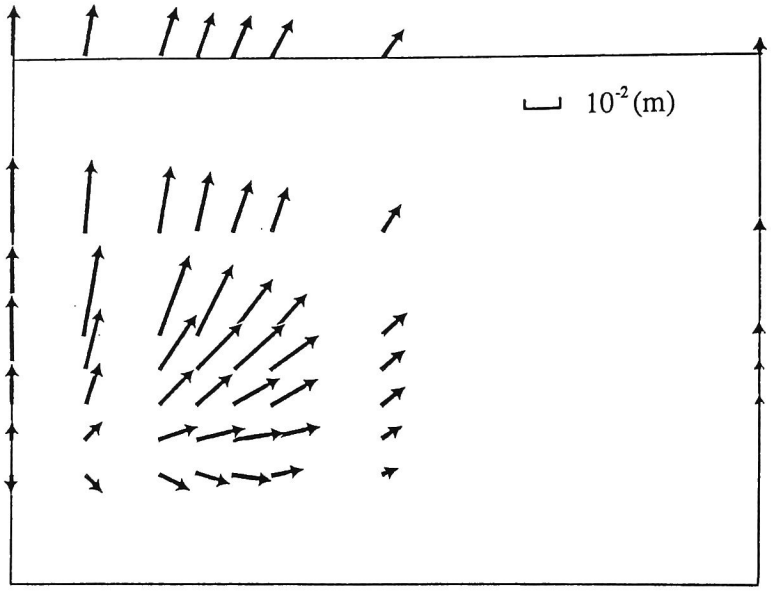


Figure 3.4.10 Displacement vector distribution at 100 years (three-dimensional analysis)

In Figure 3.4.11, the relationship between the elapsed time and the displacement from the three dimensional analysis is depicted. With decreasing distance from the heat source the displacement becomes larger. At 100 000 years the displacement ceases, resulting in a steady state for the displacement.

The ground water velocity is also influenced by the heat generated at the depository. The distribution of velocity vectors at an elapsed time of 10000 years is given in Figure 3.4.12. For location close to the heat source, the ground water flows upward and for a remote location, the effect of the heat source on the groundwater velocity is small.

3.4.5 Conclusions

For detailed assessment of the phenomena occurring at a high level radioactive waste repository, a new analysis code for the assessment of the fully coupled thermal, hydrau-

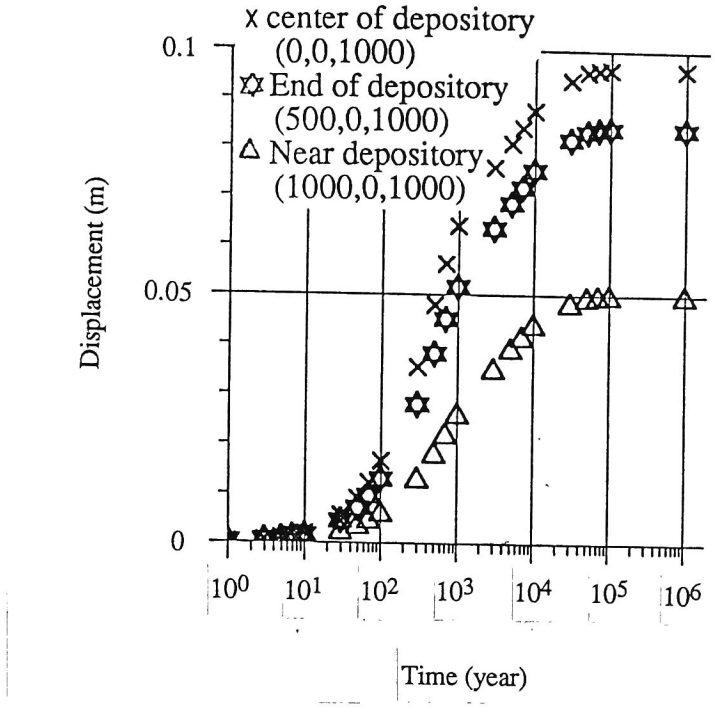


Figure 3.4.11 Relations between the elapsed time and the displacement from three-dimensional analysis

lic and mechanic behavior is developed. This code used the PCG method in order to save the computer storage and calculation time. In this section, the basic concept of this code was introduced and then verification of the results was presented. The verification was carried out for the consolidation problem, thermal stress problem and heat transfer problem in the advection-dispersion field. Furthermore, the ability of this code for the assessment of disposal was demonstrated by using an ideal repository in a granite rock mass.

The followings are clear from the above examinations:

1) This code called THAMES3D has the ability to explain exactly the coupled thermal, hydraulic and mechanic behavior.
2) The two dimensional analysis estimates larger thermal expansion due to the heat generated at the depository than the three dimensional one.

3) The fluid flow caused by the buoyancy induced from the temperature change is not small at the vicinity of site.

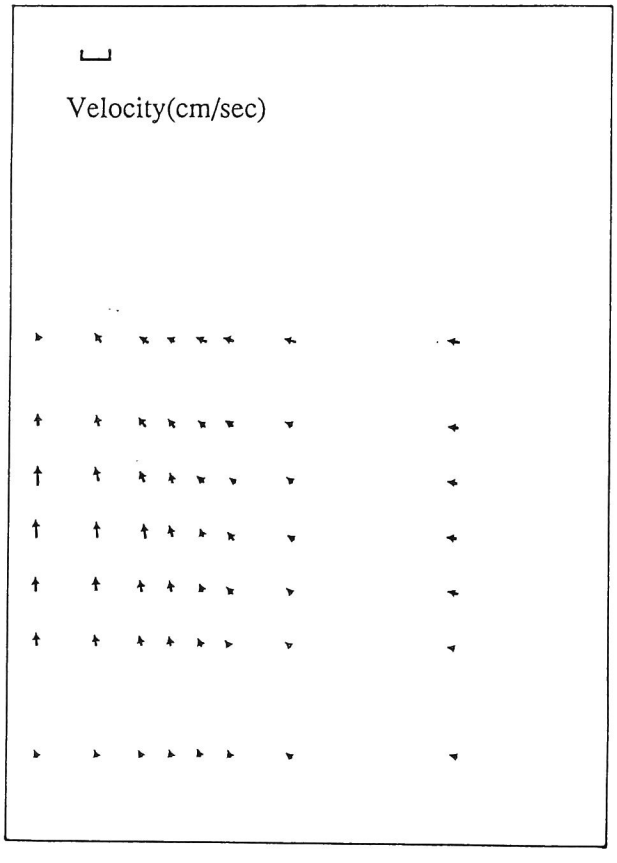


Figure 3.4.12 Velocity vector distribution at 10000 years

REFERENCES

Akai, K. and T. Tamura : Numerical analysis of multi-dimensional consolidation accompanied with elasto-plastic constitutive equation (in Japanese), Transaction of JSCE, No.269, pp.95-104, (1978)

Akai, K. and T. Uno : Study on the quasi-one-dimensional, non-steady seepage flow through soil (in Japanese), Transaction of the JSCE, No.125, pp.14-22, (1966)

Barton, N., P. Chryssanthakis and K. Monsen : Validation of MUDEC against Colorado school of mines block test data, SKB Technical report 88-14, (1988)

Bear, J. and M.Y. Carapcioglu : A mathematical model for consolidation in a thermoelastic aquifer due to hot water injection or pumping, Water Resour. Res. Vol.17, No.3, pp.723-736, (1981)

Bishop, A.W. and G.E. Blight : Some aspects of effective stress in saturated and partly saturated soil, Geotechnique, Vol. 13, No.3, (1963)

Boley, B.A. and J.H.Weiner : Theory of Thermal Stresses, Wiley, pp.288-291, (1960)

Brooks, R.H. and Corey, A.T. : Properties of porous media affecting fluid flow, ASCE, IR(92), pp. 61-88, (1966)

Carter, J.P., J.R. Booker and J.C. Small : The analysis of finite elasto-plastic consolidation, Int. J. Num. Anal. Methods in Geomech., Vol. 3, pp.107-129, (1979)

Christian, J.T. and J.W. Boehmer: Plane strain consolidation by finite elements, ASCE, J. Soil Mech. and Foundation Div., SM4, pp. 1435-1457, (1970)

Cundall, P.A.: A computer model for rock-mass behavior using interactive graphics for the input and output of geometrical data, Report MRD-2-74, (1974)

Eaton, R.R. : A numerical method for computing flow through partially saturated porous media, Numerical Methods in Thermal Problem, Vol. III, pp.911-920, (1983)

Eisenberg,D. and W. Kauzman : The Structure and Properties of Water, The Clarendon Press Oxford, (1969)

Fairhurst, C. and R.D. Hart: Verification and validation of coupled mechanical/water flow effects in rock masses some possibilities and limitations, Proc. of GEOVAL-87 Symp., Stockholm, pp. 527-545, (1987)

Farrel, D.A. and Larson, W.E. : Modeling the pore structure of porous media, Water Resour. Res., Vol. 8, pp. 699-706, (1972)

Faust, C.R. and J.W. Mercer : Geothermal reservoir simulation 1. Mathematical models for liquid- and vapor-dominated hydrothermal system, Water Resour. Res., Vol. 15, pp.23-30, (1979)

G.D.Smith : Numerical Solution of Partial Differential Equation, The Clarendon Press Oxford, (1965)

Gangi, A.F. : Validation of whole and fractured porous rock permeability with confining pressure, First Int. Symp. on Induced Seismicity, Banff, Alberta, Canada, (1975)

Ghaboussi, J.T. and E.L. Wilson : Flow of compressible fluid in porous elastic media, Int. J. Num. Meth. in Engrg., Vol.5, pp.419-442, (1973)

Goodman, R.E. : Methods of geological engineering in discontinuous rocks, West Publishing Co., (1976)

Hamajima, R., K. Hunyu, M. Kusabuka, M. Watanabe and H.Koide : Coupled analysis of stress and heat transfer for three dimensional rock masses (in Japanese), Proc. of the 19th Symposium on Rock Mechanics, Tokyo, pp.221-225, (1987)

Hart, R.D. : A fully coupled thermal-mechanical-fluid flow model for nonlinear geologic system, Ph.D. Thesis, Univ. of Minesota, (1981)

Heuze, F.E. : High-temperature mechanical physical and thermal properties of granitic rocks A review, Int. J. Rock Mech. Min. Sci. & Geomech. Abstr., Vol.20, No.1, pp.3-1, (1983)

Hillel D. and Gardner W.R. : Measurement of unsaturated conductivity and diffusivity by infiltration through an impeding layer, Soil Sci., Vol. 109, pp. 149-153, (1970)

Hodgkinson, D.P, D.A. Lever and J. Rae : Thermal aspects of radioactive waste burial in hard rock, Progress in Nuclear Energy, Vol.11, No.2, pp.183-218, (1983)

Hodgkinson, D.P. : A mathematical model for hydrothermal convection around a radioactive waste depository in hard rock, Anrals of Nuclear Energy, Vol.7, pp.313-334, (1980)

Iizuka, A. : Fundamental study on deformation and stability of the soft ground (in Japanese), Dr. dissertation, Kyoto Univ., (1988)

Irmay, S. : On the hydraulic conductivity of unsaturated soil. Trans. Amer. Geophys. Union, Vol. 35(3), pp. 463-467, (1954)

Iwai K. :" Fundamental Studies of Fluid Flow through a Single Fracture", ph.D. Dissertation, Univ. of California, Berkeley, (1976)

Kelsall, P.C., J.B. Case and C.R. Chabaaes : Evaluation of excavation-induced changes in rock permeability, Int. J. Rock Mech. Min. Sci. & Geomech. Abstr., Vol.21, No.3, pp.123-135, (1984)

Knutsson, S. : Buffer mass test-thermal calculation for the high temperature test, SKBF/KBS Internal Report 83-03., (1983)

Lambe, T.W. and Whitman, R.V.: Soil Mechanics, John Wiley & Sons, Inc., (1969)

Lewis, R.W., G.W.Robert and O.C. Zienkiewicz : A non-linear flow and deformation analysis of consolidation problem, Proc. 2nd Int. Conf. on Num Meth. in Geomechanics, Blacskurg, Virginia, (1976)

Luis, C. : A study of groundwater flow in jointed rock and its influence on the stability of rock masses, Imperial College Rock Mechanics Research Report No.10, (1960)

Matsui, T. and N. Abe : Multi-dimensional elasto-plastic consolidation analysis by finite element method, Soils and Foundations, Vol.21, No.1, pp.79-95, (1981)

Mercer, J.M. and C.R. Faust : Simulation of water- and vapour-dominated hypothermal reservoirs, Paper SPE 5520, presented at the 50th Annual Fall Meeting of the Soc. Pet. Eng. AIME, Dallas, (1975)

Mualem, Y. (1978). Hydraulic conductivity of unsaturated porous media generalized macroscopic approach, Water Resources Research, Vol. 14, No. 2, pp. 325-334.

Nakagawa,K and H. Komada : Finite element analyusis of coupled problems of soil skeleton and pore fluid (in Japanese), Technical Report of Central Research Institute of Electric Power Industry, No. 381031, (1982)

Nakai, T. and H. Matsuoka : Constitutive equations for soils based on the extended concept of "Spatial mobilized plane" and its application to finite element analysis, Soils and Foundations, Vol. 23, No.4, pp.87-105, (1983)

Nakano, M., Amemiya, Y. and Fujii, K. (1986). Saturated and unsaturated hydraulic conductivity of swelling clays, Soil Sci., Vol. 141, No. 1, pp. 1-6.

Nelson, P. and C. Willson : Thermomechical and macropermeability experiments in the Stripa granite - Status report - , Proc. Work shop on Thermomechanical Hydrau-chemical Modeling for A Hard Rock Waste Repository, LBL-11204, pp.45-55, (1980)

Nishigaki, M. : Some aspects on hydraulic parameters of saturated-unsaturated regional ground water flow (in Japanese), Journal of the Japanese Society of Soil Mechanics and Foundation Engineering. Vol. 23, No. 3, pp. 165-177, (1983).

Nishigaki, M., Kagitomi, J. and Shimo, M.: The Applicability of the Instantaneous Profile Method for the Measurement of the Water Retention Character of the Mud Stone (in Japanese), The 17th Japan National Conference on Soil Mechanics and Foundation Engineering, pp. 2385 - 2388 (in Japanese), (1982)

Noorishad T.N., P.A.Witherspoon and T.L. Brekke: A method for coupled stress and flow analysis of fractured rock masses, Geotechnical Engineering Publication Nos, 71-6, University of California, Berkeley, (1971)

Noorishad, J., C.F. Tsang and P.A. Witherspoon : Coupled thermal-hydraulic-mechanical phenomena in saturated fractured porous rocks: Numerical approach, J.G.R., Vol.89, No. B12, pp.10365-10373, (1984)

Oda, M.: An equivalent continuous model for coupled stress and fluid flow analysis in jointed rock masses, Water Resour. Res., Vol. 22, No. 13, pp. 1945-1956, (1986)

Ohnishi Y.and H. Ohtsu,: Coupled stress flow analysis of discontinuous media by finite elements (in Japanese), Transaction of the JSCE No. 322, pp. 111-120, (1982)

Ohnishi, Y. and T. Murakami : Coupled stress-flow finite element analysis of soil (in Japanese), Transaction of JSCE, No.298, pp.87-96, (1980)

Ohnishi, Y., H. shibata and A. Kobayashi: " Development of Finite Element Code for the Analysis of Coupled Thermo-hydro-mechanical Behavior of Saturated-unsaturated medium", Proc. of Int. Symp. on Coupled Processes Affecting the Performance of a Nuclear Waste Repository, Berkeley, pp.263-268, (1985)

Ohta, H., S. Yoshitani and S. Hata : Anisotropic stress-strain relationship of clay and its application to finite element analysis, Soils and Foundations, Vol.15, No.4, pp.62-79, (1975)

Pruess, K. and J.S. Wang : TOUGH- A numerical model for nonisothermal unsaturated flow to study waste canister heating effects, LBL-16946, (1984)

Push, R. and Borgesson, L. : Final report of the buffer mass test - Volume ll; test results, SKB Technical Report 85-12, (1985)

Sandhu, R.S. and E.L. Wilson: Finite element analysis of seepage in elastic media, ASCE, J. Eng. Mech. Div., EM3, pp. 641-652, (1969)

Sato, K. : Experimental determination of transfer parameters of heat flow through porous media by means of a new-designed apparatus in laboratory (in Japanese), Transaction of the JACE, No.320, pp.57-65, (1982)

Science chronological table, ed. Tokyo Astronomical observatory, Maruzen, (1990)

Shen, B. and O. Stephansson : Rock mass response to glaciation and thermal loading from nuclear waste, Proc. of GEOVAL-90 Symposium, Stockholm, 1990.

Shibata, T. and H. Sekiguchi : A method of predicting failure of embankment foundation based on elsto-viscopastic analyses (in Japanese), Transaction of JASCE, vol.301, pp.93-104, (1980)

Shimooka, H. : Numerical methods for analysis of temperature rises and thermal stresses around high level radioactive waste repository in granite (in Japanese), J. of the Atomic Energy Society of Japan, Vol. 24, No.11, pp.889-895, (1982)

Shimooka, K., K.Ishizaki, M. Okamoto, M. Kumata, K. Araki and H. Amano : Thermal characteristics of rocks for high-level waste repository (in Japanese), JAERI-M 9247, (1980)

Simpson, B. : Finite element applied to problem of plane strain deformation in soils, Ph.D. Thesis, University of Cambridge, (1973)

Small, J.C., J.R. Booker and E.H. Davis : Elasto-plastic consolidation of soil, Int. J. Solids and Structures, Vol. 12, pp.431-448, (1976)

Terzaghi, K. : Settlement and consolidation of clay. Engineering News Record, 26., (1925)

Timoshenko, S. and J.N. Goodier : Theory of Elasticity, McGraw-Hill, New York, p.59, (1951)

Tsang, C.F.: Coupled behavior of rock joints, Rock Joints, Barton & Stephansson (eds), pp. 505-518, (1990)

Utsugida, Y.: Coupled analysis of flow and heat around a high-level nuclear waste repository, Fifth Int. Conference on Numerical Methods in Geomechanics, Nagoya, pp.711-716, (1985)

Wang, J.S.Y., C.F.Tsang, N.G. Cook and P.A.Witherspoon : A study of regional temperature and thermohydrologic effects of an underground repository for nuclear wastes in hard rock, J. of Geophysical Res., Vol. 86, No.B5, pp.3759-3770, (1981)

Witherspoon, P.A., S.P. Neuman, M.L. Sorey and M.J. Lipman : Modeling geothermal systems, Technical Report No. LBL-3263, (1975)

Yokoo, Y. , K. Yamagata and M. Nagaoka : Finite element analysis of consolidation following undrained deformation, Soils and Foundations, Vol.11, No.4, pp.37-58, (1971)

Chapter 4 NUMERICAL METHODS OF SOLUTE TRANSPORT IN ROCK MASSES

4.1 Introduction

In this chapter, we discuss the solute transport problem under ground. This is the most important subject to be analyzed for the safety assessment of radioactive waste disposal. For these analyses, however, it is necessary to obtain the velocity vector distributions of the ground water and the solute flux or concentration leaking out of the repository. As a general problem of radionuclides, the concentration is dependent on time due to decay and generation by a parent-to-daughter transformation. Thus, the concentration changes with time at the boundary. This problem is also dependent on the kinds of nuclides which are disposed in the repository. Except for the radionuclide transport problem in the natural ground, therefore, the examination of the solute flux or concentration leaking out of the repository is generally considered to be an other subject. In this section, such a boundary condition is assumed to be known.

In order to analyze solute transport in the ground, two kinds of modeling are generally needed, i.e., a modeling of the geological structure and a modeling of the transport phenomena. There are two types of modeling for the former, i.e., deterministic modeling and stochastic modeling. The stochastic modeling is based on the fact that it is impossible to make a complete model of the geological structure, even if techniques used in the field survey are greatly improved. An examination applying the stochastic modeling focuses on the effects of the heterogeneity of the velocity distribution of the ground water on the solute transport. The deterministic modeling, on the other hand, uses the geometry of the geological structure deterministically obtained by proper methods. Figure 4.1.1 shows the types of modeling for the geological structure. In general, the stochastic modeling

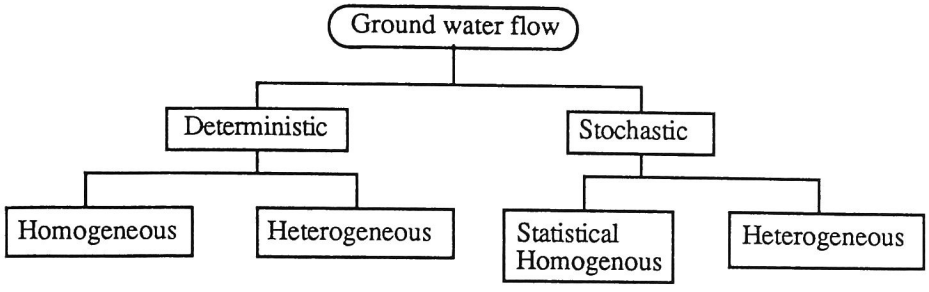


Figure 4.1.1 Modeling types for the geological structure (after Furuichi (1984))

uses assumptions on the statistical homogeneous and ergotic characteristics of the ground.

There are also many kinds of modeling for transport phenomena. Among the transport phenomena, Focus has mostly been placed on adsorption phenomena in previous works. The adsorption modeling can be roughly classified as shown in Figure 4.1.2.

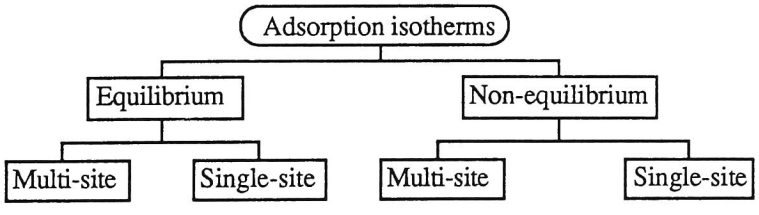


Figure 4.1.2 Types of adsorption isotherm modeling

The multi-sites modeling, e.g., the double porosity model or the two-site model, is used to explain the complex phenomena observed at the unsaturated zone and the fractured rocks whose phenomena are difficult to express with the single-site model. Thus, these kinds of models may be related to the geological structure and may be based

on the assumption that the structural heterogeneity is equivalent to the existence of various adsorption sites. Other bases for the multi-sites modeling are assumptions on the existence of multi-types solutes and multi-types water, e.g., mobile and immobile water and adsorptive and hardly adsorptive solutes. In such cases, the mechanisms of the multi-site have to be examined through detailed experimental investigations, but it seems difficult at the present time to verify the effects of such a multi-types water or solute on solute transport phenomena.

Moreover, time-dependent macro-dispersion phenomena have been studied by many researchers. Their studies have been based on observations of the apparent increase in longitudinal dispersivity according to the scale of the experiment. There are many studies about this subject, in which it is considered that the heterogeneity has a great effect on the scale effect of the dispersion coefficient (e.g., Dagan (1984) and Neuman and Zhang (1990)). In these studies, the stochastic models have been developed in order to express the effect and a longitudinal macro dispersivity depends on the log hydraulic conductivity variance and integral scale. Namely, they have used the stochastic modeling of ground water in Figure 4.1.1. It seems, however, that the reason, why the rate of the longitudinal spread increases in a non-Fickian fashion with time, is not caused only by the spatial variations in hydraulic conductivity, buy also by the non-equilibrium isothermal adsorption or a multi-sites adsorption system mentioned above. The study has been scarcely conducted, which the effect of both heterogeneity of the ground and complex adsorption mechanism is examined in a theoretical framework. In other words, it seems at the present time that the mechanism of the solute transport in non-Fickian fashion is arbitrarily understood through a model.

In addition, there are problems about the way to solve the advection-dispersion equation. The advection-dispersion equation used for solute transport analyses is difficult to solve in high velocity fields where the Peclet number is large. Many previous works have focused on how to obtain a stable solution for such a situation. On the other hand,

studies using an analytical solution for the solute transport equation have also been carried out, e.g., the particle tracking method (Yamashita and Kimura (1988)). This kind of method yields a correct solution and a good mass balance situation in any velocity field. In many cases, however, these methods are limited in the boundary conditions and the dimension that can be applied in the analyses. The examinations carried out in this paper deal with a finite element type method that can solve the partial differential equation governing solute transport.

Looking at matters mentioned above, the followings are examined in this section:

Firstly, a two-dimensional problem using the equilibrium isotherm and single-site adsorption model is examined. The upstream method is introduced and investigated for its applicability, and then the Eulerian and Lagrangian method proposed by Neuman (1981), which is very effective for any Peclet number, is examined. Both methods have been developed to get the stable solutions. Secondly, the adsorption models different from the isothermal instantaneous and single-site adsorption model are examined. The effectiveness of these models for the solute transport analysis in a heterogeneous filed is specially investigated. Finally, the new three-dimensional model for the transport problem in fractured rock masses is introduced, in which the dilution effect of the concentration in the fracture due to water leaking from the adjoining rock block is considered with the matrix diffusion. The dilution and the matrix diffusion can cause the solute spread in non-Fickian fashion.

4.2 Previous Works

Most numerical methods for solving the advection-dispersion equation can be categorized as Eulerian, Lagrangian or Eulerian and Lagrangian methods.

The most common Eulerian method is based on finite differences. This approach performs well in regards to a small Peclet number (Shamir and Harleman (1967)). When the Peclet number is large, however, the method using central difference approximation for the advection term in the governing equation produces oscillations in the solution. This oscillatory behavior is eliminated when a spatial increment is selected which satisfies the following equation :

$$\frac{v_i \Delta x_i}{D_{ii}} \leq 2 \qquad (4.2.1)$$

where v_i is the velocity vector and D_{ii} is the dispersion coefficient tensor. This limitation can prove inconvenient when large velocities or small dispersion coefficients are encountered. To prevent such inconveniences, upstream (or upwinding) approximation is used. Although this approximation will eliminate numerical oscillations, it will generate numerical dispersion to smear the sharp concentration front.

On the other hand, the finite element method has also been applied to solute transport problems. Although high-order Galerkin approximations are more accurate than standard finite difference techniques (Price et al. (1968)), they do not yield stable solutions when dealing with advection dominated problems. The upstream weighting method is used to reduce oscillations by increasing the numerical dispersion (Heinrich et al.(1977)).

Lagrangian methods can mainly be divided into two kinds. One focuses on the movement of one particle and the other is based on either a deforming grid or deforming coordinates. The method representative of the former type is a Monte Carlo method. This kind of method has mostly been used for transport problems in the atmosphere. A general

method representative of the latter type is called the methods of characteristics. By a deforming grid parallel to the characteristics, the equation to be solved is devoid of advective terms and can be solved without difficulty (O'Neill (1981)). When the velocity field is approximately uniform, this method is very effective and highly accurate at any Peclet number.

The Eulerian and Lagrangian method combines the simplicity of the fixed Eulerian grid with the computational power of the Lagrangian approach. Since the velocity of ground water is usually computed independently of the transport problem, using a fixed Eulerian grid, it would be most convenient for the advection-dispersion equation to be solved on a grid compatible with the one used in the seepage analysis. A review of the advances in this method can be shown in Neuman (1983), the most general of which is called the continuous forward particle tracking method originally suggested by Garder et al. (1964). In this method, the advection is handled by the method of characteristics applied to a set of moving particles, while the dispersion part of the problem is solved by an explicit finite difference or finite element method. Neuman (1981) pointed out, however, that the existing theory behind this version of particle tracking is vague, and he went on to derive a theory that did not leave room for ambiguity. In addition, a more efficient scheme called the single-step reverse particle tracking method was developed by Neuman and Sorek (1982) to avoid the need for a large number of moving particles. Neuman (1983) then modified this method by combining it with the forward particle tracking method.

Karasaki (1989) proposed the Eulerian and Lagrangian scheme with an adaptive gridding, whose model avoids the numerical dispersion by creating new Eulerian grid points instead of interpolating the advanced profile back to the fixed Eulerian grid.

Table 4.2.1 shows a brief comparison of the Eulerian method and the Lagrangian method.

Table 4.2.1 Comparison of Eulerian method and Lagrangian method (after Furuichi (1984))

Subjects	Eulerian method	Lagrangian method
Numerical model	Advection-dispersion equation	Characteristics Stochastic differential equation
Errors	Discretization error	round-off error
Constrain from stable condition	exist	not exist
Numerical dispersion	exist	not exist
Limitation of number of samples	not exist	exist
Treatment of hetero-geneous parameter	easy	difficult
Treatment of non-equilibrium adsorption	easy	difficult
Non-linearity	easy	difficult
Three-dimensional analyses	need large memories	relatively easy

Another study to be reviewed is one related to the dispersion phenomena in the heterogeneous velocity field. The dispersion phenomena in the geologic media can be divided into micro-dispersion and macro-dispersion. The former is the dispersion and the diffusion phenomena induced by variations in the velocity at the micro-level, which are caused by random aspects of micro-interstices in the ground. The micro-dispersion phenomena are important in the scale of the laboratory column experiments of which regions are smaller than the M.E.V. (Maximum Elementary Volume) where the heterogeneity of the hydraulic conductivity does not have any influence on the phenomenon as shown in Figure 4.2.1.

Macro-dispersion, on the other hand, is induced by fluctuations in the ground water velocity which are produced by spatial variations in the hydraulic conductivity of the field

scale, as shown in Figure 4.2.2. Values for the macro-dispersion observed in field tracer tests are considerably greater than the micro-dispersion values in the column tests (Gillham and Cherry (1982)). Field tracer tests (e.g., Peaudecef and Sauty (1978) and Freyberg (1986)) suggest that, in relatively uniform materials, the rate of longitudinal spread increases in a non-Fickian fashion with time or mean travel distance toward a constant Fickian limit.

Both micro-dispersion and macro-dispersion have been studied with statistical modeling by many researchers, e.g., Bear (1961) and Scheidegger (1961) for micro-dispersion, and Matheron and Marsily (1980), Tang et al, (1982) and Neuman and Zhang (1990) for macro-dispersion. As another study on micro-dispersion, geometric models were studied by Taylar (1953) and Aris (1956), and the probability models were studied by Schidegger (1954) and Saffman (1959). For micro-dispersion, the following equation obtained from the statistical model (Bear and Bachmat (1967)) has been used in many mass transport analyses:

$$D_{ij} = a_{ijkm}\frac{\overline{V_k}\,\overline{V_m}}{\overline{V}}\frac{P_e}{P_e + 2 + 4\delta^2} + \delta_{ij} D_d \qquad (4.2.2)$$

where D_{ij} is the hydrodynamic dispersion coefficient tensor, $\overline{V}$ is the average velocity, P_e is the Peclet number ($= L\overline{V}/D_d$ where L is some characteristic length of the pores and D_d is the coefficient of molecular diffusion for the solute in the considered liquid phase), $\overline{V_k}$ and $\overline{V_m}$ are the average velocities in the k-direction and the m-direction, respectively, δ_{ij} is Kroneker's delta and a_{ijkm} is the geometric dispersivity of the porous media which represents the influence of the geometry of the void space. The first term at the right-hand side of this equation represents mechanical dispersion. The equation was derived from a statistical model, composed of a network of interconnected capillary tubes, and is related to the void structure at the micro-level.

As shown in the equation, the hydrodynamic dispersion is a function of the velocity. Figure 4.2.3 shows a schematic representation of the results for a large number of experi-

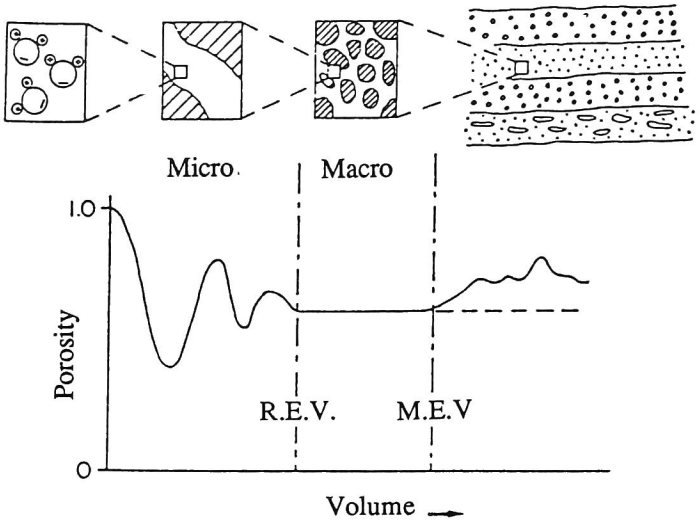


Figure 4.2.1 Concept of the representative elemental volume (after Gillham and Cherry (1982))

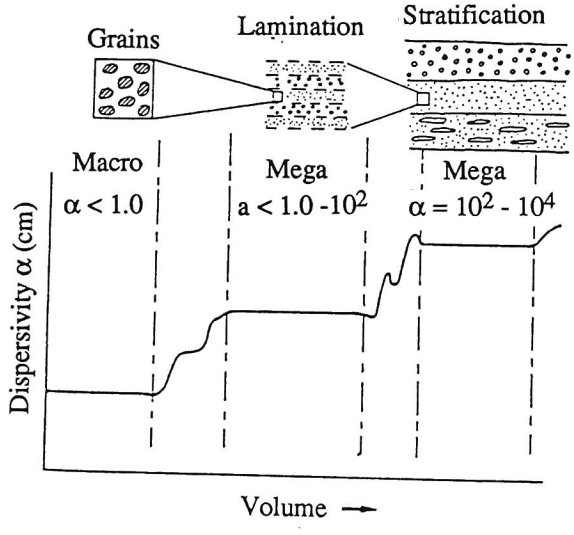


Figure 4.2.2 Concept of the scale effect of the dispersivity (after Gillham and Cherry (1982))

ments on the nonlinear effects of velocity on the hydrodynamic dispersion (Bear (1972)). It is found from this figure that molecular diffusion predominates in the low Peclet number region, and that spreading is caused mainly by mechanical dispersion as the values of the Peclet number grows.

Macro-dispersion has been modeled as a time-dependent matter (Dagan (1984), Gelhar (1987), Rubin (1990), Neuman and Zhang (1990)). Among the various studies, many researchers have used the expression for the spatial covariance of ensemble mean concentrations in a statistically homogeneous random field of mildly fluctuating log hydraulic conductivities. Thus, the expression for macro-dispersivity is based on the fact that the hydraulic conductivity is known at each point in space, while it is difficult as a problem of fact to sufficiently grasp those quantities in a whole region of interest (Jinno (1990)). The exponential covariance of log hydraulic conductivities is assumed in many cases.

While the stochastic models of macro-dispersivity are very effective for interpreting the scale effect of solute transport problems, it is generally difficult to solve the initial and boundary problems of solute transport with a time-dependent dispersion coefficient.

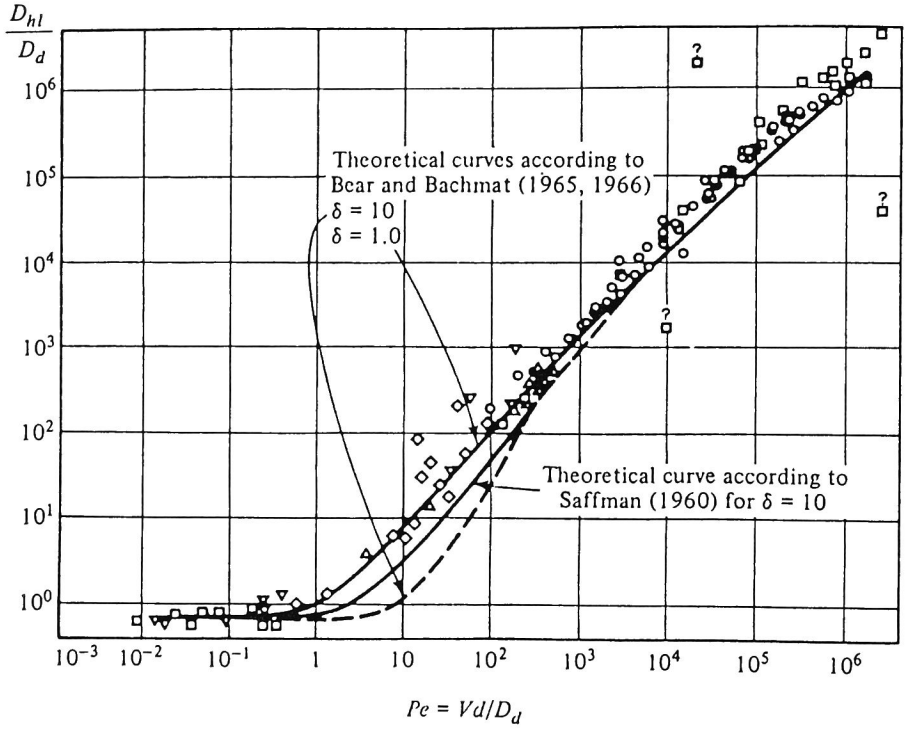


Figure 4.2.3 Relationships between molecular diffusion and convective dispersion (after Pfannkuch (1963), Saffman (1960))

4.3 Two-Dimensional Solute Transport Problem

4.3.1 Introduction

As mentioned in Section 4.1, after making models for the geological structure and the transport phenomena, the transport equation is solved. It is difficult, however, to solve this equation when the velocity is very high. As mentioned in the previous section, many studies have been carried out in an attempt to avoid the oscillation of the solutions in such a situation. Among these studies, the upstream scheme for the finite difference and the finite element methods has been the most widely used for many analyses, although more stable solution methods have been developed, e.g., Eulerian and Lagrangian method. This is probably due to the fact that they can easily be applied to computer programs. In particular, the scheme for the finite element method is simple to apply through use of an asymmetric function as the weighting function.

Firstly, the upstream scheme for the finite element method is introduced in this section and its applicability is discussed. This method has been studied by many researchers and the stability of its solutions has been discussed. It may seem, however, that the applicability of this method to real problems has not been examined well. This is probably because the meaning of the Peclet number in real phenomena does not coincide with that which is an index of the stability of the solutions. When the characteristic length of the medium and the dispersion coefficient in the definition of the Peclet number in real phenomena are defined at the microscopic level, the Peclet number is estimated at a very high value. As a result, this method cannot be applied to real problems. In this section, therefore, the definition of the characteristic length of the medium and the dispersion coefficient at the macroscopic level are discussed along with the definition used in the study on the statistical dispersion coefficient, and the applicability of this method is examined. In addition, it is demonstrated that solutions with the upstream method become

more accurate due to the introduction of a common technique to reduce the numerical dispersion.

Secondly, the Eulerian and Lagrangian method proposed by Neuman (1981) is introduced and then extended to a two-dimensional region. The Eulerian and Lagrangian scheme examined in this section is the one with the continuous forward particle tracking method, which has to obtain the projected values of the concentration changed by the advection during a time interval onto the fixed finite element grid, with which the residual dispersion problem is solved. This projection process may yield numerical errors in the solutions. To extend Neuman's theory to the two-dimensional field, the correct interpolation method has to be developed in the two-dimensional region. After briefly introducing the his theory, the new interpolation method, which considers the velocity direction, will be introduced.

In addition, the finite element approach to calculating the nodal velocity is examined. The velocity is generally obtained for the element from conventional seepage analyses with the finite element method. Hence, it is necessary to project the velocity distribution obtained at each element onto the distribution at each node in order to analyze the transport problem with the Eulerian and Lagrangian scheme. In order to avoid numerical errors in such a interpolation process, the seepage analyses method, in which the velocity is obtained at the nodes, will be introduced and then discussed.

Furthermore, in comparing the Eulerian and Lagrangian method with the method of characteristics, the nature of this method is examined. Finally, the applicability of the Eulerian and Lagrangian method is discussed .

4.3.2 Upstream finite element method

(1) Basic theory

For simplicity, the following general advection-dispersion equation is considered here:

$$\frac{\partial c}{\partial t} + v\frac{\partial c}{\partial x} = D\frac{\partial^2 c}{\partial x^2} \tag{4.3.1}$$

where c is the concentration, v is the velocity and D is the dispersion coefficient. Both v and D are assumed to be constant in this section.

When the standard Galerkin type discretization method is used for the finite element form of equation (4.3.1), the results are similar to those of the central difference approximations (Zienkiewicz and Godbole (1975) and Furuichi (1984)). The central difference expression becomes unstable when mesh size Δx is such that the local Peclet number, P_e ($=v\Delta x/D$) is greater than 2. To overcome such difficulties, it was reported that the upstream (or upwind) finite element method is effective (Heinrich et al. (1977)). This method uses asymmetric functions as weighting functions, W_I, as shown in Figure 4.3.1.

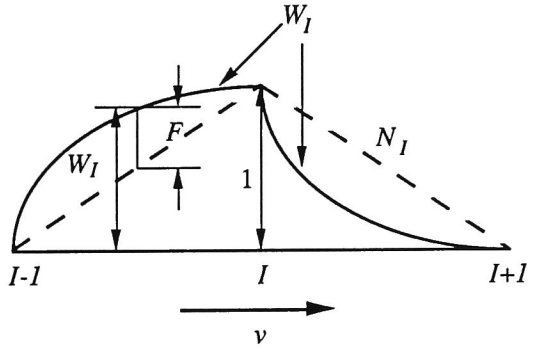


Figure 4.3.1 Shape function (N) and weighting function (W) in a one-dimensional problem

The weighting function of a node I can be written as

$$W_I = N_I \pm \alpha F \tag{4.3.2}$$

where the sign attached to the coefficient, α, is negative for elements between nodes I and $I+1$ and positive for elements between nodes $I-1$ and I. It is evident that when parameter α is set at zero, weighting functions W_I reduce to standard basis function N_I. Consequently, the upstream finite element technique becomes identical to the conventional Galerkin finite element technique.

With local $\xi-$coordinates normalized to a variation from -1 to +1, F is given as

$$F = -\frac{3}{4}\left(\xi^2 - 1\right). \tag{4.3.3}$$

With local x-coordinates varied for 0 to h which is the length of the element, F is written as

$$F = -\frac{3}{h^2}x(x-h). \tag{4.3.4}$$

Using the latter expression, an assembled finite element system for node I is constructed from the steady state of equation (4.3.1) as shown with the following equation (Heinrich et al. (1977)):

$$\left(1+\frac{P_e}{2}(\alpha+1)\right)c_{I-1} - (2 + P_e\alpha)c_I + \left(1 + \frac{P_e}{2}(\alpha - 1)\right)c_{I+1} = 0. \tag{4.3.5}$$

We note immediately that equation (4.3.5) gives a formula identical to that of central difference approximations when α is equal to 0. And, when α is set at between 0 and 1, it gives a form that is a mixture of central and backward differences. This equation is not oscillatory if a = 0, Pe < 2 or

$$P_e \geq 2, \quad \alpha \geq 1 - \frac{2}{P_e}. \tag{4.3.6}$$

In addition, Christie et al. (1976) showed that the error of the difference equation is zero in this one-dimensional problem when

$$\alpha = \left(coth\frac{P_e}{2}\right) - \frac{2}{P_e}. \qquad (4.3.7)$$

On the other hand, the assembled system in the upwinding finite difference scheme is expressed with a form which adds the pseudo-dispersion term to the normal formula (Furuichi (1984)). This is similar to the upstream finite element scheme. Thus, the effective Peclet number decreases due to a large dispersion term induced by a high velocity and a non-zero α.

Furuichi (1984) also proposed an index for the numerical errors occurring from the upstream finite element scheme and indicated the significant effects of the initial value distribution on the numerical errors.

In general, the numerical calculation for the advection-dispersion problem contains the errors between the true solutions and the calculated ones, even if stable solutions are numerically given. These are related to the Peclet number and the Courant number (C_u (= $v\,\Delta t / \Delta x$)). When both the Peclet and the Courant numbers are set at a small value, the numerical solutions are generally close to the true ones. The Peclet number can be reduced by setting Δx at a small value, while the Courant number can be reduced by setting Δx tat a large value and setting Δt at a small value. For example, Figure 4.3.2 shows a comparison of the analytical and numerical solutions obtained from the upstream finite element method under conditions where P_e = 10 and C_u = 1. α, which is given from equation (4.3.7), is 0.8 here. It is found that numerical errors occur even when the solutions are stable.

(2) Applicability of the scheme

(a) Peclet number

As shown in Figure 4.3.2, solutions obtained with the upstream finite element scheme with any α are stable for problems in which P_e is 10 and C_u is 1, while errors between true and numerical solutions occur. As mentioned above, this is related to the Peclet number and the Courant number. The Peclet number discussed here is a local one in which the characteristic length is related to the size of the element.

To solve the general advection-dispersion problem, the dispersion coefficient and the velocity vector distribution are assumed to be known and constant in the integral scale, i.e., an elemental size. In general, the dispersion coefficient and the velocity are the parameters specific to the site, and the representative elementary volume (R.E.V.) is assumed to exist to prescribe such quantities. The integral scale should be larger than the R.E.V. and smaller than the maximum elementary volume (M.E.V.) at the macroscopic level. The local Peclet number for the problem should be determined with the macroscopic dispersion coefficient and velocity in an integral scale. However, a real Peclet number is generally discussed with the expression:

$$P_e = \frac{\overline{u}\, d}{D_d} \tag{4.3.8}$$

where $\overline{u}$ is the average water velocity (= v/n where v is Darcy's velocity and n is the porosity), d is the mean diameter of the grains or the pores and D_d is the coefficient of molecular diffusion.

As in a realistic case, if the values $\overline{u}$ = 0.09 m/hr, d = 2 mm and D = 10^{-9} m^2/sec are used in equation (4.3.8), the Peclet number becomes 50 (de Marsily (1986)). While the Peclet number for the problem shown in Figure 4.3.2 is 10, the upstream finite element method cannot solve the advection-dispersion equation with sufficient accuracy, much less at a Peclet number of 50. Using this equation, the Peclet number is the index of the dispersion-dominated cases or the advection-dominated cases at the micro-level; it is not an appropriate index of the stability of the numerical solutions.

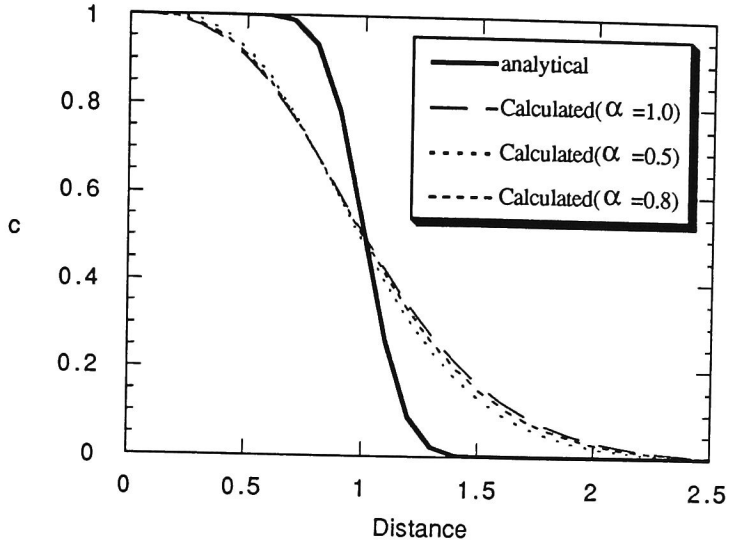


Figure 4.3.2 Concentration distribution at time of 0.01 of the one-dimensional analysis (v=100, D=1.0, Δx=0.1, Δt=0.001, P_e=10, C_u=1)

On the other hand, Neuman et al. (1990) defined the Peclet number in his study on the statistical description of the macroscopic dispersion coefficient as

$$P_e = \frac{\mu L_\mu}{D_l} \tag{4.3.9}$$

where μ is the mean water velocity, L_μ is the length of a radius vector parallel to the μ of an ellipsoid having semiaxes, L_1, L_2 and L_3 which represent the directional integral scale, and D_l is the longitudinal macro-dispersion coefficient.

The characteristic length used in the Peclet number expressed with equation (4.3.9) is an integral scale in which the asymptotic macro-dispersivity is defined. Thus, the Peclet number by equation (4.3.9) can be the index of the stability of the solutions in the analyses.

Neuman et al. (1990) applied his theory on statistical macro-dispersivity to the Borden tracer experiment in Canada (Freyberg (1986)). The characteristic length, L_μ, was obtained as 2.8 m from the work by Sudicky (1986) in his study. Sudicky estimated the L_μ from the correlation length of $ln\ K$. Consequently, the Peclet number at the Borden site in the Neuman's study was estimated to be about 7.8; this value was calculated with parameters μ = 0.091 m/d and D_l = 30.6 m^2/d. While the correlation length of $ln\ K$ has seldom been obtained in a real field, the value of it may be approximately in the order of several meters at a real field. The Peclet number at a real site may hence be estimated at ten-odd from equation (4.3.9).

From the above-mentioned discussion, it is found that the real problem of mass transport on a regional scale does not have such a high Peclet number. The integral scale in the analyses is defined from the real Peclet number, while the mesh size is constrained from the integral scale and the real treatment of input data for the analyses. In the numerical calculations, the integral scale is divided into several elements and the Peclet number in the analyses may be the unit digit. If the problem with the Peclet number of the unit digit is solved accurately, the method can be applied to problems on the regional scale. In the next section, this subject will be addressed.

(b) Applicability

Figure 4.3.3 shows the results with the upstream finite element scheme at Peclet number 5, which is obtained by setting the mesh interval at a half length for the case shown in Figure 4.3.2. The time interval, Δt, is changed to arrange the Courant number in the analyses. It is found from this figure that the numerical solution approaches the analytical one with a decrease in the Courant number, while an error between the numerical and the analytical solutions remains for the case in which the Courant number is 0.1. In addition, the accuracy of the numerical solutions is not improved even if the Courant number is set at a value less than 0.2.

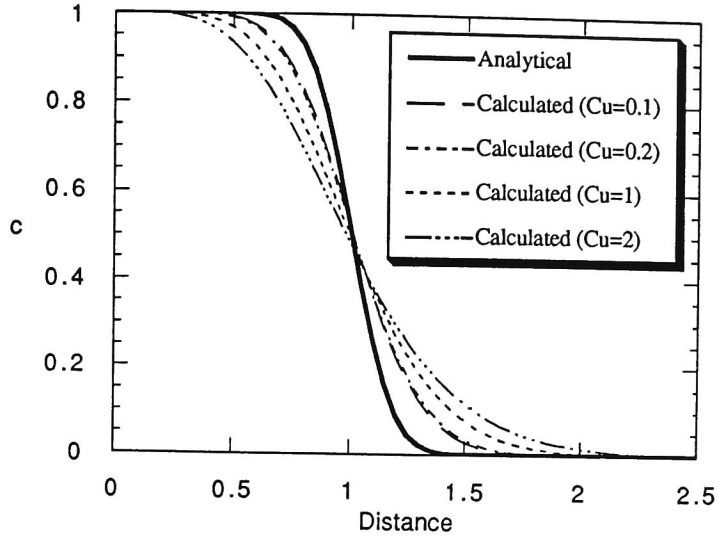


Figure 4.3.3 Concentration distribution at time of 0.01 of the one-dimensional analysis (v=100, D=1.0, Δx=0.05, P_e=5, Δt is changed to arrange the Courant number)

The results shown in Figure 4.3.3 are obtained by setting the upstream weighting factor, α, at a value estimated with equation (4.3.7). The difference among numerical results obtained from different α is small in this problem, as shown in Figure 4.3.2.

One of the reasons for the difference between the numerical and analytical solutions may be numerical dispersion. Mathematically speaking, numerical dispersion is a truncation error resulting from approximating the first derivative, $\partial c/\partial x$.

Let $c = c(x)$ be a sufficiently smooth function so that it can be expanded in the following Taylor series about x :

$$c(x + \Delta x) = c(x) + \Delta x \left.\frac{dc}{dx}\right|_x + \frac{(\Delta x)^2}{2} \left.\frac{d^2c}{dx^2}\right|_x + \frac{(\Delta x)^3}{3} \left.\frac{d^3c}{dx^3}\right|_x + \quad .....(4.3.10)$$

From equation (4.3.10), by dividing by Δx, we obtain

$$\left.\frac{dc}{dx}\right|_x = \frac{c(x+\Delta x) \quad c(x)}{\Delta x} - \frac{(\Delta x)}{2}\left.\frac{d^2c}{dx^2}\right|_x + 0(\Delta x^2) \qquad (4.3.11)$$

where the term $0(\Delta x^2)$ represents the remaining terms in the series, which may be disregarded if Δx is small. On the other hand, the term proportional to the second derivative introduces a numerical dispersion coefficient, $v\Delta x/2$, into the advection-dispersion equation. A common technique to reduce the numerical dispersion is to use $(D - v\Delta x/2)$ as a dispersion coefficient (Bear (1979)).

Introducing this procedure into the upstream finite element scheme, the same problem shown in Figure 4.3.3 is solved. Figure 4.3.4 indicates the results. When α is obtained from equation (4.3.7), i.e., $\alpha = 0.61$, the oscillation of the solution occurs at the upstream of the front, while this modified upstream scheme can simulate an abrupt front shape better than the scheme without the above procedure for numerical dispersion. This oscillation is caused by the large Peclet number induced by the small apparent dispersion coefficient made by the above-mentioned procedure. We can arrange the value of α in order to eliminate the oscillation. The results obtained by setting α at 1 are shown in Figure 4.3.4. A good agreement between the numerical and the analytical solutions is found in the figure.

Figure 4.3.5 shows the results for the same problem as that in Figure 4.3.2 where the Peclet number is 10. It is found that the difference between the numerical and the analytical solutions is small when the modified scheme is used, although an error remains. In reducing the mesh interval to a half length, however, the error becomes very small, as shown in Figure 4.3.4, when using the modified upstream finite element scheme.

From the results mentioned above, it is concluded that the transport problem on a regional scale, in which the Peclet number is about 10, is solved correctly with the upstream finite element scheme by applying a common procedure to reduce the numer-

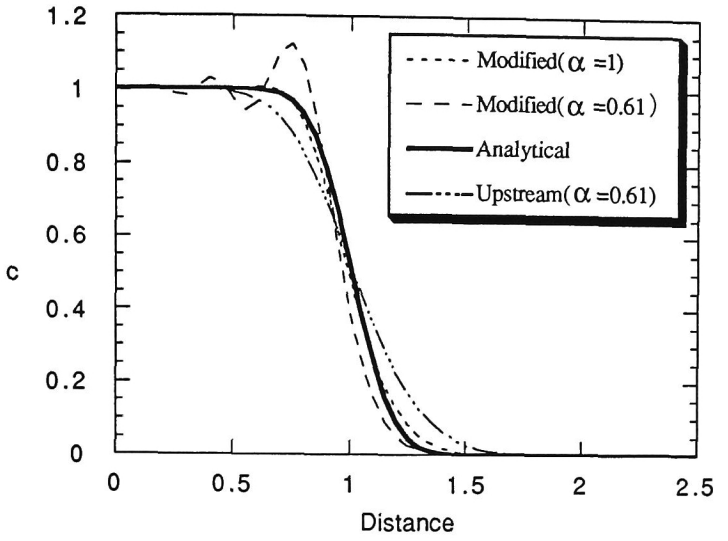


Figure 4.3.4 Concentration distribution at time of 0.01 of the one-dimensional analysis (v=100, D=1.0, Δx=0.05, Δt=0.0005, P_e=5, C_u=0.1), "Modified" means the upstream method using a common technique to reduce the numerical dispersion, and " Upstream" means the convectional upstream method.

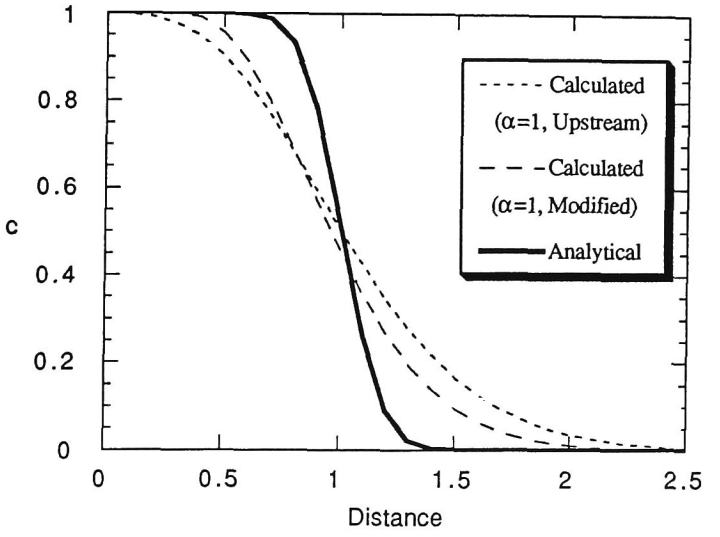


Figure 4.3.5 Concentration distribution at time of 0.01 of the one-dimensional analysis (v=100, D=1.0, Δx=0.1, Δt=0.0001, P_e=10, C_u=0.1), "Modified" means the upstream method using a common technique to reduce the numerical dispersion, and " Upstream" means the convectional upstream method.

ical dispersion. At that time, since an accurate solution is obtained by dividing the integral scale into a few elements, this method is concluded to be very practical.

4.3.3 Two-dimensional Eulerian and Lagrangian scheme

(1) Basic theory

In this section, the basic theory and the numerical approach developed by Neuman (1981) are briefly introduced.

(a) Theory

The general transport equation for the radioactive nuclide is considered here and is written as (Huyakorn and Pinder (1983)) :

$$\theta R_{dl}\frac{\partial c_l}{\partial t} = \nabla\cdot(D\nabla c_l - vc_l) + \sum_{m=1}^{M} \xi_{lm}\theta R_{dm}\lambda_m c_m - \theta R_{dl}\lambda_l c_l + q \qquad (4.3.12)$$

where θ is the volumetric water content, R_d is the retardation factor, c is the concentration (ML^{-3}), D is the dispersion coefficient (L^2T^{-1}), v is Darcy's velocity (LT^{-1}), λ is the decay constant (T^{-1}), ξ_{lm} is the fraction of parent component m transforming into daughter component l, M is the number of parent components transforming into the lth component and q is the rate of the sink/source of the nuclide ($ML^{-3}T^{-1}$). Subscript l means the lth component.

The boundary condition needed to solve equation (4.3.12) is given as

$$c_l(\mathbf{x},0) = c_l^0(\mathbf{x}) \qquad (4.3.13)$$

$$-D\nabla c_l + vc_l + \alpha(c_l - \hat{c}) = \hat{Q} \qquad (4.3.14)$$

where $c_l^0(\mathbf{x})$, $\hat{c}$ and $\hat{Q}$ are known values and $\mathbf{x}$ is the position vector. If $\alpha \to \infty$, equation (4.3.14) is a prescribed concentration condition; if $\alpha = 0$, it is a prescribed mass flux condition.

Since R_d is a positive constant, the following material derivative can be defined as

$$\frac{D}{Dt}(\cdot) = \frac{\partial}{\partial t}(\cdot) + \frac{v}{\theta R_d} \cdot \nabla(\cdot) \quad . \tag{4.3.15}$$

Using this derivative, equation (4.3.12) can be rewritten as

$$qRd\frac{Dc_l}{Dt} = d\cdot(Ddcl) - cld\cdot v + \sum_{m=1}^{M} \xi_{lm}\theta R_{dm}\lambda_m c_m - R_{dl}\lambda_l c_l + q \tag{4.3.16}$$

It should be noted that c_l no longer represents the concentration at a point in the Eulerian coordinates, but rather the concentration of fluid particles moving at a velocity of $v/\theta R_d$. The path line of this particle is described by the above material derivative of $\mathbf{x}$, which leads to the characteristic equation, i.e.,

$$\frac{D\mathbf{x}}{Dt} = \frac{v}{\theta R_d} . \tag{4.3.17}$$

Along with this characteristic curve, each particle is assumed to satisfy the following equation:

$$\frac{D\overline{c_l}}{Dt} = 0 \tag{4.3.18}$$

The $\overline{c_l}$ value of a given fluid particle remains constant along the path line. The concentration in equation (4.3.16) can be broken down into two sets, i.e., $\overline{c_l}$ and $\dot{c}_l$.

The residual concentration, $\dot{c}_l$, must satisfy the following equation obtained by subtracting equation (4.3.18) from equation (4.3.16), in other words,

$$\theta R_{dl}\frac{\partial \dot{c}_l}{\partial t} = \nabla\cdot(D\nabla\dot{c}_l) - \dot{c}_l\nabla\cdot v + \sum_{m=1}^{M} \xi_{lm}\theta R_{dm}\lambda_m c_m - \theta R_{dl}\lambda_l \dot{c}_l + q$$
$$+\nabla\cdot(D\nabla\overline{c_l}) - \overline{c_l}\nabla\cdot v \quad \theta R_{dl}\lambda_l\overline{c_l} \qquad (4.3.19)$$

The total concentration is given as

$$c_l = \dot{c}_l + \overline{c_l}. \qquad (4.3.20)$$

Equation (4.3.18) for concentration $\overline{c_l}$ is subject to the initial condition

$$\overline{c_l}(\mathbf{x},0) = \beta c_l^0(\mathbf{x}) \qquad (4.3.21)$$

and the boundary condition

$$v\overline{c_l} + \alpha(\overline{c_l} - \beta\hat{c}) = \hat{Q} \qquad (4.3.22)$$

where β is the fraction of the initial and the boundary concentration values transferred by advection. If β =1, the initial value of $\dot{c}_l$ is equal to zero. The initial and the boundary conditions for the residual concentration, $\dot{c}_l$, are given by subtracting equations (4.3.13) and (4.3.14) from equations (4.3.21) and (4.3.22), respectively, i.e.,

$$\dot{c}_l(\mathbf{x},0) = (1-\beta)c_l^0(\mathbf{x}) \qquad (4.3.23)$$

and

$$-D\nabla\dot{c}_l + v\dot{c}_l + \alpha\left(\dot{c}_l - (1-\beta)\hat{c}\right) = D\nabla\overline{c_l} \qquad (4.3.24)$$

Since it is necessary to know the value of $\overline{c_l}$ before solving equations (4.3.19), (4.3.23) and (4.3.24), equations (4.3.18), (4.3.21) and (4.3.22) are solved first.

(b) Numerical approach

To apply the above-mentioned theory, the velocity is assumed to be obtained at each node on the grid for the advection analyses. Let's consider any particle p located at point $\mathbf{x}_p$ at time t_k, assigned a $\overline{c_l}$ value equal to $\overline{c_p}$. Let the velocity at point $\mathbf{x}_p$ for the duration of the time interval Δt ($=t_{k+1}-t_k$) be v_p. At the end of the time step, each particle p reaches a new position, namely

$$\mathbf{x}_p^{k+1} = \mathbf{x}_p^k + \frac{v_p}{\theta R_d}\Delta t \qquad (4.3.25)$$

The concentration at $\mathbf{x}_p^{k+1}$ is given by equation (4.3.18) as

$$\overline{c_p^{k+1}} = \overline{c_p^k} \qquad (4.3.26)$$

At this stage, there is a need to project $\overline{c_l}$ onto the nodes, n, of the finite element grid used in the dispersion analyses. Neuman (1981) used the linear interpolation method for the one-dimensional problems and recommended the use of bilinear interpolation to obtain more accurate solutions.

Subtracting the total concentration , c_{ln}^k, at the last time step, $t,^k$ from the concentration obtained from projecting it onto node n, the concentration, $\overline{c_{ln}^{k+1}}$, is calculated for each node.

Equation (4.3.19) is rewritten here as

$$\theta R_d \frac{\partial \dot{c}_l}{\partial t} = \nabla\cdot(D\nabla\dot{c}_l) - f\dot{c}_l + \sum_{m=1}^{M} \xi_{lm}\theta R_{dm}\lambda_m c_m + g + q \qquad (4.3.27)$$

where

$$f = -\nabla \cdot v - \theta R_{dl} \lambda_l \tag{4.3.28}$$

and

$$g = \nabla \cdot (D \nabla \overline{c_l}) + f \overline{c_l} \tag{4.3.29}$$

Equation (4.3.27) is discretized with the Galerkin method as follows:

$$(\mathbf{A} - \mathbf{B} + \mathbf{F})\, \dot{c}_{IJ}^{k+1} + \mathbf{S} \frac{\dot{c}_{IJ}^{k+1} - \dot{c}_{IJ}^{k}}{\Delta t} = \mathbf{Q} \tag{4.3.30}$$

where

$$\mathbf{A}_{IJ} = \int_v N_{I,i} D \dot{N}_{J,j}\, dv \qquad \mathbf{B}_{IJ} = \int_v N_I f \dot{N}_J\, dv ,$$

$$\mathbf{S}_{IJ} = \int_v N_I \theta R_{dl} \dot{N}_J\, dv$$

and

$$\mathbf{Q} = \int_s \left\{ N_I D \left(\dot{N}_{J,j}\, \dot{c}_{IJ} + \overline{N_{J,j}}\, \overline{c_{IJ}} \right) \right\} \mathbf{n}\, ds + \int_v N_I\, q\, dv$$

$$- \int_v N_I \sum_{m=1}^{M} \xi_{lm} \theta R_{dm} \lambda_m c_m dv - \int_v \left(N_{I,i}\, D\, \overline{N_{J,j}} + N_I f \overline{N_J} \right) \overline{c_{IJ}}\, dv \tag{4.3.31}$$

The first term of the force vector, **Q**, means the boundary condition. If α in equation (4.3.24) is set at infinity, **Q** is equal to zero and the prescribed concentration condition is applied. If α is set at zero, the first term of **Q** is written by substituting equation (4.3.24) as follows:

$$\int_{\Gamma} \{N_I D (\dot{N}_{J,j} \dot{c}_{IJ} + \overline{N_{J,j}}\,\overline{c_{IJ}})\}\mathbf{n}\, ds = \int_{\Gamma} \{N_I v \dot{c}_{IJ} \dot{N}_{J,j}\}\mathbf{n}\, ds \quad . \tag{4.3.32}$$

Since the above equation includes an unknown variable, $\dot{c}_I$, this term is added on to the coefficient matrix as **F**, such that

$$\mathbf{F}_{IJ} = -\int_{\Gamma} \{N_I v \dot{c}_{IJ} \dot{N}_{J,j}\}\mathbf{n}\, ds \quad . \tag{4.3.33}$$

In this treatment, a third-type of boundary condition is supposed. If the boundary is the out flow boundary, **F** is set at zero because the particle flowing out does not have any effect on the concentration in the region being analyzed. When the Neuman (second-type) boundary condition is applied, the first term in the right-hand side of equation (4.3.31) is treated as the prescribed flux condition and **F** is set at zero.

Finite differences are used to approximate the time derivative. Since the particle moves along the characteristics during Δt, a backward difference scheme has to be used.

Using the concentration obtained from the above-mentioned finite element method, $\dot{c}_{ln}^{k+1}$, the total concentration on node n at time t^{k+1} is calculated as

$$c_{ln}^{k+1} = \overline{c_{ln}^{k+1}} + \dot{c}_{ln}^{k+1} . \tag{4.3.34}$$

During the above treatment, the mesh for the advection analyses does not have to coincide with the mesh for the dispersion analyses with the finite element method.

Neuman (1981) reported that a more accurate solution was obtained when using the finer mesh for the advection analyses than for the dispersion analyses.

(2) Two-dimensional interpolated method

The above-mentioned Eulerian and Lagrangian scheme needs a projection of the change in concentration brought about by the advection behavior onto the nodes of the finite element mesh with which the dispersion behavior is analyzed. This projection process has a great effect on the accuracy of the solution. Figure 4.3.6 shows a comparison of the results from the linear interpolation method and those from another interpolation method, in which the concentrations on the nodes are obtained by averaging the concentrations of the particles included in a given influence region around the nodes through use of the following equation:

$$\overline{c_{ln}^{k+1}} = \frac{\sum_{p}^{M_p} \left(\overline{c_p^{k+1}} / r_p \right)}{\sum_{p}^{M_p} (1 / r_p)} \qquad (4.3.35)$$

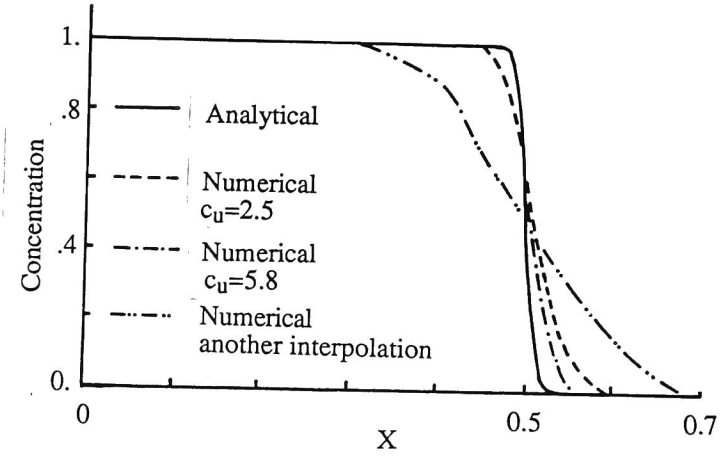


Figure 4.3.6 Comparison of the concentration distributions
" another interpolation" means the results from equation (4.3.35)

where M_p and r_p are the total number of moving particles within the influence region of node n and the distance between node n and a certain moving particle, p, respectively.

These results are related to the one-dimensional problem of solving

$$\frac{\partial c}{\partial t} = D\frac{\partial^2 c}{\partial x^2} - v\frac{\partial c}{\partial x} \qquad \text{on } 0 \le x \le x_R \qquad (4.3.36)$$

subject to

$$c\,(x,0) = 0,$$

$$c\,(0,t) = 1,$$

and

$$c\,(x_R, t) = 0. \qquad (4.3.37)$$

The results are obtained under the conditions that the Peclet number, P_e (= $v\Delta x/ D$), is 200 and the Courant number, C_u, is 5.8. It is found from Figure 4.3.6 that a drastic change in the concentration at the front is not simulated with the other interpolation method and the effects of the interpolation method on the accuracy of the solution are significant.

Concerning the two-dimensional interpolation methods, Fujinawa (1986) used the above-mentioned interpolation method in which $\overline{c_{ln}^{k+1}}$ is obtained by averaging the concentrations of particles within a certain influence region around node n. The area of influence has a great effect on the accuracy of the solution, however, and the criterion for determining this area is not clear. Terawaki (1984) proposed an interpolation method in which linear interpolation is carried out between neighboring nodes. This method is only

effective for rectangular meshes, however, and is difficult to apply to meshes having arbitrary shapes.

In this section, the new interpolation method, which is effective for meshes having arbitrary shapes, is introduced.

Firstly, the nearest solute particles are selected in four quadrants around the principal direction of the velocity on the node, as shown in Figure 4.3.7. Secondly, the three particles nearest to the node are selected among the four particles obtained in each quadrant and then plane, of which the z-direction is the concentration, is made with the three particles in the space between the two-dimensional coordinate and the concentration system, as shown in Figure 4.3.8. Finally, the concentration at the location of the node is calculated from the equation of the plane.

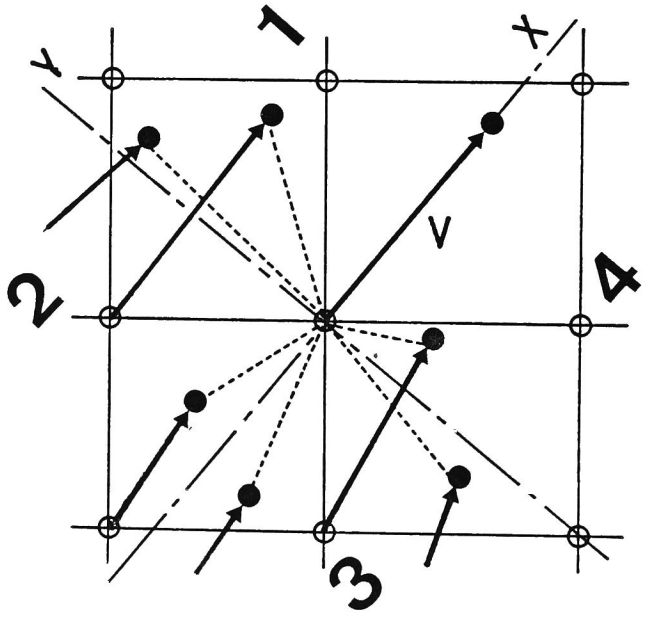


Figure 4.3.7 Schematic representation of the process to find the four representative concentration point around the nodal point

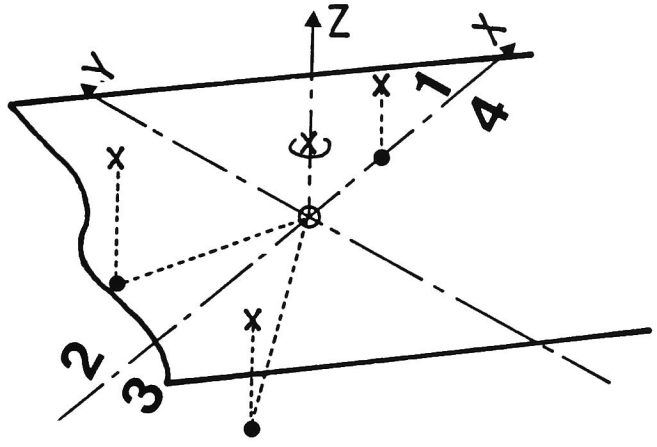


Figure 4.3.8 Schematic representation of concentration plane around the nodal point

The reason for selecting the nearest particles to the four particles obtained in each quadrant around the principal velocity direction is to avoid selecting the particles, which the plane is made, in the biased side of the upward or downward region around the node.

In one-dimensional problems, only two particles are chosen in the upward and downward sides of the node and the plane cannot be made. In such cases, the concentration on the node is obtained from equation (4.3.35) with the concentrations and distances of the two particles. This procedure yields the same results as the linear interpolation method.

It should be noted in this interpolation method that the mesh for the advection analyses does not have to be the same as the mesh used in the dispersion analyses.

(3) Seepage analysis using velocity as an unknown variable

(a) General remarks

As mentioned in the previous section, the Eulerian and Lagrangian method needs the velocity vector on the node. It is common for the velocity vectors to be calculated

for the element, however, when conventional finite element methods are used in the seepage analysis. To obtain the velocity on the node, the proper interpolation method has to be applied to the velocity vector distribution obtained for the elements. If the hydraulic conductivity distribution is heterogeneous, a numerical error may occur in the interpolation process.

The seepage analysis method, using velocity as an unknown variable, is effective for avoiding such a numerical error. The penalty function method, on the other hand, has been used in analyses of viscous fluids, in which velocity is the only unknown variable. However, It is often in the ground water seepage analyses that the boundary condition is given as the prescribed pressure condition, and the validation of the analyses is carried out by comparing the water pressures measured at in-situ sites with the calculated ones. Hence, the method using both velocity and total pressure as unknown variables is examined in this section.

(b) Finite element discretization

The basic equation for the flow of ground water is written as

$$S_s \frac{\partial P}{\partial t} + \frac{\partial v_i}{\partial x_i} = 0 \qquad (4.3.38)$$

where S_s is the specific storage coefficient, p is the total pressure and v_i is Darcy's velocity vector.

On the other hand, the equation of motion is given as the following equation which uses Darcy's law:

$$v_i = -k_{ij}\, p_{,j} \qquad (4.3.39)$$

where k_{ij} is the hydraulic conductivity tensor.

Using the Galerkin method, both equations are discretized. The results are obtained as

$$\begin{bmatrix} \mathbf{A}^x & 0 & \mathbf{B}^x \\ 0 & \mathbf{A}^y & \mathbf{B}^y \\ \Delta t\mathbf{C}^x & \Delta t\mathbf{C}^y & \mathbf{D} \end{bmatrix} \begin{Bmatrix} v_x \\ v_y \\ p \end{Bmatrix} = \begin{Bmatrix} 0 \\ 0 \\ \mathbf{D}p + \mathbf{F} \end{Bmatrix} \tag{4.3.40}$$

where

$$\mathbf{A}^m_{IJ} = \int_v (\overline{N_I}\,\overline{N_J}) dv \quad , \qquad \mathbf{C}^m_{IJ} = \int_v (\dot{N}_{I,m}\,\overline{N_J}) dv \quad ,$$

$$\mathbf{B}^x_{IJ} = \int_v \left(\overline{N_I}\,K_{xx}\,\dot{N}_{J,x} + \overline{N_I}\,K_{xy}\,\dot{N}_{J,y}\right) dv \quad , \qquad \mathbf{B}^y_{IJ} = \int_v \left(\overline{N_I}\,K_{yx}\,\dot{N}_{J,x} + \overline{N_I}\,K_{yy}\,\dot{N}_{J,y}\right) dv \quad ,$$

$$\mathbf{D}_{IJ} = \int_v \left(\dot{N}_I\,S_s\,\dot{N}_J\right) dv \quad , \qquad \mathbf{F}_I = \int_s \left(\dot{N}_I\,\overline{N_J}\,v_{Ji}\,n_i\right) ds \quad ,$$

where V is the elemental volume, S is the surface area of the element, n_i is the normal vector to the surface, $\dot{N}_I$ is the shape function for pressure and $\overline{N_I}$ is the shape function for velocity.

(c) Shape function

When equation (4.3.40) is solved, the pressure works so as to restrain the velocity. This is similar to what happens in the consolidation analysis by Biot's theory, in which the pressure works so as to restrain the deformation occurring through the increase in effective stress. Thus, if the shape function for the pressure is the same as the one for the velocity, the solution is expected to have oscillation because a coupled deformation and seepage analysis using the same shape function for the deformation and pressure has oscillation in the solutions.

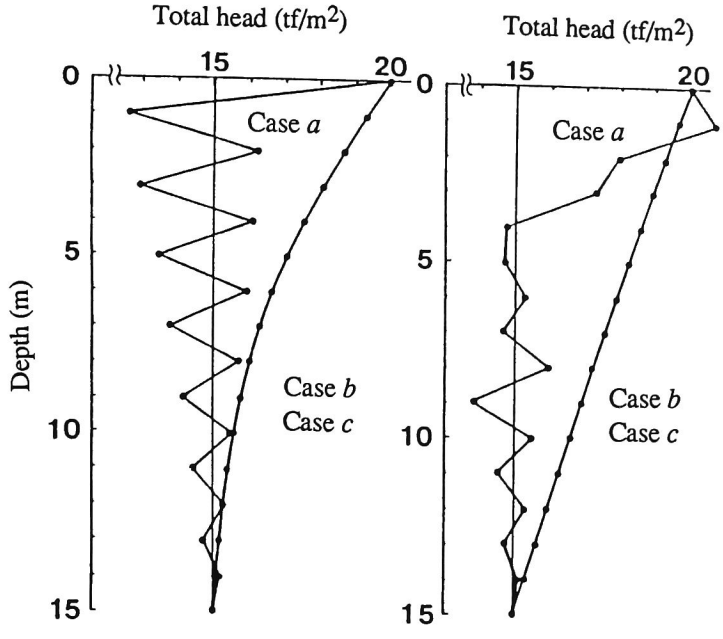
To investigate such a tendency, results by the following three cases are compared: Case *a* where the same linear shape function is used for pressure and velocity, Case *b* where the shape function for the pressure is linear and the shape function for the velocity is quadratic, and Case *c* where the conventional finite element method is used in which the linear shape function is applied. The problem to be solved is the one-dimensional vertical seepage problem whose length is 15 m, initial water table is set at 15 m from the bottom of the region, pressure at the top is fixed at 20 tf/m^2 and pressure at the bottom is fixed at 15 tf/m^2.

Figure 4.3.9 shows comparisons for the total head distributions obtained from the three cases after two time periods of about 10 minutes and one hour from the beginning of the analyses. It is found that the results from Case *a* shows oscillation, while the results from Case *b* do not show oscillation and are almost the same as those from Case *c*. Figure 4.3.10 shows the vertical downward velocity distributions for Cases *b* and *c*. Since the results from Case *a* have oscillation, the results from Case *a* are excluded from Figure 4.3.10. It is found that the results from Cases *b* and *c* agree well.

(d) Conclusions

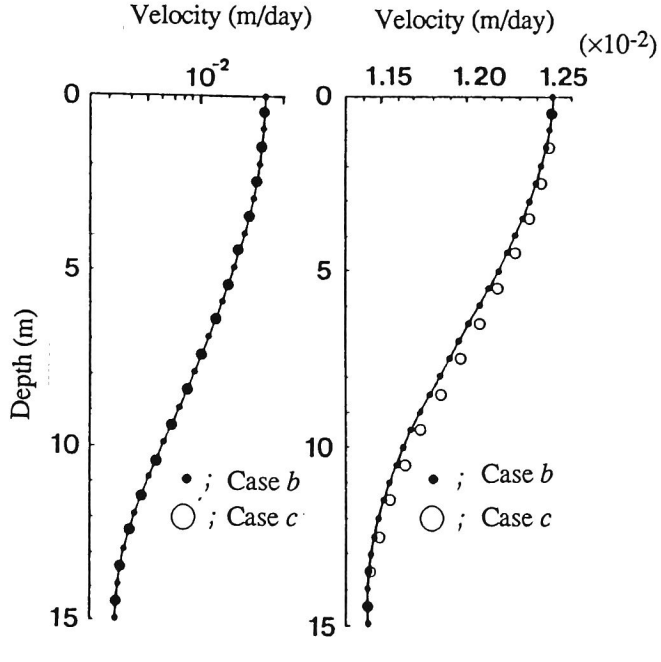
To avoid the numerical error caused by the process which projects the elemental velocities onto the nodal velocities, the seepage analysis method using velocity and pressure as the unknown variables was proposed, and the nature related to the shape functions was examined.

As conclusions, it was found that stable solutions could be obtained from the analysis method using the linear shape function for the pressure and the quadratic shape function for the velocity. And, it was reported in the study by Neuman (1981) that when the mesh used in the advection analysis was finer than the one employed in the dispersion analysis, the solution would be more accurate than the solution from a case in which the meshes were the same. Considering such a tendency, the seepage



(a) Time = 11.5 min. (b) Time = 1.2 hr.

Figure 4.3.9 Comparison of the total head distributions



(a) Time = 11.5 min. (b) Time = 1.2 hr.

Figure 4.3.10 Comparison of the vertical downward velocity distributions

analysis method proposed here is expected to be very effective for the transport analysis with the Eulerian and Lagrangian scheme.

(4) The effects of the Peclet number and the Courant number

Figure 4.3.6 shows the results obtained when applying different Courant numbers. In a general method to solve the advection-dispersion equation, such as equation (4.3.1), it is necessary to set the Courant number at a value smaller than 1 to obtain a stable solution. Using the Eulerian and Lagrangian method, however,, it is found from this figure that the results become more accurate as a larger Courant number is applied and that the Courant number can be set at a value larger than 1.

Figure 4.3.11 shows the results of a two-dimensional problem obtained through use of the interpolation method mentioned in the previous section. The solved model is written as

$$\frac{\partial c}{\partial t} = D_x \frac{\partial^2 c}{\partial x^2} + D_y \frac{\partial^2 c}{\partial y^2} - v_x \frac{\partial c}{\partial x} - v_y \frac{\partial c}{\partial y} \qquad (4.3.41)$$

and is subject to the initial condition

$$c(\mathbf{x},0) = f(x,y)$$

and the boundary condition

$$c(\infty,t) = 0$$

where

$$f(x,y) = g(x)h(y)$$

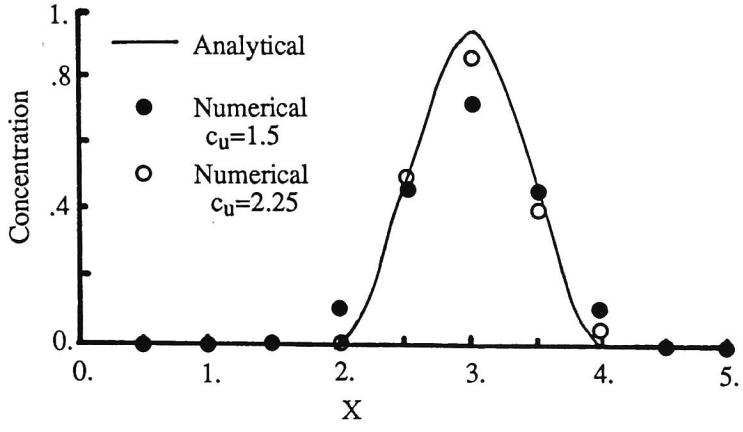


Figure 4.3.11 Comparison of two-dimensional problem
Numerical results are obtained from the Eulerian and Lagrangian method using the proposed interpolation method

$$g(x) = \begin{cases} 1 & ; |x| \le 0.25 \\ 0 & ; |x| > 0.25 \end{cases}, \qquad h(y) = \begin{cases} 1 & ; |y| \le 0.25 \\ 0 & ; |y| > 0.25 \end{cases}.$$

For the analyses, D_x and D_y are set at 0.0025 and v_x and v_y are set at 0.5 and 0, respectively. The calculations are carried out for two types of meshes, in which the mesh intervals in the x-direction are set such that the Peclet numbers in the x-direction become 100 and 66.6. The Courant number in each case is 1.5 and 2.25, respectively. Figure 4.3.11 shows the concentration distribution in the x-direction at t = 4.5. It is also found from the figure that the results obtained when using a large Courant number are more accurate than the results derived from the small Courant number and that the Courant number can be set at a value larger than 1 in the two-dimensional problem.

In this section, the effects of the Peclet and the Courant numbers on the accuracy of the solutions are investigated through use of a one-dimensional problem in which various parameters and meshes are applied. An error in the numerical solutions is obtained from

the root-mean-square of the differences between the numerical and the analytical solutions at a certain time.

Figure 4.3.12 shows the influences of the Peclet number on the relation between the Courant number and the root mean square of the numerical errors. It is found that the numerical errors decrease with an increase in the Courant number and that the numerical errors increase with an increase in the Peclet number.

The white circles in the figure, which represent the results using Courant numbers of 1 and 2.5 when the Peclet number is 12.5, show different tendencies. This is probably because the number of time steps, with which those results are obtained, are 1 and 2, respectively. Hence, it may be concluded that a sufficient number of time steps is needed to obtain accurate solutions, while it is effective for the time intervals to be set at large values in order to apply a large Courant number.

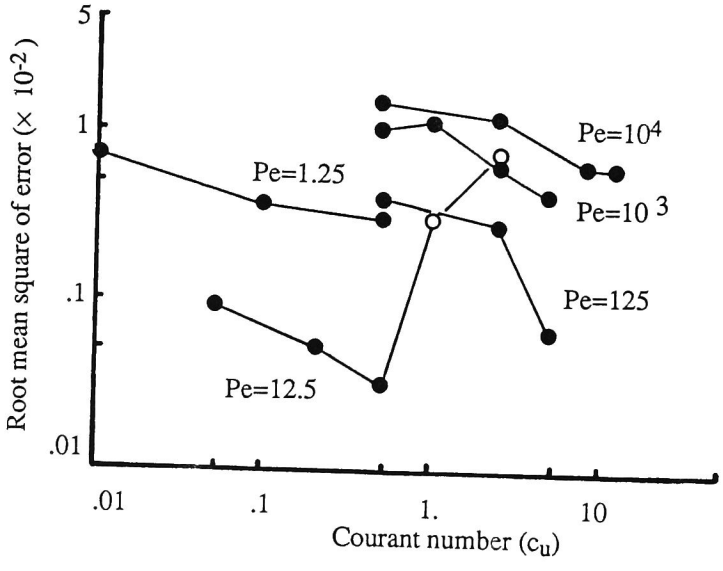


Figure 4.3.12 Influences of the Peclet number on the relationships between the Courant number and the root mean square of the numerical errors

(5) Comparison with conventional characteristics method

Although the Eulerian and Lagrangian method proposed by Neuman is one of the methods of characteristics, the solution process is different from the conventional approach. The method of characteristics is adopted to solve a parabolic transport equation. It is particularly effective when the transport is dominated by convective terms. Such an application has been presented by several researchers, e.g., Garder et al. (1964) and Pinder and Cooper (1970), and applied to the finite difference approach in many cases. In such a conventional method of characteristics, equation (4.3.12) reduces to the following equation along the characteristics:

$$\theta R_{dl}\frac{Dc_l}{Dt} = \nabla\cdot(D\nabla c_l) \quad c_l\nabla\cdot v + \sum_{m=1}^{M} \xi_{lm}\theta R_{dm}\lambda_m c_m - \theta R_{dl}\lambda_l c_l + q \quad . \quad (4.3.42)$$

Although various projection methods from the mesh for advection analyses onto the mesh for dispersion analyses have been studied, the interpolation method mentioned in the previous section is used in this section.

Equation (4.3.42) is solved with an explicit finite difference approximation (Huyakorn and Pinder (1982)) written as

$$\Delta c_{ij}^{k} = \frac{\Delta t}{\theta R_{dl}}\frac{1}{2}\{\ \delta_x\left(D_{xx}\delta_x c^{\dot{k}\text{-}1} + D_{xy}\delta_y c^{\dot{k}\text{-}1}\right) + \delta_y\left(D_{yy}\delta_y c^{\dot{k}\text{-}1} + D_{yx}\delta_x c^{\dot{k}\text{-}1}\right) +$$
$$\delta_x\left(D_{xx}\delta_x\overline{c^{k\text{-}1}} + D_{xy}\delta_y\overline{c^{k\text{-}1}}\right) + \delta_y\left(D_{yy}\delta_y\overline{c^{k\text{-}1}} + D_{yx}\delta_x\overline{c^{k\text{-}1}}\right)\ \}$$
$$+\left\{ -\left(\nabla\cdot v + \theta R_{dl}\lambda_l\right)\frac{c^{\dot{k}\text{-}1} + \overline{c^{k\text{-}1}}}{2} + \sum_{m=1}^{M} \xi_{lm}\theta R_{dm}\lambda_m c_m + q \right\}\frac{\Delta t}{\theta R_{dl}} \quad .(4.3.43)$$

where δ_x and δ_y denote the central difference operators corresponding to $\partial/\partial x$ and $\partial/\partial y$, respectively, and subscripts i and j stand for the grid nodes.

After Δc_{ij}^{k} has been obtained, the final nodal concentrations at time level k are computed from

$$c_{ij}^{k} = \overline{c_{ij}^{k}} + \Delta c_{ij}^{k} \qquad (4.3.44)$$

Instead of solving finite difference equation (4.3.43), the following finite element method is applied, here. Firstly, except for the time derivative term in equation (4.3.43), the concentrations are replaced by

$$c_l = \frac{\dot{c_l^{k-1}} + \overline{c_l^{k}}}{2} \qquad (4.3.45)$$

Then, equation (4.3.43) is solved for unknown variable Δc_{ij}^{k} in the time derivative term. In other words, this method is similar to the finite element scheme with an explicit method for the dispersion analyses.

Comparing equations (4.3.19) and (4.3.43), it is found that the treatment of the concentration in the time derivative term is different. In the conventional method of characteristics approach, since only changes in concentration in the time derivative term are calculated with an explicit method, concentration changes due to the advection behavior during time intervals does not appear in the governing equation. Therefore, it may be concluded that the Eulerian and Lagrangian method by Neuman differs from the conventional method of characteristics in that the concentration is thoroughly separated into $\overline{c_l}$ and $\dot{c_l}$ in the dispersion analyses and that the implicit solving method can be used in the dispersion analyses. Since an implicit solving method can be used, the Eulerian and Lagrangian method can yield more stable solutions than the conventional methods of characteristics.

Figure 4.3.13 shows the results obtained from using the conventional method of characteristics for the two-dimensional problem mentioned in the previous section. Comparing this figure with Figure 4.3.12, the results are mostly the same as those derived by the Eulerian and Lagrangian method, except for a little bit of oscillation observed at the upstream side of the concentration front in Figure 4.3.12. The Peclet

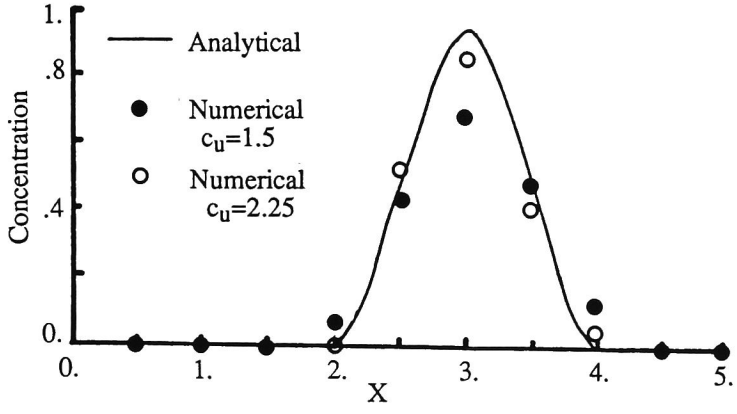


Figure 4.3.13 Comparison of analytical result and numerical result from the convectional method of characteristics

number in this problem is 100. Hence, the effectiveness of the Eulerian and Lagrangian method may be presented for problems in which the Peclet number is over 100.

(6) Discussions

As mentioned above, the Eulerian and Lagrangian method can produce stable and accurate solutions for advection-dispersion problems having a considerably wide range of Peclet numbers. If we solve the problem expressed in equation (4.3.12), this method is very effective and the solutions are reliable. However, a few shortcomings do exist in the Eulerian and Lagrangian method. For example, the interpolation method which makes a projection of the concentration distribution in the coordinates of the advection analyses onto that of the dispersion analyses has a great effect on the solutions. Thus, an accurate interpolation method is needed in cases where the velocity distribution is complex. Furthermore, the interpolation method used to project the velocity distribution onto the nodal values, obtained as the elemental value, may affect the solutions in such fields having a complex distribution of velocity. Numerical errors will occur through such interpolation processes. In this section, to avoid such a numerical error, the interpolation

method of concentration distribution and the seepage analyses method using the velocity as the nodal value were proposed and examined in a two-dimensional region. In other words, such special techniques are needed to use the Eulerian and Lagrangian method.

In addition, this method is difficult to extend to the complex transport model, e.g., the non-equilibrium sorption model and the two-site model, because the material derivative introducing the characteristics uses the positive constant, R_d. It has been observed that the transport phenomena in a small region is too complex to explain with the equilibrium isothermal adsorption model.

4.3.4 Conclusions and discussions

In this section, the two-dimensional transport model was examined. To avoid oscillation in solutions for problems having a large Peclet number, the upstream finite element method and the Eulerian and Lagrangian method were introduced, and the nature and applicability of both methods were discussed.

To examine the applicability of the upstream finite element scheme, the definition of a Peclet number for real phenomena was discussed. Then, the upstream scheme was modified to improve the accuracy of the solutions.

To apply the Eulerian and Lagrangian method to a two-dimensional problem, the interpolation method of concentration distribution and the seepage analysis method, using velocity as the nodal value, were proposed. In addition, the effects of the Peclet number and the Courant number on the accuracy of the solutions were investigated, and the difference between a conventional method of characteristics and the Eulerian and Lagrangian method proposed by Neuman (1981) was discussed.

Conclusions can be summarized as follows:

1) Although stable solutions are obtained for the advection-dispersion problem with the upstream scheme, an error remains between the numerical and the true solutions for problems whose Peclet number is large.

2) The Peclet number of real phenomena should be estimated by the equation proposed by Neuman (1990), of which the characteristic length corresponds to the integral scale in the analyses and the dispersion coefficient is a macroscopic one. Using such a definition, the Peclet number of real phenomena on a regional scale may be in the order of ten-odd.

3) Introducing a common technique to reduce numerical dispersion into the upstream finite element scheme, can improve the accuracy of the solutions, and the upstream finite element scheme can be applied to transport problems on a regional scale.

4) To avoid numerical errors in the Eulerian and Lagrangian method, the interpolation method of concentration distribution and the seepage analysis method, using velocity as the nodal value proposed here, are effective. In other words, such special techniques are needed to use the Eulerian and Lagrangian method.

5) Using the Eulerian and Lagrangian method, numerical errors decrease with an increase in the Courant number, while numerical errors increase with an increase in the Peclet number.

   In addition, a sufficient number of time steps is needed to obtain accurate solutions, while it is effective for the time intervals to be set at a large value in order to apply a large Courant number.

6) The Eulerian and Lagrangian method by Neuman (1981) is different from the conventional method of characteristics in that the concentration is thoroughly separated into $\overline{c_l}$ and $\dot{c}_l$ in the dispersion analyses, and the implicit solving method can be used in the dispersion analyses.

7) The Eulerian and Lagrangian method may be difficult to extend to a complex transport model, e.g., a non-equilibrium sorption model and a two-site model, which are often used for analyzing problems in a small region.

4.4 Transport Problem in Complex Geology

4.4.1 Introduction

In Japan, low level radioactive waste disposal facilities have been planned for shallow underground repositories. It is anticipated, however, that the barrier function of the natural ground will prevent the transport of radionuclide leaking out of the repositories. Moreover, environmental pollution problems related to the contamination of ground water have recently become controversial in Japan, e.g., pollution by agricultural medicines leaking from farms and golf courses and pollution by organic chemical compounds from high-tech plants.

Since a natural shallow ground generally has a very complicated structure, infiltration through such soils may be substantially different from infiltration through relatively homogeneous materials. Solute transport phenomena through such a complex flow field are expected to show intricate concentration distributions of the solute. For example, two peaks in the vertical concentration distribution was observed in field tests related to the high level radionuclide waste disposals by AECL (Melnyk, et al. (1983)), and the vertical distribution of the concentration of fall-out radionuclide in the ground had multi peaks (Morisawa, et al. (1983)).

In a deep geology, many fractures and cracks are expected to exist in a complex way. When flow and solute transport analyses are conducted for a region near a high level radioactive waste repository, the ground must be regarded as a medium having great heterogeneity and anisotropy induced by existing discontinuities. While the flow in a deep geology occurs in a saturated system, the modeling of the flow and the solute transport phenomena in the medium is difficult to create, as are that of the phenomena in a shallow region. It may be a matrix diffusion, flow channeling in a fracture plane and the scale effect of the dispersion coefficient on which the focus is placed for the flow and solute transport phenomena in the fractured rocks at the present time. These subjects are

derived from the fact that a skewness or a tailing of the tracer breakthrough curve, which cannot be explained by a simple one-dimensional Fickian-type model, exists.

To analyze the solute transport phenomena generally, two kinds of modelings are needed. One is the modeling of the geometry of the geological structure and the other is the modeling for the adsorption and diffusion phenomena. They are related to each other depending on the models. It seems, however, that the models for the adsorption behavior are mainly studied for analyses of the phenomena observed in a shallow ground and the modelings of the geological structure are given priority for analyses of the phenomena in a deep geology. Looking at things on a large scale, where each flow path is difficult to identify, the region may be considered as a continuous and relatively homogeneous medium and the adsorption phenomena may be treated as having multi-sites or non-equilibrium isotherm system in order to express the complex concentration distributions and the effluent breakthrough curve. On the contrary, looking at matters on a small scale, where the chemical adsorption phenomena along each flow path are difficult to model, although each flow path can be inferred through use of a stochastic method, the anisotropy and heterogeneity of the ground may be physically modeled and the adsorption phenomena at each phase may be modeled simply. Thus, whether or not the effects of structural heterogeneity and anisotropy on the transport phenomena are expected to be greater than those of the chemical adsorption and the physical diffusion phenomena seems dependent on the model.

In this section, the results obtained from a few types of numerical solute transport models are compared and the nature of the models is examined. Focus is placed on the effect of the heterogeneity of a medium on the effluent breakthrough curve and the concentration distribution in a medium. Firstly, the flow fields are calculated for many samples of a heterogeneous field with a statistical method, and the transport phenomenon is represented as the mean phenomenon through the many flow fields. In this section, such a case is called the heterogeneous model . Sequentially, the breakthrough curve and the concentration distribution obtained from the heterogeneous model are simulated with

continuous homogeneous models, i.e., the double porosity model, the two-site model and the non-equilibrium isothermal model. The results from each model are compared with the results from the heterogeneous model, and the ability of each model to express the results through a heterogeneous field is examined.

4.4.2 Numerical models

(1) General description

Since the phenomena observed in a shallow ground, e.g., multi-peaks of the concentration distribution, cannot be explained by the equilibrium isothermal adsorption model (called the Kd-model in this section), a model which assumes two adsorption sites has been used in the analyses by AECL (Melyk, et al. (1983) and Morisawa (1983)). It is generally difficult, however, to find proper physical meanings for the two adsorption systems. In some cases, one is assumed to be an ion-exchange site and the other is assumed to be an oxyhydroxide site. In other cases, both the adsorptive and the hardly adsorptive solutes are assumed to exist together. It seems, however, that no experiments have ever made the mechanism of the two types of adsorption sites clear, and the theoretical framework has not yet been established. In addition, it should be noted that such adsorption models used in the analyses were not related to the complex geological structure. In other words, the two adsorption site model comprehensively present the phenomena occurring in the field about which the geometric and chemical information is not sufficient. This is probably due to the difficulty of making a detailed model of the geological structure in the ground.

On the contrary, to model the transport phenomena in fractured rock masses, the geometric structure of the fracture networks has firstly been modeled in recent studies (e.g., Long, et al (1989) and Herbert,et.al. (1989)). Then, the simple Kd-model is used for the transport analyses through such an intricate fracture network field. Moreover, for the problem in a single fracture plane, Kobayashi and Yamashita (1989) tried to obtain a

velocity field induced by the heterogeneous aperture distributions before the solute transport analyses with Kd-model. This is probably because the adsorption phenomena in rocks are not well understood and the effects of structural heterogeneity and anisotropy on the transport phenomena are intuitively judged to be great.

As mentioned above, in order to examine the models to explain the skewness and the tailing of the breakthrough curve and the non-smooth concentration distribution in a medium, the models shown in Table 4.4.1 are used in this section.

Table 4.4.1 Models used in the analyses

Model	Remarks
Kd-model	Model used in the heterogeneous model
Double porosity model	Model considering superposing two continua
Non-equilibrium model	Model using a non-equilibrium isothermal adsorption system
Two-site model	Model with two non-equilibrium isothermal adsorption sites

(2) Numerical models

(a) Kd-model

The Kd-model is known as the linear equilibrium isotherm model. It assumes that the adsorption is instantaneous, reversible and linear. This model is given as

$$F = K_d C \qquad (4.4.1)$$

where F is the concentration on a solid surface (= mass of adsorbed component per unit mass of solid), c is the concentration in liquid (= mass of solute per unit volume of liquid) and K_d is called the distribution coefficient.

This model is used for the heterogeneous model.

(b) Double porosity model

This model considers superposing two continua in which one has a highly adsorptive nature and the other has a hardly adsorptive nature. The concept of this model is the same as the one shown in Figure 2.4.1 of Section 2.4. Although the relation between adsorptivity and hydraulic conductivity is not clear, the velocity distributions of both continua are generally different due to the different components of each continuum. For example, the clay stratum generally has a higher adsorptivity and a lower hydraulic conductivity than the sand stratum. Due to the different adsorption processes and velocity distributions, the concentration distributions differ at an unsteady state, and the transport of a solute occurs between both continua through diffusion. The mathematical meaning of this model is the same as that of mobile-immobile and matrix diffusion models, while the diffusion in immobile water and a rock matrix is not considered.

The governing equation for one continuum having a highly adsorptive nature used in these analyses is written as

$$\theta_1 R_{d\,1}\frac{\partial c_1}{\partial t} = \theta_1 D_{1ij}\frac{\partial^2 c_1}{\partial x_i^2} - \theta_1 v_{1i}\frac{\partial c_1}{\partial x_i} - \Gamma \qquad (4.4.2)$$

where θ is the volumetric moisture content, R_d is the retardation factor, c is the concentration, D is the hydrodynamic dispersion coefficient, v_i is the pore water velocity vector and Γ is the solute transport rate between both media. Subscript 1 stands for the continuum having a highly adsorptive nature.

In the same way, the advection-dispersion equation for the other continuum is given as

$$\theta_2 R_{d\,2}\frac{\partial c_2}{\partial t} = \theta_2 D_{2ij}\frac{\partial^2 c_2}{\partial x_i^2} - \theta_2 v_{2i}\frac{\partial c_2}{\partial x_i} + \Gamma \qquad (4.4.3)$$

where subscript 2 stands for the other continuum.

Γ is written as

$$\Gamma = \alpha D_1(c_1 - c_2) \qquad (4.4.4)$$

where α is the non-dimensional coefficient used to adjust the transport rate between the two continua, whose coefficient is related to the geometry of both media.

The total concentration in water is obtained by

$$c_{total} = \frac{\theta_1 c_1 + \theta_2 c_2}{\theta_1 + \theta_2} \qquad (4.4.5)$$

(c) Non-equilibrium model

The model to describe a non-equilibrium state of solute between liquid and solid phases is applied.

The governing equation for mass transport in porous media is written by

$$\frac{\partial}{\partial t}\left(c'\theta + \rho F(1-n)\right) = \frac{\partial}{\partial x_i} D_{ij}\frac{\partial c'}{\partial x_j} - v_i\frac{\partial c'}{\partial x_i} \qquad (4.4.6)$$

where c' is the solute concentration of a liquid phase (i.e., the mass of solute per unit volume of liquid) and F is the solute concentration on a solid phase (i.e., the mass of solute per unit mass of solid).

In the non-equilibrium model used in this investigation, the adsorption is assumed to be represented by the first-order reversible kinetic model. The governing equation for this adsorption model is written by

$$\frac{\partial F}{\partial t} = K_1 c' - K_2 F \qquad (4.4.7)$$

where K_1 and K_2 are constants. The dimensions of K_1 and K_2 are $[L]^3/([T][M])$ and $[T]^{-1}$, respectively.

The solute concentration in the solid is obtained at the equilibrium state from the following:

$$F = \frac{K_1}{K_2} c' \qquad (4.4.8)$$

where K_1/K_2 coincides with distribution coefficient K_d.

(d) Two-site model

A two-site model assumes that the solute adsorbs at two different sites in the soil, e.g., the ion-exchange site and the oxyhydroxide site. At each site, the reversible first-order kinetic model is used to describe the adsorption behavior. The advection-dispersion equation with two adsorption sites in the soil phase is written as

$$\frac{\partial}{\partial t}\left(c'\theta + \rho(F_i + F_o)\,(1-n)\right) = \frac{\partial}{\partial x_i} D_{ij} \frac{\partial c'}{\partial x_j} - v_i \frac{\partial c'}{\partial x_i} \qquad (4.4.9)$$

The adsorption model for one site, e.g., the ion-exchange site, is given by the following equation:

$$\frac{\partial F_i}{\partial t} = K_1 c' - K_2 F_i \qquad (4.4.10)$$

where F_i is the solute concentration adsorbed in the solid phase, and K_1 and K_2 are constants. On the other hand, the adsorption model for the other site, e.g., the oxyhydroxide site, is given by

$$\frac{\partial F_o}{\partial t} = K_1' c' - K_2' F_o \tag{4.4.11}$$

where F_O is the solute concentration adsorbed in the solid phase by the other reaction, and K_1' and K_2' are the first-order rate constants for sorption and release, respectively.

In this approach, if parameters K_1' and K_2' are set at zero, the equation is the same as that of the non-equilibrium sorption model mentioned above.

4.4.3 Results

(1) Heterogeneous model

To represent a heterogeneous field, two kinds of materials are assumed to exist in the field and the distributions of those materials are set randomly. One material has a permeability of 3.6 and a retardation factor of 10, while the other has a permeability of 0.036 and a retardation factor of 50. The dispersivity of both materials is set at 0.3. The unit of the parameter does not have to be specified here. Calculations are carried out for two cases, i.e., Case1 in which the volumetric rate of the more permeable elements is 20% and Case 2 in which the volumetric rate is 50%. The number of elements is 100 (10 x 10) in which the distance between the neighboring nodes is set at 1. Figure 4.4.1 shows a schematic view of the model.

Figure 4.4.2 shows the results of Case 1. In this case, four realizations of the flow field are calculated and the average breakthrough curve is obtained. On the other hand, Figure 4.4.3 indicates the results of Case 2. In this case, six realizations of the flow field

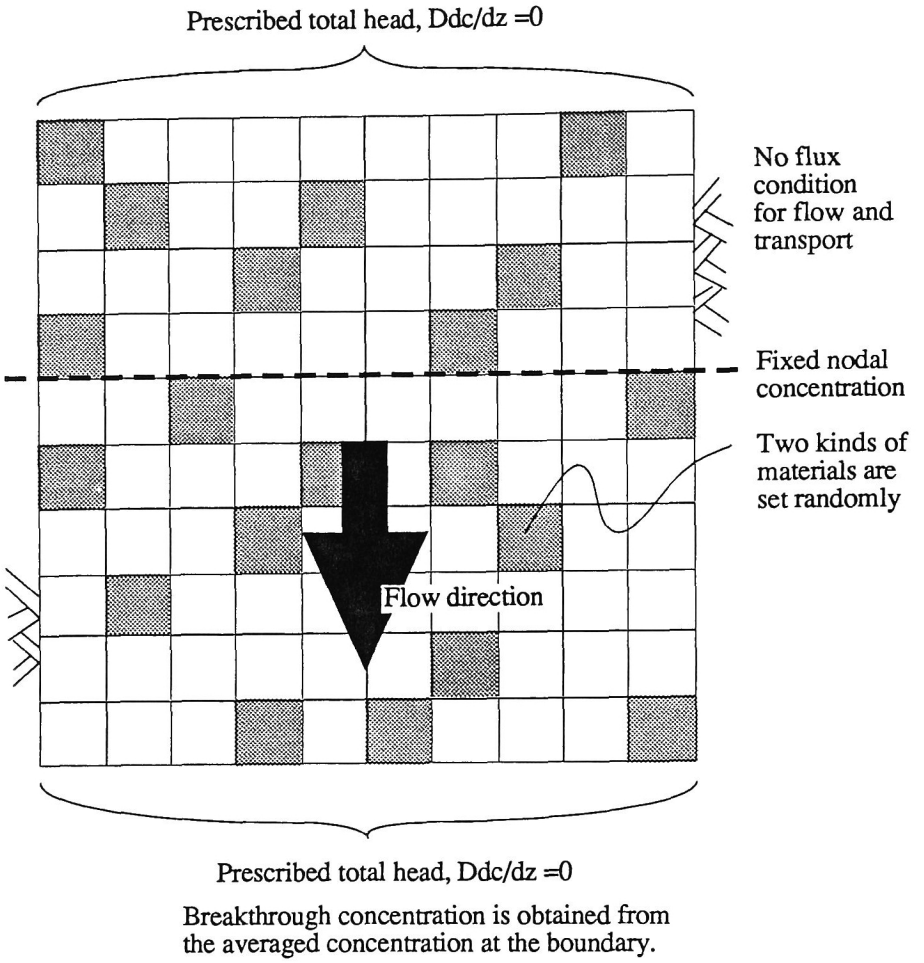


Figure 4.4.1 Schematic view of the heterogeneous model

are calculated and the average breakthrough curve is obtained. For both cases, the hydraulic boundary conditions are set so as to obtain a hydraulic gradient of 0.2 in a one-dimensional way and the steady flow analyses are carried out. The concentration at a distance of 4 from the upward boundary is fixed at 1 during the transport analyses and the breakthrough curve is obtained as the relation between time and the averaged concentration averaged at the downward boundary, as shown in Figure 4.4.1.

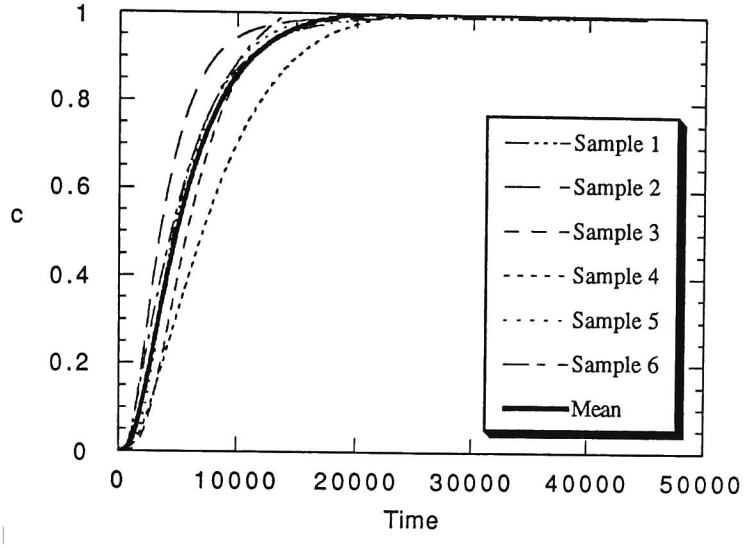


Figure 4.4.2 Breakthrough curves of Case 1 of the heterogeneous model

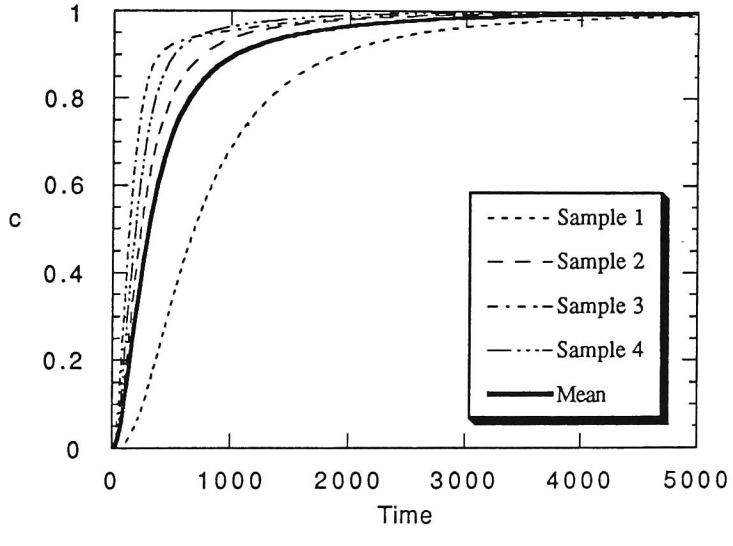


Figure 4.4.3 Breakthrough curves of Case 2 of the heterogeneous model

It is found from Figures 4.4.2 and 4.4.3 that the apparent dispersion of Figure 4.4.2 is less than that of Figure 4.4.3 and that the tailing of Figure 4.4.2 is longer than that of Figure 4.4.3. Namely, the skewness of the breakthrough curve is introduced by a situation in which the volumetric rate of the more permeable and less adsorptive parts is less than that of the impermeable and well adsorptive parts in a medium. The tailing phenomenon is produced by the situation in which the volumetric rate of the more permeable and less adsorptive parts is equal to that of the impermeable and well adsorptive parts in a medium.

Figure 4.4.4 shows the concentration distributions in the flow direction of a realization of Case 1 at a time of about 9×10^3. Figure 4.4.5 shows the concentration distributions at the center of each realization of Case 1 at the same time as Figure 4.4.4. It is found from both figures that the concentration distribution is not smooth. It can be inferred from these figures that the heterogeneity of the ground is one of the reasons why the multi-peaks were observed in the real concentration distribution in the shallow ground.

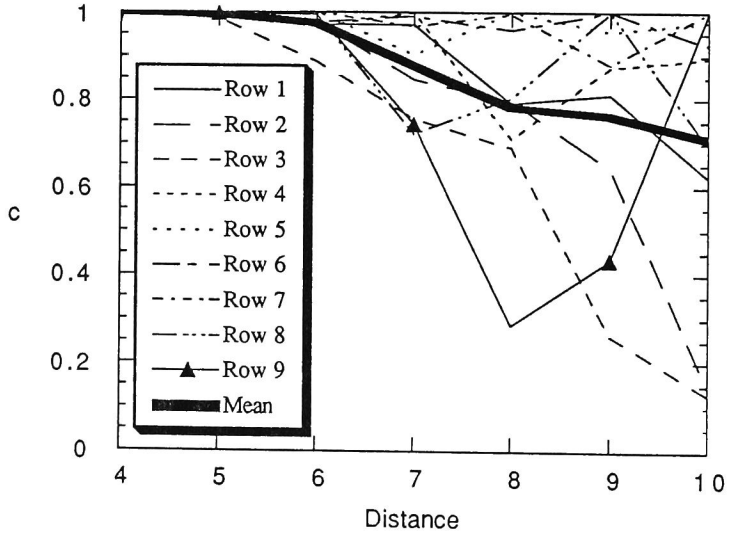


Figure 4.4.4 Concentration distributions in the flow direction of a realization of Case 1 of the heterogeneous model at time of about 9×10^3

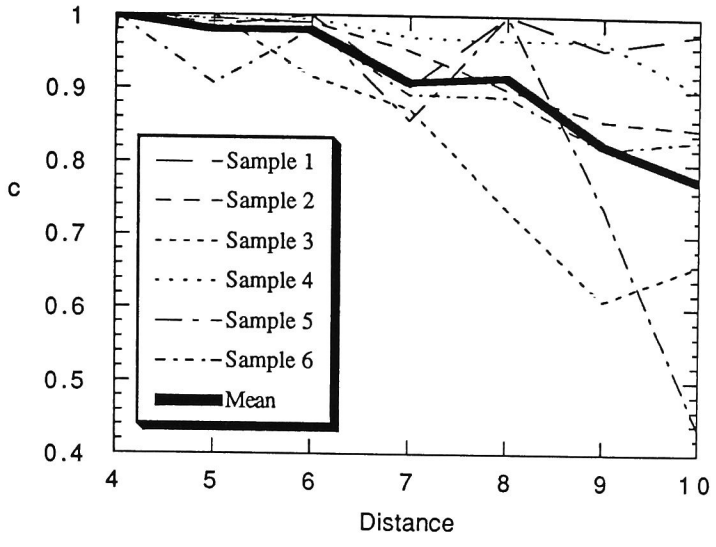


Figure 4.4.5 Concentration distributions at the center of each realization of Case 1 of the heterogeneous model at time of about 9×10^3

(2) Double porosity model

Figure 4.4.6 shows the breakthrough curve obtained from the double porosity model using the same parameters as those of both media in the analyses of the heterogeneous model. The steady velocity of the very permeable medium is assumed at 0.72 due to a permeability of 3.6 and a hydraulic gradient of 0.2, while that of the relatively impermeable medium is 0.0072. Because the total concentration in water is obtained from equation (4.4.5), the concentration prescribed at a distance of 4 from the upward boundary has to be divided into both media. The prescribed concentration in the very permeable medium is assumed to be 0.2, while the prescribed concentration in the relatively impermeable medium is 0.8, since the volumes of those media are divided into the ratio 0.2:0.8 in the heterogeneous model.

Figure 4.4.6 indicates a more rapid rising of the breakthrough curve and a larger apparent dispersion after the initial rising than the results of the heterogeneous models.

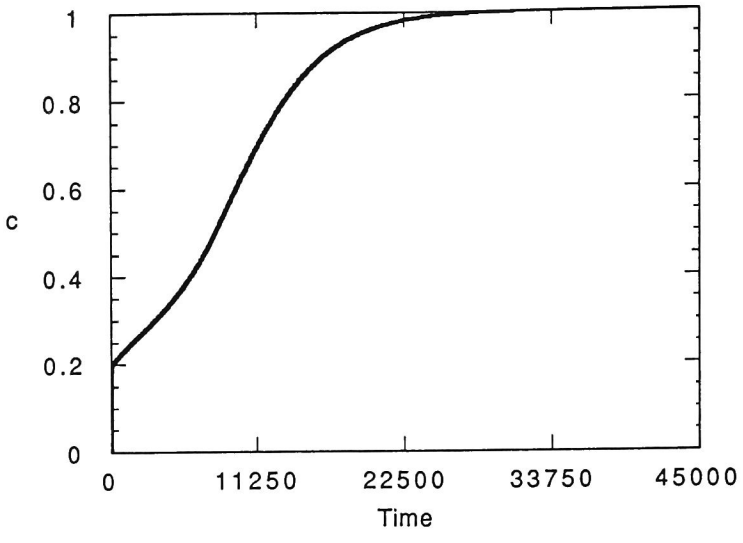


Figure 4.4.6 Breakthrough curve obtained from the double porosity model using the same parameters as those of both media in the analyses of the heterogeneous model

This curve is not continuously smooth, and we can infer from this figure that the two different paths of solute exist in the medium. This kind of non-smooth breakthrough curve is not expressed by the heterogeneous model.

Figure 4.4.7 shows the concentration distribution in the flow direction at the same time as Figures 4.4.4 and 4.4.5. At this time, the solute in the very permeable medium already goes throughout the medium and the concentration of the medium is the same from the inlet point to the downward boundary. Thus, the concentration distribution in the figure is dependent on that of a relatively impermeable medium.

Figure 4.4.8 is the result of an adjustment to the retardation factor of the very permeable medium in order to obtain a continuously smooth curve. The retardation factor used in this analysis is 1200; this is larger than that of a relatively impermeable medium. The tendency toward a higher retardation factor in a fairly permeable geology is inconsistent with the real one.

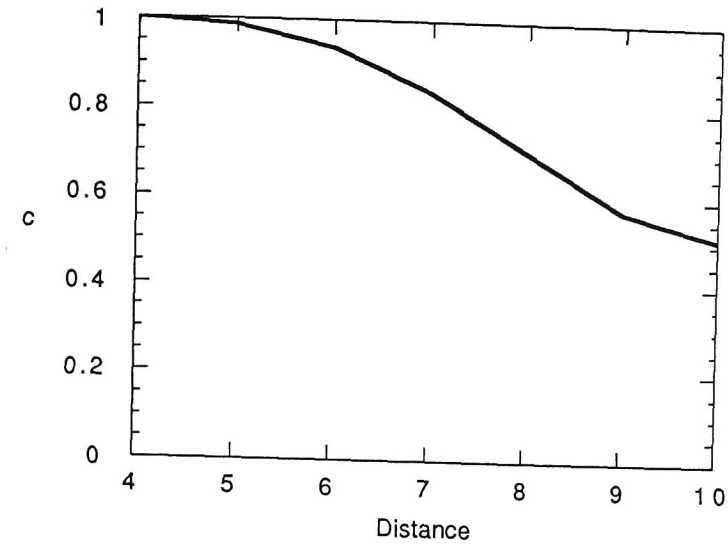


Figure 4.4.7 Concentration distribution in the flow direction of the double porosity model at time of about 9×10^3

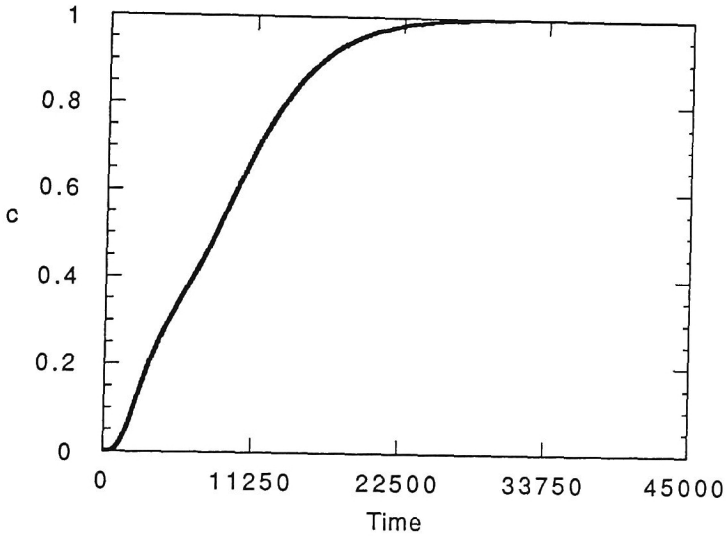


Figure 4.4.8 Breakthrough curve obtained from the adjustment to the retardation factor of the very permeable medium of the double porosity model in order to obtain a continuously smooth curve

The concentration distribution in the flow direction from this analysis is mostly the same as the distribution in Figure 4.4.7 and the non-smooth distribution expressed by the heterogeneous model does not appear in this model.

(3) Two-site model

Although the distribution coefficient coincides with K_1/K_2 at the steady state as shown in equation (4.4.8), the values of both coefficients at an unsteady state generally have to be obtained from parametric studies. For the analysis using a two-site model, the average velocity in the medium is obtained from the volumetric average of both media in the double porosity model, i.e., about 0.36. The dispersivity is the same as that used in the above analyses, i.e., 0.3.

After trial and error, Figure 4.4.9 came to show that the breakthrough curve mostly agrees with the results shown in Figure 4.4.3. At this time, K_1 is 10^{-3}, K_2 is 10^{-6}, K_1' is 10^{-1} and K_2' is 10^{-3}. The tailing phenomenon, such as that shown in Figure 4.4.2, is also indicated in this figure.

Figure 4.4.10 gives the results from a case in which K_1' decreases to 0.05 and the other parameters are set at the same values as those of the parameters used in the analysis shown in Figure 4.4.9. It is found from this figure that a more rapid rising of the curve is expressed here than in Figure 4.4.9. While a similar phenomenon is expressed by the double porosity model shown in Figure 4.4.6, the curve from the two-site model is continuously smooth and a tailing is appeared.

Figure 4.4.11 shows the concentration distribution in the flow direction obtained from the analysis shown in Figure 4.4.9 at the same time as Figure 4.4.4. The distribution is very smooth and a rugged distribution such as that shown in Figure 4.4.5 does not appeared.

(4) Non-equilibrium model

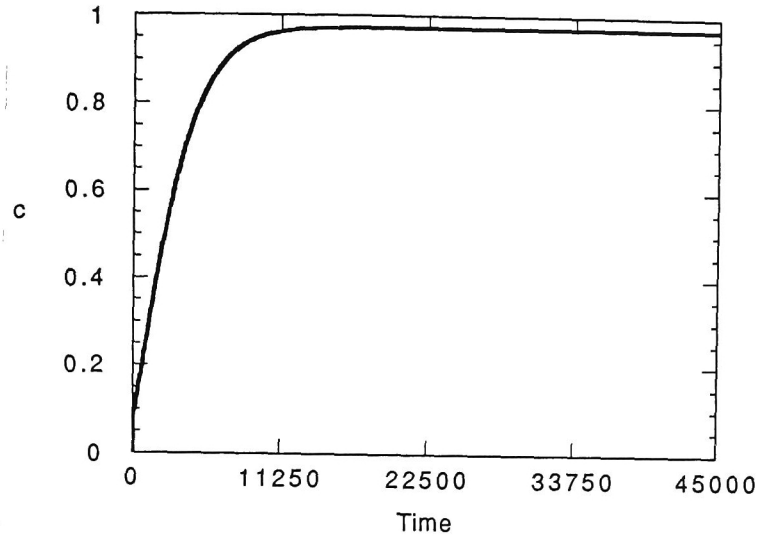


Figure 4.4.9 Breakthrough curve obtained from the two-site model of which $K_1 = 10^{-3}$, $K_2 = 10^{-6}$, $K_1' = 10^{-1}$ and $K_2' = 10^{-3}$

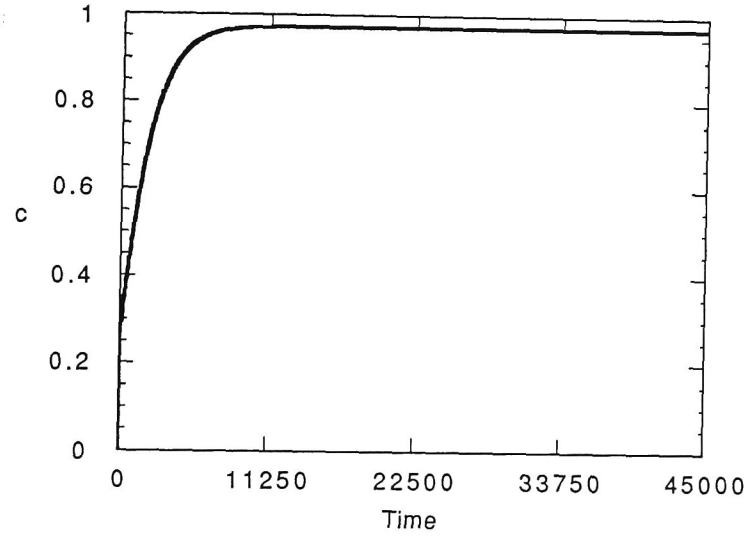


Figure 4.4.10 Breakthrough curve obtained from the two-site model of which $K_1 = 10^{-3}$, $K_2 = 10^{-6}$, $K_1' = 0.05$ and $K_2' = 10^{-3}$

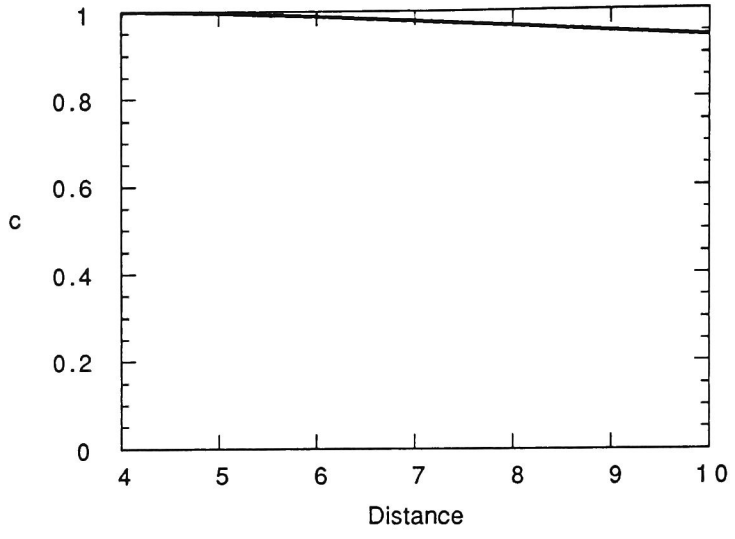


Figure 4.4.11 Concentration distribution obtained from the two-site model of which $K_1 = 10^{-3}$, $K_2 = 10^{-6}$, $K_1' = 10^{-1}$ and $K_2' = 10^{-3}$ at time of about 9×10^3

As mentioned above, the non-equilibrium model coincides with the model in which K_1' and K_2' are set at zero for the two-site model. In other words, one of two retardation systems is nothing in the two-site model. Figure 4.4.12 shows the breakthrough curve from the non-equilibrium model in which K_1 is set at 10^{-1} and K_2 is set at 10^{-3}. This is the same as the curve shown in Figure 4.4.9, except for the tailing. Figure 4.4.9 is obtained from the two-site model in which K_1' is 10^{-3} and K_2' is 10^{-6}. It is found from both figures that the tailing in Figure 4.4.9 is induced by one adsorption mechanism of the two-site model.

Figure 4.4.12 expresses the large apparent dispersion similar to Figure 4.4.3, obtained from the heterogeneous model, of which the volumetric rate of the very permeable and less adsorptive materials are less than those of relatively impermeable and more adsorptive one.

4.4.4 Conclusions

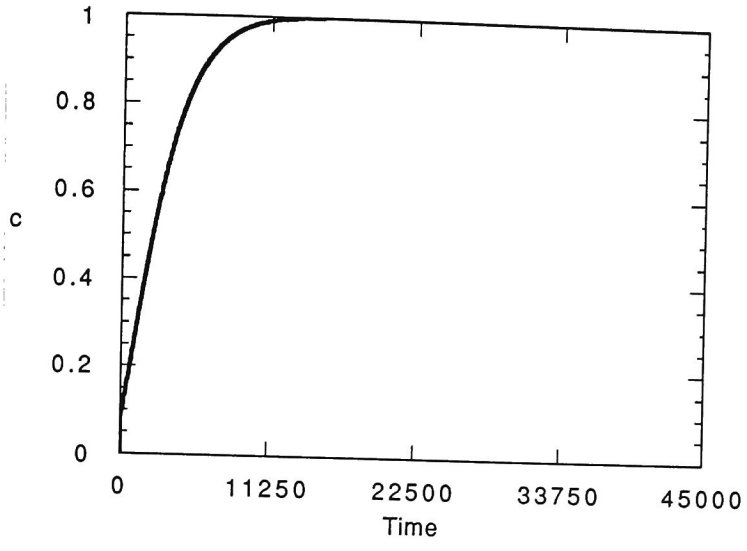


Figure 4.4.12 Breakthrough curve obtained from the non-equilibrium of which $K_1 = 10^{-1}$ and $K_2 = 10^{-3}$

In this section, the effects of geological heterogeneity on the effluent breakthrough curve and solute concentration distribution in a medium were examined by the numerical method. In addition, the ability of the homogeneous model to express phenomena such as the skewness and the tailing of breakthrough curves and the non-smooth concentration distributions in a medium was examined through a comparison of the results of various models.

The conclusions can be summarized as follows:

1) The skewness of a breakthrough curve is introduced by a situation in which the volumetric rate of the more permeable and less adsorptive parts is less than that of the impermeable and very adsorptive parts in a medium. The tailing phenomenon is produced by a situation in which the volumetric rate of the more permeable and less adsorptive parts is equal to that of the impermeable and very adsorptive parts in a medium.

2) The concentration distribution obtained from the heterogeneous field is not smooth. The heterogeneity of the ground may be one of the reasons why the multi-

peaks are observed in the real concentration distribution in a shallow ground. In addition, a non-smooth distribution is difficult to express with the homogeneous models.

3) The double porosity model can express the non-smooth breakthrough curve from which we can definitely infer the existence of two different paths of solute. On the other hand, the breakthrough curve expressed by the heterogeneous model and the two-site and non-equilibrium models is continuously smooth.
4) If a continuously smooth breakthrough curve is simulated by the double porosity model, the values of the parameters may be inconsistent with the real tendency in certain cases.
5) The two-site model can simultaneously express the large apparent dispersion and tailing in the breakthrough curve, although the meaning of the parameters may not be clear.
6) The non-equilibrium model can express the large apparent dispersion similar to that of the heterogeneous model, although the values of the parameters may not have a clear relation to the heterogeneity.

It is found from the above conclusions that various models can explain the large apparent dispersion and the tailing phenomena in a breakthrough curve and that the modelings of the geological structure and adsorption behavior are difficult to divide. Moreover, the non-smooth distribution is not expressed by the homogeneous models, i.e., the double porosity, two-site and non-equilibrium models, for the problem subject to the steady inlet condition of the tracer.

Although these results cannot give the definite solution to understand the mechanism of the phenomena that the rate of the longitudinal spread increases in a non-Fickian fashion with time, it is found that only the geological structure does not have an effect on the phenomena, but the adsorption behavior also have an effect. Numerical models should be based on the observations of the phenomena basically. Thus, the following in-situ investigations are recommended from the results in this section:

1) Whether the adsorption system of the regional scale can be expressed by the Kd-model?

2) How is the relation between the complex adsorption behavior and the heterogeneous geological structure? The adsorption behavior should be modeled for the integral scale.

4.5 Three-Dimensional Transport Model

4.5.1 Introduction

In this section, a three-dimensional transport model for fractured rock masses is introduced. Focus is placed on a relatively large scale problem here. In such a problem, it would seem effective for the relatively large and permeable discontinuities to be explicitly modeled and the others to be implicitly modeled in the adjoining rock block. This is the same way that the seepage analysis model introduced in Section 2.6 of this paper was handled. Based on such a concept, the new three-dimensional transport model is developed.

As discussed in Section 2.6, water leaking from an adjoining rock block to the large fracture has a great effect on the flow in the fracture. Although the conditions and the rate of flow into the fracture are dependent on the site of interest, the water leaking from the rock block is expected to dilute the concentration of a solute in the fracture. It should be noted that this process is different from matrix diffusion at the point at which the solute moves through the small fractures included in the rock block. In general, matrix diffusion is a phenomenon in a rock matrix. This kind of process may be very important for the safety assessment of radioactive waste disposal.

Moreover, this process is considered to be one of the reasons for the tail of the effluent tracer breakthrough curves, which can be observed in many of the field experiments, e.g., Raven, et al. (1988). Adding this mechanism to the matrix diffusion, the model can explain the various phenomena.

4.5.2 Basic theory

As shown by equation (2.6.3) in Section 2.6, the flow rate from the rock block into the fracture per unit volume is obtained by

$$\Gamma = \alpha \frac{k_1 \rho_f}{\mu}(p_1 - p_2) \qquad (4.5.1)$$

where k_1 is the permeability of the primary porosity, i.e., the rock block medium, μ is the dynamic viscosity of water, p is the total head and α is the dimensionless parameter related to the average length in the rock block from the fracture plane and the specific surface of the fractures in the rock block. Subscripts 1 and 2 mean the primary and the secondary fracture media, respectively. If the total head in the rock block is higher than the total head in the fractures, Γ is positive, if not, Γ is negative.

In the model, the solute is assumed to be transported from the fracture to the rock block or vise versa by advection at this flow rate, and the change in the concentration of a medium due to this process is expressed as the source term in the mass transport equation with the following term:

$$Q = \pm \Gamma (c_2 - c_1) \qquad \begin{cases} + \text{ for fracture} \\ - \text{ for rock block} \end{cases} \qquad (4.5.2)$$

where c is the concentration. It is noted that the concentration in a medium is not affected by the effluent solute, and thus, this term is not considered when the water flows out of a medium. In other words, if Γ is positive, and thus, the water flows from the rock block to the fracture, the term Q dose not appear in the governing equation of the rock block, but holds for the fracture medium.

The matrix diffusion is assumed to happen independently of the above process in the model, because the water movement between the fracture and the adjoining rock block occurs through the small cracks included in the rock block and the matrix diffusion is the solute transport through micro pores in the rock matrix. In the model, the interaction between the solute in the rock matrix and the solute in the small cracks in the rock block is assumed to be negligible because of the relatively small contact area. The water flow between the rock block and the fracture is affected by the hydraulic boundary conditions of the region under analysis, while the matrix diffusion is only influenced by the local

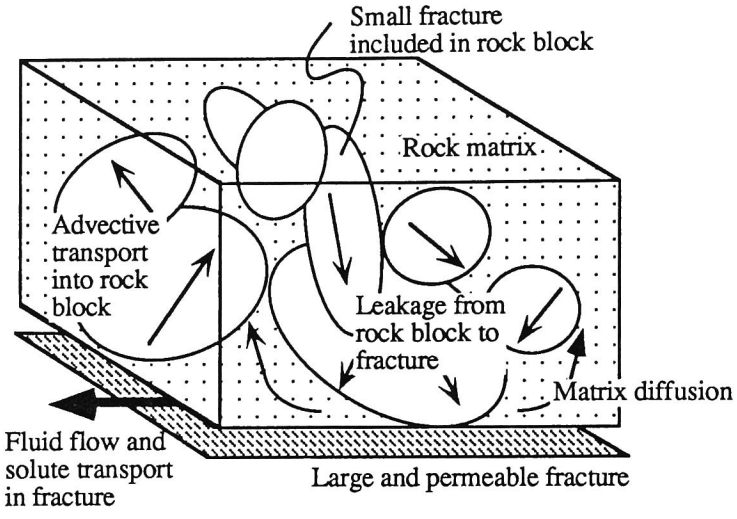


Figure 4.5.1 Schematic view of the model

solute concentration in the fracture. Figure 4.5.1 shows a schematic view of the concept used in the model.

Based on the above concept, the governing equation of the transport problem considering the advective solute transport between the rock block and the fracture is given as

$$\theta_2 R_2 \frac{\partial c_2}{\partial t} - D_{2ij} \frac{\partial^2 c_2}{\partial x_j^2} + v_{2i} \frac{\partial c_2}{\partial x_i} + \Gamma (c_2 - c_1) + \beta (c_2 - c_3) = 0 \tag{4.5.3}$$

$$R_3 \frac{\partial c_3}{\partial t} - \beta (c_2 - c_3) = 0 \tag{4.5.4}$$

$$\theta_1 R_1 \frac{\partial c_1}{\partial t} - D_{1ij} \frac{\partial^2 c_1}{\partial x_j^2} + v_{1i} \frac{\partial c_1}{\partial x_i} - \Gamma (c_2 - c_1) = 0 \tag{4.5.5}$$

where R is the retardation factor, D_{ij} is the dispersion coefficient, v is Darcy's velocity and θ is the volumetric water content. Subscript 3 stands for the rock matrix.

In this model, the fracture is expressed deterministically in the three-dimensional space and is regarded as a relatively large and permeable plane. Thus, equations (4.5.3) and (4.5.4) hold for the fracture plane. In the finite element discretization, the three independent variables, c_1, c_2 and c_3, are obtained for the nodes included in the fracture plane element. The one independent variable, c_1, is calculated for the node included in the rock block solid element, except for the node included in the fracture plane. It is noted that since the fourth terms in equations (4.5.3) and (4.5.5) do not stand simultaneously, as mentioned above, both equations are independent of each other.

In cases where the solid rock block element is not considered in the analysis, for example, a case in which the boundary condition for the transport problem is applied only for the fracture medium and Γ is negative or zero, it is not necessary to solve equation (4.5.5) and the two independent variables, c_2 and c_3 , are obtained. At that time, if the water leaking from the rock block is considered, c_1 is treated as 0 and Γ is positive in equation (4.5.3).

4.5.3 Examples

Some simple examples for the above model are introduced here and the ability of this model is examined. The first example is a case in which only the fracture is considered and the three-dimensional solid element is not treated. The problem is a one-dimensional one wherein the velocity is constant, the boundary conditions for the fracture medium are the prescribed concentration, i.e., c_2 =1 for the inlet boundary and c_2 = 0 for the outlet boundary, and the physical and grid parameters are D_2 = 0.01, v_2 = 0.05, R_2 = 1.0, D_3 = 0.01, R_3 = 1.0, x_o = 2.5 and Δx = 0.05, Δx being the distance between neighboring grid points. The results of the analysis are arranged for the changes in concentration at a distance 1 from the inlet point as a function of time. Figure 4.5.2 shows a schematic view of this problem.

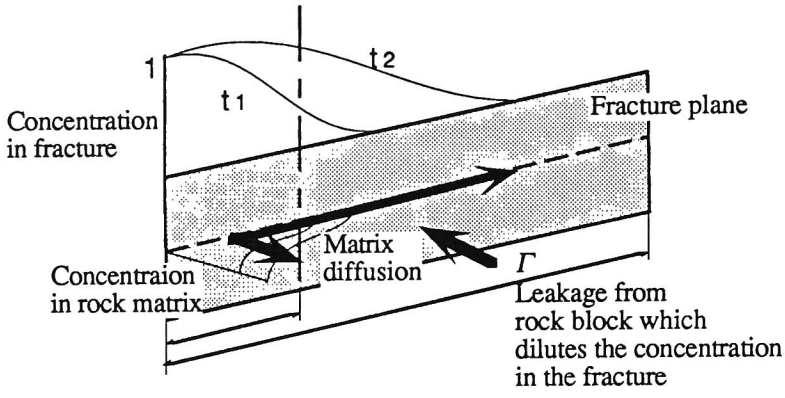


Figure 4.5.2 Schematic view of the first example problem

For comparison, the results from the advection-dispersion model (AD model) and the advection-dispersion with matrix diffusion model (ADM model) are shown together with the results from the advection-dispersion with matrix diffusion and leakage from rock block model (ADML model, i.e., the new model introduced above) in Figure 4.5.3. The ADM model is obtained by setting Γ at zero in the ADML model. The two results from the ADML model are shown in this figure, i.e., the Γ of ADML model 1 is 0.0001 and the Γ of ADML model 2 is 0.001. The results from the AD model can be compared with the analytical solution, while the analytical solution is valid when x_0 is infinite. It is found from the figure that the results agree well with the analytical ones.

It is shown from the figure that the ADM model indicates the skewness and the tailing of the curve and that ADML model 2 indicates more tailing of the curve than the ADM model. On the other hand, the results of ADML model 1 are almost the same as those of the ADM model. The skewness of the ADML model is induced by the dilution due to the water leaking from the rock block to the fracture and the matrix diffusion. As shown in equation (4.5.3),the mathematical effect of Γ on the results of the analysis is the same as for β. Thus, when Γ is small, the water leaking from the rock block does not have much effect on the concentration in the fracture. While Γ is generally obtained from the hydraulic boundary conditions and the location and properties of the fracture, which are

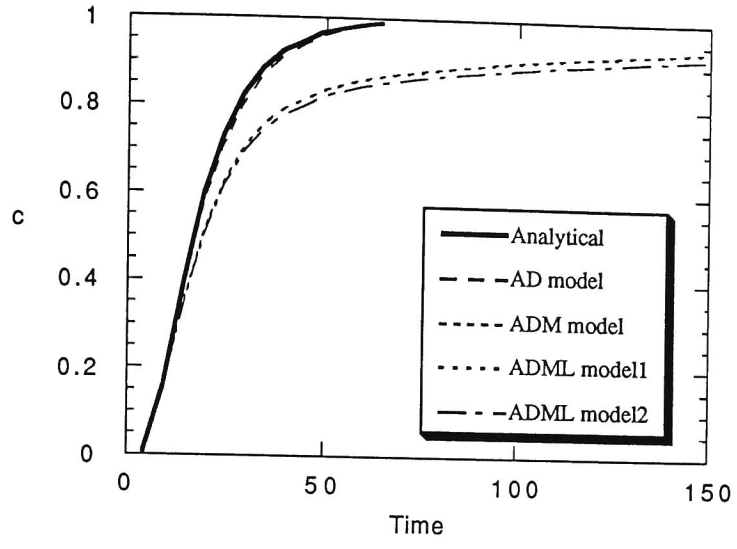


Figure 4.5.3 Comparison of the breakthrough curves
AD model is the advection-dispersion model, ADM model is the advection-dispersion model with matrix diffusion and ADML model is the new model. Γ of ADML model 1 is 0.0001 and Γ of ADML model 2 is 0.001.

generally specific for each site, the parameter related to the matrix diffusion for some geology is very similar at any place.

The second example is a problem with a three-dimensional solid element of which one side has a fracture plane element, as shown in Figure 4.5.4. The velocity in the fracture, v_2, is 0.05 and the velocity in the rock block, v_1, is 0.005. The retardation factor and dispersion coefficient of the fracture, rock matrix and rock block are the same as those in the previous problem. Γ is set at 0.001. Figure 4.5.4 shows a schematic view of the phenomena considered in the problem.

Figure 4.5.5 shows the results of the concentration distribution at time 9.27. The results of the rock block and the fracture can be compared with the analytical results, which are valid when x_0 is infinite. While the numerical results of the rock block agree well with the analytical ones, the numerical results of the fracture are smaller than the analytical ones. This is due to the matrix diffusion and dilution by leakage from the rock

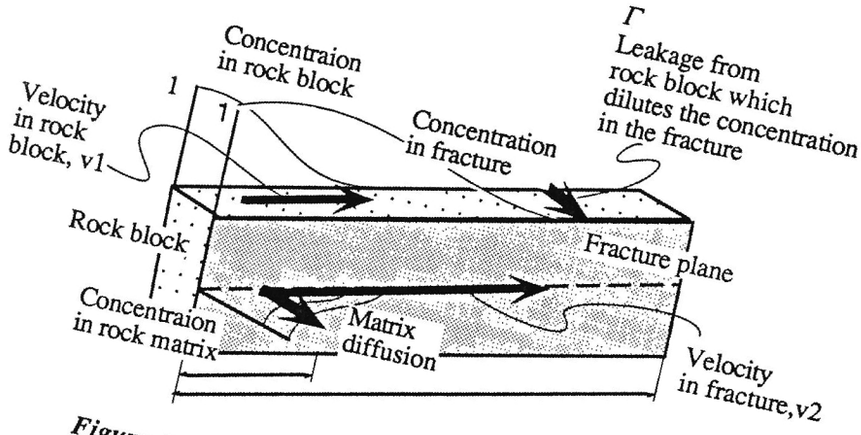


Figure 4.5.4 Schematic view of the second example

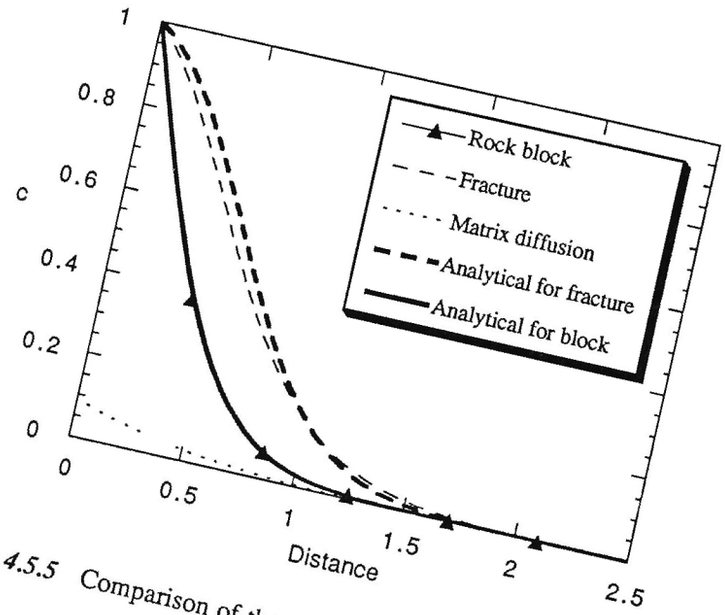


Figure 4.5.5 Comparison of the concentration distributions at time 9.27.

block. In this case, Γ is positive and the concentration of the rock block is independent of that of the fracture.

Table 4.5.1 shows a comparison among the concentrations of the rock block, the fracture and the rock matrix at a distance of 1 from the inlet boundary at time 24.27. Three cases in which Γ is negative, Γ is zero and Γ is positive are shown in the table.

Table 4.5.1 Comparison of concentrations at distance of 1 at time 24.27

Cases	Rock block	Fracture	Rock matrix
Γ is -0.001	0.178	0.625	0.650
Γ is zero	0.189	0.625	0.650
Γ is +0.001	0.189	0.621	0.646

When Γ is positive, the concentration of the fracture is diluted by the water leaking from the rock block to the fracture and the concentration of the rock block is the same as in the analytical solution, as shown in Figure 4.5.5. When Γ is zero, the concentrations of the fracture are the same as the analytical ones, as shown in Figure 4.5.3 (ADM model). When Γ is negative, the concentrations of the fracture and the rock matrix are the same as those in cases where Γ is zero. The concentration of the rock block is smaller than that in cases where Γ is zero and positive. Namely, when Γ is positive, the effect of the water leaking from the rock block is not given to the concentration in the rock block medium and the transport behavior in the rock block is the same as for the ordinary advection-dispersion phenomenon. When Γ is negative, the effect of the water leaking from the fracture to the rock block is not given to the concentration in the fracture medium and the transport behavior in the fracture is the same as for the ordinary advection-dispersion phenomenon with the matrix diffusion.

Based on this concept, the behavior in the rock block can be considered separately from the behavior in the fracture medium. In general, since the sign of Γ is determined

from the hydraulic boundary conditions and the locations and properties of the fractures, however, the phenomena in both media are difficult to consider separately.

4.5.4 Conclusions

In this section, a new three-dimensional transport model was introduced and the ability of the model was examined. This model considers the effect of the water leaking from the rock block to the fracture, based on the concept that large and permeable discontinuities should be explicitly expressed as plane fractures and that other small cracks are included implicitly in the rock block surrounding the fracture planes. The leakage from the rock block occurs through the small cracks in it. The solute transport from the fracture to the rock block is assumed to be advective along the leakage.

The matrix diffusion is considered independently of the above process because the diffusion is assumed to occur through the micro pores in the rock matrix constituting the rock block. This concept is based on the assumption that the hydraulic interaction between the small cracks and the rock matrix in the rock block is negligible.

The dispersion coefficient of the rock matrix is basically the same if the geology is the same. On the other hand, the transport properties of the rock block are very heterogeneous and anisotropically specify for each site. Using this new model, therefore, the large skewness in the breakthrough curve may be logically expressed. In addition, when the direction of the leakage is one way for a whole region, the transport phenomenon in the rock block is treated independently of the phenomenon in the fracture. This may help to understand the phenomena conceptually.

REFERENCES

Aris,R.:On the Dispersion of a Solute in a Fluid Flowing through a Tube, Proc. Roy. Soc. A, 235, pp.67-77, (1956)

Bear, J. and Y. Bachmat: A Generalized Theory on Hydrodynamic Dispersion in Porous Media, I. A. S. H. Symp. of Artificial Recharge and Management of Aquifers. Haifa, Israel, IASH, P. N. 72, pp. 7-16, (1967)

Bear, J.: Hydraulics of Groundwater, McGraw-Hill, (1979)

Bear, J: Dynamics of Fluids in Porous Media, American Elsevier, (1972)

Christie. I, Griffiths, D. F. A.R.Mitchell and Zienkiewicz. O. C, `Finite element methods for second order differential equations with significant first derivatives`, Int. J. num. Meth. Engng, 10, pp. 1389-1396 (1976)

Dagan, G.: Solute transport in heterogeneous porous formation, J. Fluid Mech., 145, pp.151-177, (1984)

de Marsily, G: Quantitative hydrogeology Groundwater hydrology for engineers, Academic Press, Inc., (1986)

Freyberg, D.L.A.: A natural gradient experiment for solute transport in a sand aquifer, 2, Spatial moments and the advection and dispersion of nonreactive tracers, Water Resour. Res., 22(13), pp.2031-2046, (1986)

Fujinawa, K.: A 'Characteristic' finite element method for dispersion-convection equation, J. Japanese Assoc. Groundwater Hydrology, Vol.25, No.2, pp.93-108, (1983)

Furuichi, T: Study on the numerical simulation and analysis method of advection-dispersion phenomena (in Japanese), Doctoral dissertation, Kyoto University, (1984)

Garder, A. O., D. W. Peaceman and A. L. Pozzi, Jr.: Numerical calculations of multidimensional miscible displacement by the method of characteristics, Soc. Petrol. Engin.Jour., 4, pp.26-36, (1964)

Gelhar, L.W.: Stochastic subsurface hydrology from theory to application, Water Resour. Res., Vol. 22, No. 9, pp.135S-145S, (1986)

Gillham,R.W.,J.A.Cherry:Contaminant Migration in Saturated Unconsolidated Geologic Deposits Recent Trends in Hydrogeology,ed. by T. N. Narasimhan, Geolog. Soc. Amer, pp. 31-62, (1982)

Heinrich, J. C. et al.: An `Upwinding` Finite Element Scheme for Two-Dimensional Convective-Transport Equation, Int. J. num. Meth. Engng., 11, pp.131-143, (1977)

Heinrich,J.C.,O.C.Zienkiewicz:An upwind finite element scheme for two-dimensional transport equation,Int.Jour.Num.Meth.Engin.,11,pp.131-143,(1977)

Herbert, A.W. and J.E. Gale: Fracture flow modeling of the test site characterization and validation area in the Stripa mine - Draft - , Stripa symp., Stockholm, (1989).

Huyakorn, P.S. and G.F. Pinder: Computational methods in subsurface flow, Academic Press, (1983)

Jinno, K.: Analysis of groundwater pollution and monitoring method (in Japanese), The 26th Summer Seminar on Hydraulic Engineering, Course A, pp.A-6-1-A-6-25, (1990)

Karasaki, K.: A new advection-dispersion code for calculating transport in fracture networks, LBL Report, (1988)

Kobayashi, A. and R. Yamashita: Preliminary results on Case9 -By using the non-uniform velocity distribution -, The third INTRAVAL Workshop, Stockholm, (1989)

Long, J.C.S., K. Karasaki, A. Davey, J. Peterson, M. Landsfeld, J. Kemeny and S. Martel: Preliminary prediction of inflow into the D-holes at the Stripa mine, Stripa symp., Stokholm, (1989)

Matheron,G., G.DE Marsily : Is Transport in Porous Media Always Diffusive? A Counterexample, Water Resour. Res., 16, No.5, pp.901-917, (1980)

Melnyk, T.W.,F.B. Walton and L.H. Johnson: High-level waste glass field burial field burial tests at CRNL: The effect of geochemical kinetics on the release and migration of fission products in a sandy aquifer, AECL-6836, (1983)

Morisawa, S.,Y. Inoue, H. Kamada and S. Uchida: Prediction of fallout Strontium-90 transport and vertical profile in layered aerated zone (in Japanese), Journal of the Atomic Energy Society of Japan, Vol.25 No.12, pp.70-84, (1983)

Neuman, S.P. and Y.-K. Zhang: A quasi-linear theory of non-Fickian and Fickian subsurface dispersion 1. Theoretical analysis with application to isotropic media, Water Resour. Res., Vol. 26, No. 5, pp. 887-902, (1990)

Neuman, S.P.: Computer prediction of subsurface radionuclide transport -- An adaptive numerical method, NUREG/CR-3076, RW, (1983)

Neuman,S.P., S.Sorek: Eulerian-lagrangian methods for advection-dispersion, Finite-Elements in Water Resources,Proc.4th Intern.Conf.in Hannover, Germany, K. P. Holz, U. Meissner, W. Zielke, C. A. Brebbia, G. F. Pinder, W. G. Gray, editors, Springer Verlag, Berlin, 14.41-14.68,(1982)

Neuman,S.P.:A Eulerian-lagrangian numerical scheme for the dispersion-convection equation using conjugate space-time grids, Jour. Comp. Phys., 41(2), pp.270-294, (1981)

O'Neill,K.:Highly efficient,oscillation free solution of the transport equation over long times and large spaces,Water Resour. Res., 17(6), pp.1665-1675,(1981)

Peaudecerf, G. and J.-P. Sauty: Application of a mathematical model to the characterization of dispersion effects on groundwater quality, Prog. Water Technol., 10, pp.443-454, (1978)

Pinder, G.F. and Cooper, H.H., Jr.: A numerical technique for calculating the transient position of the salt water front, Water Resour. Res., Vol. 6, No. 3, pp.875-882, (1970)

Price,H.S.,J.C.Cavendish and R.S.Varga:Numerical methods of higher-order accuracy for diffusion-convection equations, Soc. Petrol. Engin. Jour., 8,pp.293-300,(1968)

Raven, K.G., K.S. Novakowski and P. A. Lapcevic: Interpretation of Field Tracer Tests of a Single Fracture Using Transient Solute Storage Model, Water Resour. Res., Vol. 24, No. 12, pp.2019-2032, (1988)

Rubin, Y.: Stochastic modeling of macrodispersion in heterogeneous porous media, Water Resour. Res., Vol. 26, No.1, pp.133-141, (1990)

Saffman, P. G,. A theory of dispersion in a porous medium, J. Fluid Mech. No.3, 6, pp. 321-349, (1959)

Scheidegger, A. E., Statistical hydrodynamics in porous media, J. Appl. Phys. No.25, pp. 994-1001, (1954)

Scheidegger, A.E.: General theory of dispersion in porous media, J. Geophys. Res., 66, pp.3273-3278, (1961)

Shamir,U.,D.R.F.Harleman:Numerical solutions for dispersion in porous mediums, Water Resour. Res., 3,pp.557-581, (1967)

Sudicky, E.A.: A natural experiment on solute transport in a sand aquifer: Spatial variability of hydraulic conductivity and its role in the dispersion process, Water Resour. Res., Vol. 22, No. 13, pp.2069-2082, (1986)

Tang, D.H., F.W. Schwartz and L.Smith: Stochastic modeling of mass transport in a random velocity field, Water Resour. Res., Vol. 18, No. 2, pp. 231-244, (1982)

Taylor,G.I.:Dispersion of Soluble Matter in Solvent Flowing Slowly through a Tube, Proc. Roy. Soc. A, 219, pp.186-203, (1953)

Terawaki, M.: Fundamental study on the seepage flow and contaminant transport in a saturated fractured rocks - Numerical analyses using a finite element penalty method and two-dimensional Eulerian and Lagrangian method - (in Japanese), Master Thesis of Kyoto University, (1984)

Yamashita, R. and H. Kimura: Mass transport analysis for fracture networks considering matrix diffusion, Proc. of JSCE, No.412/III-12, pp.69-77, (1989)

Zhang, Y.-K. and S.P. Neuman: A quasi-linear theory of non-Fickian and Fickian subsurface dispersion, 2, Application to anisotropic media and the Borden site, Water Resour. Res., Vol. 26, No.5, pp.903-913, (1990)

Zienkiewicz. O. C. and Godbole. P.N. 'Viscous incompressible flow with special reference to non-Newtonian (plastic) fluids', Chap. 2, Finite Elements in Fluid Mechanics, Wiley, London , (1975)

Chapter 5 APPLICATION OF SOLUTE TRANSPORT ANALYSES

5.1 Introduction

In this chapter, solute transport analysis methods are applied to real and imaginary problems. In order to solve solute transport problems, seepage analyses have to be conducted beforehand to obtain the velocity distribution in a given field of interest, since it is very rare in many cases for the solute concentration in a ground to have a great effect on the ground water flow. Hence, the process of the solute transport analyses involves seepage and coupled phenomena analyses mentioned in previous chapters.

Since many types of uncertainties exist in the model which explains the seepage flow and the solute transport behavior in the ground, it is difficult to grasp the phenomena correctly and to predict them at the present time. And, it may be true that the phenomena are understood in various ways through use of many models. Numerical models mathematically express an characteristics of the phenomena. If the model cannot explain the other characteristics of the phenomena, the model should be revised and extended. Since the other characteristics of the phenomena are discovered through laboratory and in-situ experiments, the application of numerical models to experimental results is very effective for developing the better model to express the real phenomena. However, there seems to exist a limitation in the modeling of a whole real phenomenon. As for the other points of view about the use of the numerical models, we can apply the numerical models to aid in the understanding of the phenomena. The models generally contain many assumptions about the phenomena. Understanding such assumptions and limitations of the model, we can observe the phenomena through the window of the model and can infer the phenomena, which cannot be explained by the simulation using the model, through a comparison of the numerical and the experimental results.

Moreover, other important factors seem to exist concerning the model development, that are related to the objective of the model used. If the numerical analyses are carried out for a rough examination of the design, the accuracy of the calculation does not have to be so high if the model is conservative.

Two examples related to the model development whose objective is to understand the phenomena, are firstly introduced in this chapter. Then, an example of the rough examination of the feasibility of a radioactive waste depository in a deep geology is introduced.

Two tests are to be analyzed in order to understand the phenomena. They are the laboratory tracer test for a single fracture in granite, conducted by the AECL in Canada, and the in-situ tracer test at the Chalk River National Laboratory of AECL. The example for the rough examination of the radioactive waste depository design is concerned with an imaginary tracer test in a rock mass under a temperature gradient. For the laboratory test, the effects of a non-uniform velocity distribution in a single fracture on the breakthrough curves are examined. For the in-situ test, considering the effects of both the leakage of ground water from neighboring rock blocks into a fracture and the matrix diffusion on the solute transport in a fractured rock mass, the transport phenomenon at a regional scale is examined. For the imaginary test, the effects of changes in velocity induced by temperature changes on the solute transport in a rock mass are examined.

5.2 Transport in a Single Fracture Plane

5.2.1 Model description

(1) Experimental design

A large block experiment has been carried out by AECL to aid in the understanding of the processes which affect the migration of tracers in a single fracture. The granite block contains a single, natural fracture. This block has been positioned so that the fracture is approximately horizontal. The block is 91.5 cm long in the flow direction, 86.5 cm wide and 49.0 cm high. The average fracture aperture was estimated from the volume of water required to completely fill the fracture up to approximately 800 μm. The outside surface of the block, as well as the edges of the fracture on the 91.5 cm sides, have been coated with a silicone-based rubber to avoid evaporation of the transport solution through the porous rock matrix. Suitable reservoirs have been designed so that as uniform a gradient as possible can be imposed across the entire width of the fracture. The volumetric flow rate is established at 20 ml/h The outlet reservoir consists of a shallow channel cut into a Plexiglas plate. The channel is divided into five compartments of equal length, and the outlet port of each compartment is hooked up to a separate fraction collector. Figure 5.2.1 shows a schematic view of this arrangement. During the experiment, the outlet concentrations are measured as functions of time. The tracers used in the experiment are Uranine, the non-adsorbing tracer, and Cesium (^{137}Cs), the adsorbing one.

Details of the experimental design and the tracer tests can be found in the draft on the experiment presented as a problem of Case 9 in INTRAVAL phase 1 (Noronha and Gureghian (1988)).

Using the numerical method, a non-uniform flow in the fracture and solute transport considering transport mechanisms, i.e., advection, dispersion and retardation by sorption, are simulated. Then, the calculated results are displayed in comparison with the measured data on breakthrough curves in the experiment.

(2) Computational method

(a) Modeling of channels

A model of channels, in which channel aperture b varies two-dimensionally on the fracture plane, is firstly produced. This procedure is the same as the one mentioned in Section 2.5 and the schematic view of the model of the channels is shown in Figure 2.5.2. The reason why focus is placed on the modeling of the geometric structure of the paths of a solute is because one of the objects of this experiment is to investigate the channeling flow in a single fracture. This seems to be the reason for dividing the outlet reservoir into five ports.

The assumptions used for modeling the channels are:

1) The probability distribution of channel aperture b is approximated by the Gamma function.
2) Each finite element has a constant representative channel aperture.
3) The water volume through the channels is 50% of the volume of the fracture. In other words, the porosity in the fracture, ϕ, is 0.5.

The Gamma function is given by the following form:

$$n(b) = \frac{b}{b_0^2} e^{-b / b_0} \qquad (5.2.1)$$

where b_0 is the aperture value at the distribution peak.

The aperture for each element is produced according to this distribution function using random numbers generated by a computer code. Since the Gamma function needs only one parameter, this function is selected as the aperture distribution due to an insufficient amount of information on the channels.

The transmissivity of each element is obtained by

$$k(b) = 0.5\frac{gb^3}{12\mu} \qquad (5.2.2)$$

where g is the gravitational acceleration and μ is the viscosity of water.

The third power of the aperture in this equation is obtained by multiplying $0.5 \cdot (g b^2)/(12\ \mu)$ by fracture aperture b. This equation means that each element has a representative elementary volume for channels and that the hydraulic conductivity is isotropic in an element.

The constant in equation (5.2.2), 0.5, is derived from the third assumption. This assumption, namely, $\phi = 0.5$, is obtained by the following process:

The substantial velocity through the fracture, v_f^s, was estimated from the measured breakthrough curve of the Uranine migration by AECL (Noronha and Gureghian (1988)), i.e.,

$$v_f^s = 1\times10^{-3} \quad (cm/sec). \qquad (5.2.3)$$

The total flow rate is 20 cm^3/h . Therefore, the following equation is obtained:

$$v_f^a \times 86.5 = \bar{b}\phi v_f^s \times 86.5 = 20/3600 \qquad (5.2.4)$$

where $\bar{b}$ is the mean fracture aperture.

At this point, it is assumed that the aperture at the distribution peak, b_0, is 0.06 cm. The mean value of the Gamma distribution is $2b_0$. Thus, $\bar{b}$ is obtained from

$$\bar{b} = 2b_0 = \frac{20}{3600 \cdot 86.5 \cdot \phi \cdot v_f^s} = 0.12 \qquad (5.2.5)$$

From above-mentioned equations, porosity ϕ is given as $\phi = 0.5$.

The assumed value of b_0 is derived from the averaged fracture aperture, which was estimated with the Uranine experiment by AECL (Noronha and Gureghian (1988)).

The fracture plane is divided into 225 elements (15 × 15). Thus, the distance between neighboring nodes is 6 cm.

(b) Seepage analysis

For the seepage analysis, the followings assumptions are made:

1) The water flow into the rock matrix is negligible.

2) Hydraulic heads are constant at the inlet and the outlet boundaries.

The first assumption is expected to be reasonable because the residence time of the fluid in the fracture is very short. The hydraulic heads at the inlet and the outlet boundaries are prescribed to fit the calculated flow rate to the measured one through trial and error.

The governing equation is the mass balance equation of the water flow at a steady state, i.e.,

$$\nabla \cdot \left(k(b)\, \nabla h\right) = 0 \qquad (5.2.6)$$

where h is the total hydraulic head. This equation is discretized by the Galerkin finite element method and is solved with the following boundary conditions:

$$h = h_1 \qquad on\ x = 0 \qquad (5.2.7)$$

$$h = h_2 \qquad on\ x = L_x \qquad (5.2.8)$$

$$\frac{\partial h}{\partial y} = 0 \qquad on\ y = 0\ and\ L_y \qquad (5.2.9)$$

where the x-direction coincides with the flow direction, h_1 is the prescribed total head at the upstream boundary of $x = 0$ and h_2 is the prescribed total head at the downstream boundary of $x = L_x$.

Prescribed head values are chosen with the following equation such that the total flow rate, Q, is equal to the measured value, 20 ml/h.

$$Q = \int_{o}^{L_y} k(b)\frac{\partial h}{\partial x}\Big|_{x = Lx}\, dy. \qquad (5.2.10)$$

Consequently, the total head at the upstream side is set at 0.00105 cm, while the total head at the downstream side is set at 0 cm, after tRial and error, to fit the calculated flow rate to the measured one.

(c) Transport analysis

Solute migration is simulated under the following assumptions:

1) The matrix diffusion is negligible.
2) The instantaneous equilibrium sorption model is used as a retardation mechanism.
3) The dispersion tensor is isotropic.

The first assumption is expected to be reasonable because the residence time of the solute in the fracture is very short. The second and third assumptions may not be appropriate. However, we try to infer the real transport phenomena occurring in the fracture by comparing numerical and observed results through these assumptions. This seems like a good way to grasp the phenomena in cases where sufficient observations and examinations are not given.

The governing equation used for the advection-dispersion analysis is written by

$$\phi b R_d \frac{\partial c}{\partial t} = \phi b \nabla \cdot (D_f \nabla c) - \phi b v_f^s \nabla c - \phi b R_d \lambda c \qquad (5.2.11)$$

where R_d is the retardation factor, D_f is the dispersion coefficient, λ is the decay constant and c is the concentration.

The dispersion coefficient is assumed to be calculated from the velocity with

$$D_f = \alpha v_f^s \qquad (5.2.12)$$

where α is the dispersivity which is adjusted so that the calculated results are fitted to the measured ones.

The retardation factor is given as

$$R_d = 1 + \frac{2K_f}{b} \qquad (5.2.13)$$

where K_f is the fracture surface sorption coefficient.

Since the solute was injected at the step release mode in the experiment, the initial and the boundary conditions for the above equation are set as follows:

$$c = 0 \qquad at\ t = 0,$$

$$c = c_0 \qquad on\ x = 0\ during\ t > 0,$$

$$\frac{\partial c}{\partial x} = 0 \qquad on\ x = L_x\ during\ t > 0$$

and

$$\frac{\partial c}{\partial y} = 0 \qquad on\ y = 0\ and\ L_y\ during\ t > 0 \qquad (5.2.14)$$

The governing equation is discretized by the ordinary Galerkin finite element method and is solved under the above initial and boundary conditions.

5.2.2 Analyses results

(1) Seepage analyses

Figure 5.2.1 shows the finite element mesh used for the seepage and transport analyses. Three sets of the random numbers for obtaining the aperture distribution are generated. Figure 5.2.2 indicates the generated aperture distributions. Figure 5.2.3 shows the velocity vector distributions for the 3 cases. It is found from these figures that water flows along the portions having large permeabilities. This is the same tendency as that shown in Figure 2.5.3 of Section 2.5.

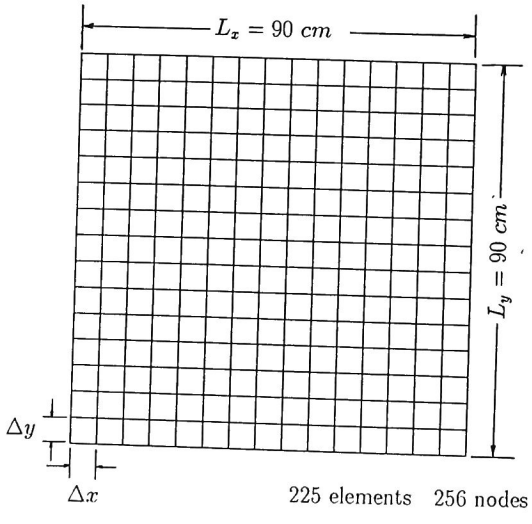
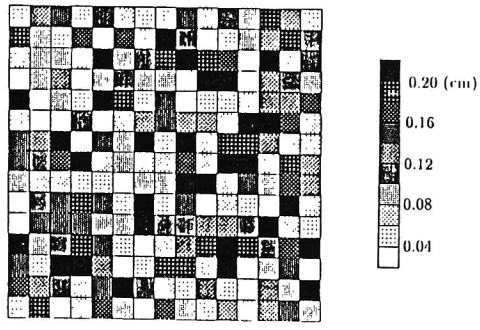
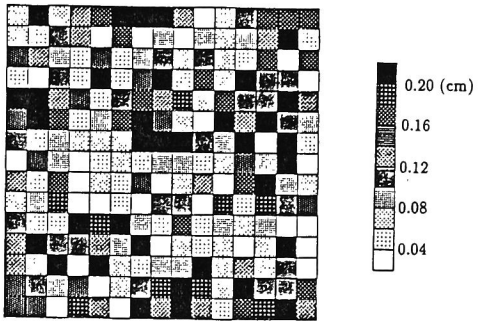


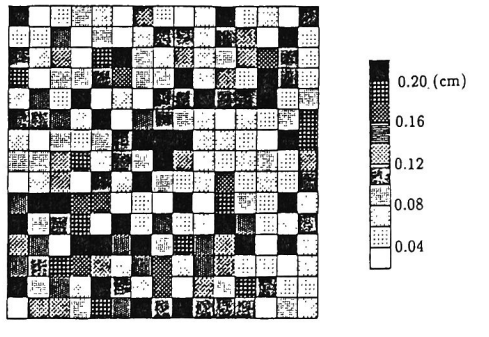
Figure 5.2.1 Finite element mesh used in the analyses of flow and transport problem in a single fracture plane



(a) Run-1

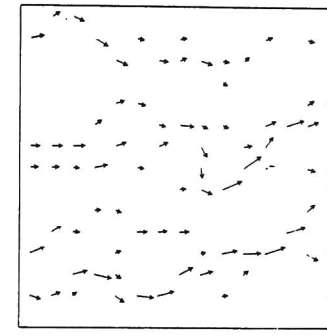


(b) Run-2

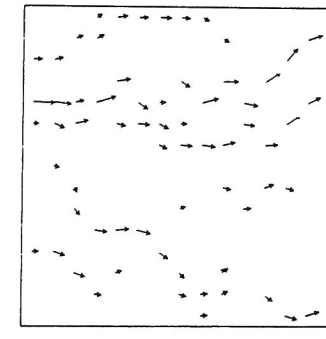


(c) Run-3

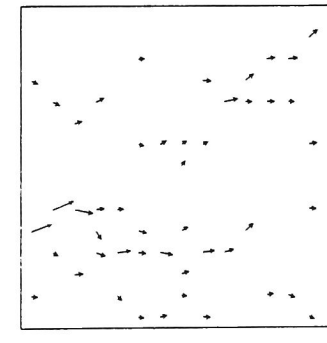
Figure 5.2.2 Generated aperture distributions



(a) Run-1 $\overrightarrow{3.15E-4}$ (cm/s)



(b) Run-2 $\overrightarrow{2.83E-4}$ (cm/s)



(c) Run-3 $\overrightarrow{3.23E-4}$ (cm/s)

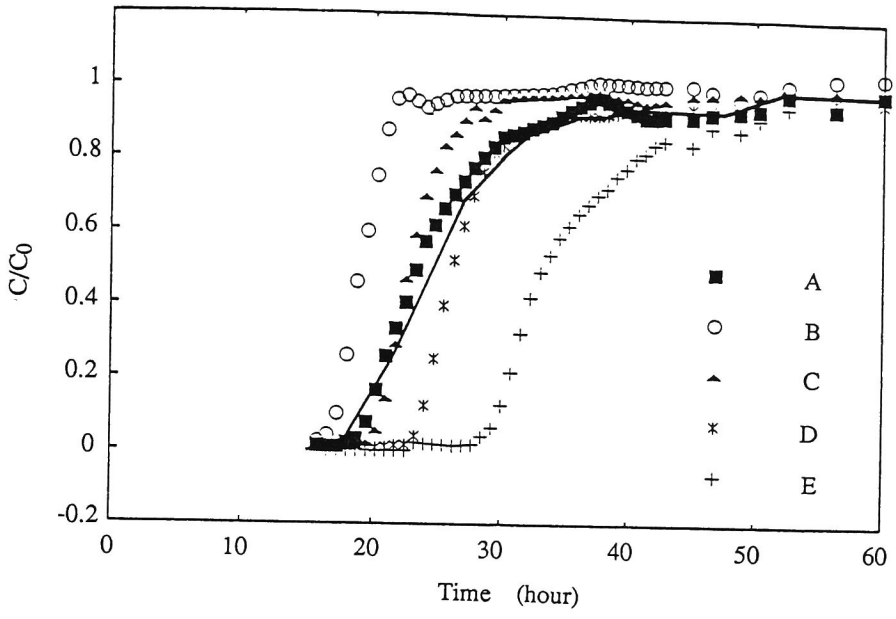
Figure 5.2.3 Velocity vector distributions

(2) Transport analysis

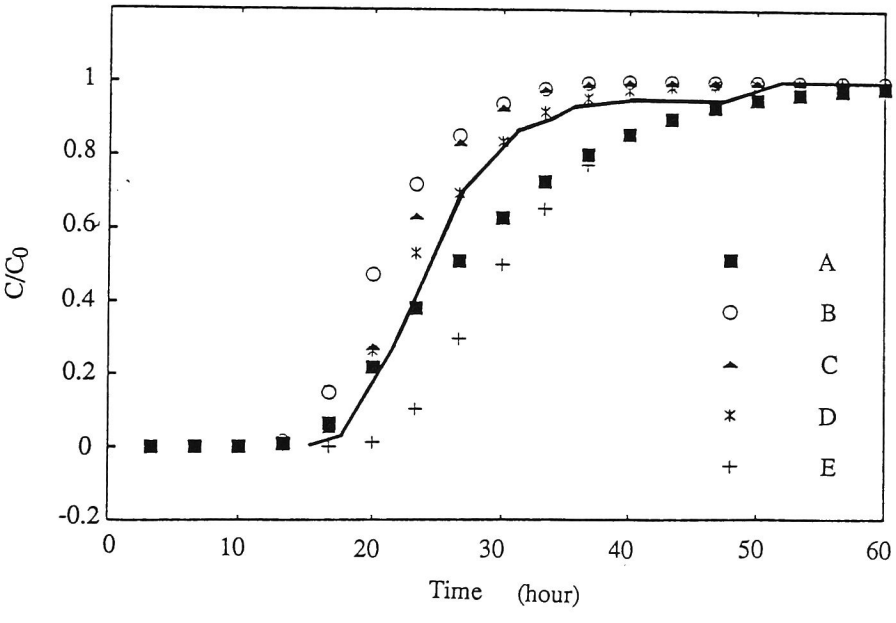
Figure 5.2.4 shows a comparison between calculated breakthrough curves of the non-adsorbing tracer, Uranine, and the measured ones. Figure 5.2.4 (a) indicates the experimental results and Figures 5.2.4 (b) - (d) show the calculated results obtained from using a dispersivity α of 0.4 cm. The solid line in the figures shows the arithmetically averaged breakthrough curves for five plots in Figure 5.2.4 (a), and infers the breakthrough curve averaged for the entire medium.

It is found that the calculated breakthrough curves agree well with the arithmetical average of the observed breakthrough curves, while the breakthrough curves measured at each outlet partition have less skewness than the calculated ones. The maximum difference of rising time for each observed breakthrough curve is about 10 hours, as shown in Figure 5.2.4 (a), although that for the calculated curve is about 5 hours. This may be due to the fact that there is little interaction between flow paths in the real fracture and the that advection-dominated aspect of the solute transport occurs in each path. It may be concluded, therefore, that for the non-adsorbing tracer test, the phenomena occurring in each path cannot be explained by the model so well, while the calculations express the averaged phenomena of the entire medium. The reason for the difference between the numerical and the observed breakthrough curves in each path may lie in the assumptions of isotropic dispersivity and aperture distribution. These are related to the modeling of the channels.

Figure 5.2.5 shows a comparison between the calculated breakthrough curves of the adsorbing tracer, Cesium, and the measured ones, in which (a) represents the experimental results and (b) (d) are the calculated results obtained when using an isotopic dispersivity of α = 0.4cm. The fracture surface sorption coefficient in equation (5.2.13) is set at 0.13 cm in those analyses. The retardation factors used in the analyses are set according to the aperture distribution, and thus, the portions with a high velocity,

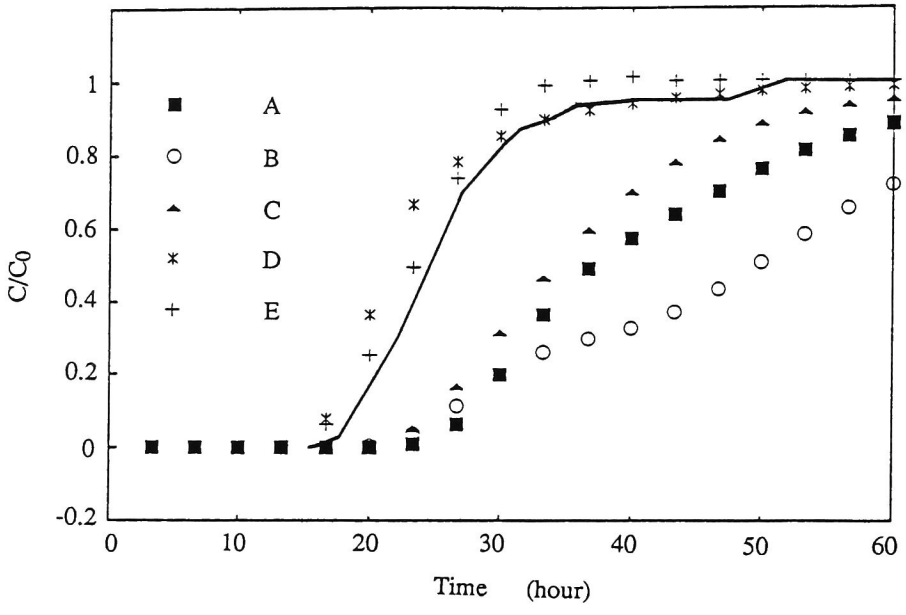


(a) Measured results

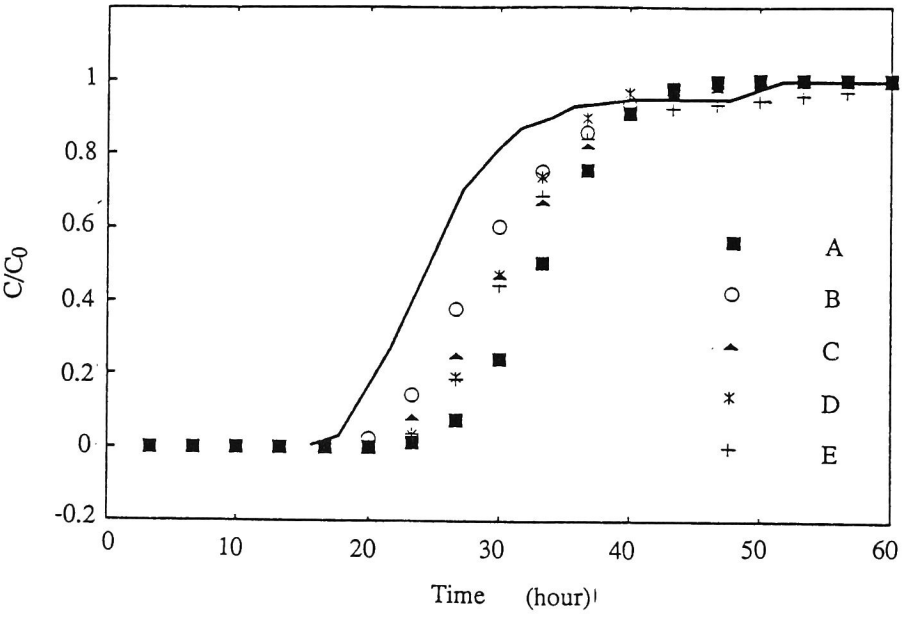


(b) Run-1

Figure 5.2.4 Comparison between calculated breakthrough curves of the non-adsorbing tracer, Uranine, and measured ones



(c) Run-2



(d) Run-3

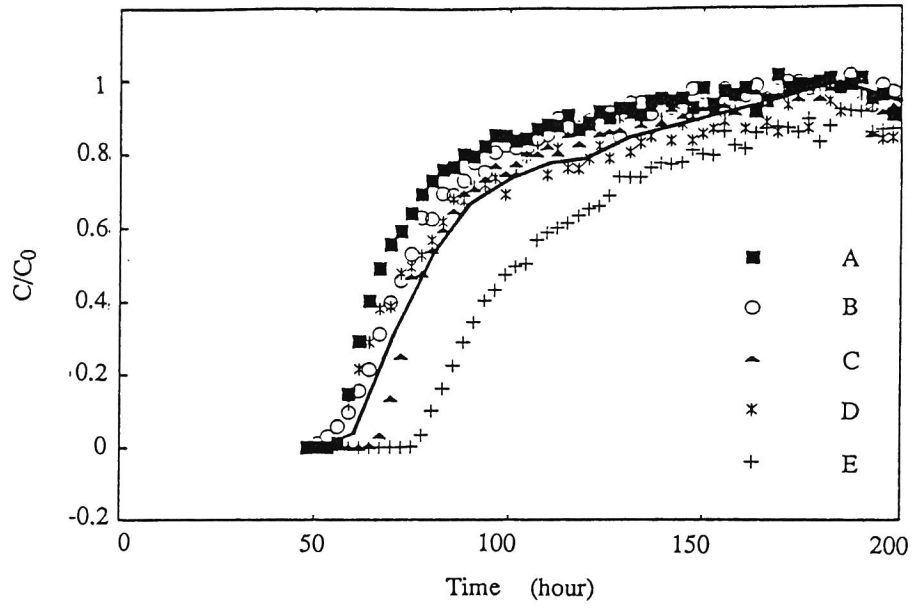
Figure 5.2.4 Comparison between calculated breakthrough curves of the non-adsorbing tracer, Uranine, and measured ones (continued)

i.e., the large aperture, have a small retardation factor. The solid line in those figures shows the arithmetically averaged breakthrough curve for five plots in Figure 5.2.5 (a).

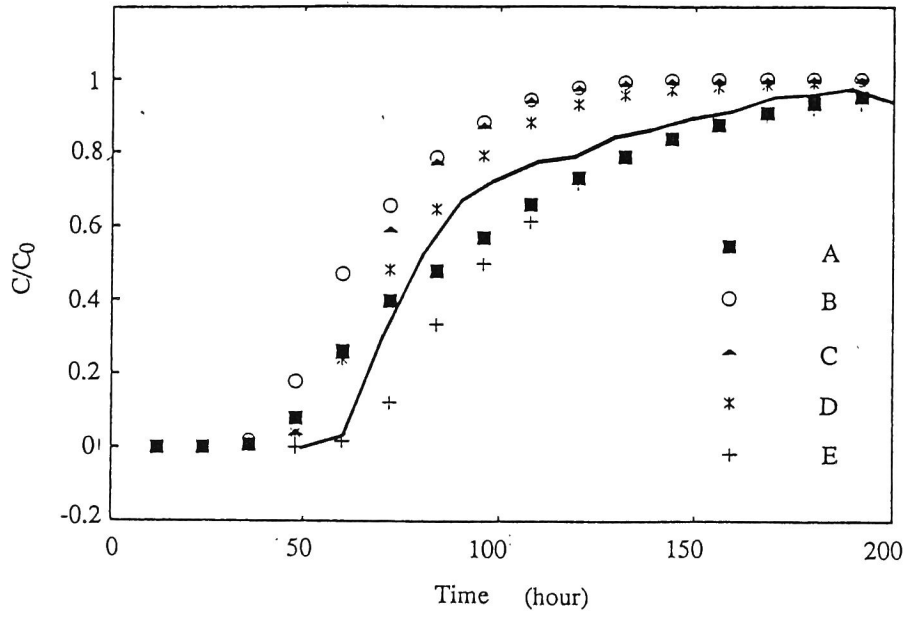
It seems that the results calculated in this case express the degree of skewness for breakthrough curves measured at each outlet partition better than in the case of Uranine, while the difference in the rising time of the measured curve remained larger than that of the calculated results. The skewness of the breakthrough curves measured at each outlet partition is not so different from that of the arithmetically averaged curve. It may be concluded, therefore, that the model used in these analyses can express both the phenomenon occurring in each path and the averaged phenomenon, while the velocity distribution is not expressed well by the calculations. In other words, the phenomena occurring in this case are not affected by the velocity distribution, but are very affected by adsorption and dispersion behavior.

It is inferred from the above results that the real transport phenomenon in each path is dominated by advection in cases where adsorption does not occur and is dominated by dispersion in cases where adsorption does occur. In general, whether the phenomena are advection-dominated or dispersion-dominated is dependent on the Peclet number, P_e, which is given as $P_e = vL/D$ in which v is velocity, L is the characteristic length and D is the dispersion coefficient. Since the dispersion coefficient is given by equation (5.2.12) in the analyses, the Peclet number in the analyses becomes L/α. Thus, the P_e in both cases is the same for all elements and is difficult to use for judging whether the advection or dispersion dominated phenomena are occurring in the media for both cases. This is probably because the velocity distributions are not simulated well by the models. In other words, it is necessary to correctly model the velocity field in order to examine cases using a non-adsorbing tracer.

5.2.3 Conclusions

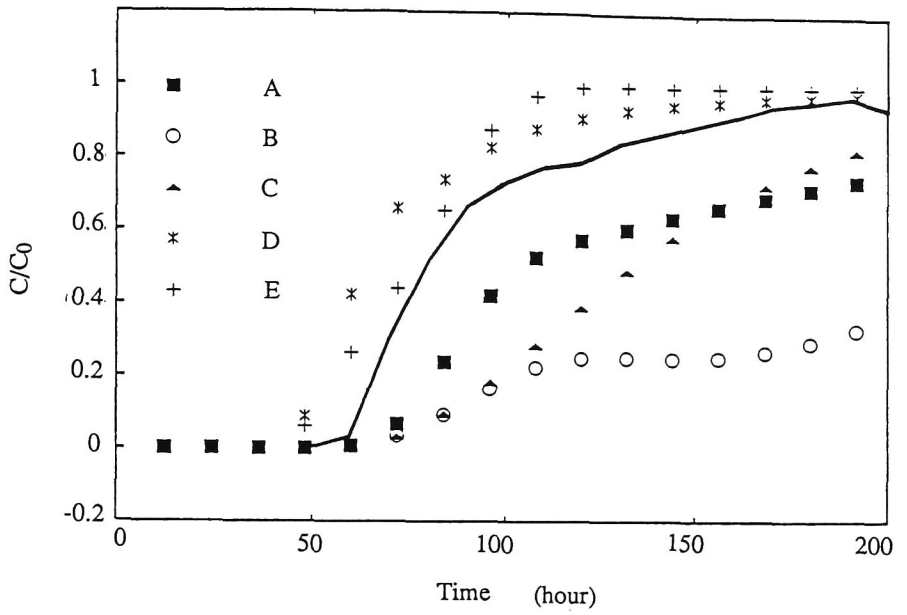


(a) Measured results

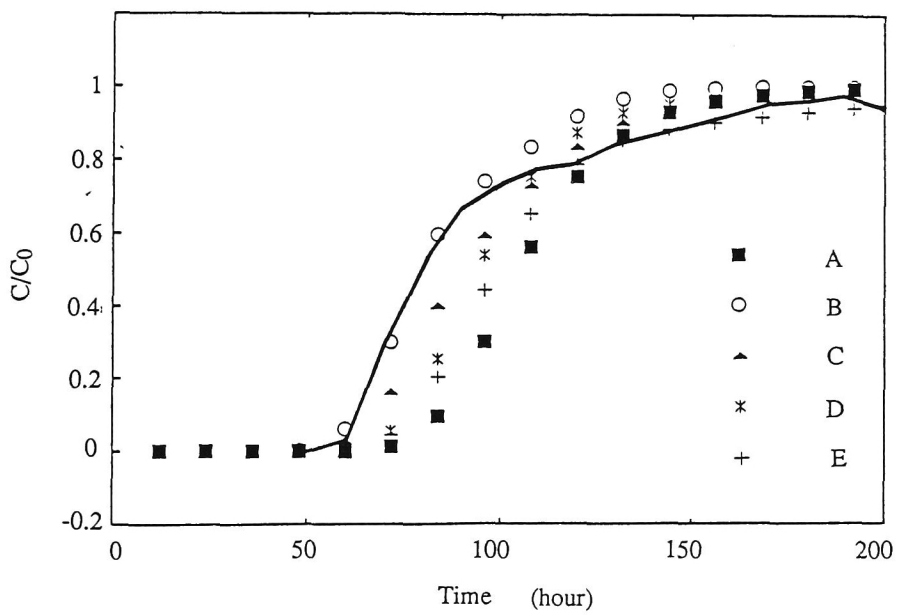


(b) Run-1

Figure 5.2.5 Comparison between calculated breakthrough curves of the adsorbing tracer, Cesium, and measured ones



(c) Run-2



(b) Run-3

Figure 5.2.5 Comparison between calculated breakthrough curves of the adsorbing tracer, Cesium, and measured ones (continued)

single fracture on a laboratory scale. This problem was introduced as Case 9 of INTRAVAL project phase 1.

Since the rock block used in this experiment had a natural fracture, it was expected that the fracture aperture would not be uniform. The channel flow was simulated by the stochastic approach, in which the probability density distribution of the aperture was assumed as a Gamma function. Then, the transport analyses were carried out and the calculated breakthrough curves were compared with the measured ones.

The conclusions can be summarized as follows:

1) The velocity distribution in the fracture was not simulated correctly. This is probably because the Gamma function is not as appropriate as the aperture distribution.
2) While the solute transport phenomenon in each path of the fracture was not sufficiently expressed by the model for the non-adsorbing tracer case, the breakthrough curve averaged at the outlet boundary was simulated roughly by the model.
3) Both the phenomenon occurring in each path and the averaged phenomenon for the adsorbing tracer test were expressed well by the numerical model used in this section.
4) The phenomena occurring in the adsorbing tracer test may not be affected by the velocity distribution, but are greatly affected by adsorption and dispersion behavior.
5) The real transport phenomenon in each path is expected to be dominated by advection in cases where the adsorption does not occur and by dispersion in cases where adsorption does occur.

In spite of an insufficient amount of information on the aperture distribution in the fracture, the phenomena in both the non-adsorbing and the adsorbing tracer tests were roughly simulated by the numerical model using the non-uniform velocity field.

However, for a more detailed examination of the phenomena, further information on the aperture is necessary and an examination of the velocity fields must be carried out.

5.3 Analyses of Field Tracer Test

5.3.1 Field tracer test

Field tracer tests in a single fracture zone were performed at a study site located on the property of the Chalk River Nuclear Laboratories (CRNL), Atomic Energy of Canada, Ltd. (AECL) (Raven, et al. (1988)). This is the same place where the hydraulic characterization tests were conducted; they are analyzed in Section 2.6. While focus is placed on the fracture zone 1, shown in Figures 2.6.12 and 2.6.13, in the analyses of the hydraulic characterization tests, fracture zone 3 is used for the tracer tests. Figure 5.3.1 shows the borehole layout and the approximate extent of fracture zone 3, which is modeled for the region shown with a solid line in the figure. Five tracer tests were performed with a three-borehole array of FS-6, 11 and 15. The tracer experiments were performed in the central high-permeability region of the fracture zone to reduce far-field boundary effects or distortion of the flow field. Although the natural ground water flow direction was northeast following the dip direction of the fracture zone with gradients of 0.001-0.1 and the hydraulic gradient between boreholes FS-6, 11 and 15 were 0.001-0.002, the hydraulic gradients imposed through the tracer tests were 25 times greater than the natural field gradient. Thus, the fracture zone can be modeled as a horizontal plane.

The test conditions of the five tests are summarized in Table 5.3.1. During test 1, radioactive gamma-emitting ^{82}Br (half-life of 35.5 hours) was injected into an injection withdrawal flow field, established without recirculation, and pumped at equal rates between borehole FS-6 (injection) and borehole FS-15 (withdrawal). In the second tracer experiment, Na Fluorescein was injected in a similar flow field, except that the injection borehole (FS-15) and the withdrawal borehole (FS-6) were reversed from the first test. Radioactive ^{82}Br was used as the tracer in the third test, which was performed in a radial convergent flow field toward borehole FS-15 from borehole FS-6. Tracer tests 4 and 5 were conducted together between boreholes FS-6, 11 and 15 using radioactive ^{82}Br as the tracer. An injection-withdrawal flow field, with recirculation of the withdrawn fluid,

Table 5.3.1 Summary of tracer test conditions (after Raven,et al. (1988))

Test	Tracer	Injection	Withdrawal	Flow Field	Borehole Spacing, m	M_{ini}	Q L/hour	ΔH m
1	82Br	FS-6	FS-15	injection-withdrawal	12.7	27 MBq	30.0	4.60
2	Na Fluorescein	FS-15	FS-6	injection-withdrawal	12.7	100 mg	32.0	4.90
3	82Br	FS-6*	FS-15	radial-convergent	12.7	27 MBq	14.0	0.70
4	82Br	FS-6	FS-15†	injection-withdrawal	12.7	40 MBq	36.6	2.35
5	82Br	FS-6	FS-11	injection-withdrawal	29.8	40 MBq	36.6	5.95

* Passive injection

† Passive withdrawal

was established between boreholes FS-6 (injection) and FS-11 (withdrawal) during these tests and the breakthrough of the tracer was monitored at both the withdrawal borehole FS-11 (test 5) and the passive intervening borehole FS-15 (test 4).

Steady flow conditions were established in the fracture approximately 5-10 hours prior to the tracer injection for each tracer test. Steady flow conditions were confirmed with the attainment of the steady hydraulic head, ΔH and the flow rate, Q shown in Table 5.3.1. ΔH is the sum of the net changes in the hydraulic head from the equilibrium values for both the injection and the withdrawal boreholes.

5.3.2 Model description

(1) Seepage analysis model

Figure 5.3.2 shows the finite element mesh used in the seepage flow analyses, whose mesh is modeled for the zone indicated with a solid line in Figure 5.3.1. The fracture zone is modeled by the plane elements at the bottom of the three-dimensional rock block elements. The seepage flow analyses are carried out with the model introduced in Section 2.6, which considers the leakage from the rock blocks adjoining the fracture. For the analysis of all tests, the initial water level is set at 27 m, i.e., the height at the top of the

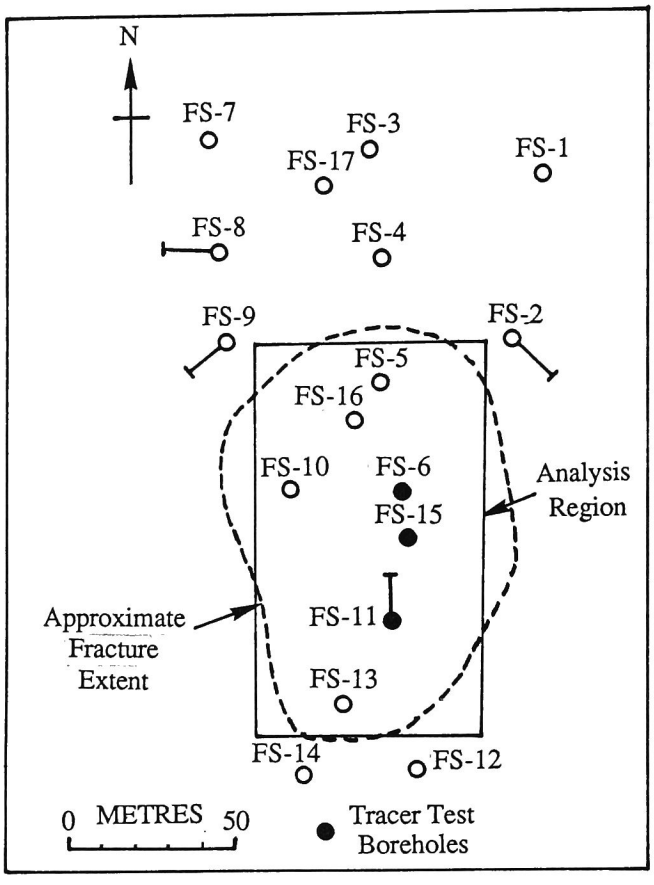


Figure 5.3.1 Borehole layout and approximate extent of fracture zone 3
A solid line indicates an analysis region

three-dimensional model shown in Figure 5.3.2. All boundary conditions are set at no flux conditions. The injection and the withdrawal flow rates, Q are given in Table 5.3.1 as the sink and source conditions, and the unsteady flow state in the fracture zone is analyzed with the model considering the leakage from the rock blocks. The calculated results of the sum of the hydraulic head for both the injection and the withdrawal boreholes at 10 hours from the start of the analysis are compared with ΔH, shown in Table 5.3.1. Moreover, it is ascertained whether or not a change in the calculated ΔH is very small.

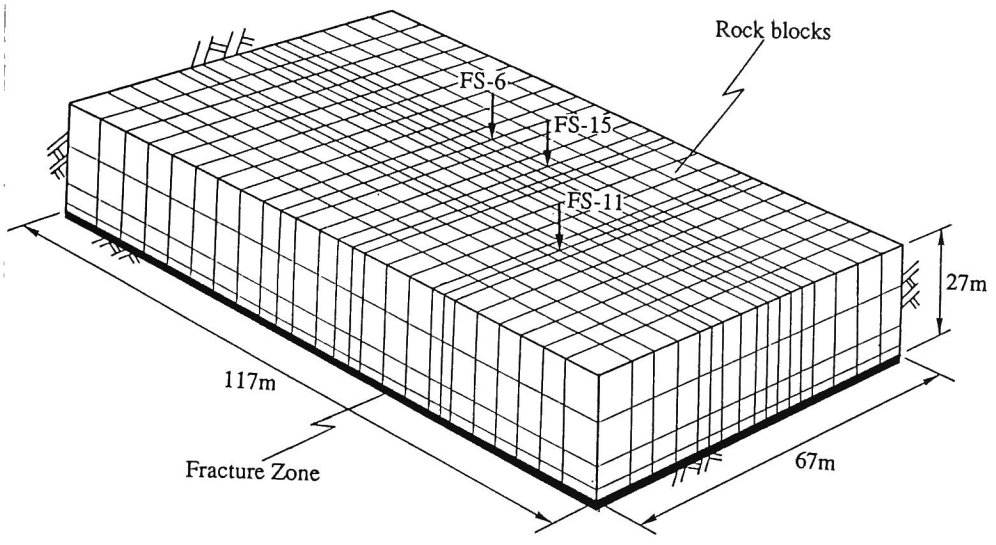


Figure 5.3.2 Finite element mesh used in the flow analyses of CRNL tracer test

Table 5.3.2 shows the permeability and the storage coefficient used in the analyses. They are the same as those shown in Section 2.6. The permeability of the rock blocks is obtained by calculating the log-mean of the permeabilities estimated from the straddle-packer injection tests by Raven (1985). The principal direction to three geographic reference axes is defined by three direction cosines, i.e., l_1, m_1, n_1 for K_1. Geographic reference axes (one south, two east and three down) are used in Table 5.3.2. The anisotropic permeability is obtained by transforming to our coordinate system, i.e., x is east, y is north and z is upward for the seepage analyses. The transmissivity of the fracture zone in Case *a* of Table 5.3.2 is obtained from the aperture, which has been estimated from interference tests performed before the tracer tests by Raven (1985). The aperture in this case is larger than those shown in Table 5.3.3, which were estimated from the concentrated hydraulic characterization tests by Raven et al. (1988) prior to the tracer test.

(2) Transport analysis model

Transport analyses are carried out by applying the velocity field in the fracture and the leakage rate from the adjoining rock blocks obtained from the above seepage analyses. The analyses are performed with the two-dimensional finite element mesh, which models

Table 5.3.2 Parameters used in the seepage analyses

Zone	Principal Permeability (m/s) K_1	K_2	K_3	Storativity S	Principal direction* l_1 m_1 n_1	l_2 m_2 n_2	l_3 m_3 n_3
					-0.100	-0.128	-0.058
Rock blocks	9.13×10^{-9}	7.03×10^{-9}	1.40×10^{-9}	5×10^{-7}	-0.0298	0.066	-0.160
					-0.060	-0.223	0.223

Fractures	Transmissivity (m^2/s)	Storativity	Aperture (mm)	α
Case *a*	3.05×10^{-6}	-	155	-
Case *b*	1.33×10^{-6}	2.5×10^{-6}	118	0.021
Case *c*	1.06×10^{-7}	2.5×10^{-5}	50.5	0.048
Case *d*	1.06×10^{-7}	2.5×10^{-5}	50.5	0.078

* Direction cosines relative to geographic reference axes.

Table 5.3.3 Parallel plate openings determined from hydraulic tests (after Raven, et al (1988), unit is micrometers)

Activation Boreholes	Observation Boreholes FS-5	FS-6	FS-10	FS-11	FS-13	FS-15	FS-16
FS-5	35						
FS-6		140	120	110	100	145	135
FS-10			15				
FS-11		141	190	190	150	140	
FS-13					96		
FS-15		110		124		145	
FS-16							42

only the fracture plane because the tracer is injected and withdrawn only at the fracture zone by a straddle-packer system. Numerical examinations are conducted for tests 1, 2 and 3 because tests 4 and 5 performed recirculation of the withdrawn fluid, which is difficult to simulate due to an insufficient amount of information on the recirculation conditions. The initial conditions are set at a zero concentration for the whole region and all the boundaries are set at no-flux conditions.

(3) Strategy of the analyses

What was reported about the tracer test results is the sum of the net change in the hydraulic head for both the injection and the withdrawal boreholes, ΔH, shown in Table 5.3.1, the flow rates pumped between both injection and withdrawal boreholes, Q shown in Table 5.3.1, the fracture aperture calculated from both the injection tests and the hydraulic interference tests shown in Table 5.3.3 and the residence time distributions of the tracers which are corrected for radioactive decay. The numerical results have to agree with these measured results. In addition, the porosity of the fracture zone has to be less than 1. The retardation factor should be set at 1 because a non-adsorptive tracer was used for these tests and coefficient R_3, which is the product of the porosity and the retardation factor in the rock matrix, has to be less than 1 due to a retardation factor of 1. The calibrations of the flow and the transport model have to be carried out such that all the above conditions are satisfied. In this section, the calibrations for tests 1, 2 and 3 are performed with the process shown in Figure 5.3.3 and then the calibrated values of the parameters for each test are compared. If the parameter values for each test are approximately the same, it can be concluded that the model is valid for the various behavior occurring at the site and can express such phenomena in the future.

5.3.3 Results of the analyses

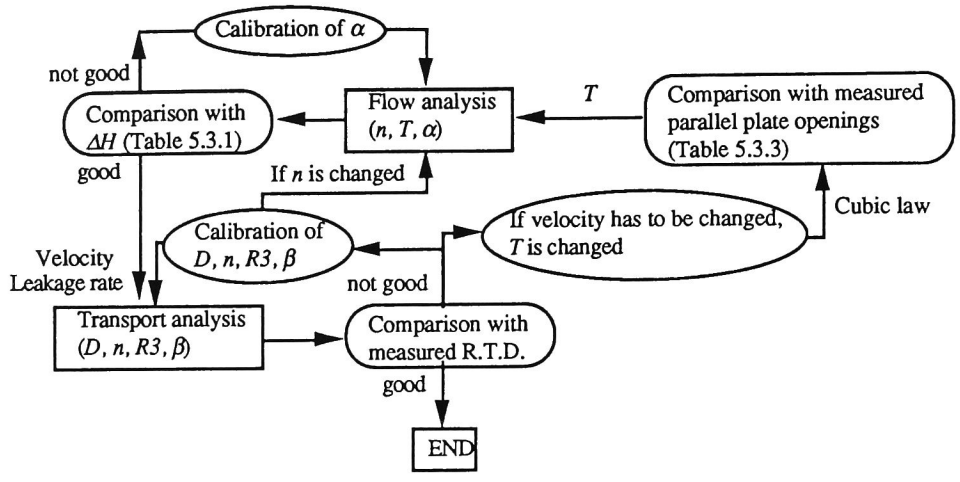


Figure 5.3.3 Calibration process of flow and transport analyses, in which n is the porosity in the fracture, T is the transmissivity in the fracture, α is the coefficient related to the leakage, D is the dispersion coefficient in the fracture, R_3 is the product of the porosity and the retardation factor in the rock matrix and β is the matrix diffusion coefficient.

Seepage analyses are carried out by applying the injection and the withdrawal flow rates, Q in Table 5.3.1 as the sink and source conditions, and the calculated results of the sum of the changed hydraulic head at both the injection and the withdrawal boreholes are compared with the measured ones. The calculated results of the transport analyses are calibrated to the residence time distribution (R.T.D.) curves expressed in the relative form E/E_p, in which E is given as

$$E(t)=c(t)Q/M_{inj} \qquad (5.3.1)$$

where $c(t)$ is the concentration time response at the withdrawal borehole, Q is the steady volumetric flow rate, M_{inj} is a mass of the injected tracer and E_p is the peak value of $E(t)$. Since the R.T.D. curve presented by Raven ,et al. (1988) is corrected for radioactive decay, the radioactive decay of ^{82}Br does not have to be considered in the transport analyses. The R.T.D. curves measured with the borehole γ counter are used for a comparison with the calculated ones.

(1) Test 1

This test case is the basic case of the calibration process for tests 2 and 3. The parameter values calibrated for this test are used for the other tests first and then calibrated to fit the calculated R.T.D. curve to the measured one.

As the first trial, Case *b* in Table 5.3.2 is used for the flow analysis. The aperture of this case is obtained from the mean value of the apertures shown in Table 5.3.3. Since the most suitable apertures by Raven et al. (1988) are between 115 and 45 μm and the mean value of the apertures is 118 μm, the peak time of the R.T.D. curve is expected to be faster than the real one if the aperture in Case *a*, 155 μm, is used for the analysis. The storativity is calculated as the product of the porosity in the fracture and the compressibility of the water. For these tracer tests, the storativity does not have much influence on the velocity distribution because the flow in the fracture reached approximately the steady state. The porosity in the fracture has great meaning for the transport analysis, in which the solute particles are transported as an advection behavior. The porosity is obtained by trial and error of the transport analyses such that the R.T.D. curve, calculated with R_3 and n less than 1, is fitted to the measured one. In the process of the calibration shown in Figure 5.3.3, the porosity is identified at 0.05 from the transport analysis first and then coefficient α, related to the leakage, is calibrated to fit the calculated ΔH to the measured one. ΔH, obtained using the parameters of Case *b* in Table 5.3.2, is the same as the measured one, i.e., 4.6 m. Figure 5.3.4 shows the calculated R.T.D. curve and the measured one. The peak time of the calculated curve is faster than the measured one. This is because the velocity in the fracture is faster. As a second trial, the transmissivity is calibrated to fit the peak time. After trial and error, according to the process in Figure 5.3.3, α, R_3 and β are identified as shown in Test 1 of Table 5.3.4 and the best fitting results of the R.T.D.curve are obtained as shown in Figure 5.3.5. The parameters for Case *c* in Table 5.3.2 are the ones used for the flow analysis.

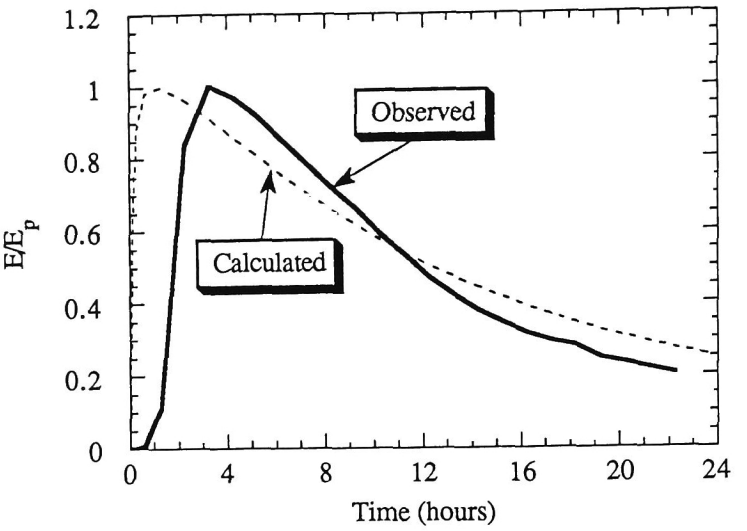


Figure 5.3.4 Comparison between calculated and measured R.T.D. of Test 1 with the aperture of Case b

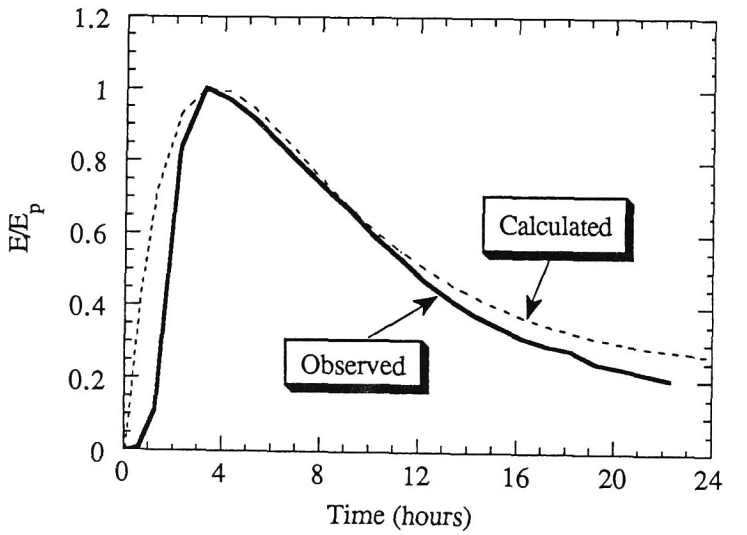


Figure 5.3.5 Comparison between calculated and measured R.T.D. of Test 1 with the aperture of Case c

Table 5.3.4 Parameter values yield a good agreement with the observed results

Parameters	Test		
	1	2	3
Dispersivity (m), α_L	0.3	0.3	0.3
Porosity of the fracture, n*	0.05	0.05	0.05
Retardation factor of the fracture, R_2	1.	1.	1.
Matrix dispersion coefficient, β	0.01	0.01	0.003
Product of retardation factor and porosity of the rock matrix, R_3	0.65	0.65	0.65
Aperture (μm)	50.5	50.5	50.5
Coefficient related to leakage, α	0.048	0.048	0.078

* Notation is represented as θ_2 in Section 4.5

(2) Test 2

Using the same values for all the parameters as those shown in Test 1 of Table 5.3.4, the flow and the transport analyses are carried out for Test 2. ΔH, obtained by applying the parameters of Case *c* in Table 5.3.2, is 4.98 m. This agrees well with the measured one, i.e. 4.9 m. The dotted line in Figure 5.3.6 shows the R.T.D. curve obtained with the same values as those used in the analysis given in Figure 5.3.5. The calculated curve shown with a dotted line in Figure 5.3.6 shows a approximately good agreement with the measured one. Since this experiment was done to test the repeatability of the experiment (Raven et.al. (1988)), the values of the parameters used in the transport analysis should be the same for both cases. Since a fairly good agreement between the numerical results and the experimental ones is obtained for both cases, using the same

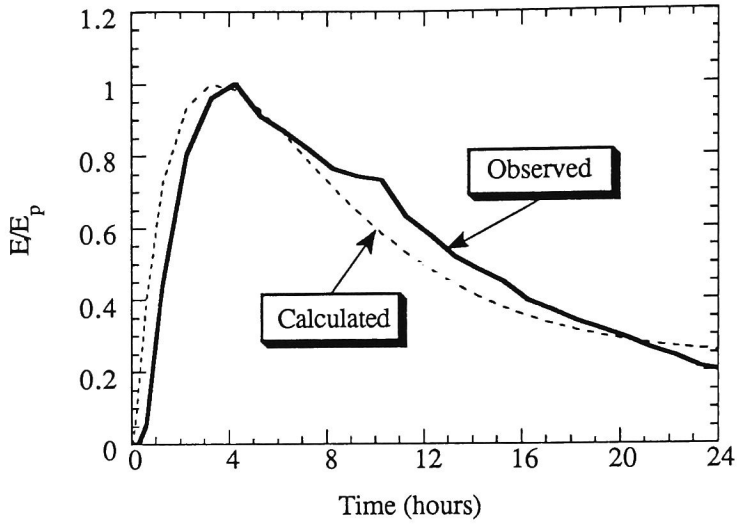


Figure 5.3.6 Comparison between calculated and measured R.T.D. of Test 2

values for the parameters, it may be concluded that the repeatability of the test is recognized by these analyses. In other words, it is concluded that the model can predict the flow and the transport behavior through use of the calibration results of a similar flow field.

(3) Test 3

Test 3 is performed in a radial convergent flow field toward borehole FS-15 from borehole FS-6, which is different from the flow field of Tests 1 and 2. For the flow analysis of this test, the parameters in Case *c* of Table 5.3.2 are used first. Figure 5.3.7 shows the result obtained by using the same data used for the flow and transport analyses of Tests and 1 and 2, in which the faster peak time and lager tailing than observed ones are indicated. These tendencies are related to the value of the voefficients α and β. Then α is calibrated to fit the calculated ΔH to the measured one.When α is set at 0.078, as shown in Case *d* of Table 5.3.2, the calculated ΔH is 0.71 m, which agrees well with the

measured one, 0.7 m. α in Case d is larger than that in Case c, which yields a good agreement with the measured ΔH of Tests 1 and 2. Using the velocity field from the flow analysis with the parameters of Case d, the transport analysis is carried out and β is calibrated. Figure 5.3.8 shows the best fitting curve to the measured one. At this time, β is 0.003, which is less than the β used in Tests 1 and 2, as shown in Table 5.3.4. A different α and β from those in Tests 1 and 2 is probably due to the effects of the boundary conditions and the properties of the rock blocks far from the withdrawal borehole. The ground water flow between boreholes FS-6 and FS-15, arising in Tests 1 and 2, is not expected to be greatly affected by the boundary conditions and properties of the fractures and rock blocks far from the boreholes, because the injection and the withdrawal are carried out at both boreholes. On the other hand, the ground water flow in Test 3 is generally affected by the boundary conditions and properties far from borehole FS-15, because of the radial convergent flow to FS-15. However, the model can express the phenomena in Test 3, radial convergence flow, by modifying α a little for the flow analysis and β for the transport analysis from the values obtained by the calibration for the other flow field of Test 1, the flow between injection-withdrawal wells. The result for Test 3, obtained by using the same parameters used in Test 1, shows the conservative one for the assesment of the transport problem of a waste disposal becuse of the fast travel time and large tailing. Although this result is dependent on the spceise and the bounday condition, this means that the model may be able to predict conservative phenomena in the future by changing α and β parametrically from values calibrated from tests in other flow fields.

5.3.4 Discussions

The aperture of the fracture was 50.5 μm in the analyses. Although this value is about half of the mean value of the observed apertures shown in Table 5.3.3, it is not such an unlikely value because the smaller apertures were observed in the fracture zone. The apertures used in the analyses by Raven, et al. (1988) are in the range of 45 to 115 μm,

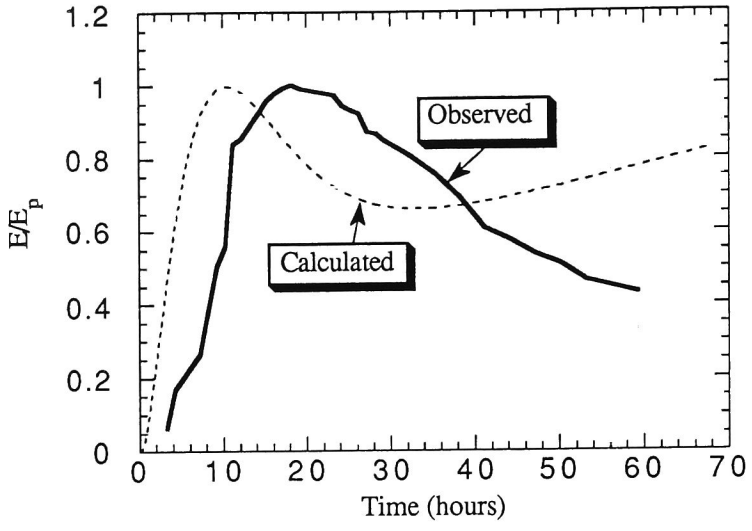


Figure 5.3.7 Comparison between measured and calculated R.T.D. of Test 3 obtained by using the same parameters as the ones in the analyses of Tests 1 and 2

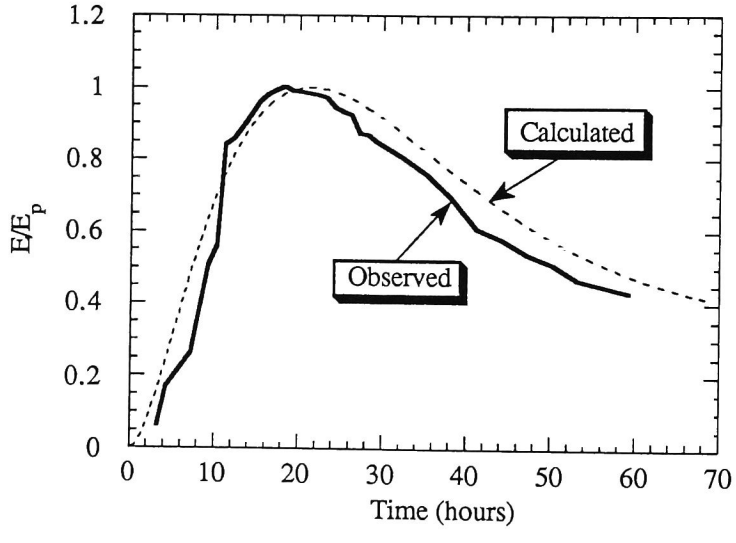


Figure 5.3.8 Comparison between measured and calculated R.T.D. of Test 3 by using the parameters shown in Table 5.3.4

which also proves the aperture of 50.5 μm to be realistic. The porosity in the fracture was 0.05 in the analyses. This is related to the regime of the flow in a fracture, e.g., the channel flow. The report at the Stripa project said that about 10% of the volume of the fracture plane contributes to the fluid flow in it (Abelin, et al. (1985)). Numerical experiments conducted in Section 2.5 concluded that the area of fluid paths in a fracture plane is very small. Thus, a porosity of 5% is not so unlikely. R_3 was 0.65 in the analyses, which is the product of the porosity and the retardation factor of the rock matrix and has to be less than 1 due to a retardation factor of 1. This parameter in the examination by Raven et al. was in the range of 0 to 0.65. This may prove the R_3 to be probable. The dispersivity, α_L was 0.3 m in our analyses. Since this parameter did not have much effect on the R.T.D. curve, the value of it was not calibrated in the calibration process. Incidentally, the dispersivity used in the analyses by Raven et al. was in the range of 0.95 to 6.3 m. The matrix dispersion coefficient, β, and the coefficient related to the leakage, α, had a great effect on the transport and flow analyses. Since these parameters are difficult to identify directly from the experiment results, they have to be calibrated through analyses with in-situ test results prior to the prediction. α is a special parameter of the model considering leakage from the adjoining rock blocks to the fracture. Figure 5.3.8 shows the contour of the leakage rate of Test 1. The ground water moves from the fracture zone to the adjoining rock blocks in the region around FS-6, which is the injection borehole, due to high pressure in the fracture, while the ground water moves from the adjoining rock blocks to the fracture in the region around FS-15. It is found from this figure that the dilution of the solute concentration in the fracture is expected to occur around withdrawal borehole FS-15. On the other hand, Figure 5.3.9 shows the distribution of the leakage rate for Test 3. The ground water moves from the rock blocks to the fracture in the whole region. Since the leakage rate is less than the value of β, as shown in Figures 5.3.9 and 5.3.10, this leakage rate has a greater effect on the flow behavior in the fracture than the transport behavior in it. Thus, for the calibration process, the R.T.D. curve was adjusted by calibrating β in the transport analysis after the velocity distribution was obtained by calibrating α in the flow analysis.

For transport analyses, in addition to the parameters, i.e., the dispersion coefficient, the retardation factor and the decay constant, the velocity distribution in the field of interest is also necessary. This is obtained from the hydraulic conductivity, storativity and the hydraulic initial and boundary conditions. In general, the initial and the boundary conditions are given from the results of geological and topographical surveys. Calibrating these parameters, the most suitable parameters are identified to express the observed phenomena of solute transport and ground water flow. Then, future phenomena are predicted through calculation using those identified parameters. Thus, the parameters used in the analyses have to be calibrated before the prediction using the initial and the boundary conditions at that time. It seems important for the calibration to identify the parameter values consistent with the phenomena from the various points of view.

To given an example in this section, the velocity distribution of each test has to be identified to express the summation of the drawdown of the water levels of the injection and the withdrawal wells, ΔH. At that time, the aperture, which is used to estimate the transmissivity by the cubic theory, has to be consistent with the results observed in the single borehole injection tests and the hydraulic interference tests conducted for this area before the tracer tests. It is necessary, however, for the conventional seepage analysis methods to calibrate the transmissivity in order to change the calculated pressure distribution in the fracture, as mentioned in Section 2.6. This causes a change in the velocity in the fracture and the calibration of the transport behavior becomes difficult. Using the model introduced in Sections 2.6 and 4.5, on the other hand, the calibration process is easy and systematic, as shown in Figure 5.3.3.

The flow model considering the leakage from the adjoining rock blocks was able to express the observed ΔH in Test 3 by applying the same aperture as the one used in the analyses of Tests 1 and 2 and by adjusting the leakage rate. Using the velocity distribution from the above flow analysis, the transport phenomenon of Test 3 was explained by using the same transport parameters as those used in Tests 1 and 2, except for β. This approximate consistency of the parameter values through different tests may

prove the flow and the transport models considering the leakage from the adjoining rock blocks in this area.

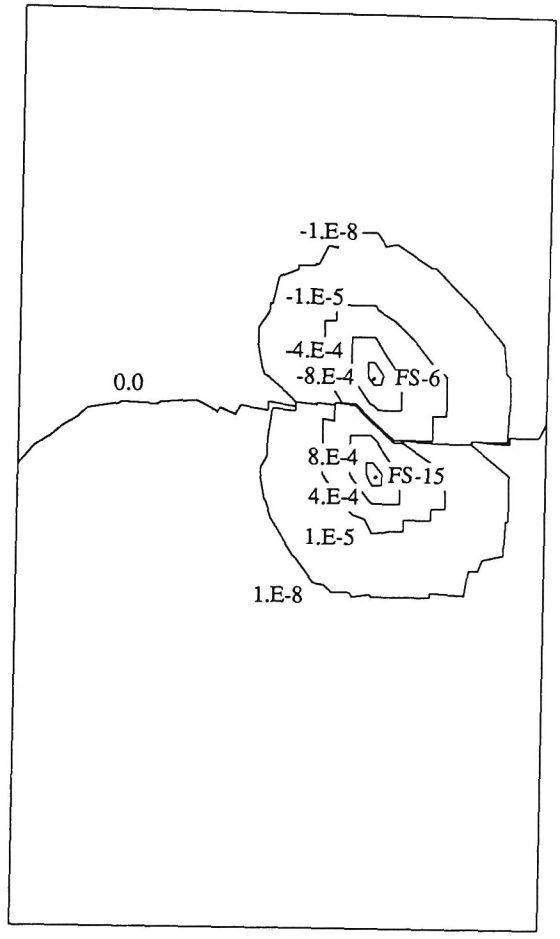


Figure 5.3.9 Distribution of the leakage rate for Test 1

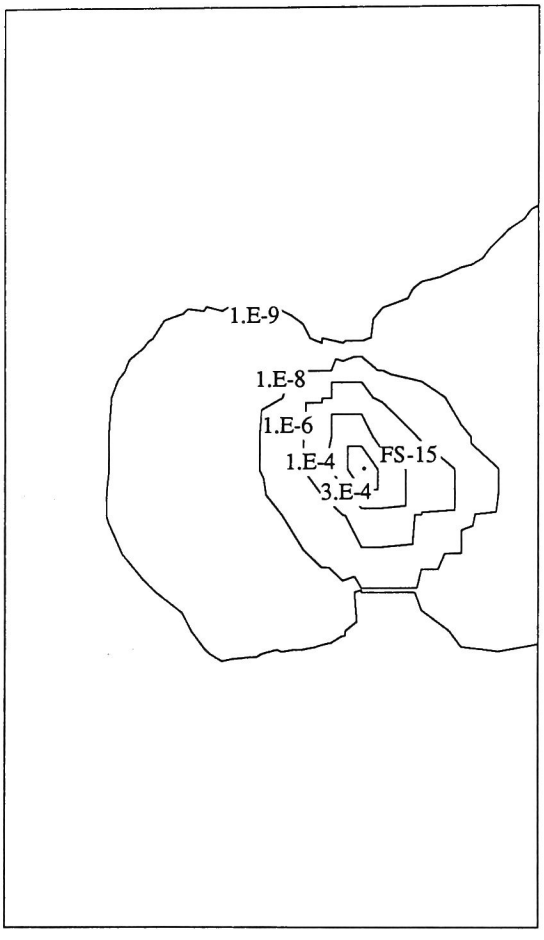


Figure 5.3.10 Distribution of the leakage rate for Test 3

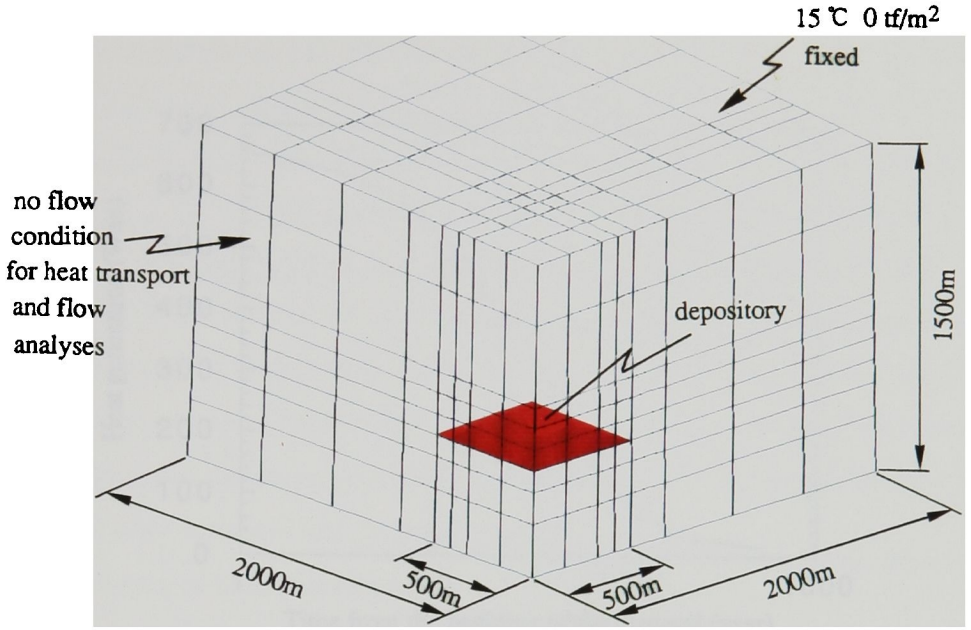
5.4 Transport under Coupled Phenomena

5.4.1 Model description

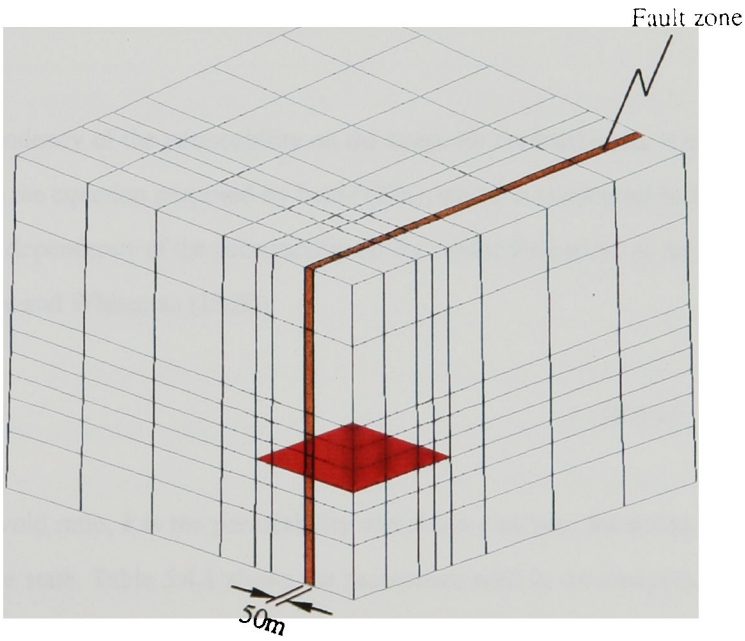
In this section, an imaginary depository of high level radioactive waste is examined for its safety. The depository is set at the depth of 1000 m under the ground surface as shown in Figure 5.4.1. The region to be analyzed is 2000 m x 2000 m (horizontal area) x 1500 m (depth). The heat from the depository is generated by the radioactive decay of the waste disposed in it. The vitrified wastes are assumed to be disposed after the interim storage of 30 years, of which heat generation is assumed as shown in Figure 5.4.2.

The total number of vitrified wastes is assumed to be 10000, which are disposed at the area of 1,000,000 m^2. Thus, the density of the disposed vitrified wastes is one canister per 100 m^2.The analyses are carried out for the quarter of the total region. The total hydraulic head at the ground surface is fixed at 0 tf/m^2, and the other boundary conditions are set at no-flow condition. Namely, the natural ground water flow is assumed to be negligible, which situation is approximately achieved at a place between mountains or a valley. The ground water flow is occurred due to the only temperature gradient. In the analyses, the natural temperature gradient in the direction of depth is assumed to be 3°C/100 m, and the buoyancy due to the natural temperature gradient is not calculated explicitly and the natural temperature gradient is given as the initial condition. Thus, the buoyancy is occurred from the temperature change due to the heat generation of the canisters at the depository because the initial state is considered as the reference state in the analyses. The effect of the natural temperature gradient on the ground water flow is examined separately from the examination of the effect of the heat generation from the depository.

The analyses are carried out for two cases; Case 1 is the case where the ground consists of a kind of rock and Case 2 is the case where the ground have two kinds of geology as shown in Figure 5.4.1. The permeability is assumed to be dependent on the stress at the point for the hard rock and dependent on the void ratio change for the fault



(a) Case 1



(b) Case 2

Figure 5.4.1 Schematic view of the imaginary depository and finite element mesh used for the coupled analyses

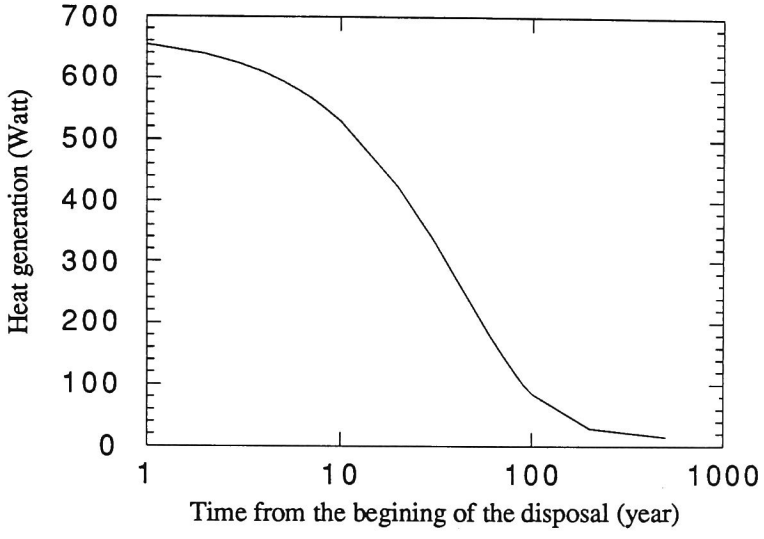


Figure 5.4.2 Heat generation from a vitrified waste

zone. The dependency of the permeability on the stress for the hard rocks is assumed to be according to the equation proposed by Iwai (1976), which is introduced in the section 3.3, and the the dependency of the permeability on the void ratio is given as the following equation (Lambe and Whiteman (1969));

$$k = k_0 \, 10^{\frac{e - e_0}{d}} \qquad (5.4.1)$$

where e is the void ratio, k is the permeability and d is a constant. Subscript, 0, stands for the reference state. Table 5.4.1 shows the parameters used in the analyses, in which the parameters without the description of the geology hold for both hard rock and fracture zone.

Transport analyses is carried out by using the velocity field obtained from the coupled analyses. The concentration at the depository is set at 1 during the analysis, which means

the solute leaks from the depository homogeneously and steadily. Since the leakage condition of the solute from the depository is dependent on the various conditions of the depository system, it is very difficult to decide the leakage concentration and the point in the depository. Thus, this assumption is convenient while this is very conservative for the safety assessment of a depository. Since the source concentration is 1, the evaluated concentration of the solute is estimated as the percentage of the source concentration. All boundary condition of the transport analyses is given as

$$D\frac{\partial c}{\partial \mathbf{n}} = 0 \tag{5.4.2}$$

where **n** is the normal vector of the boundary.

Table 5.4.1 Parameters used in the coupled and transport analyses

Coupled analyses		Transport analyses	
Parameters	Values	Parameters	Values
Young's Modulus (Hard rock)	5×10^5 tf/m^2	Dispersivity	10 m
Young's Modulus (Fault zone)	5×10^4 tf/m^2	Retardation factor (Cs)	64
Poisson's Ratio	0.3	Retardation factor (Pu)	3151
Initial void ratio (Hard rock)	0.02	Decay coefficient (Cs)	0.0231
Initial void ratio (Fault zone)	0.4	Decay coefficient (Pu)	2.888×10^{-5}
Intrinsic permeability (Hard rock)*1	10^{-12} m^2		
Intrinsic permeability (Fault zone)*2	10^{-10} m^2		
Specific heat of solid	42.6 m/°C		
Heat conductivity of solid	2.12×10^{-4} tf/°Cs		
Thermal expansion coefficient	6.0×10^{-6} °C^{-1}		

*1; Permeability is isotropic and is set according to equation (3.3.40) proposed by Iwai (1976). The coefficients in equation (3.3.40) is set such that the permeability at the depth of depository comes to be 10^{-8} sc.

*2; Permeability is isotropic and is set according to equation (5.4.1). The coefficient d is set at 0.1.

5.4.2 Analysis method and strategy

The velocity field is obtained from the coupled thermal, mechanical and hydraulic analysis with THAMES3D introduced in Chapter 3. The permeability is dependent on the stress state or the void ratio as mentioned above. The deformation and ground water flow are occurred from the change in temperature induced by the heat generation from the depository. In the analyses, the natural temperature gradient is set at 3°C/100 m and the temperature at the ground surface is fixed at 15°C. These natural temperature state is given as the initial state for the model. Since the reference state is equal to the initial state in the analyses, the thermal expansion and buoyancy due to the natural temperature gradient is not introduced into the numerical results.

The density of water is obtained from

$$\rho_f = \rho_{f0}\left[1 - \beta_T(T - T_0) + \beta_p(p - p_0)\right] \qquad (5.4.3)$$

where ρ_f is the density of water at the temperature T and the water pressure p. The subscript, 0, stands for the reference state. β_p is the compressibility of water, 4.9 x 10^{-6} $tf^{-1}m^{-2}$ and β_T is the thermal expansion coefficient of water, 5 x 10^{-4} $°C^{-1}$. Using the above equation and setting the reference state at the state at the ground surface, i.e., the temperature of 15°C and the density of water of 0.99910 t/m3, the steady hydraulic gradient induced by the natural temperature gradient is about 9.5 x 10^{-6}. Using this hydraulic gradient and the permeability at the place near the ground surface, which is the largest value of the permeability of the analysis region, the steady velocity of the ground water is estimated at about 4 x 10^{-6} m/year. As the results of the coupled analyses, the velocity near the depository is larger than the steady velocity by the natural temperature gradient until 200 years from the beginning of the disposal. As the fact of matter, since the permeability at the depth of 1000 m is much smaller than the one near the surface, the steady velocity by the natural temperature gradient, estimated above, is expected to be very conservative. Thus, the velocity of ground water induced by the heat generation at

the depository is expected to be larger than the steady velocity by the natural temperature gradient during a few hundreds years. In this section, the solute transport analyses with the velocity induced by the heat generation at the depository are carried out for the period of 500 years from the beginning of the disposal of the wastes. Then, the transport analyses at the steady state is carried out by using the steady velocity induced from the natural temperature gradient. Through both analyses, the safety of the high level radioactive waste disposal is examined. The radioactive nuclides to be analyzed are ^{137}Cs and ^{239}Pu, which are selected as the representatives of the short and long half life nuclides. The transport analyses are carried out with the finite element mesh which is refined by dividing a element into eight elements in order to reduce the numerical dispersion. The parameters used in the transport analyses are shown in Table 5.4.1.

5.4.3 Results

(1) Coupled analyses of Case 1

In this case, the model shown in Figure 5.4.1 (a) is used for the analyses. Figure 5.4.3 shows the temperature history at the center of the depository and the place at 100 m over the center of the depository. It is found that temperature history has the peak, which is delayed with the distance from the depository. The value of the peak is small at the place distant from the depository.

Figures 5.4.4 (a) and (b) show the temperature distributions after 50 years and 500 years from the beginning of the disposal. Although the temperature at the depository after 50 years is higher than the one after 500 years, the temperature at the place about 300 m distant from the depository after 500 years is higher than the one after 50 years (refer the scale shown in Figure 5.4.1). Figure 5.4.5 shows the velocity distribution of ground water after 50 years. It is found that the ground water moves radially from the depository. The value of velocity at the place 100 m over the center of the depository is changed as shown in Figure 5.4.6. The velocity has the peak also, although the time of

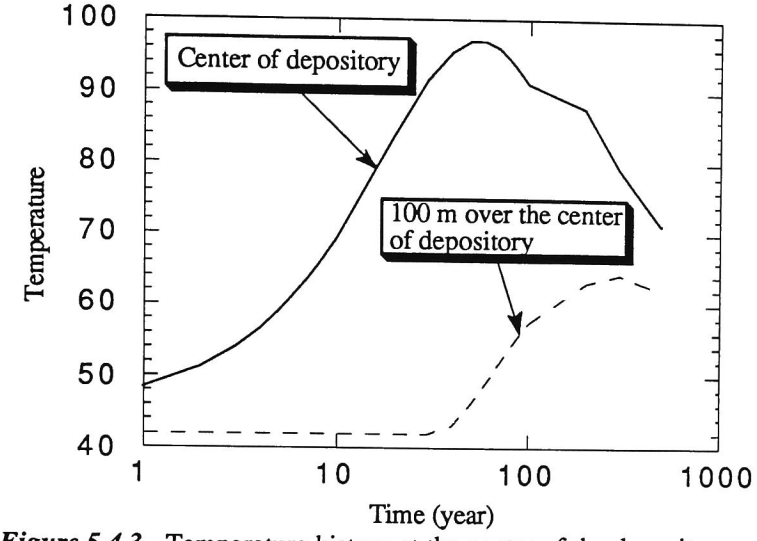
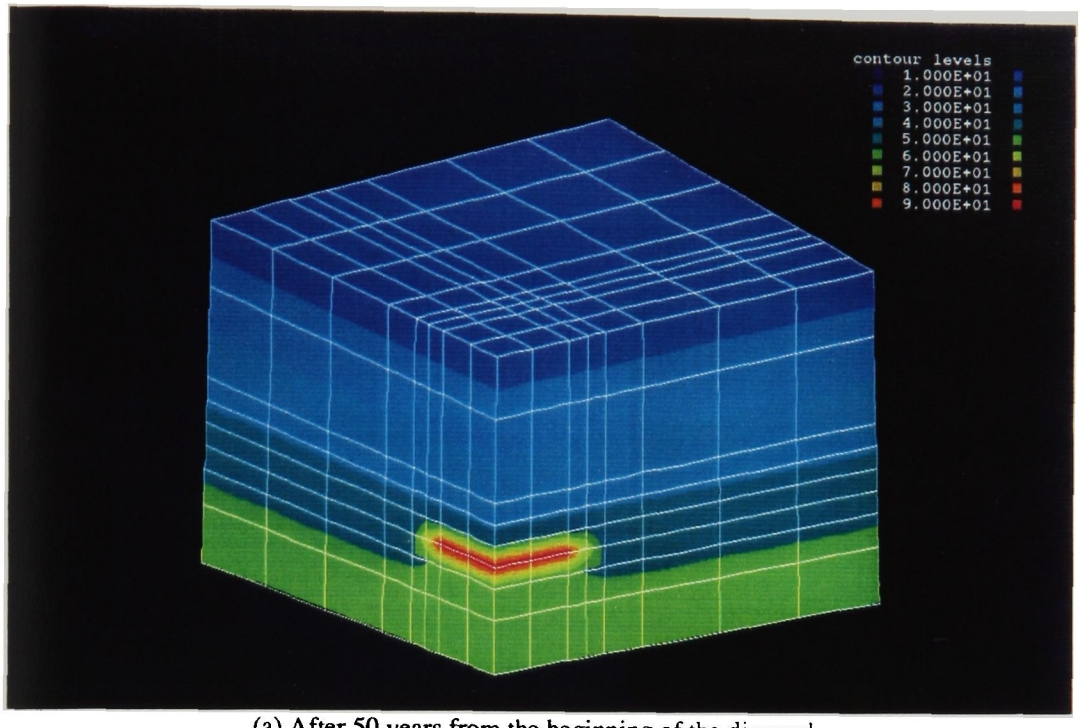


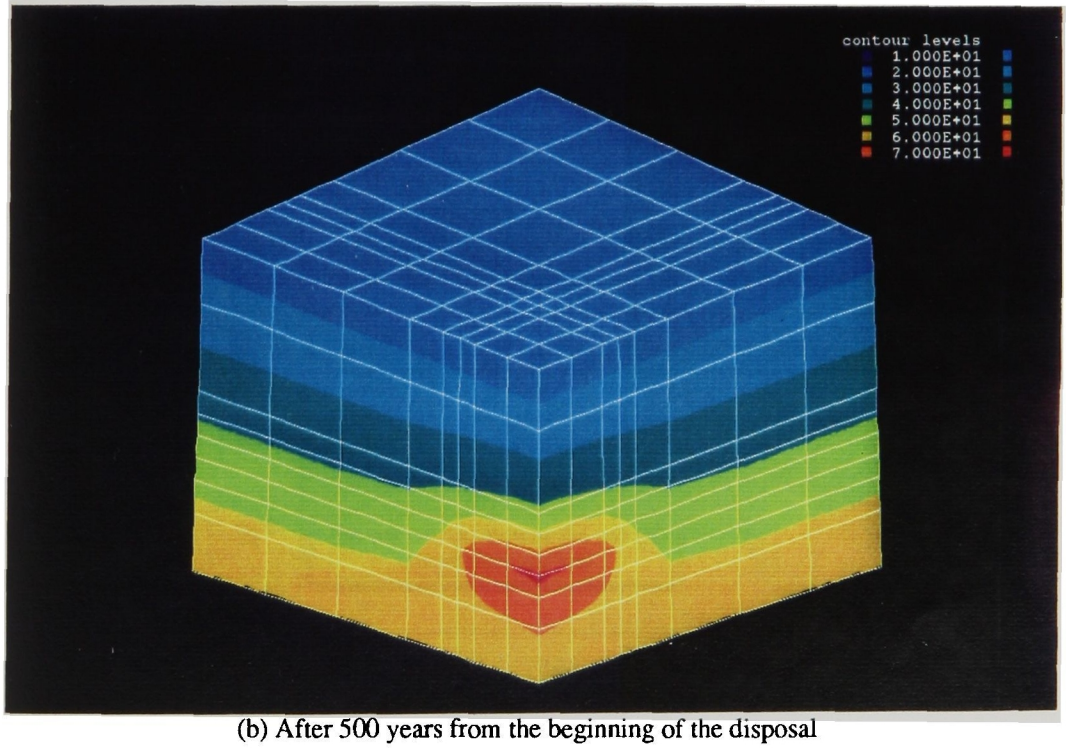
Figure 5.4.3 Temperature history at the center of the depository and the place at 100 m over the center of the depository.

the peak of the velocity is faster than that of the temperature shown in Figure 5.4.3. The velocity inferred from the natural temperature gradient is also shown in Figure 5.4.6. As mentioned above, the velocity induced by the heat generation at the depository becomes smaller than the one induced by the natural temperature gradient after a few hundred years from the beginning of the disposal. This is because the temperature gradient induced by the heat generation at the depository is smaller than the natural one.

Figure 5.4.7 shows the deformation distributions after 50 and 500 years. It is found that the deformation after 50 years is occurred near the depository, while the deformation after 500 years is occurred at the place far from the depository (in the figure, one node near the repository has the fixed deformation condition in error. The deformation should be examined without considering the node.). Figure 5.4.8 shows the history of the upward deformation at the place 100 m over the center of the depository. The peak of the thermal expansion is faster than the peak of the temperature shown in Figure 5.4.3. The shrinking occurs due to the decrease in temperature of the lower place.



(a) After 50 years from the beginning of the disposal



(b) After 500 years from the beginning of the disposal

Figure 5.4.4 Temperature distribution of Case 1

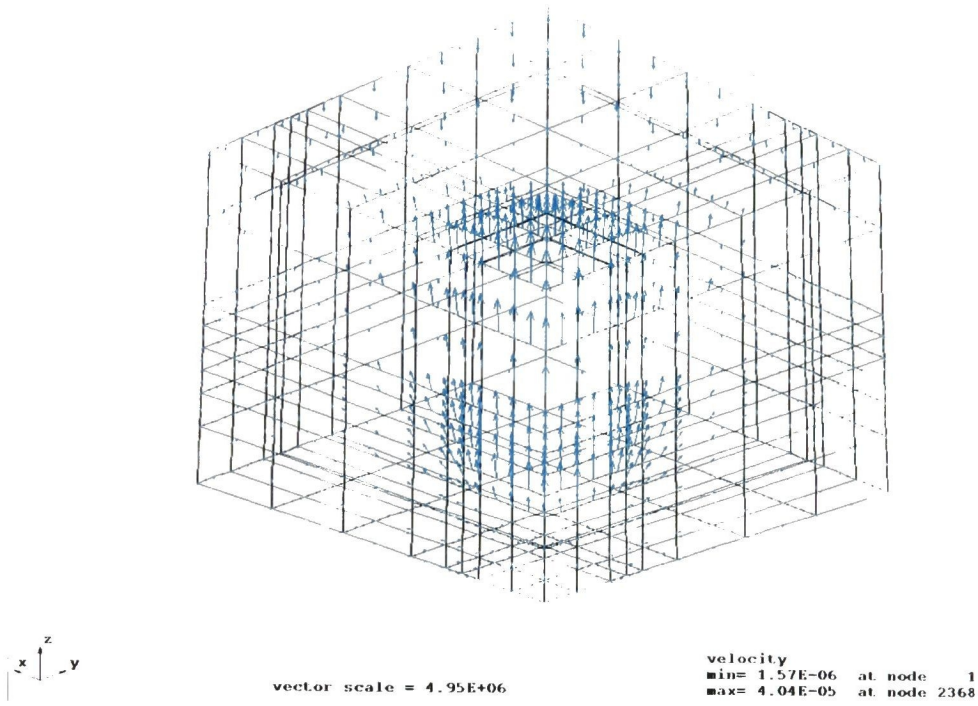


Figure 5.4.5 Velocity distribution of Case 1 after 50 years from the beginning of the disposal

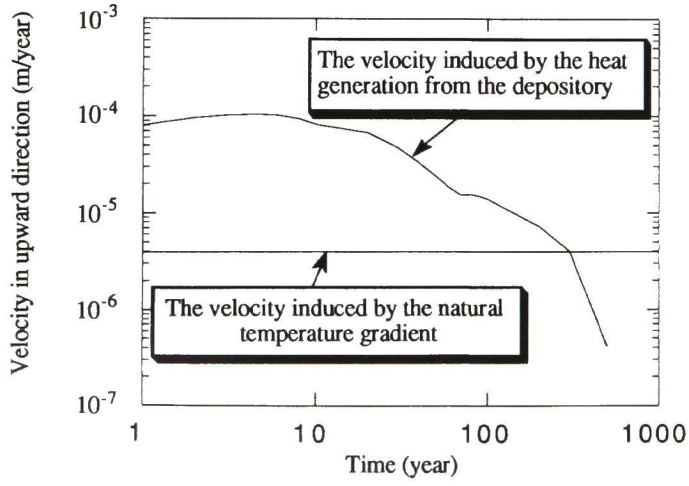
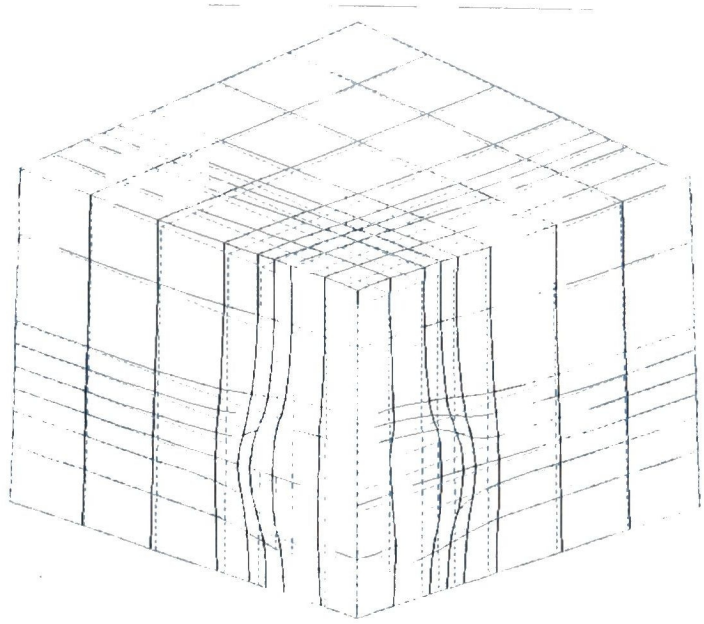
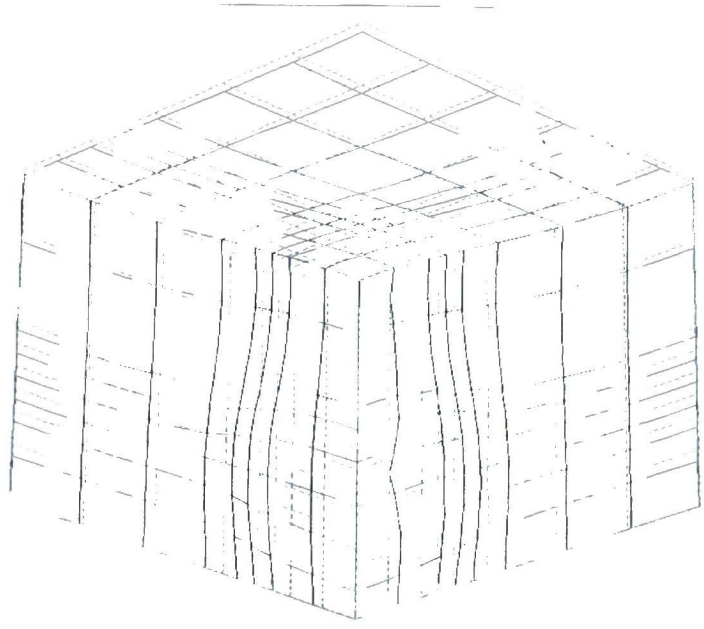


Figure 5.4.6 History of upward velocity at the place 100 m over the center of the depository



(a) After 50 years from the beginning of the disposal



(b) After 500 years from the beginning of the disposal

Figure 5.4.7 Deformation distribution of Case 1

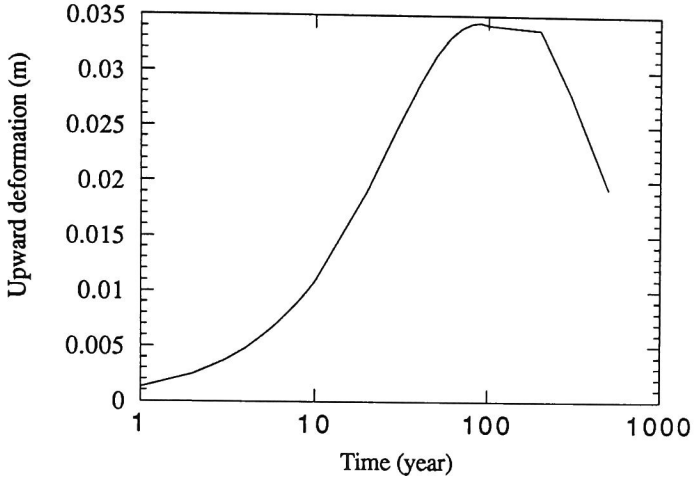


Figure 5.4.8 History of upward deformation at the place 100 m over the center of the depository

(2) Coupled analyses of Case 2

In this case, the fault zone is set such as to cross the depository as shown in Figure 5.4.1, which zone is supposed to be very soft and permeable. Figure 5.4.9 shows the temperature distribution after 50 years from the beginning of the disposal. It is found that the heat transfers faster at the fault zone than at the hard rock and that the temperature at the depository across the fault zone is higher than 100 °C. This is because that the great convection due to high permeability of the fault zone accelerates the upward heat transfer and that the high void ratio of the fault zone induces the high specific heat of the ground. Figure 5.4.10 shows the velocity distribution of the ground water after 50 years from the beginning of the disposal. The velocity is high at the fault zone and the ground water moves radially from the depository. Figure 5.4.11 shows the deformation of the ground at the same time. The fault zone near the depository is much deformed due to the expan-

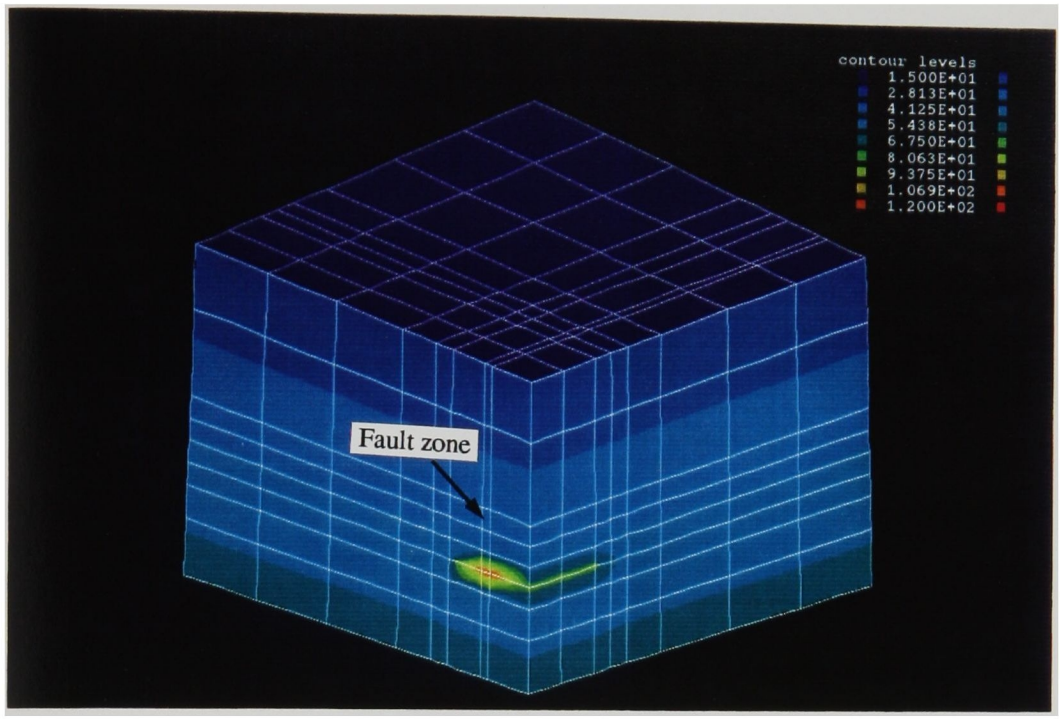


Figure 5.4.9 Temperature distribution of Case 2 after 50 years from the beginning of the disposal

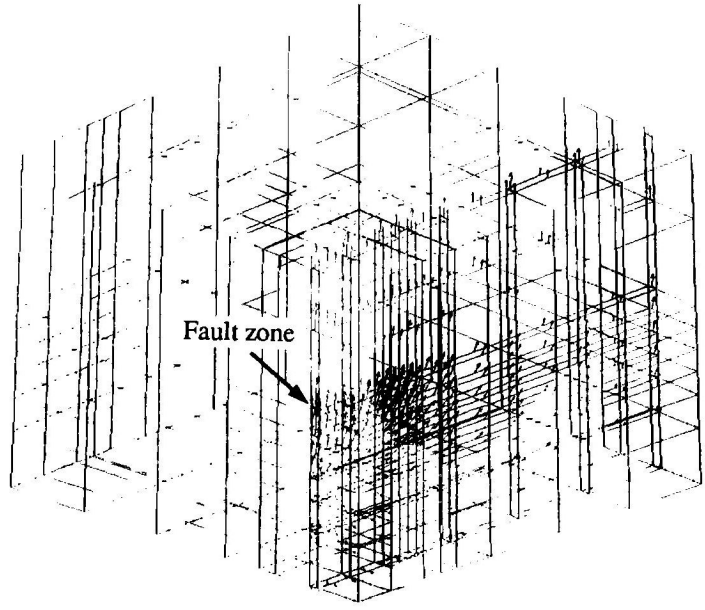


Figure 5.4.10 Velocity distribution of Case 2 after 50 years from the beginning of the disposal

sion of the adjoining hard rock. The situation of Case 2 is very critical for the high level radioactive waste depository. The depository is primarily expected not to be constructed at the place where the large fault zone exists. However, many important structures have been constructed on the faults in Japan because of the difficulty of identification of the fault. Thus, it may be well that the depository encounter the fault zone such as the one is shown in Figure 5.4.1 (b). If the safety is confirmed for such a case, the performance of the depository will be proved for the validity.

(3) Transport analyses of Case 1

As mentioned above, ^{137}Cs and ^{239}Pu are considered as the solute leaking out of the depository. ^{137} Cs has the half life of 30 year and ^{239}Pu has the half life of 2.4×10^4 year. Figure 5.4.12 shows the concentration distribution of ^{137}Cs after 50 years from the beginning of the disposal. Although the stripes in the figure show the oscillation of the solution, those do not have a great effect on the examination because those oscillation occurs at the region of zero concentration in substance. Since the velocity is very small and the half life is very short, ^{137}Cs does not move so much from the depository. After 500 years, the concentration of ^{137}Cs in the ground becomes very small due to the radioactive decay. Figure 5.4.13 shows the concentration distribution of ^{137}Cs after 50 years at the case in which the velocity is set at 100 times the value of the velocity obtained from the coupled analysis. This situation approximately coincides with the case in which the permeability is 100 times the one used in the coupled analyses. The permeability at the depth of 1000 m from the ground surface is about 10^{-6} m/year in this case. This is very permeable geology and such a geology may not exist at the depth of 1000 m of the real ground. In spite of such a situation, ^{137}Cs is expected not to move so much from the depository as shown in Figure 5.4.13.

Figure 5.4.14 shows the concentration distribution of ^{239}Pu after 500 years from the beginning of the disposal. Since ^{239}Pu has a long half life, the decrease in the concentration due to radioactive decay is not occurred at this time. However, ^{239}Pu does

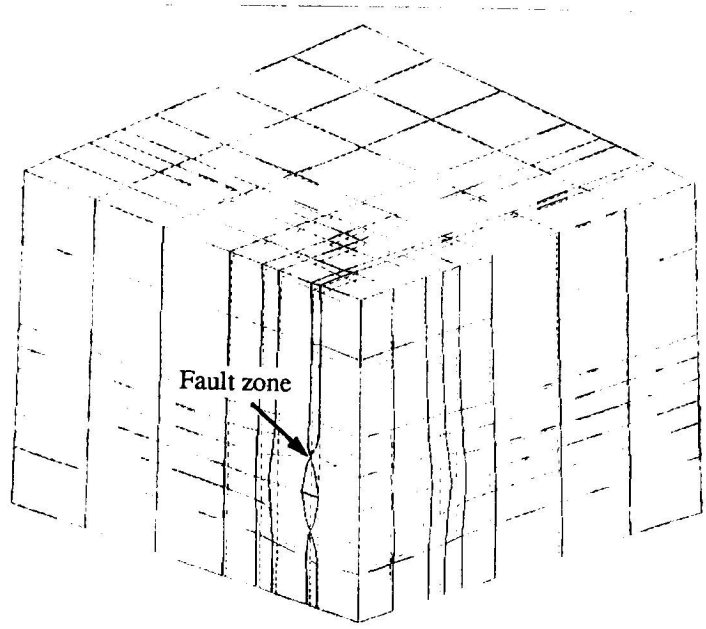


Figure 5.4.11 Deformation distribution of Case 2 after 50 years from the beginning of the disposal

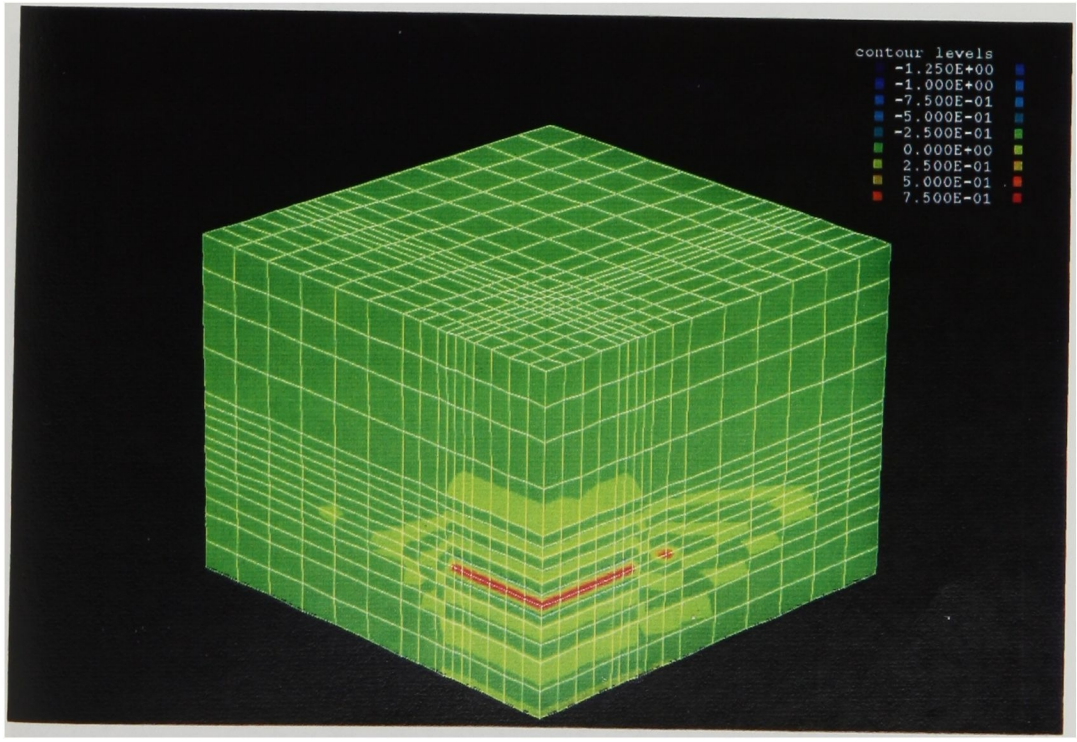


Figure 5.4.12 Concentration distribution of ^{137}Cs after 50 years from the disposal in Case 1

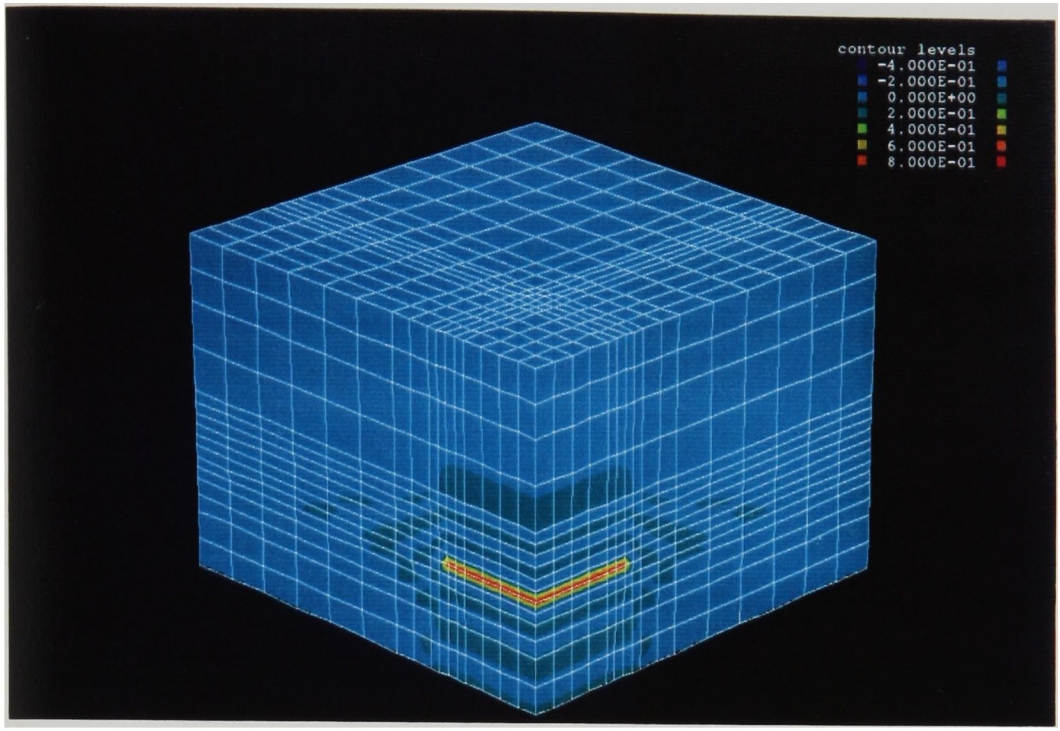


Figure 5.4.13 Concentration distribution of ^{137}Cs after 50 years from the disposal at the case in which the velocity is set at 100 times the one obtained from the coupled analysis of Case 1

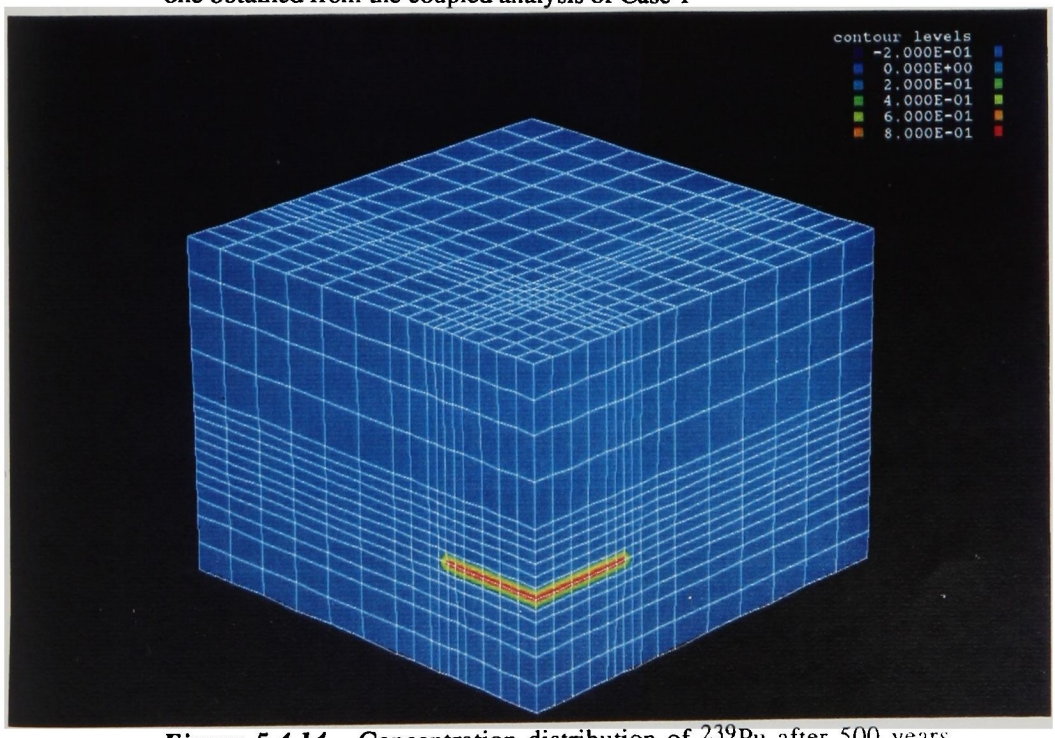


Figure 5.4.14 Concentration distribution of ^{239}Pu after 500 years from the disposal in Case 1

not move from the depository so much because of the very slow velocity and the large retardation factor. Figure 5.4.15 shows the concentration distribution after 500 years at the case in which the velocity is 100 times the one obtained from the coupled analysis. It is also found in this case that ^{239}Pu does not move so much. After a few hundreds years, the ground water flow induced by the heat generation at the depository is expected to be slower than the flow induced by the natural temperature gradient as shown in Figure 5.4.6. The upward velocity induced by the natural temperature gradient is about 4×10^{-6} m/year even if the permeability at the place of the depth of 1000 m is estimated conservatively. Thus, the solute will not move so far from the depository during $10^{4\sim5}$ years while ^{239}Pu does not decay so much during this period of time. Figure 5.4.16 shows the result of the steady state analysis for ^{239}Pu. The velocity used in this analysis is the steady one induced by the natural temperature gradient. It is found from the figure that ^{239}Pu decays before moving so far from the depository.

(4) Transport analyses in Case 2

In this case, the ground water moved mainly through the fault zone. Figure 5.4.17 shows the concentration distribution of ^{127}Cs after 50 years from the beginning of the disposal. ^{127}Cs does not move from the depository. Figure 5.4.18 shows the concentration distribution of ^{127}Cs after 50 years at the case in which the velocity is set at 100 times the one obtained from the coupled analyses. It is found that ^{127}Cs moves through the fault zone. The color of red indicates the concentration over 0.05 % of the source concentration. Figure 5.4.19 shows the concentration distribution after 500 years at the case in which the velocity is set at 100 times the one obtained from the coupled analyses. The color of red in this figure indicates the concentration over 0.1 % of the source concentration. The concentration at the fault zone near the depository becomes higher than the one after 50 years, while the place of zero concentration does not move so much. This is because of the radioactive decay of ^{127}Cs. It may be concluded, thus, that ^{127}Cs does not move to the place far from the depository due to the decrease in the

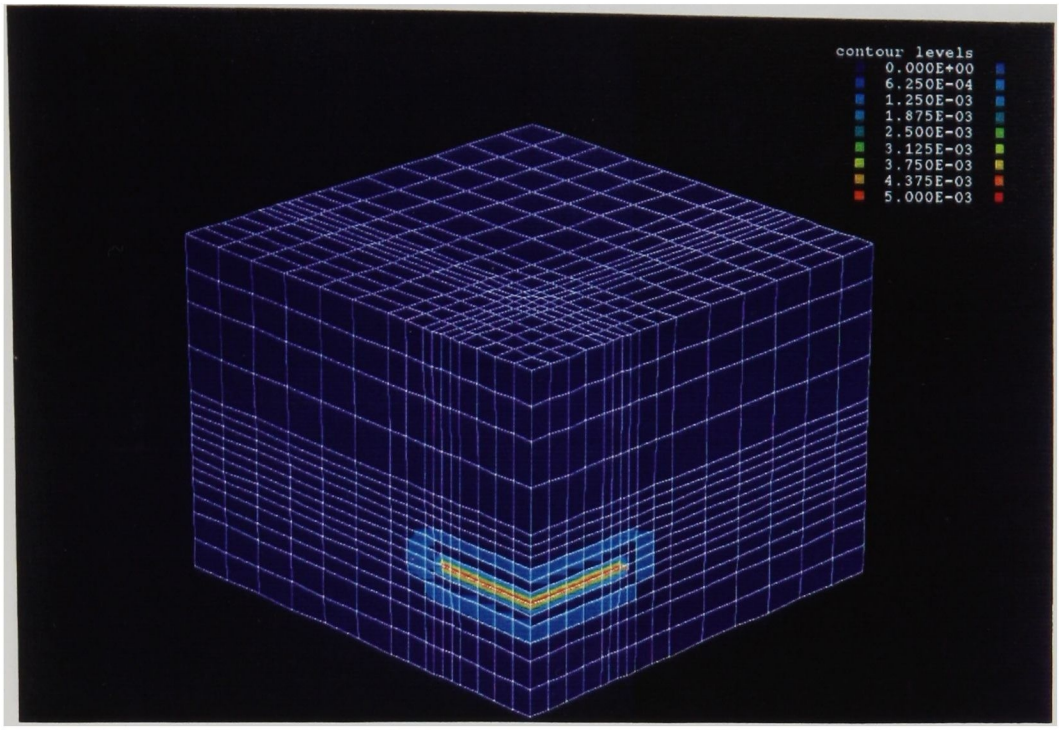


Figure 5.4.15 Concentration distribution of ^{239}Pu after 500 years from the disposal at the case in which the velocity is set at 100 times the one obtained from the coupled analysis of Case 1

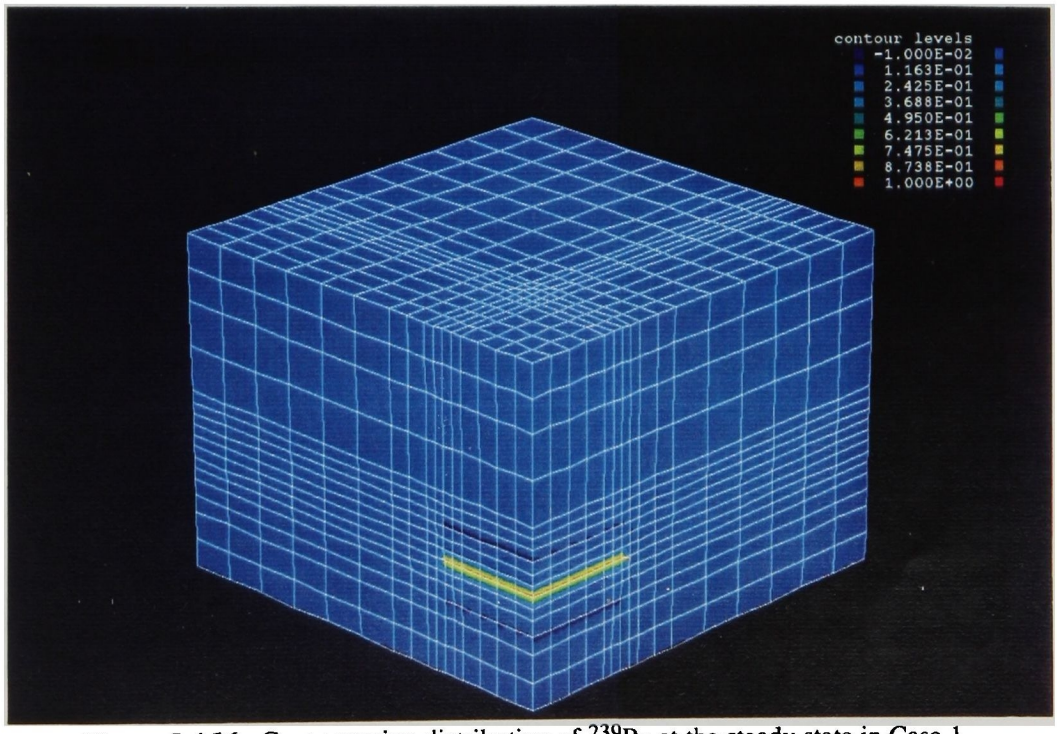


Figure 5.4.16 Concentration distribution of ^{239}Pu at the steady state in Case 1

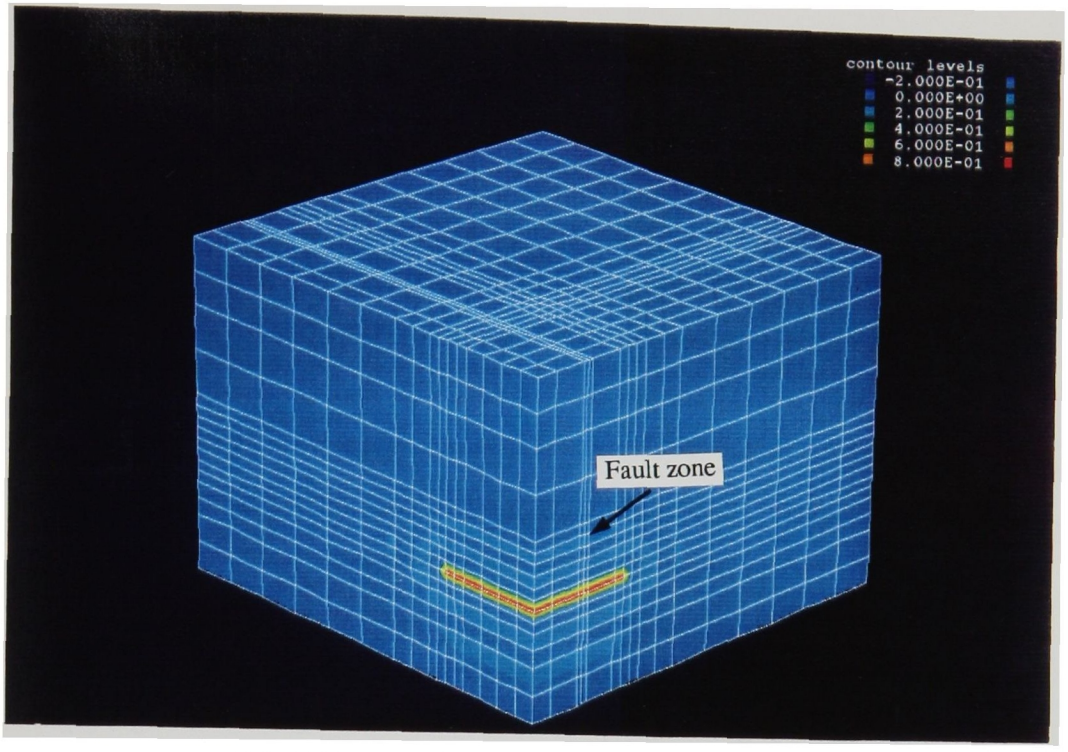


Figure 5.4.17 Concentration distribution of ^{137}Cs after 50 years from the disposal in Case 2

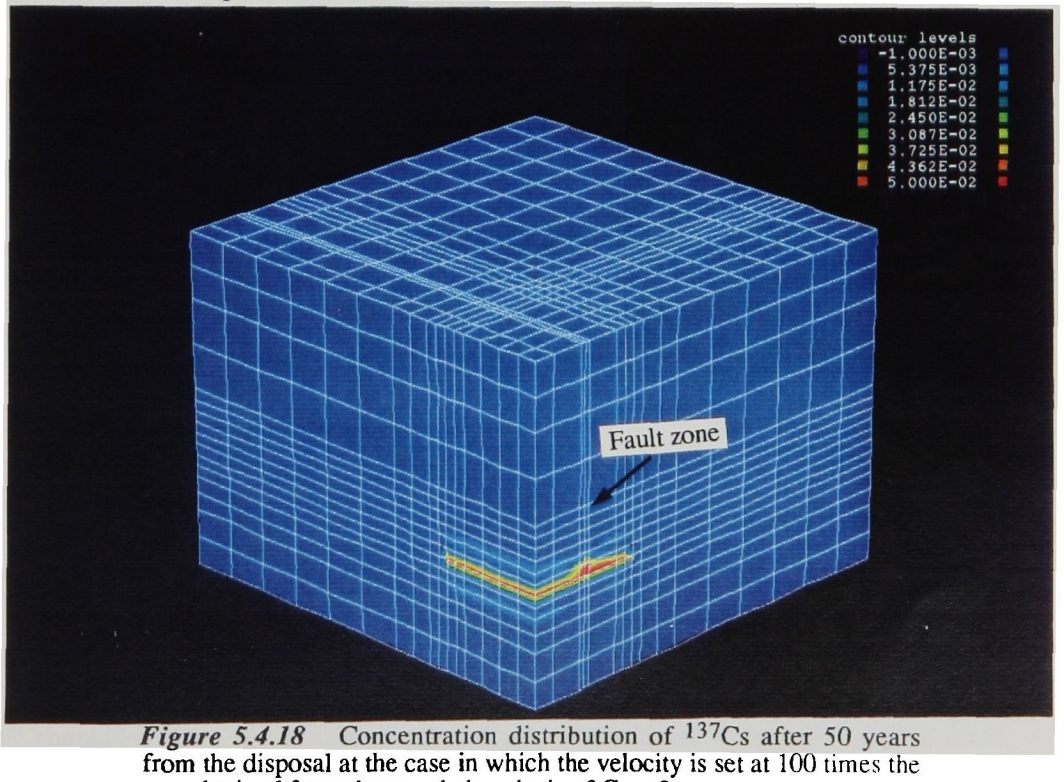


Figure 5.4.18 Concentration distribution of ^{137}Cs after 50 years from the disposal at the case in which the velocity is set at 100 times the one obtained from the coupled analysis of Case 2

concentration by the radioactive decay. Figure 5.4.20 shows the concentration distribution of ^{239}Pu after 500 years from the beginning of the disposal. ^{239}Pu does not move so much from the depository, too. Figure 5.4.21 shows the concentration distribution of ^{239}Pu after 50 years at the case in which the velocity is set at 100 times the one obtained from the coupled analyses. ^{239}Pu moves along the fast velocity in the fault zone. The color of red in this figure indicates the concentration over 0.005 % of the source concentration. Figure 5.4.22 shows the concentration distribution after 500 years at the case in which the velocity is set at 100 times. It is found from Figures 5.4.21 and 22 that the region of which concentration is over 0.005 % of the source concentration is extended and the place of zero concentration is also extended during the period of time. Since the decrease in the concentration due to radioactive decay of ^{239}Pu is little during 500 year, ^{239}Pu moves fast in the fault zone during the period of time. On the other hand, Figure 5.4.23 shows the results of steady analysis by using the steady velocity induced by the natural temperature gradient. The upward velocity in the fault zone is assumed to be 4×10^{-4} m/year. It is found from Figure 5.4.23 that ^{239}Pu decays before moving far from the depository. Thus, ^{239}Pu transported according to the velocity induced by the heat generation at the depository is expected to decay before moving far from the depository during long time because the velocity by the heat generation is expected to be slower than the one by the natural temperature gradient.

5.4.4 Conclusions

In this section, the safety of the imaginary depository was examined by using the thermal, hydraulic and mechanical coupling analyses and the transport analyses. Two type of geology was examined; one was the homogeneous rock and the other was the geology with the large fault zone. The solutes to be analyzed were ^{127}Cs and ^{239}Pu, which are selected as the representatives of the short and long half life nuclide. It was concluded from the results mentioned above that if the depository of high level radioactive waste was constructed at the place where the natural ground water flow was

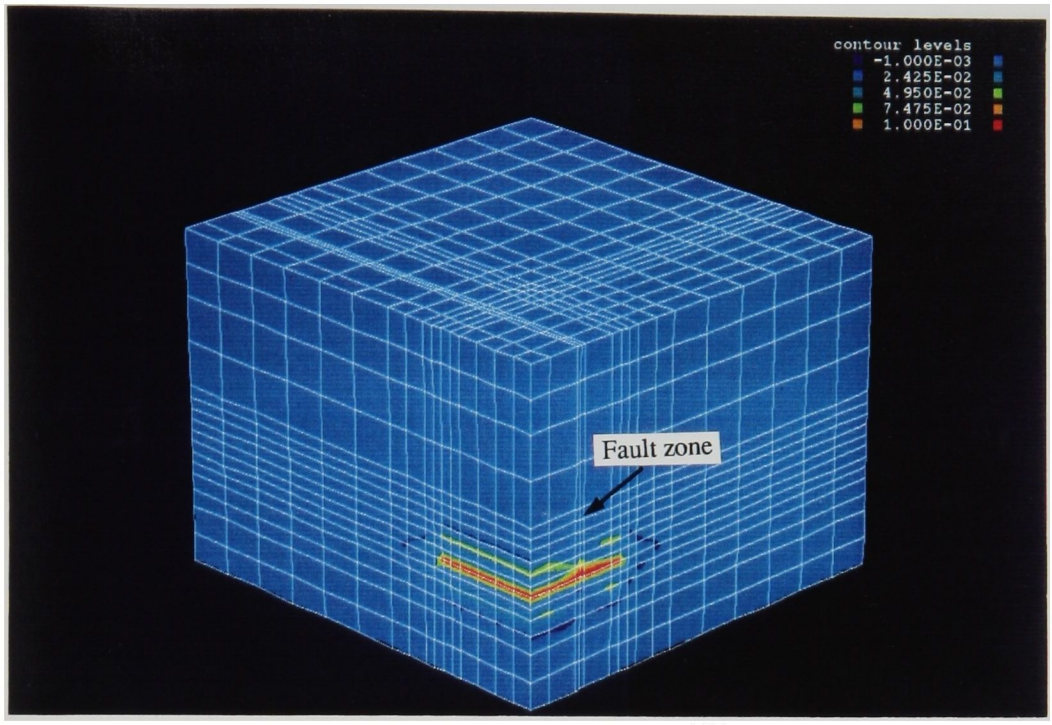


Figure 5.4.19 Concentration distribution of ^{137}Cs after 500 years from the disposal at the case in which the velocity is set at 100 times the one obtained from the coupled analysis of Case 2

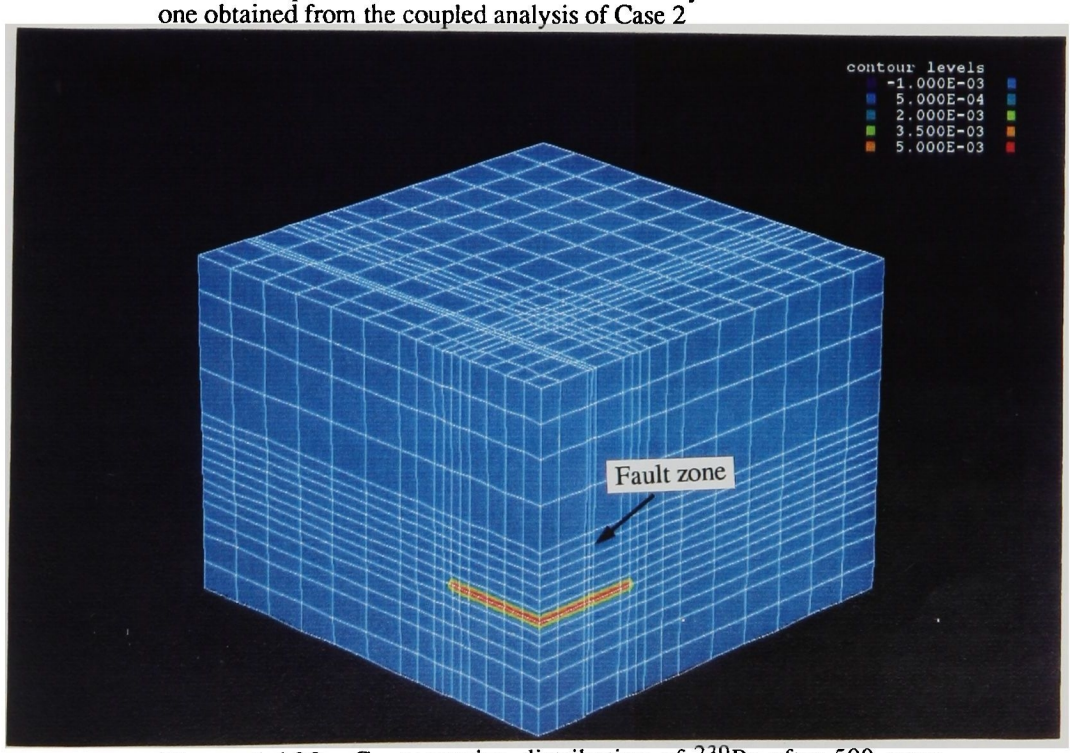


Figure 5.4.20 Concentration distribution of ^{239}Pu after 500 years from the disposal in Case 2

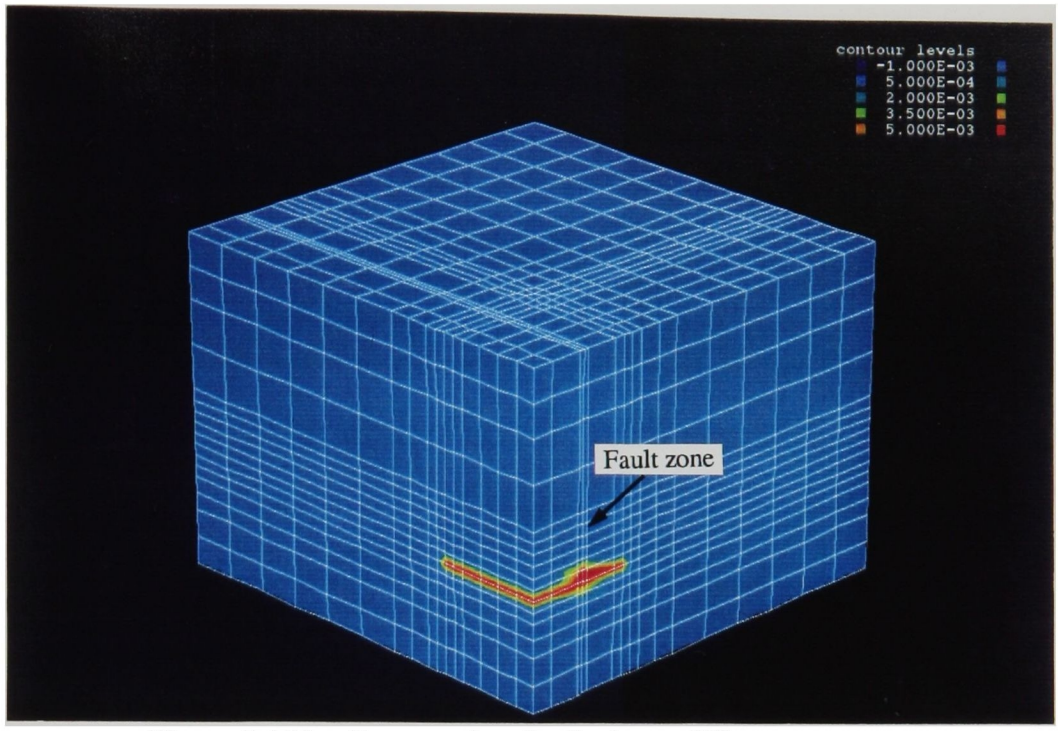


Figure 5.4.21 Concentration distribution of ^{239}Pu after 50 years from the disposal at the case in which the velocity is set at 100 times the one obtained from the coupled analysis of Case 2

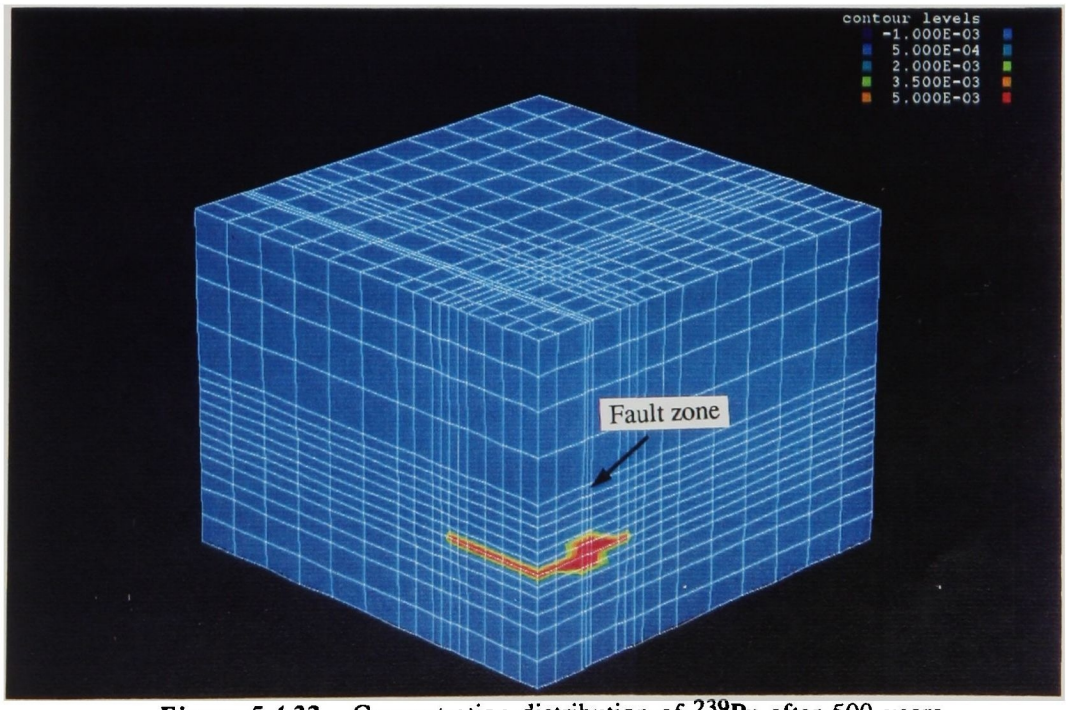


Figure 5.4.22 Concentration distribution of ^{239}Pu after 500 years from the disposal at the case in which the velocity is set at 100 times the one obtained from the coupled analysis of Case 2

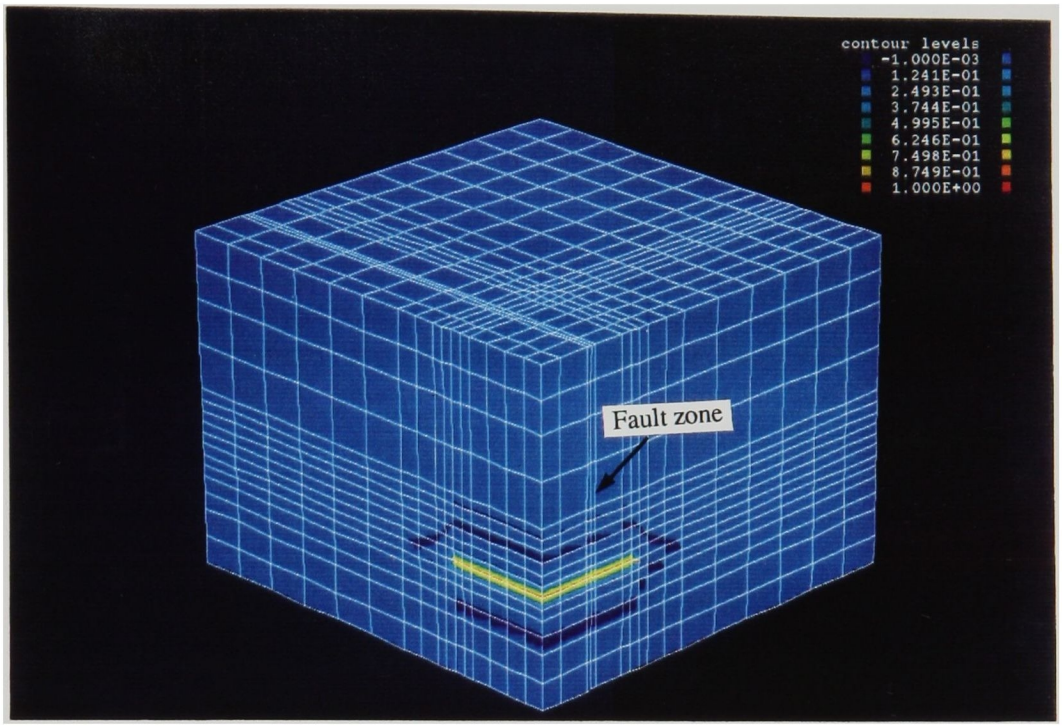


Figure 5.4.23 Concentration distribution of ^{239}Pu at the steady state in Case 2

very small, e.g., the place between mountains and valleys, the radioactive nuclide leaking out of the depository decayed before moving far from the depository. Furthermore, the velocity of the ground water flow induced by the heat generation at the depository became smaller than the one induced by the natural temperature gradient after a few hundreds years from the beginning of the disposal. Thus, the velocity induced by the natural temperature gradient should be used for the examination of the solute transport during very long time. However, the radioactive nuclide is expected to decay before moving far from the depository because the velocity induced by the natural temperature gradient is very slow.

REFERENCES

Noronha, C.J. and A.B. Gureghian: Calibration and validation of the FRACFLO code using the large block migration experiments, Case 9, Draft, Battele Project Management Division, Office of Waste Technology Development, (1988)

Raven, K.G., K.S. Novakowski and P.A. Lapcevic: Interpretation of field tracer tests of a single fracture using a transient solute storage model, Water Resour. Res., Vol. 24, No.12, pp.2019-2032, (1988)

Raven, K.G.: Hydraulic characterization of a small groundwater flow system in fractured monzonitic gneiss, The fourth HYDROCOIN Work shop, (1985)

Abelin, H., I.Neretnieks, S. Tunbrant, L. Moreno: Final report of the migration in a single fracture - Experimental results and evaluation -, Stripa project 85-03, SKB, (1985)

Iwai, K: Fundamental studies of fluid flow through a single fracture, Ph. D. Dissertation, Univ. of California, Berkeley, (1976)

Lambe, T.W. and R.V. Whiteman: Soil mechanics, John Wiley & Sons, Inc., (1969)

Chapter 6 Conclusions

The primary objectives of this study were to investigate the behavior of ground water flow and solute transport in a rock mass and to devise methodologies to analyze such observed phenomena and to predict the future phenomena. Several numerical models were developed to be used for analyzing such phenomena. Firstly, the models to explain the ground water flow in fractured rock masses were examined, and secondly, the coupled effects of the mechanical and thermal phenomena on the hydraulic phenomena were investigated. Thirdly, the models to be used for the solute transport analyses were investigated, and finally, the models of the solute transport in rock masses were applied to a few problems.

In Chapter 2, the ground water flow through fractured media was investigated by numerical analyses. Firstly, the basic theory used for the conventional continuous model was briefly introduced. This theory was extensively used for other newly developed models by the author. Secondly, the technique to investigate a coupled mechanical and hydraulic behavior of saturated-unsaturated fractured rock mass was presented through a double porosity model. This method was applied to the analysis of a secondary compression problem, the Lugeon test simulation and the two-dimensional consolidation problem. It was found that this method could express the various phenomena occurring in a ground. Thirdly, the aperture distribution on a fracture plane was examined through a use of the inhomogeneous permeability distribution in a fracture. The examination was carried out by comparing the dimensionless aperture from the numerical results with that observed at the Stripa mine. As a result, the lognormal distribution, with a large standard deviation, was found to be the real distribution function of the aperture in the Stripa mine. Fourthly, the three-dimensional models of flow in a fractured medium were investigated. The joint element network model was verified by the laboratory test results and the automatic mesh generator, which could define the closed blocks surrounded by randomly distributed fracture planes, was then introduced. Moreover, a new seepage

analysis method, which can express the discontinuous pressure field at a fracture plane in the three-dimensional region, was introduced through a extension of the conventional double porosity model. The proposed three-dimensional mesh generator and flow model were developed by based on the fact that a discontinuous fracture modeling has to be applied to the possible main paths of the ground water, since it is difficult for the Japanese rocks to model all fractures by joint elements. The rock blocks in such a model have many small cracks and fissures and their permeability is not negligible. Applying this new model to the in-situ hydraulic test conducted by CRNL in Canada, the influence of seepage in a rock block on a fracture was examined. As a result, the leakage from adjoining rock block to the fracture was found to have much effects on the flow in the fracture.

In Chapter 3, the coupled effects of the mechanical and thermal behavior on the hydraulic behavior was examined through a newly developed numerical model. The model considers the fully coupled behavior between hydraulic, mechanical and thermal behavior. Firstly, the theory of this model was introduced and this model was verified for the fundamental function of it by comparing with the analytical and experimental solutions. Secondly, the the effects of variable parameters on the coupled behavior were examined through numerical experiments. The dependencies of the parameters of granite on the temperature and stress change were investigated through previous studies. It was found that the thermal conductivity, specific heat, thermal expansivity and permeability of granite had a greater dependency on temperature than the other parameters. The dependency of permeability on temperature was mainly caused by changes in the fracture aperture caused by the thermal expansion of adjoining rock matrix block. It was also found through the numerical experiments that the dependency of thermal conductivity of a granite on temperature had the greatest effect on heat transfer, the dependency of the permeability of a granite on temperature had the greatest effect on the fluid flow and the dependency of the thermal expansivity of a granite on temperature had the greatest effect on thermal expansion. The other dependencies did not affect the coupled phenomena. Among those sensitive dependencies, the changes of the permeability was the most

significant. The permeability very much depended on the low stress level, and its nonlinearity had much influence on the coupled behavior. The second most important dependency was the dependency of the thermal expansivity of a granite on temperature. That of the thermal conductivity was very small for a granite. Thirdly, using this coupled code and considering the material dependencies on temperature and stress, the ground water flow around an underground opening was examined by comparing with the results observed at the macro-permeability test in Stripa project. As results, It was found that a decrease in the flow rate into the opening was caused by an increase in the tangential stress around the opening which was induced by the excavation. In addition, when the temperature was increased, the permeability around the opening decreased due to a closing of the fracture apertures induced by the thermal expansion of adjoining rock matrix blocks. In cases where the temperature was changed, the dependency of the kinematic viscosity on temperature was found to have a great influence on the flow rate change into the opening. Fourthly, the application of the coupled thermal, hydraulic and mechanical analysis methods to the Buffer mass test conducted in the Stripa project was carried out and the examination of the coupled phenomena was tried through comparison between calculated and observed results. It was found that the temperature distribution was not so much dependent on the complicated heat conductivity distribution in the highly compacted clay, but dependent on the change rate of heat conductivity. In addition, evaporation was inferred to have a serious effect on the water content distribution in the highly compacted clay. It was also found that thermal expansion had much influence on the expansion behavior in the clay in comparison with swelling behavior and that the expansion process was influenced by the material placed in the slot. Although these examinations were carried out through use of many assumptions, the results would be helpful for understanding the phenomena observed at the site. The phenomena are expected to be better understood by refined experiments based on the results of these analyses. Finally, the three-dimensional analysis code for the detail assessment of the fully coupled thermal, hydraulic and mechanic behavior was developed. This code used the preconditioned conjugate gradient method in order to save

the computer storage and calculation time. The verification of the code was carried out for the consolidation problem, thermal stress problem and heat transfer problem in the advection-dispersion field. Furthermore, the ability of this code for the assessment of disposal was demonstrated by using an imaginary repository in a granite rock mass. From the comparison with two-dimensional analysis results, it was found that the two-dimensional analysis estimates larger thermal expansion due to the heat generation at the depository than the three dimensional one. In addition, the fluid flow due to the buoyancy was found not to be small at the vicinity of site.

In Chapter 4, the solute transport problem under ground was discussed. Firstly, a two-dimensional problem using the equilibrium isotherm and single-site adsorption model was examined. The upstream method was introduced and investigated for its applicability. As a result, in order to examine this applicability, the Peclet number of real phenomena should be estimated by the equation proposed by Neuman (1990), of which the characteristic length corresponds to the integral scale in the analyses and the dispersion coefficient is a macroscopic one. Using such a definition of the Peclet number and a common technique to reduce numerical dispersion into the upstream finite element scheme, it was found that the upstream finite element scheme could be applied to transport problems on a regional scale. Then, the Eulerian and Lagrangian method proposed by Neuman (1981), which was very effective for any Peclet number, was examined. It was found that the proposed interpolation method of concentration distribution and the seepage analysis method, using velocity as the nodal value, are effective to avoid numerical errors in the Eulerian and Lagrangian method. Moreover, using the Eulerian and Lagrangian method, numerical errors were found to decrease with an increase in the Courant number, while numerical errors increased with an increase in the Peclet number. In addition, it became clear that the Eulerian and Lagrangian method by Neuman was different from the conventional method of characteristics at the point that the concentration is thoroughly separated into the one moved by advection and the one moved by dispersion in the dispersion analyses, and that the implicit solving method could be used in the dispersion analyses. Secondly, the adsorption models different from

the isothermal instantaneous and single-site adsorption model were examined. The effectiveness of these models for the solute transport analysis in a heterogeneous filed was specially investigated. The effects of the geological heterogeneity on the effluent breakthrough curve and solute concentration distribution in a medium was examined with numerical method, in which the mean behavior was obtained from many realizations of a heterogeneous flow field. Moreover, the ability of the homogeneous model to express the phenomena such as the skewness and tailing in breakthrough curve and the non-smooth concentration distribution in a medium was examined through the comparison of the results of various models, i.e. double porosity, non-equilibrium and two-site models. As results, it was found that the skewness of the breakthrough curve was introduced by the situation where the volumetric rate of the more permeable and less adsorptive parts was less than that of impermeable and well adsorptive parts in a medium. The tailing phenomena was produced by the situation where the volumetric rate of the more permeable and less adsorptive parts was equal to that of impermeable and well adsorptive parts in a medium. The concentration distribution obtained from the heterogeneous field was not smooth, while the non-smooth distribution was difficult to express by the homogeneous models. The homogeneous models could express the large apparent dispersion and tailing in the breakthrough curve, although the meaning of the parameters were not clear well.

Finally, the new three-dimensional model for the transport problem in fractured rock masses was introduced, in which the dilution effect of the concentration in the fracture due to water leaking from the adjoining rock block was considered. This model was based on the concept that large and permeable discontinuities should have been explicitly expressed as plane fractures and that other small cracks were included implicitly in the rock block surrounding the fracture planes. The leakage from the rock block occurs through the small cracks in it. The matrix diffusion was considered independently of the dilution process because the matrix diffusion was assumed to occur through the micro pores in the rock matrix constituting the rock block. The dilution and the matrix diffusion could cause the solute spread in non-Fickian fashion.

In Chapter 5, the solute transport analyses were applied to real and imaginary problems. Two tests were to be analyzed in order to understand the phenomena. They were the laboratory tracer test for a single fracture in granite, conducted by the AECL in Canada, and the in-situ tracer test at the Chalk River Nuclear Laboratories, AECL. The example for the rough examination of the radioactive waste depository design was concerned with an imaginary tracer test in a rock mass under a temperature gradient.

Since the rock block used in the laboratory experiment by AECL had the natural fracture, the fracture aperture was expected not to be uniform. The channel flow was simulated by using the stochastic approach in which the probability density distribution of aperture was assumed as Gamma function. Then the transport analyses were carried out and the calculated breakthrough curves were compared with the measured ones. It was found that while the solute transport phenomena in each path in the fracture was not sufficiently expressed by the model for the non-adsorbing tracer case, the breakthrough curve averaged at the outlet boundary was simulated roughly by the model. Moreover, both the phenomena occurred in each path and the averaged phenomena for the adsorbing tracer test were expressed well by the numerical model used in this section. The real transport phenomena in each path was expected to be dominated by advection in the case that the adsorption was not occurred and by dispersion in the case that the adsorption was occurred.

Using the model considering the leakage from the adjoining rock blocks to the fractures, the in-situ tracer test at Chalk River Nuclear Laboratories was examined. For transport analyses, in addition to the parameters, i.e., the dispersion coefficient, retardation factor and decay constant, the velocity distribution in the filed of interest is also necessary, which is obtained from the hydraulic conductivity, storativity and the hydraulic initial and boundary conditions. In general, the initial and boundary conditions are given from the results of the geological and topographical surveys. Calibrating these parameters, the most suitable parameters are identified to express the observed phenomena of solute transport and ground water flow. Then, using those identified parameters, the future phenomena is predicted through a calculation. Thus, the

parameters used in the analyses have to be calibrated before prediction by using the initial and boundary conditions at that time. It seems important for the calibration to identify the parameter values consistent with the phenomena from the various points of view. For example of this problem, the velocity distribution of the test had to be identified to express the summation of the drawdown of the water levels of the injection and withdrawal wells, ΔH. At that time, the aperture, which was used to estimate the transmissivity through the cubic theory, had to be consistent with the results observed at the single borehole injection test and the hydraulic interference tests conducted for this area before the tracer tests. It is necessary, however, for the conventional seepage analysis methods to calibrate the transmissivity in order to change the calculated pressure distribution in the fracture. This causes the change in the velocity in the fracture and the calibration of the transport behavior comes to be difficult. On the other hand, using the flow and transport models considering the interaction between rock blocks and fractures, it was found that the calibration process was easy and systematic. The flow model considering the leakage from the adjoining rock blocks was able to express the observed ΔH by using the same aperture as the one used in the analyses of another tests and by adjusting the leakage rate. Using the velocity distribution from the above flow analysis, the transport phenomena was explained by using the approximately same transport parameters as the ones used in another tests. This approximate consistency of the parameter values through different tests might prove the flow and transport model considering the leakage from the adjoining rock blocks for this area.

The safety of the imaginary depository was examined by using the three-dimensional thermal, hydraulic and mechanical coupling analyses and the transport analyses. Two type of geology was examined; one is the homogeneous rock and the other is the geology with the large fault zone which crosses the depository. The solutes to be analyzed were ^{127}Cs and ^{239}Pu, which were selected as the representatives of the short and long half life nuclide. It was concluded from the analyzed results that if the depository of high level radioactive waste was constructed at the place where the natural ground water flow was very small, e.g., the place between mountains and valleys, the radioactive nuclide leaking

out of the depository decayed before moving far from the depository. Furthermore, the velocity of the ground water flow induced by the heat generation at the depository became smaller than the one induced by the natural temperature gradient after a few hundreds years from the beginning of the disposal. Thus, the velocity induced by the natural temperature gradient should be used for the examination of the solute transport during very long time. However, the radioactive nuclide is expected to decay before moving far from the depository because the velocity induced by the natural temperature gradient is very slow.

A fluid flow analysis is needed for a solute transport analysis in order to obtain the velocity distribution. However, many uncertain mechanisms of the ground water flow exist in a rock mass. To carry out the solute transport analysis with high accuracy, it is necessary to reduce such uncertainties. In this paper, the author has tried to understand the mechanism of the flow in rock masses. For this purpose, a few new numerical methods were developed and applied to the supposed field experiments, the real field experiments and the laboratory experiments. It is very difficult to understand the real phenomena only by the results of the field and laboratory measurements. Thus, a numerical approach that can express various behavior is very effective for understanding the phenomena.

Recently, the validation of the model has frequently been discussed. However, the author did not try to validate the developed models in this chapter. He attempted to obtain the information vital to the judgment on whether or not a model was suitable for the object of the analysis. This is because the ground conditions are dependent on the site of the given project and also because the problems to be solved are specific to the site and project.